

CRITICAL FLAW SIZE IN SILICON NITRIDE BALL BEARINGS

By

GEORGE ARTHUR LEVESQUE

A DISSERTATION PRESENTED TO THE GRADUATE SCHOOL  
OF THE UNIVERSITY OF FLORIDA IN PARTIAL FULFILLMENT  
OF THE REQUIREMENTS FOR THE DEGREE OF  
DOCTOR OF PHILOSOPHY

UNIVERSITY OF FLORIDA

2009

© 2009 George Arthur Levesque

To My Father

## ACKNOWLEDGMENTS

This project was funded by the United States Air Force under Versatile Affordable Advanced Turbine Engines (VAATE) Contract# F33615-03-D-2353-003 and managed by Robert Wolfe, Manager, Materials Technology, Timken Company, Canton, Ohio. Robert Wolfe is thanked for extensive discussions on all aspects of critical flaw size determination. William Ogden and Herb Chin of Pratt & Whitney Co., Nelson Forster and Vaughn Svendsen of the Air Force Research Labs and Michael J. O'Brien of the Aerospace Corporation are thanked for their insightful contributions. This work has been done while supported by the Timken Company, Canton, OH, and Air Force Research Labs, Dayton, OH.

At the University of Florida there were two collaborations worth noting. Dr. John J. Mecholsky and Karthik Gopalakrishnan have contributed an experimental endeavor on the Brazilian disc test. Also, Dr. Nam-Ho Kim and Sriram Pattabhiraman have contributed in the endeavor of an uncertainty analysis of rolling element survival. In addition, my labmates and my advisor Dr. Nagaraj Arakere are thanked for their support throughout my graduate career

# TABLE OF CONTENTS

	<u>Page</u>
ACKNOWLEDGMENTS.....	4
LIST OF TABLES.....	8
LIST OF FIGURES.....	9
LIST OF ABBREVIATIONS.....	14
NOMENCLATURE.....	15
ABSTRACT.....	19
CHAPTER	
1 INTRODUCTION.....	21
1.1 General Background.....	21
1.1.1 Bearing Design Issues.....	21
1.1.2 Issues With Silicon Nitride.....	22
1.2 Objective And Scope Of Research Work.....	23
1.3 Literature Review.....	24
1.3.1 Rolling Contact Fatigue Loading In Ball Bearings.....	24
1.3.2 Limitations Of Lundberg-Palmgren Theory.....	26
1.3.3 Hertzian Fracture Of Brittle Materials.....	27
1.3.4 Computational Simulation Of Surface Flaws.....	28
1.3.5 Mixed-Mode Fracture Testing.....	30
1.4 State Of The Art From Literature Survey.....	32
1.5 Outline Of Thesis.....	33
1.6 Figures.....	37
2 DETERMINATION OF SURFACE FLAW GEOMETRY.....	45
2.1 Introduction.....	45
2.2 Analysis.....	46
2.2.1 Stress-State Analysis.....	47
2.2.2 Incremental Crack Growth Analysis.....	53
2.3 Results On Crack Shape Determination.....	55
2.4 Conclusions.....	57
2.5 Figures.....	59

3	GENERAL MODELING ISSUES OF SURFACE FLAWS SUBJECT TO ROLLING CONTACT FATIGUE .....	70
3.1	Introduction .....	70
3.2	Computing Stress Intensity Factors .....	71
3.3	Parametric Studies .....	73
3.4	Physical Effects .....	74
3.5	Conclusions .....	75
3.6	Figures .....	76
4	EXPERIMENTAL ANALYSIS .....	84
4.1	A Novel Fracture Toughness Test .....	84
4.2	V-Ring Test .....	85
4.2.1	Experimental Procedure to Determine Growth Regime .....	85
4.2.2	Specimen Analysis .....	86
4.2.3	Stress Intensity Factor Determination Of Individual Test Specimens .....	86
4.2.4	Calculating A $K_{eff}$ .....	87
4.3	Brazilian Disc Test .....	87
4.3.1	Experimental Procedure .....	88
4.3.2	Analytical Expressions for Mixed-Mode Stress Intensity Factors .....	89
4.3.3	Stress Intensity Factor Calculation Via Finite Element Modeling .....	89
4.3.4	Mixed-Mode Fracture Criteria .....	92
4.3.5	Analysis Procedure .....	96
4.3.6	Results And Discussion .....	97
4.4	Conclusions .....	99
4.5	Figures .....	100
5	CFS EVALUATION: COMPUTATIONAL INVESTIGATION .....	117
5.1	Introduction .....	117
5.2	Analytical Procedure .....	120
5.2.1	Crack Geometries Induced By Oblique Interactions Of Silicon Nitride Balls .....	120
5.2.2	Finite Element Modeling Of A Three-Dimensional Surface Flaw .....	122
5.3	Mixed-Mode Stress Intensity Factors Due to Rolling Contact Fatigue .....	124
5.3.1	Effect Of The Variation Of Load Ellipticity On Stress Intensity Factors ..	126
5.3.2	Comparison Of C-Cracks And Semi-Elliptical Cracks .....	127
5.3.3	The Effect Of Traction .....	128
5.3.4	Critical Flaw Size Evaluation Results .....	129
5.4	Conclusions .....	130
5.5	Figures .....	132

6	EMPIRICAL STRESS INTENSITY FACTOR EQUATIONS FOR SURFACE CRACKS UNDER RCF .....	142
6.1	Introduction .....	142
6.2	Analysis.....	143
6.3	Crack Geometry.....	144
6.4	Orientation Of Load .....	145
6.5	Load .....	146
6.6	Results .....	148
6.7	Conclusions .....	149
6.8	Figures .....	157
7	UNCERTAINTY ANALYSIS FOR FATIGUE FAILURE PROBABILITY OF SILICON NITRIDE ROLLING ELEMENT .....	161
7.1	Introduction .....	161
7.2	Modeling Rolling Contact Fatigue Orientation Effects .....	165
7.3	Uncertainty Analysis .....	167
7.3.1	Uncertainty Quantification .....	167
7.3.2	Surrogate Modeling – Uncertainty Propagation.....	169
7.3.3	Uncertainty Analysis – Monte Carlo Simulation Using Surrogate.....	173
7.3.4	Parameter Study.....	176
7.4	Conclusions .....	178
7.5	Figures .....	179
8	DISCUSSION AND CONCLUSIONS.....	186
8.1	Discussion.....	186
8.2	Conclusions .....	188
8.3	Future Work.....	188
 APPENDIX		
A	THE NORMAL INDENTATION OF BRITTLE SPHERES .....	190
B	BUILDING A C-CRACK MODEL.....	195
LIST OF REFERENCES.....		216
BIOGRAPHICAL SKETCH.....		223

## LIST OF TABLES

<u>Table</u>	<u>Page</u>
1-1	Comparison of material properties between fully densified silicon nitride and a common ball material predecessor M50 steel. .... 37
1-2	Measurements for a sense of scale of the problem. .... 41
1-3	RCF tests on ceramics and their failure modes in literature. .... 41
2-1	Estimated c-crack geometries produced by different values of $\mu$ from stress-state analysis. .... 62
4-1	V-ring test conditions for 28.575 mm (1 in.) balls. .... 105
4-2	The sample number, turning angle, crack dimensions and fracture load of each specimen examined. .... 106
4-3	The mean $K_c$ values in $\text{MPa}\sqrt{\text{m}}$ for each method $\pm$ the standard variation ( $\sigma_{\text{std}}$ ). .... 106
6-1	The $x_d$ distances (nondimensionalized w.r.t. the crack semi-width) where $K_I$ was maximal. .... 150
6-2	Coefficients for all parametric cases for $K_I$ , $K_{II}$ , and $K_{III}$ for $\theta = 0^\circ$ . .... 151
6-3	Coefficients for all parametric cases for $K_I$ , $K_{II}$ , and $K_{III}$ for $\theta = 45^\circ$ . .... 153
6-4	Coefficients for all parametric cases for $K_I$ , $K_{II}$ , and $K_{III}$ for $\theta = 60^\circ$ . .... 155
7-1	Input parameters and their distributions for uncertainty analysis ..... 181
7-2	Cross validation errors (PRESSRMS) for different surrogate models. .... 182
7-3	Probability of failure values for different sample sizes ..... 182
7-4	Effects of improvements pertaining to crack size on probability of failure ..... 183
7-5	Effects of improvements pertaining to fracture toughness on probability of failure ..... 183
7-6	Effects of combined improvements pertaining to crack size and fracture toughness on probability of failure. .... 183

## LIST OF FIGURES

<u>Figure</u>	<u>Page</u>
1-1 Image of silicon nitride microstructure where the relative size of the $\alpha$ and $\beta$ grains are apparent. ....	37
1-2 A) Example of a cone crack in silicon nitride B) Experimental image of oblique sphere interaction with contact patch and resultant c-crack shown. ....	38
1-3 Before and after of Timken test #7 of the V-ring single ball test. ....	39
1-4 Image of steel raceway spall from RCF. ....	40
1-5 The elliptical contact patches between the ball and raceways. ....	42
1-6 FEA simulation of a steel raceway section being subjected to contact with a sphere. ....	43
1-7 Fracture stress as a function of dominant defect dimension. ....	44
1-8 Image of a spalled c-crack clearly showing its face as it extends into the material. ....	44
2-1 A) Example of a cone crack in silicon nitride B) Experimental image of oblique sphere interaction with contact patch and resultant c-crack shown. ....	59
2-2 Diagram of coordinate system for the equations of stress for oblique colliding spheres. ....	60
2-3 Surfaces representing constant values of the max principal stress field. ....	61
2-4 A) Cone crack as generated from the Hertzian stresses without traction. B) A c-crack generated for $\nu=0.3$ and $\mu=0.1$ . ....	62
2-5 Initial configuration of crack and load at the beginning of the crack growth analysis in the FE model. ....	63
2-6 Incremental images of crack growth for $\mu=0.1$ . ....	64
2-7 Incremental images of crack growth for $\mu=0.5$ . ....	65
2-8 Cracks produced for $\mu= 0.1, 0.2, 0.3, 0.4,$ and $0.5$ and $\nu=0.28$ . ....	66
2-9 Cross-sections of multiple “natural” c-cracks on 12.7 mm diameter balls that (after manufacturing) had a typical $0.01 \mu\text{m}$ roughness. ....	67
2-10 Cross-sections of artificially produced c-cracks. ....	68

2-11	For $\mu=0.1$ , superposed images of half-cracks produced by the stress-state and the incremental growth. ....	69
3-1	A partial cone crack geometry generated from some experimental cross-sections of the crack created with a spline technique.....	76
3-2	General J-integral equation reference coordinate system.....	76
3-3	Crack tip coordinate systems for CTOD.....	77
3-4	A c-crack specimen with subsurface crack face highlighted above. In tension below, indicating opening of the crack faces.....	78
3-5	Elements from the crack tip in fig 3-3 reoriented to show that different parts of the crack tip undergo all three of the different types of deformation. ....	79
3-6	Visual illustration of the Matlab code which is used to create, submit, post-process, and organize the desired FEA results. ....	80
3-7	An illustration of a ball in a ball-bearing raceway system to indicate the location and orientation of the contact patches.....	80
3-8	Relative orientation of an elliptical load near a surface crack. ....	81
3-9	$K_I$ for $\theta=60^\circ$ near $r=1b$ load for varying aspect ratio. ....	82
3-10	A) worst case orientation of crack and load but if the traction direction is reversed as in B) the crack tends to close. ....	82
3-11	$K_I$ as a function of the coefficient of friction on the surface for $p_o=540$ ksi (3.7 GPa), Crack angle = $30^\circ$ , $b=250$ mm, $a=75$ mm, $a/b=0.3$ . ....	83
4-1	On the left, the designed fixture and a tested ball are displayed. On the right, the platens and ball are placed into the fixture in the orientation for testing.....	100
4-2	Close-up of indentation flaw, with measurement taken in the direction of growth due to applied load. Arrows indicate direction of tensile field.....	101
4-3	The fracture toughness of tested specimens versus the final crack length they became, indicating a lack of interdependence.....	101
4-4	The fracture toughness of tested specimens versus the Vickers indentation load indicating a lack of interdependence. ....	102
4-5	FEA of the ball in the platens undergoing compression, clearly indicating the tensile field along the equator of the ball.....	102
4-6	Pendulum device for impacting balls and inducing cracks .....	103

4-7	Images of V-ring single ball test rig. Lower image shows contact path and cracks oriented within them. ....	104
4-8	Diagram illustrating measurement parameters to classify a c-crack as observed on the surface of a cracked specimen. ....	105
4-9	Schematic showing the flaw orientation on a Brazilian disk specimen as well as the coordinates and components used in the analytical stress equations. ....	107
4-10	Nondimensionalized $K_I$ and $K_{II}$ from empirical equations for different angles of loading orientation for $b=.02m$ $a=.0025m$ . ....	108
4-11	BD test model showing a) global uncracked model with square partition indicating submodel boundaries b) cracked meshed submodel.....	109
4-12	The displacement field of Sample 1 for $\theta=20^\circ$ , to illustrate the presence of $K_{II}$ at the face and $K_{III}$ at the depth.....	109
4-13	$K_I$ for all analyzed specimens as a function of position along the crack front. ....	110
4-14	$K_{II}$ for all analyzed specimens as a function of position along the crack front. ..	111
4-15	$K_{III}$ for all analyzed specimens as a function of position along the crack front. .	112
4-16	$K_{eff}$ using Tanaka's relationship of three SIFs as a function of crack front position. ....	113
4-17	$K_{eff}$ using the strain energy density release rate using all three SIFs as a function of crack front position where a) includes $K_{III}$ and b) neglects it. ....	114
4-18	Plot of $K_{Mi} = \sqrt{(K_I + B K_{III} )^2 + K_{II}^2}$ where $B=1$ . ....	115
4-19	Fractured specimens at various values of $\theta$ .....	115
4-20	Fracture surface of BD specimen showing the crack front growing as it links up with newly formed cracks from indents along the surface.....	116
5-1	Images of artificially induced c-cracks a) ball surface view, and b) a subsurface cross-section extending into the material.....	132
5-2	The elliptic contact patches on the ball surface and the band which they remain in. ....	133
5-3	A) The coordinate system used in the equations to plot the C-crack and B) the rendered 3D crack with notation for the SIF plots to be discussed.....	134
5-4	Illustration of A) displacement correlation variables around an opening two dimensional crack and B) the coordinate systems near the crack tip. ....	135

5-5	Elliptical Hertzian contact load coordinate system and variables for elliptical load simulation. ....	135
5-6	The cross-section of the general worst case orientation with traction for crack tip deformation.....	136
5-7	$K_I$ stress intensity factor for a circular load ( $a_c=250 \mu\text{m}$ ) near a c-crack with a variation in the max pressure magnitude. ....	136
5-8	A plot of the three SIFs as a function of moving load of $P_o=2.8 \text{ GPa}$ . ....	137
5-9	The effect of the ellipticity of the load, on the SIFs on the semi-minor axis of the ellipse, for $P_o=2.8 \text{ GPa}$ (412 Kpsi).....	138
5-10	Superimposed SIFs for a c-crack and penny crack of similar dimensions under elliptical load. ....	139
5-11	The max $K_I$ found on the crack front of a semi-elliptical flaw as a function of varying friction coefficients.....	140
5-12	The nondimensionalized crack semi-width plotted against a) the max $K_{Ieq}$ and b) the max $K_I$ .....	141
6-1	Model configuration displaying orientation of load and defining variables $\theta$ , $\phi$ , and $x_d$ .....	157
6-2	$K_I$ for a single load geometry with and without contact defined.....	158
6-3	$K_I$ for $r=1b$ along the crack front for all variations of crack angle and depth. ....	159
6-4	$K_I$ for $r=2b$ along the crack front for all variations of crack angle and depth. ....	159
6-5	$K_I$ for $r=3b$ along the crack front for all variations of crack angle and depth. ....	160
7-1	Before and after of a partial cone crack placed under rolling contact fatigue. ...	179
7-2	Elliptical Hertzian contact load coordinate system and variables for elliptical load orientation simulation. ....	180
7-3	The elliptic contact patches on the ball surface and the band which they remain in. ....	180
7-4	Surrogate models for the contribution of lateral position to the stress intensity factor .....	181
7-5	Surrogate models for the contribution of crack orientation to the stress intensity factor .....	182

7-6	Cumulative distribution function of the limit state function $g = K_{eq} - K_{th}$ .....	183
7-7	Variation of probability of failure with percentage reduction of crack size. ....	184
7-8	Variation of probability of survival with crack size.....	184
7-9	Variation of probability of survival with crack size for a $K_{th}$ of $4.5 \pm 0.54$ MPavm.....	185

## LIST OF ABBREVIATIONS

<u>Abbreviation</u>	<u>Definition</u>
3D	Three dimensional
BD	Brazilian disc
BEA	Boundary element analysis
CFS	Critical flaw size
EHD	Elastohydrodynamic
FE	Finite element
FEA	Finite element analysis
FPI	Fluorescent penetrant inspection
MCS	Monte Carlo simulation
NDE	Non-destructive evaluation
RCF	Rolling contact fatigue
SIF	Stress intensity Factor\
VAATE	Versatile Affordable Advanced Turbine Engines
w.r.t.	With respect to

## NOMENCLATURE

$a$	Semi-elliptical crack depth
$a'$	Axis dimension of ellipse in x-direction
$a^*$	Revolved ellipse axis dimension in the x-direction for a c-crack
$a_c$	Radius of contact patch size
$a_i$	Coefficients of a polynomial for $K_I$
$b$	Semi-elliptical crack semi-width
$b'$	Axis dimension of ellipse in z-direction
$b^*$	Axis dimension of revolved ellipse in the z-direction for a c-crack
$b_i$	Coefficients of a polynomial for $K_{II}$
$c_d$	Distance between crack and load edge
$c_i$	Coefficients of a polynomial for $K_{III}$
$ds$	Length element along the contour $\Gamma$
$e$	$e = \sqrt{1 - \alpha^2}$
$E$	Young's Modulus
$E_1, E_2$	Young's Moduli for bodies 1 and 2, respectively
$E^*$	Effective Young's Modulus, $\left( \frac{1 - \nu_1}{E_1} + \frac{1 - \nu_2}{E_2} \right)^{-1}$
$f$	Coefficient of Friction
$g$	Limit state function
$G$	Strain energy release rate, $G = \frac{1}{E} (K_I^2 + K_{II}^2) + \frac{2(1 - \nu)}{E} K_{III}^2$
$h$	x-coordinate of crack at surface on x-z plane.

$I_j$	Index function
$J_R$	Rice's contour integral
$J$	$\frac{xy}{3r^4} \left[ \left( \frac{z}{u} \right)^3 - 3 \left( \frac{z}{u} \right) + 2 \right]$
$k$	z-coordinate of crack at surface on x-z plane.
$K_{eq}$	$K_{eq} = \left\{ E \left[ \frac{1}{E} (K_I^2 + K_{II}^2) + \frac{2(1-\nu)}{E} K_{III}^2 \right] \right\}^{0.5}$
$K_{eq}^*$	$K_{eq}^* = K_{eq} / P_o \sqrt{a}$
$K_I$	Opening stress intensity factor
$K_i^*$	$\frac{K_i}{P_o \sqrt{\pi \frac{a}{Q}}} \text{ where } i = I, II, III$
$K_{II}$	Sliding stress intensity factor
$K_{III}$	Tearing stress intensity factor
$K_{th}$	Mixed-mode threshold SIF for crack growth
$m$	Ball mass (when single ball is discussed)
$m^*$	Effective ball mass, (for contacting balls $m = \left( \frac{1}{m_1} + \frac{1}{m_2} \right)^{-1}$ )
$N$	A harmonic potential function (Love, 1927)
$N$	Number of Monte Carlo simulation samples
$N_f$	Number of simulation samples that fail
$N_C$	Number of simulation samples that lie in the contact patch
$O$	Coordinate origin
$p_o$	Max value of pressure in elliptical pressure dome

$p_o^*$	Max Pressure to induce cracking
$P$	Total load
$P_F$	Probability of failure
$Q$	Shape factor for elliptical crack
$R_1, R_2$	Radius of sphere 1 and 2, respectively
$r$	Radial cylindrical coordinate, $\sqrt{x^2 + y^2}$ for circular contact
$r_d$	Distance from crack tip where $u$ , $v$ , and $w$ are measured
$R$	Effective ball radius for a ball on ball interaction, $R \equiv \left( \frac{1}{R_1} + \frac{1}{R_2} \right)^{-1}$
$T$	A harmonic potential function (Love, 1927) with partial derivatives
$T_i$	Components of traction vector
$\mu$	Friction coefficient
$u$	$\sqrt{\frac{1}{2} \left\{ r^2 + z^2 - 1 + \sqrt{(r^2 + z^2 - 1)^2 + 4z^2} \right\}}$
$u, v, w$	Crack face opening, sliding, and shearing displacements
$u_i$	Displacement vector components
$w$	Strain energy density
$\nu$	Poisson's ratio
$V$	Velocity of moving ball
$V_z$	Velocity component of moving ball normal to the contact surface
$x_d$	x-displacement of pressure distribution from coordinate origin
$x_D$	Lateral position of crack to contact patch center
$y_d$	y-displacement of pressure distribution from coordinate origin

$\alpha$	Aspect ratio of load ( $b/a$ )
$\Gamma$	Arbitrary counterclockwise path around the crack tip
$\rho$	Material density
$\phi$	Position along crack front
$\varphi_{pl}$	Angle of principal plane
$\theta$	Angle of crack inclination towards the vertical
$\theta_{max}$	Half the total amount which the crack subtends a circle.
$\sigma_c$	Critical max periphery stress to induce cracking
$\mu'$	Elastic potential
$\nu$	Poisson's ratio
$\nu_1, \nu_2$	Poisson's ratios for bodies 1 and 2 respectively
$\sigma_1, \sigma_2, \sigma_3$	First, second, and third principal stresses where $\sigma_1 \geq \sigma_2 \geq \sigma_3$
$\sigma_c$	Contact periphery stress to induce cracking
$\sigma_{max}$	Contact periphery stress
$\sigma_{max f}$	Contact periphery stress with friction
$\sigma_{ij}^N$	Stress components from normal load
$\sigma_{ij}^T$	Stress components from traction load
$\sigma_{PF}$	Standard deviation of the probability of failure
$\tau_{ij}^N$	Shear components of stress from normal load
$\tau_{ij}^T$	Shear components of stress from traction load
$z, \theta$	Parameters to sample points on a sphere

Abstract of Dissertation Presented to the Graduate School  
of the University of Florida in Partial Fulfillment of the  
Requirements for the Degree of Doctor of Philosophy

CRITICAL FLAW SIZE IN SILICON NITRIDE BALL BEARINGS

By

George Arthur Levesque

December 2009

Chair: Nagaraj K. Arakere  
Major: Mechanical Engineering

Aircraft engine and bearing manufacturers have been aggressively pursuing advanced materials technology systems solutions to meet main shaft-bearing needs of advanced military aircraft engines. Ceramic silicon nitride hybrid bearings are being developed for such high performance applications. Though silicon nitride exhibits many favorable properties such as high compressive strength, high hardness, a third of the density of steel, low coefficient of thermal expansion, and high corrosion and temperature resistance, they also have low fracture toughness and are susceptible to failure from fatigue spalls emanating from pre-existing surface flaws that can grow under rolling contact fatigue (RCF). Rolling elements and raceways are among the most demanding components in aircraft engines due to a combination of high cyclic contact stresses, long expected component lifetimes, corrosive environment, and the high consequence of fatigue failure. The cost of these rolling elements increases exponentially with the decrease in allowable flaw size for service applications. Hence the range of 3D non-planar surface flaw geometries subject to RCF is simulated to determine the critical flaw size (CFS) or the largest allowable flaw that does not grow under service conditions.

This dissertation is a numerical and experimental investigation of surface flaws in ceramic balls subjected to RCF and has resulted in the following analyses:

**Crack Shape Determination:** the nucleation of surface flaws from ball impact that occurs during the manufacturing process is simulated. By examining the subsurface Hertzian stresses between contacting spheres, their applicability to predicting and characterizing crack size and shape is established. It is demonstrated that a wide range of cone and partial cone cracks, observed in practice, can be generated using the proposed approaches.

**RCF Simulation:** the procedure and concerns in modeling nonplanar 3D cracks subject to RCF using FEA for stress intensity factor (SIF) trends observed from parametrically varying different physical effects are plotted and discussed. Included are developments in contact algorithms for 3D nonplanar cracks, meshing of nonplanar cracks for SIFs, parametric studies via MATLAB and other subroutines in python and FORTRAN.

**Establishing Fracture Parameters:** the fracture toughness,  $K_c$ , is determined by using numerical techniques on experimental tests namely the Brazilian disc test and a novel compression test on an indented ball. The fatigue threshold for mixed-mode loading,  $K_{eff}$ , is determined by using a combination of numerical modeling and results from the V-ring single ball RCF test

**CFS Determination:** the range of 3D non-planar surface flaw geometries subject to RCF are simulated to calculate mixed mode SIFs to determine the critical flaw size, or the largest allowable flaw that does not grow under service conditions. The CFS results are presented as a function of Hertzian contact stress, traction magnitude, and crack size.

**Empirical Equations:** accurate empirical equations (response functions) for the  $K_I$ ,  $K_{II}$ , and  $K_{III}$  SIFs for semi-elliptical surface cracks subjected to RCF as a function of the contact patch diameter, angle of crack to the surface, max pressure, position along the crack front, and aspect ratio of the crack are developed via parametric 3D FEA.

**Statistical Probability of Failure:** since the variability in mechanical properties for brittle materials is high a probabilistic investigation of variations in flaw size, flaw orientation, fracture toughness, and Hertzian load on failure probability is conducted to statistically determine the probability of ball failure for an existing flaw subjected to the service conditions.

## CHAPTER 1 INTRODUCTION

### 1.1 General Background

#### 1.1.1 Bearing Design Issues

Advanced rotor systems for military aircraft engines are consistently being designed to operate at higher speeds and efficiencies. The bearings of these aircraft engines are often designed to their limits to meet the increased demands of thrust, speed, and weight. Developments in materials consistently push these limits and the case with hybrid bearings is no different. By combining steel raceways and silicon nitride ( $\text{Si}_3\text{N}_4$ ) balls, researchers have established that:

- $\text{Si}_3\text{N}_4$  balls can improve bearing fatigue life by up to 4 times than their M50 steel replacements and when they reach the end of their fatigue lives they fail in a similar fashion (Miner et al., 1996).
- Hybrid bearings display superior thermal characteristics to their all steel components (Miner et al., 1996).
- Hybrid bearings survived longer (by about 5 times) oil starvation periods than their all steel predecessors (Miner et al., 1996).
- $\text{Si}_3\text{N}_4$  exhibits favorable corrosion resistance (Klemm, 2002).

Though this hybrid system is an improvement over its all-steel predecessors, the research and problems from the implementation are justifiably pursued considering the benefits that the balls provide. Silicon nitride ( $\text{Si}_3\text{N}_4$ ) exhibits favorable material properties for application in hybrid high speed ball bearings such as high compressive strength, high hardness, third of the density of steel, low coefficient of thermal expansion, and high corrosion and temperature resistance. Its corrosion resistance and high hardness are good matches for new raceway materials that are very hard and corrosion resistant. Also, its corrosion resistance is beneficial for harsh environments,

like a NASA shuttle turbo pump (Miner et al., 1996). Comparison is drawn between it and its steel replacement as rolling elements (see Table 1-1) and notes the high modulus, hardness and compressive strength that allow the ball to survive the loads and number of cycles that the engines are designed for.

Silicon nitride is a ceramic that has gone through much development over the past few decades. Silicon nitride balls used in rolling-element bearings is an engineered ceramic product made from  $\beta$  phase  $\text{Si}_3\text{N}_4$  needle-like crystals of approximately  $2\ \mu\text{m}$  grain size held by a glassy phase. Balls for aerospace applications are made by sintering and hot isostatic pressing of  $\text{Si}_3\text{N}_4$  grains with the glassy phase forming roughly 1% of the volume fraction with ball diameter and surface finish held to submicron levels (see Fig 1-1). The final ball dimension is achieved in a lapping process that produces (unavoidable) low velocity ball collisions resulting in surface cracks initiated by the radial tensile stress field at the contact periphery (Wang and Hadfield, 2000, Levesque and Arakere, 2008) (see Fig 1-2).

### **1.1.2 Issues With Silicon Nitride**

Even though there are many beneficial properties of silicon nitride ( $\text{Si}_3\text{N}_4$ ), it also has low fracture toughness (Piotrowski and O'Brien, 2006). Hertzian fractures resulting from light collisions in the manufacturing process are cone cracks for normal interactions and, the more common, c-cracks (or partial cone cracks) for oblique interactions (see Fig 1-2). These surface flaws would be subjected to rolling contact fatigue (RCF) if placed into service as a rolling contact element. These surface flaws often propagate to a fatigue spall and are the leading cause of ball failure (Hadfield, 1993b) (see Fig 1-3). Ball failure quickly results in raceway failure as the higher ball

hardness and rapid rotational speeds machine away the raceway from a simple raceway spall (see Fig 1-4) to a damaged surface.

In addition, brittle materials generally exhibit much variation for similar interactions. For example, there is a significant variation in the depth of a crack from a controlled impact (Lawn 1967, Wang and Hadfield 2000). Also, there is a noted variation in the fracture toughness specimen to specimen (for example  $4.85 \pm 0.36 \text{ MPa}\sqrt{\text{m}}$ , Piotrowski and O'Brien, 2006). The material variations have a direct dependence on how each specimen is manufactured.

While the flaws (illustrated in Fig. 1-2) can be readily induced and are generally present, methods for their detection prior to service is still in development. Development of a non-destructive evaluation (NDE) method is complicated because these cracks are often no more than  $500 \mu\text{m}$  (approximately the width of two human hairs) long on the surface and are difficult to find under a microscope. In addition, the material is nonconductive and only slightly translucent which complicates optical inspection procedures. From a fracture mechanics and structural integrity perspective, the largest allowable surface flaw that does not propagate under RCF loading is of design significance, and is termed the critical flaw size.

## **1.2 Objective And Scope Of Research Work**

The main objective of the study presented in this thesis is utilize and develop numerical and analytical techniques to investigate general three dimensional (3D) nonplanar surface flaws subjected to the physical effects of RCF to determine their influence on the possibility of rolling element survival after the service conditions.. The scope of this study includes: (1) determining a surface flaws shape from known nucleation conditions, (2) simulating the range of possible flaws under RCF in finite

element analysis to determine how physical effects decrease fatigue life, (3) developing empirical equations to make these SIF results transferrable to future engineers (4) numerically analyzing experimental data to determine how three stress intensity factors (SIFs) are best combined into  $K_c$  or  $K_{eff}$  parameters, and (5) exploring statistical methods to determine how variations in the RCF system affect ball survival probabilities.

### **1.3 Literature Review**

#### **1.3.1 Rolling Contact Fatigue Loading In Ball Bearings**

The study of stresses resulting from contact has a long history. After the solutions for a point contact (Boussinesq, 1878) the stresses of two contacting elastic spheres were developed (Hertz, 1882a). For a thorough derivation of these theories and other elastic contacts see Love, 1944. Since then there has been much development in the field of elastic contact (Johnson, 1987). In the case of ball bearings, the contact patch between the ball and raceway are ellipses (see Fig 1-5) and, in general, the contact between any two objects that have two radii of curvature have elliptical contact patches. The stresses beneath an elliptical contact can be calculated by integrating derived equations (Hills et al., 1993) and has been analyzed previously in FEA (see Fig 1-6) (see Arakere et al., 2009). As both the elliptical loads (as each the inner and outer raceways have elliptical contacts on opposing ends of the ball) circumnavigate the ball, each point near the contact band experiences two cycles of fatigue and, as a result of possibly high operating speeds (see Table 1-2) high cycle fatigue threatens survival of these surfaces. This is rolling contact fatigue in action.

The differences between rolling contact fatigue and standard fatigue have been previously listed in a literature review on rolling contact fatigue (Sadeghi et al., 2009) as:

1. The state of stress in non-conformal contacts where RCF occurs is complex and multi-axial and governed by the Hertzian contact theory.
2. Contrary to most classical fatigue phenomena, rolling contact fatigue is typically a multi-axial fatigue mechanism.
3. Contrary to classical fatigue, the loading history at a point below the surface is non-proportional, i.e., the stress components do not raise and fall with time in the same proportion to each other. [For example], the stress history for a point located at the depth where the orthogonal shear stress  $\tau_{xz}$  is maximal. [T]here is a complete reversal of the shear stress  $\tau_{xz}$ , while the normal stresses  $\sigma_x$  and  $\sigma_z$  always remain compressive. Also, the [maximal] peaks of the two normal stresses do not coincide [in time] with the peaks for the shear stress.
4. There is a high hydrostatic stress component present in the case of non-conformal contacts, which is absent in classical tension-compression or bending fatigue.
5. The principal axes in non-conformal contacts constantly change in direction during a stress cycle due to which the planes of maximum shear stress also keep changing. Thus, it is difficult to identify the planes where maximum fatigue damage occurs.
6. The phenomenon of RCF occurs in a very small volume of stressed material, because the contact stress field is highly localized. Typical bearing contact widths are of the order of 200–1000  $\mu\text{m}$ .
7. [In ductile materials] the evolution of RCF damage leading to a fatigue spall involves a three-stage process: (i) shakedown, (ii) steady-state elastic response, and (iii) instability. Localized plastic deformation and development of residual stresses are precursors to fatigue damage, and therefore the ability to compute the 3D elastic-plastic stress fields that accounts for cyclic loading and traction effects, and acknowledge microstructural changes, are necessary tool for quantifying raceway fatigue damage.

Rolling contact fatigue in metal bearings is manifested as a flaking off of metallic particles from the surface of raceways and/or rolling elements. This process commences as a crack *below* the surface and is propagated to the surface, eventually forming a pit or *spall* in the load-carrying surface. Lundberg and Palmgren (year) postulated that the maximum orthogonal shear stress is a subsurface crack initiation parameter (though not all researchers accept that this is the significant stress initiating failure) and they postulated that fatigue cracking commences at weak points subsurface

(Lundberg and Palmgren, 1947). However, modern (beyond 1990s) metallic bearing failures are frequently associated with surface initiated flaws.

The Lundberg-Palmgren (LP) theory is widely used for fatigue life estimation in metal ball and roller bearings. The damage indicator in the LP theory, and life, can be written as:

$$\text{Damage Parameter} = \ln \frac{1}{s} \alpha \left( \frac{N^e \tau_0^c V}{Z_0^h} \right), \quad \text{Life, } L = \left( \frac{C}{P} \right)^3 \quad (1-1)$$

Where  $N$  is the number of cycles endured with a probability of survival  $s$ ,  $\tau_0$  is the maximum value of the subsurface orthogonal shear stress,  $V$  is the volume of the subsurface material subjected to stress,  $z_0$  is the depth at which  $\tau_0$  occurs.  $L$  is the fatigue life in millions of revolutions, which 90% of the bearings will achieve;  $L_{10}$  or rating life.  $C$  is the basic dynamic capacity of the bearing as provided in the bearing manufacturers catalogs, calculated according to LP methods.  $P$  is the contact load.

### 1.3.2 Limitations Of Lundberg-Palmgren Theory

The fatigue damage process in ceramic rolling elements is very different from metal bearings discussed above. Metals are weaker in shear than tension. In contrast to metallic materials, *Si3N4 material is weaker in tension than compression or shear*. The LP methods do not nor cannot account for this significant difference in material behavior. On the other hand, the fracture mechanics approach proposed is fully capable of modeling such material characteristics along with the complex systems design, lubrication and tribological interaction in bearing contact under steady state and adverse operating conditions.

The LP approach does not deal with fracture mechanics issues in predicting the subsurface initiated flaws. Also, it does not apply to this application as pre-existing surface flaws in the ball grow under RCF and they are not initiated subsurface as the result of material cleanliness. It is akin to the stress-life approach or the S-N approach to fatigue life evaluation. Surface cracks and initial flaws also cannot be effectively addressed by the LP lifing, because of its probabilistic approach. A fracture mechanics methodology that evaluates the *critical flaw* size in balls and raceways is required. Failure typically occurs, for hybrid bearings, when the stress field at the crack tip equals the fracture properties of the material.

### **1.3.3 Hertzian Fracture Of Brittle Materials**

Normal contact of spheres made of brittle materials has been analyzed extensively and is known to generate cone cracks (Chen et al., 1995, Lawn, 1994) (Fig. 1-2a). Normal indentation of a hard sphere into a brittle material typically results in a ring crack on the surface, which then propagates into a frustum of a cone. Auerbach (1891) and Hertz (1895) first investigated this problem in the 1890's and many have revisited the problem since. Lawn (1994) provides a comprehensive review of extensive investigations made subsequently, to elucidate a qualitative and quantitative description of the initiation and growth of cone cracks in brittle materials. Mackerle (2001) has provided a biography of indentation simulations and with an emphasis on ceramic materials (Mackerle, 2002). In contrast to these bodies of work, cracks generated by oblique contact have received much less attention.

Partial cone or c-cracks are the observed result of the oblique impact of brittle materials (Frank and Lawn, 1967) (Fig. 1-2b). These c-cracks are considered the most damaging surface defect that limits ball life in hybrid bearings under RCF (Evans, 1983,

and Hadfield et al., 1993a). (See Fig 1-7). These cracks, when subjected to RCF often undergo spallation which occasionally gives a clear image of the crack front and its interior shape (see Fig 1-8). C-cracks are more commonly observed in sphere-to-sphere interactions and they not only have non-planar crack faces but also possess non-planar crack tips, as opposed to the axisymmetric cone cracks. This makes their shape more difficult to describe and, therefore, more difficult to analyze in any linear elastic fracture mechanics (LEFM) based analysis.

### **1.3.4 Computational Simulation Of Surface Flaws**

Surface cracks are among the most common flaws (Hadfield 1993a) and most critical in structural components (Evans, 1993) and are directly exposed to RCF in multiple systems. The stress intensity factors (SIFs) are important for analysis of growth and fracture nucleating from these flaws. Due to the complexity of the three dimensional (3D) subsurface Hertzian stress field at the ball-raceway interface and the steep stress gradients from the edge of contact to the surface crack, exact solutions are intractable. Accounting for these complexities entails the use of a comprehensive 3D finite element contact/fracture mechanics analysis. Previous researchers have only provided a limited amount of approximations for SIFs for this system.

In earlier works, where the investigated geometries had similar levels of complexity to the current work, FEA was not always used. Zalounia (1993) used the Fourier transforms method to obtain SIFs for an edge crack penetrating the interface in a coated solid subjected to contact loading. Keer and Bryant (1983) used a two dimensional linear elastic theory to simulate a crack in a rail wheel to examine the effects of contact friction, lubricant pressure and friction between the crack faces on the  $K_I$  and  $K_{II}$  stress intensity factors. Karapetian and Hanson (1994) derived weight

equations for the simpler geometry of a submerged circle crack subjected to point loads on the crack face. Later, these equations would be applied by Kida (2000) (with some untested approximations) to the case of a subsurface penny crack subjected to RCF at the surface. Hasebe and Qian (1995) visited the problem of an indenter of different geometries contacting a plane strain infinite plate with an angled surface flaw in multiple notable works by using complex stress functions derived by the rational mapping function (Hasebe, Qian, 1999, Qian, 1997, Qian, 1996). The results presented were in graphical form and not readily applicable to a 3D problem.

Noda and Miyoshi (1996) used the body force method to come up with an integral equation that could be integrated with a polynomial stress distribution for a half penny crack in a semi infinite body. Pommier (1998) in a related work on semi-elliptical cracks which are normal to the surface provided a set of equations for  $K_I$  for a polynomial stress distribution that could be explained by the equation:

$$\sigma_{xx} = \sigma \left( \frac{x}{a} \right)^m \left( \frac{y}{b} \right)^n \quad (1-2)$$

where the stress state is normal to the crack and n and m are constants whose sum is less than 4.

Kaneta et al. (1991) investigated the penny crack by using the body force method. Their mode I SIFs occasionally went negative, due to a neglect of crack closure, when the contact patch started to go over the load. Kaneta et al. (1989) also visited the problem of an inclined subsurface penny crack subjected to line contact loading to investigate subsurface crack growth under RCF.

FEA would also be used for analysis for a similar family of crack problems. Komvopoulos and Cho (1997) used two dimensional (2D) FEA to simulate a subsurface

plane strain crack that was parallel to the surface under sliding asperity contact. Zhang et al. (1999) also used FEA but for the analysis of multiple (two) vertical surface cracks under contact loading in 2D. Kojima (1999) used 2D FEA to analyze the angled surface crack under contact loading with a viscous lubricant to penetrate the crack. For the case of cone cracks with an internal circularly symmetric load, FEA was used to find the worst “crack angle” and the “critical flaw” size as determined by what causes the SIFs to reach the  $K_{eff}$  to initiate fatigue (Warrier, 2000).

Fletcher and Beynon (1999a, 1999b) applied their work to calculating SIFs for the specific case of contact loading for inclined cracks. Their method for calculating SIFs involved edge Green’s functions presented graphically in the works of Rooke et al. (1991) which must then be integrated based on the amount of crack opening. The method uses an approximation of an infinitely wide crack to calculate SIFs for the deepest point of a semi-circular surface crack. Problematically, this point may not be where the highest SIFs occur along the crack front depending on the depth of the crack (Newman and Raju, 1981).

### **1.3.5 Mixed-Mode Fracture Testing**

Mixed-mode fracture has been investigated by many researchers for finding a single parameter which is effective at determining fracture toughness, or  $K_c$ , or the mixed-mode fracture toughness of a given material. In reality, there has been much divergence in the equations provided for brittle materials which are often empirical in nature and both material and experiment dependent (Qian and Fatemi, 1996). While there are a variety of tests for fracture parameters, this thesis contains analyses with three: the Brazilian disk test, the V-ring test, and a novel fracture test from Michael J. O’Brien (Piotrowski and O’Brien, 2006).

The Brazilian disk (BD) test, first proposed by Carniero and Barcellos in 1953 has since been used to measure the tensile strength and fracture toughness of brittle materials like rocks, concrete and ceramics. The BD test consists of a circular disk that, like most mixed-mode fracture tests, have inserted planar flaws, by the process known as pre-cracking, in the middle of these samples. There are two widely used approaches for producing pre-cracks in a specimen to determine its fracture toughness,  $K_c$ , either from surface flaws produced by indentations (where small flaws are needed) (like Ayatollahi and Aliha, 2005) or by using the chevron notch, or a sharp edged notch, for larger cracks since there is stable crack growth during the initial pre-cracking (like Fowell, 1995). For silicon nitride, the high loads that are required to grow a centrally placed flaw under testing conditions require a larger crack to be capable by common load frames and since the material is very tough to cut or grind (a favorable material property for the harsh conditions it will face) a Chevron notch is not favorable.

The BD test consists of a precracked circular disk loaded in compression that results in a tensile stress at the center (perpendicular to the loading direction) and can split the disk along the load axis (Canerio, 1953). With the crack size visible at the end of the experiment, and the final load to fracture known from the load frame, fracture toughness can be calculated (Piotrowski and O'Brien, 2006). The advantage of this test is that it can be performed under a range of mode-mixities (from pure mode I to a mix of mode I and II for through cracks) to evaluate a mixed-mode fracture toughness along with simple specimen geometry and minimal requirements for implementation. Brazilian disk specimen can also be used to measure interfacial fracture toughness in biomaterials (Banks-Sills, 1999).

There have been quite a number of Brazilian disc studies conducted on fracture toughness via multiple approaches on different materials. Zhou et al. (2006) tested Polymethylmethacrylate (PMMA) with a chevron notch to determine its mode I fracture toughness in the BD test. Tong, et al. (2007) used the Brazilian disk test to determine the interfacial fracture toughness in bone-cement interfaces. Awaji and Sato (1978) employed this test for examining the fracture toughness of graphite, plaster and marble in mixed-mode loading using machined central cracks. Petrovic and Mendiratta (1976) have examined mixed-mode fracture toughness in hot pressed silicon nitride using controlled surface flaws produced by Knoop indentation in a four-point bending test. Khandelwal, et al. (1995) have found the high temperature mixed-mode fracture toughness of hot isostically pressed, PY6 silicon nitride using bend bars which contained cracked indentations produced using the Vickers hardness indenter and tested using the four point bend test.

Beyond the BD test, there is a group at Bournemouth University that uses a four-ball test rig to test rolling contact fatigue and it has become a centerpiece of their publications (Wang and Hadfield, 2000). In this test a single ball is rotated axially in a collet and contacts three balls below which rotate in a cup. Surface flaws are induced in the upper ball and are carefully placed in the contact path such that on each upper ball rotation the flaw goes through three RCF cycles as a result of touching the three balls below. This test and others are summarized in table 1-3.

#### **1.4 State Of The Art From Literature Survey**

C-cracks or partial cone cracks are commonly found on the surface of silicon nitride balls and, if subjected to rolling contact fatigue can result in spallation failure. The Hertzian fracture process has been largely ignored for these partial cone cracks even

though they are more common than the symmetrical cone crack. Numerical simulation of 3D nonplanar flaw for SIF calculation is also a relatively unanalyzed field (especially near an elliptical bearing load). A  $K_{eff}$  parameter, while researched by many, has left no consensus for a general case or material type and, even in specific analyses, empirical equations are often provided. Probability of bearing survival has only been looked at by empirical equations for steels rather than a fracture mechanics approach for pre-existing flaws on the ball surface.

### **1.5 Outline Of Thesis**

In chapter 2, subsurface Hertzian stresses between contacting spheres are examined, using an analytical stress solution, to investigate their applicability to predicting and characterizing crack size and shape. Also, these cracks are incrementally developed through an iterative crack growth procedure using a 3D finite element analysis. Comparisons are then made to experimental images of the flaws in silicon nitride. By varying the initial conditions during the contact interaction of the balls it can be demonstrated that a wide range of cone and partial cone cracks, observed in practice, can be generated using both the analytical and numerical fracture mechanics approaches. Furthermore, an expression is presented for the impact velocity that induces a cone crack from a maximum radial stress criterion at the contact periphery.

In chapter 3, the researchers discuss the modeling techniques that were developed to simulate the resultant types of flaws. Included are developments in contact algorithms for 3D curvilinear cracks, meshing of curvilinear cracks in 3D, parametric studies via MATLAB and more. In addition, SIF trends observed from parametrically varying different physical effects are plotted and discussed.

In chapter 5, the range of three-dimensional non-planar surface flaw geometries subject to RCF is simulated to calculate mixed mode stress intensity factors to determine the critical flaw size, or the largest allowable flaw that does not grow under service conditions. The cost of non-destructive evaluation methods for silicon nitride balls scales exponentially with decreasing CFS and increasing ball diameter and can become a significant fraction of the overall manufacturing cost. Stress intensity factor variability is analyzed for variations of the location and orientation of the load relative to the crack, the geometry of load, and full-slip traction. The modeling techniques utilized in the creation of a three dimensional FEA model is discussed and the maximum tensile contact periphery stress is examined for effect on crack driving force under RCF. The CFS results are presented as a function of Hertzian contact stress, traction magnitude, and crack size.

In chapter 4,  $K_C$  and  $K_{eff}$  are determined via the experimental/numerical analysis of three tests: Brazilian disc test, a novel test from Michael J. O'Brien, and the V-ring test. Mixed-mode fracture toughness parameters are tested for applicability via the Brazilian disc test on silicon nitride. Specimens are pre-cracked, measured, loaded to fracture and then simulated individually in finite element analysis to calculate the specific stress intensity factors under failure. Avoiding empirical equations, the max strain energy release rate criterion is found to be the easiest and acceptably accurate for mixed-mode conditions. In a novel test from Michael J. O'Brien, full silicon nitride balls are tested by indenting them and compressing them in a load frame until the tension developed at the equator propagates the cracks extending from the Vickers indentation. Empirical equations are then used to calculate the fracture toughness of each specimen. The V-

ring test is the only test utilized to calculate a  $K_{eff}$ . Herein, two opposing inner rings squeeze a rotating ball at a certain cyclic rate and load. An assortment of flaws are measured and placed in the contact path to interact with both the upper and lower rings. The test is stopped when a fatigue spall trips an accelerometer or a certain number of cycles is reached. Each test's dimensions and orientation are modeled to calculate SIFs associated for tests that fail and do not fail to determine what SIFs are sufficient for a ball failure.

Chapter 6 contains empirical equations for the  $K_I$ ,  $K_{II}$ , and  $K_{III}$  stress intensity factors for semi-elliptical surface cracks subjected to rolling contact fatigue as a function of the contact patch diameter, angle of crack to the surface, max pressure, position along the crack front, and aspect ratio of the crack. The equations were developed from SIFs calculated by parametric 3D finite element evaluation for a range of contact patch radii ( $1b$ ,  $2b$ , and  $3b$ ) and angles of the crack to the surface ( $0^\circ$ ,  $45^\circ$  and  $60^\circ$ ). The comprehensive empirical curve fits presented are accurate to within 0.5% of FE simulations. The results are of particular relevance to hybrid silicon nitride ball bearings which are susceptible to failure from fatigue spalls emanating from pre-existing surface cracks, due to crack growth driven by RCF.

Chapter 7 contains an uncertainty analysis of rolling element survival under rolling contact fatigue. Previous chapters focused on a deterministic categorization of allowable flaw size. This chapter determines ball survivability if there is a variation in tolerable crack size, fatigue threshold, and crack orientation on the ball. First we create a surrogate modeling based on the physics of the SIFs under rolling contact fatigue to account for variations in crack size, max pressure, and orientation and then conduct a

Monte Carlo Simulation to determine the effect of crack size and fatigue threshold on ball survivability.

## 1.6 Figures

Table 1-1. Comparison of material properties between fully densified silicon nitride and a common ball material predecessor M50 steel.

Parameter		M50 Steel	Silicon Nitride
Specific Gravity		7.8	3.25
Young's modulus	(GPa)	207	310
	(ksi)	30	45
Vickers hardness	(GPa)	8	14-18
Coeff. of Thermal Expansion	( $\times 10^{-6}/^{\circ}\text{K}$ )	12	3
	( $\times 10^{-6}/^{\circ}\text{F}$ )	6.7	7.1
Specific Heat	(J/kg- $^{\circ}\text{K}$ )	450	800
	(Btu/hr-ft- $^{\circ}\text{F}$ )	0.11	0.19
Thermal Conductivity	(W/m- $^{\circ}\text{K}$ )	30	20
	(Btu/hr-ft- $^{\circ}\text{F}$ )	17.3	11.5
Upper use temperature	( $^{\circ}\text{K}$ )	600	1300
	( $^{\circ}\text{F}$ )	620	1800
Fracture Toughness	(MPa m <sup>0.5</sup> )	18	6

\*Note: Toughness from (Rescalvo, 1998) and (Piotrowski, 2006). All other properties (Galbato, 1992).

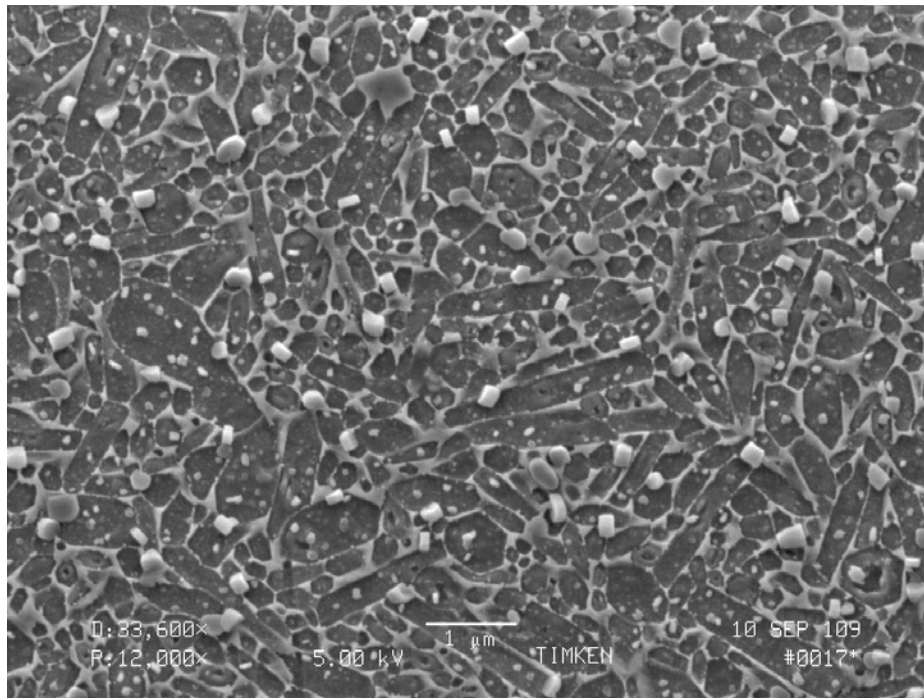


Figure 1-1. Image of silicon nitride microstructure where the relative size of the  $\alpha$  and  $\beta$  grains are apparent [Image courtesy of The Timken Company].

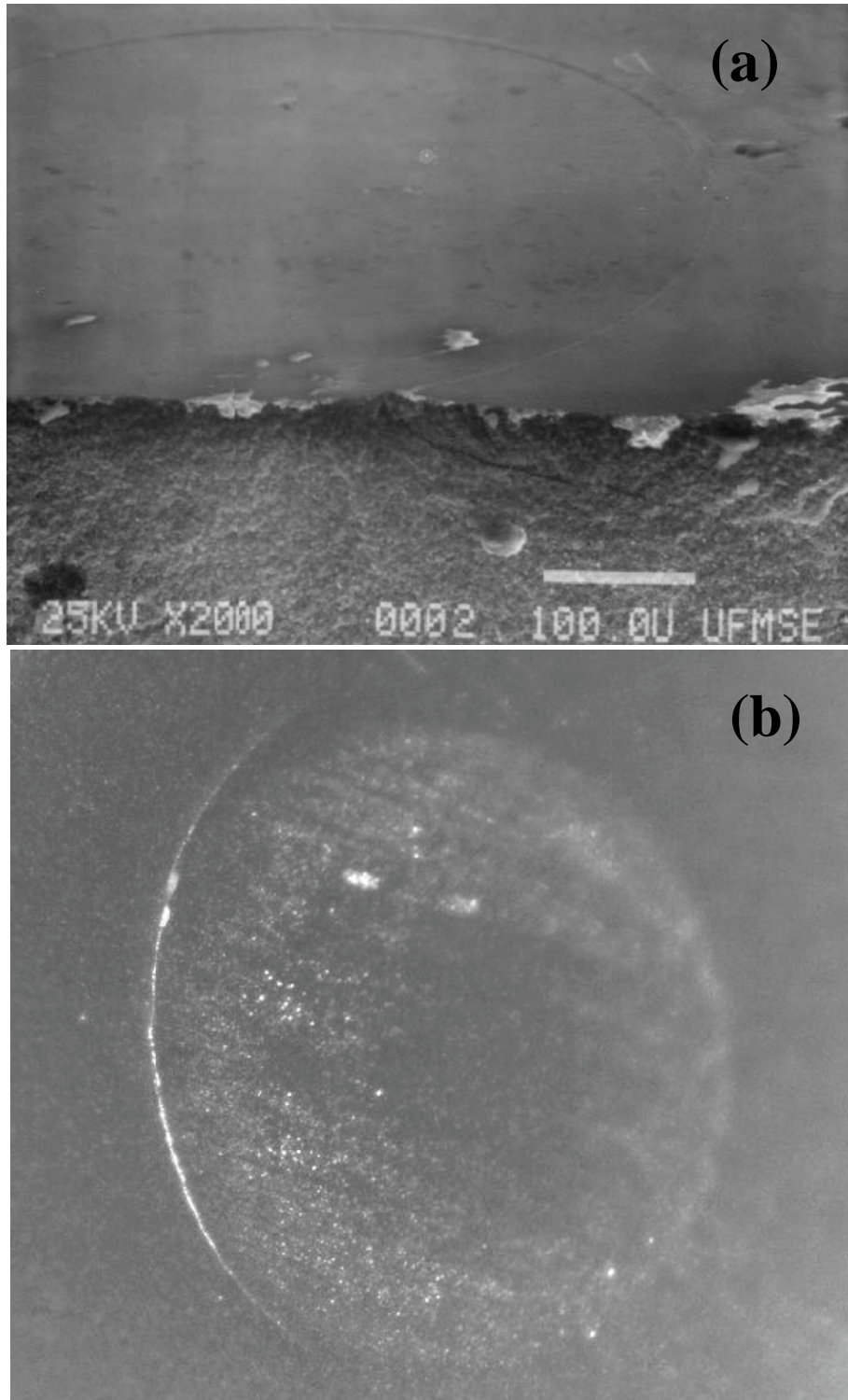


Figure 1-2. A) Example of a cone crack in silicon nitride (Mecholsky, 2008), B) Experimental image of oblique sphere interaction with contact patch and resultant c-crack shown. Image in proportion but scales are not shown (Image courtesy of The Timken Company).

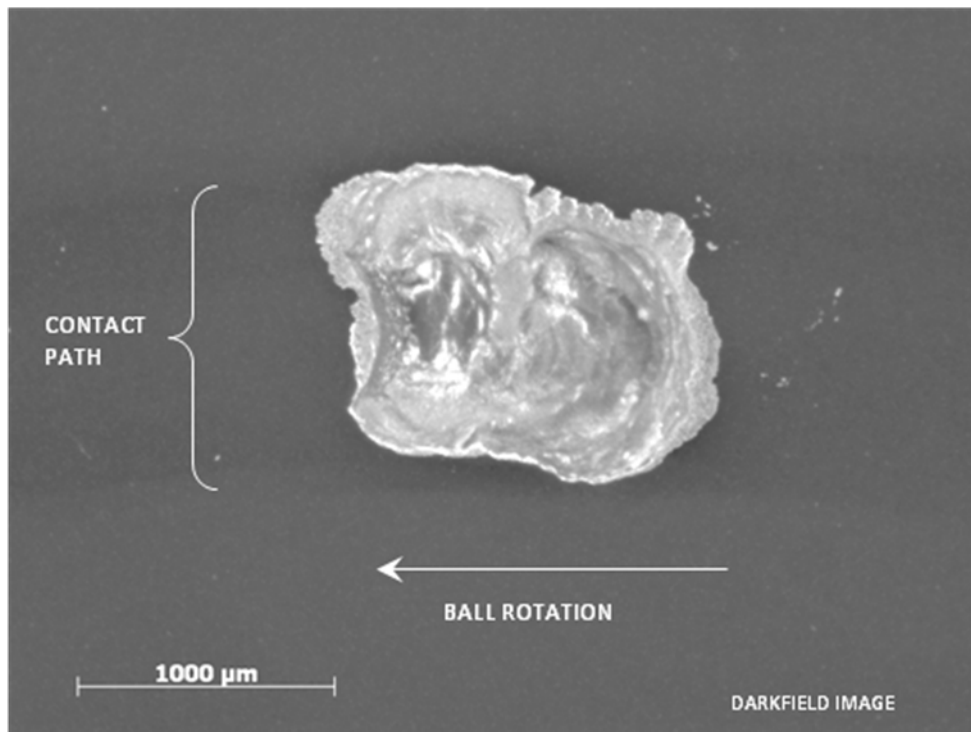
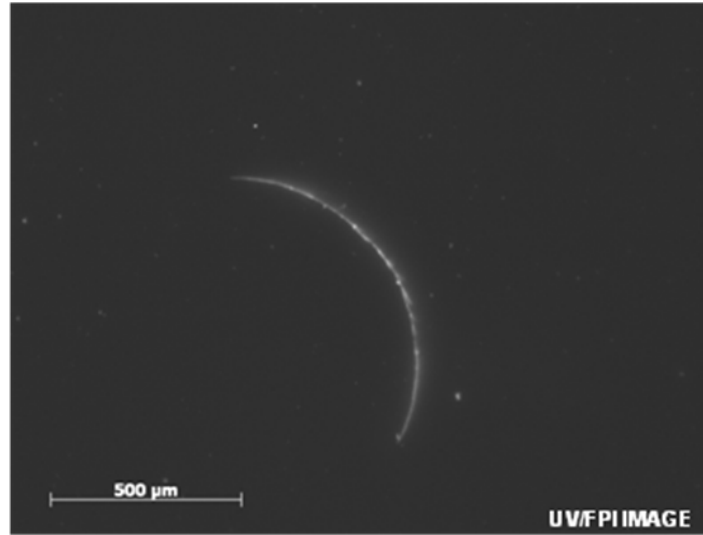


Figure 1-3. Before and after of Timken test #7 of the V-ring single ball test.

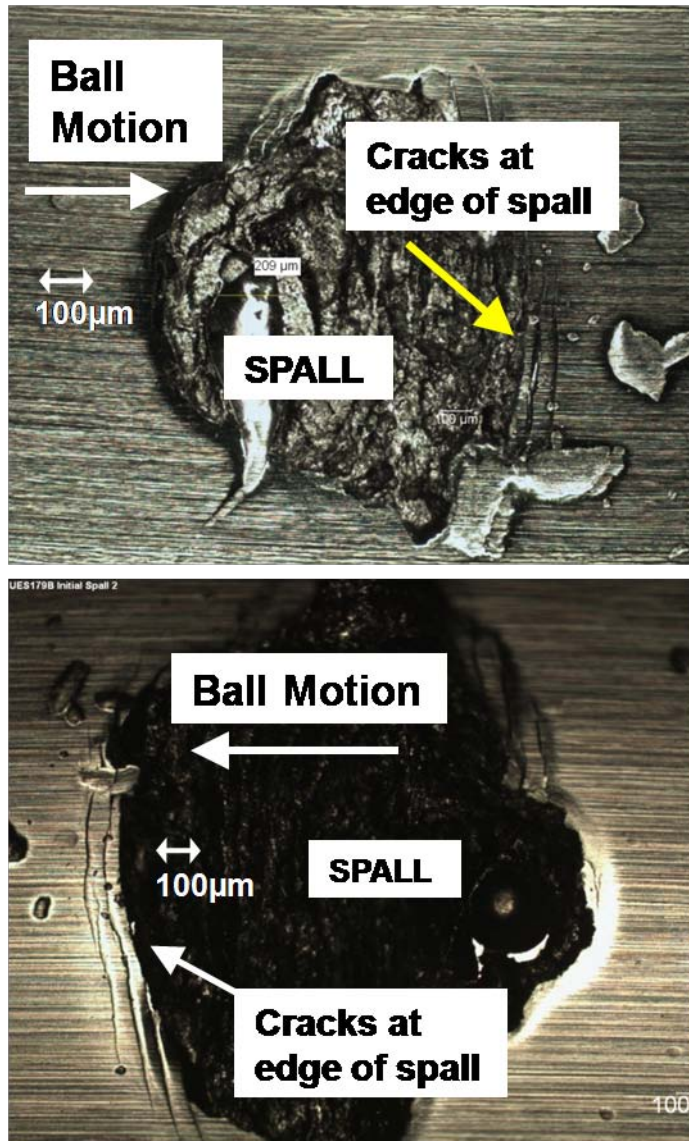


Figure 1-4. Image of steel raceway spall from RCF (Branch et al., 2009).

Table 1-2. Measurements for a sense of scale of the problem (Miner et al., 1996).

Feature	Measurement
Size of Balls	14.29-25.4 mm (9/16-1 in)
Crack Width on Surface	300-1000 $\mu\text{m}$
Grain Length	$\beta=10 \mu\text{m}$ $\alpha=2 \mu\text{m}$
Speed	11000 rpm
Radial Load	9000 lb
Axial Load	1300 lb
$\rho_o$	3800 MPa

Table 1-3. RCF tests on ceramics and their failure modes in literature.

Publication	Test	Failure
Parker and Zaretsky, 1975	Five-ball test on 12.7mm dia. HIPed $\text{Si}_3\text{N}_4$ at 4.3-6.2 GPa, 9600rpm, and 30° contact angle	Spallation without edge cracking
Lucek and Crowley, 1978	Disc-on-rod on hot-pressed ceramic 4.1-5.5GPa	“Non-catastrophic” spallation failure.
Hadfield and Stolarski, 1995	Disc on rod test of varying ceramics and lubricants	“Non-catastrophic” spallation failure.
Morrison et al., 1984	$\text{Si}_3\text{N}_4$ hybrid bearings with M50 steel between 1.95-2.44 GPa	Spallation with no cases of ball fracture.
Fujiwara et al., 1989	Ball-on-plate machine to test $\text{Si}_3\text{N}_4$ raceways up to 6.4 GPa at 1400rpm.	Spalling is most common long term failure but “cave-in” and peeling also occurred in short tests.
Lucek, 1990	Hot-pressed $\text{Si}_3\text{N}_4$ rods at 6.4GPa up to 8600 rpm	Spallation occurred
Hadfield, 1993a,b,c	Four-ball test at 6.4 GPa at 5000 rpm with different lubricants	“Non-catastrophic” spallation
Burrier, 1996	Ball on rod test of 11 $\text{Si}_3\text{N}_4$ materials at 5.93 GPa at 3600rpm	Large life dependency on finer microstructure with primary failure of spallation.

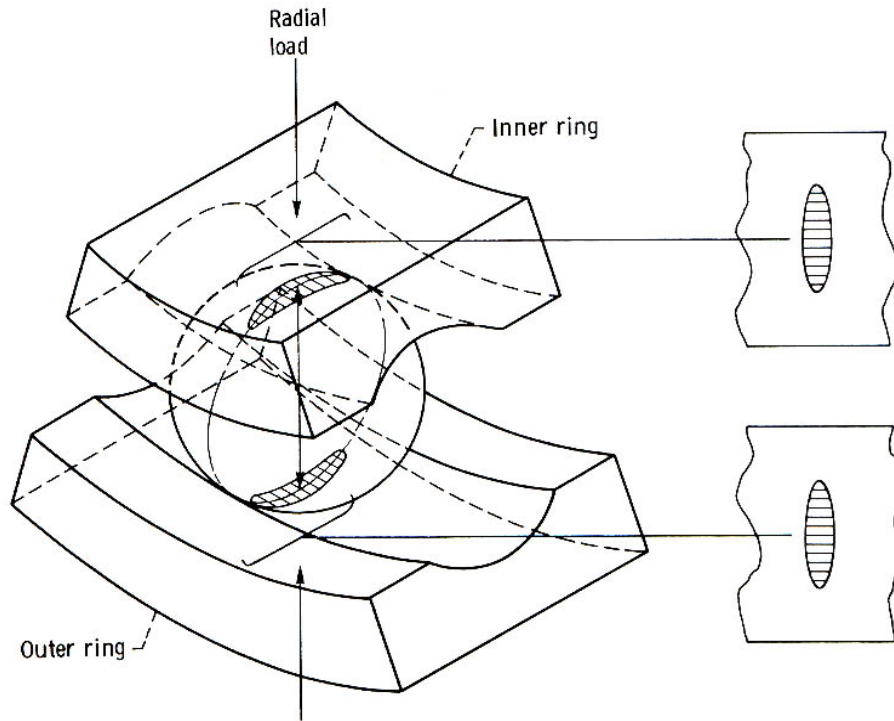


Figure 1-5. The elliptical contact patches between the ball and raceways. The contact patch size and the subsurface stress distribution are a function of raceway geometry, conformity between the ball and raceways, radial and thrust loads, etc.

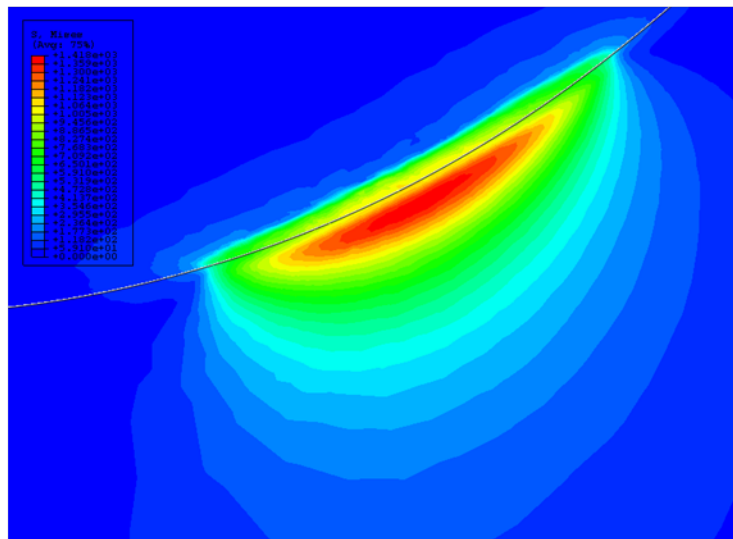
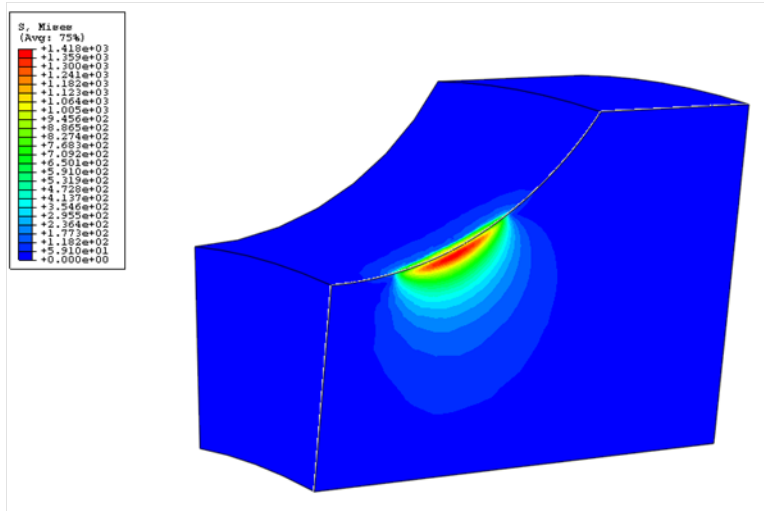


Figure 1-6. FEA simulation of a steel raceway section being subjected to contact with a sphere from a distance and with a cutaway section revealing the subsurface stresses.

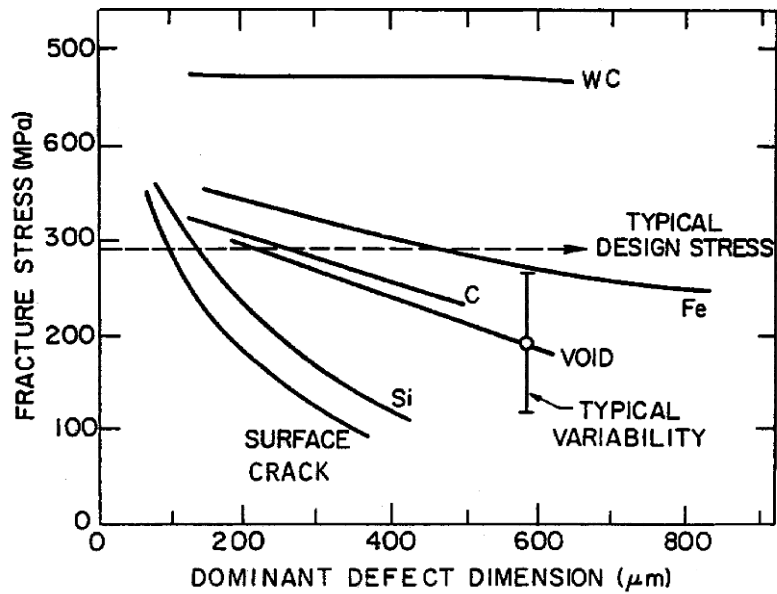


Figure 1-7. Fracture stress as a function of dominant defect dimension (Evans, 1983).

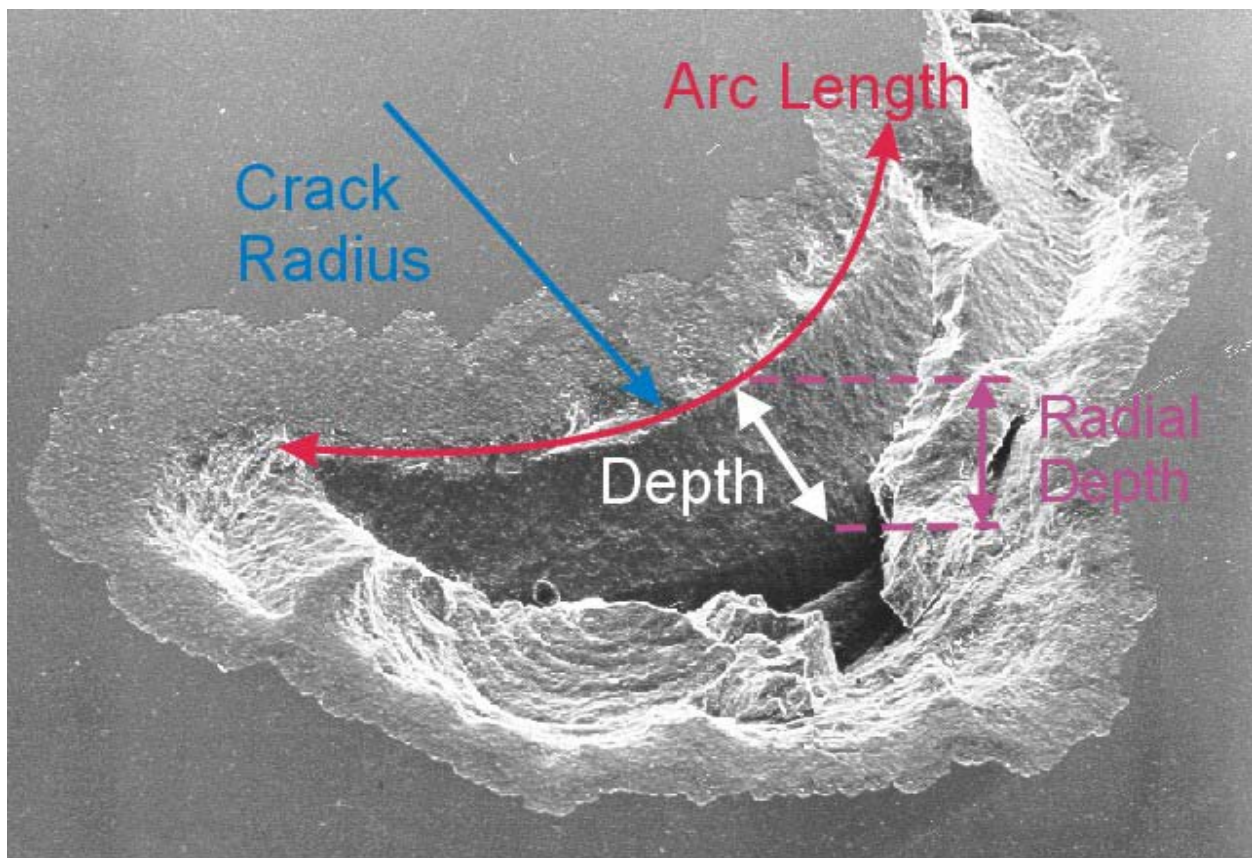


Figure 1-8. Image of a spalled c-crack clearly showing its face as it extends into the material. Other markers are indicating possible dimensions of measurement for further classification and analysis.

## CHAPTER 2 DETERMINATION OF SURFACE FLAW GEOMETRY

### 2.1 Introduction

In this chapter, the goal is to obtain the possible range of crack shapes in three-dimensions that result from oblique interaction for future finite element (FE) analysis. The analysis of crack shapes produced by oblique interactions has direct and immediate application. The performance of hybrid silicon nitride ball/steel raceway bearings has been shown to be much superior to steel bearings (Miner et al., 1996 and Tanimoto et al., 2000). However, silicon nitride balls are sensitive to surface defects and can fail from fatigue spalls emanating from pre-existing c-cracks, due to crack growth driven by RCF (Hadfield et al., 1993b). Silicon nitride ( $\text{Si}_3\text{N}_4$ ) exhibits favorable material properties for application in hybrid high speed ball bearings such as high compressive strength, high hardness, a third of the density of steel, low coefficient of thermal expansion, and high corrosion and temperature resistance. However, it also has low fracture toughness (Piotrowski and O'Brien, 2006). The final ball dimension is achieved in a lapping process that produces (unavoidable) low velocity ball collisions resulting in surface cracks initiated by the radial tensile stress field at the contact periphery (Wang and Hadfield, 2000).

A qualitative and quantitative description is presented on the range of possible partial cone crack shapes in 3D as functions of initial conditions (coefficient of friction and contact patch size) during oblique spherical contact. The emphasis is not on simulating the dynamics of oblique contacts, but simulating the interaction forces via the coefficient of friction and contact patch size, and then focusing on the effect of resulting subsurface Hertzian stress fields in inducing brittle fracture. The resulting 3D geometry

of crack faces is predicted using the following two approaches: 1) An analytical description of 3D subsurface stress state is used to predict the crack front based on the max principal stress “trajectory” and 2) A 3D finite element contact stress analysis is used in conjunction with a numerical 3D fracture analysis program, FRANC3D, to grow the partial cone crack incrementally. Results from the two methods are compared and show good agreement. Qualitative features are examined from experimentally produced C-cracks in silicon nitride balls. By varying the initial conditions of the contact interaction it is shown that a wide range of partial cone cracks, observed in practice, can be generated using both the analytical and numerical fracture mechanics approaches. The results generated are of immediate engineering relevance to the hybrid ball bearing industry towards evaluating critical flaw size for defining limits for non-destructive evaluation methods for silicon nitride ball quality control and for developing a fracture mechanics based life prediction methodology for hybrid bearings.

## **2.2 Analysis**

Here the stress state and fracture mechanics approaches mentioned earlier are discussed to yield the range of partial cone crack shapes produced during oblique interaction. The stress-state analyses have been done for normal indentation for some time. The cone crack path due to a spherical indenter was shown by Frank and Lawn (1967), to a first approximation, to be orthogonal to the maximum tensile principal stress distribution of the statically loaded elastic half space. Later, Lawn (1967) showed that traction forces induced by a sliding spherical indenter strongly influenced the quasi-static stress field, and generated an early partial cone crack profile for brittle materials in two-dimensions. After the works of Frank and Lawn (1967), there was a continuing use of the max principal stress trajectory in cone crack analyses. As a result of this history,

this body of work will extend the stress-state analysis to describe the crack shapes in three-dimensions and discuss a couple variations.

Crack shape analysis has also been done using an incremental growth approach as endorsed by Kocer and Collins (1998). In later work on cone cracks, Kocer emphasizes that the study of stress in an uncracked body to determine a crack shape had not been analytically supported to be reminiscent of the resultant crack shape (as once a crack exists, the stress field changes significantly and the crack grows in compliance with this new stress field) and so believed that the crack shape should be acquired based upon an iterative crack growth analysis (or an experimental approach). An incremental crack growth analysis is conducted, and in the case of the partial cone cracks, an iterative crack growth study can only be done correctly in three-dimensions. Doing such a fracture mechanics analysis using 3D FEA requires the ability to incrementally grow cracks and remesh, resulting in a computationally intensive endeavor.

These two analyses are compared with experimental images that were obtained through multiple sources. The surface dimension of c-cracks typically seen in  $\text{Si}_3\text{N}_4$  balls ranges from 50-400  $\mu\text{m}$ , depending on the ball diameter (Wang and Hadfield, 2000). Experimental examination of crack shape of these very small cracks that are embedded in a non-translucent material like  $\text{Si}_3\text{N}_4$  which is difficult to cut or grind, and hence poses considerable difficulty.

### **2.2.1 Stress-State Analysis**

To attempt to generate the crack shape from its uncracked stress state, the stress state of obliquely interacting spheres must first be obtained. Oblique impact with contact friction gives rise to tangential tractions potentially leading to micro-slip at the interface.

The complex interaction between tangential traction and micro-slip and their time-history dependence has been visited by Mindlin and Deresiewicz (1953) and analyzed by Maw et al. (1976, 1981). However, these surface tractions are not closed-form and more difficult to incorporate into a 3D subsurface stress-field solution and are not worth the possible loss in accuracy (Andersson, 1996). Also, balls are typically well lubricated during the lapping process where these cracks originate. With this support, a sliding contact analysis is conducted.

To investigate cone and c-crack size and shape as a function of normal and traction force distributions, a comprehensive 3D analytical subsurface stress solution is used for efficiency. The Hertz theory of quasi-static impact holds for evaluating the variation of contact size and contact pressure during impact under familiar criteria of ball velocities relative to wave speeds (Johnson, 1987). Applying superposition for normal and tangential stresses, the Hertz normal pressure is given by

$$p(r) = -p_o \sqrt{1-r^2} \quad (2-1)$$

where  $p_o$  is the peak pressure and  $r$  is the cylindrical coordinate. For a contact in full slip the tangential traction distribution is  $\mu * p(r)$ , where  $\mu$  is the coefficient of friction.

Hamilton and Goodman (1966) presented the 3D subsurface stress distribution for a spherical sliding contact. Solutions are given elsewhere (Hamilton, 1983, Sackfield and Hills, 1983, and Hills et al., 1992). The Cartesian coordinate system is used in the configuration displayed in Fig. 2-2. To acquire a solution, the harmonic potentials, N and T, are chosen to satisfy the necessary boundary conditions, namely:

$$\sigma_{zz} = \frac{\tau_{zx}}{f} = p(r) \quad r \leq a \quad (2-2a)$$

$$\sigma_{zz} = \tau_{zx} = 0 \quad r > a \quad (2-2b)$$

So they may be substituted into the relations for displacements  $u$ ,  $v$ , and  $w$ , (Love, 1921) namely:

$$2\mu u = -(1-2\nu)N_{,x} - zN_{,xz} + 2\nu T_{,xx} + 2T_{,zz} - zT_{,xxz} \quad (2-3a)$$

$$2\mu v = -(1-2\nu)N_{,y} - zN_{,yz} + 2\nu T_{,xy} - zT_{,xyz} \quad (2-3b)$$

$$2\mu w = 2(1-\nu)N_{,z} - zN_{,zz} + (1-2\nu)T_{,zx} - zT_{,xzz} \quad (2-3c)$$

where commas denote derivatives and  $\nu$  is the Poisson's ratio.

Solutions are given elsewhere (Hamilton, 1983, Sackfield and Hills, 1983, and Hills et al., 1992) and are reproduced below for completeness.

$$\begin{aligned} \frac{\sigma_{xx}^N}{p_o} &= (1-2\nu) \frac{1}{3r^4} (x^2 - y^2) \left(1 - \frac{z^3}{u^3}\right) \\ &+ \frac{z}{u} \left[ (1+\nu)u \arctan\left(\frac{1}{u}\right) - 2\nu - (1-\nu) \frac{u^3}{1+u^2} - (1-2\nu) \frac{x^2}{r^2(1+u^2)} - \frac{x^2 u^4}{(1+u^2)^2(u^4+z^2)} \right] \end{aligned} \quad (2-4a)$$

$$\begin{aligned} \frac{\sigma_{yy}^N}{p_o} &= (1-2\nu) \frac{1}{3r^4} (x^2 - y^2) \left(\frac{z^3}{u^3} - 1\right) \\ &+ \frac{z}{u} \left[ (1+\nu)u \arctan\left(\frac{1}{u}\right) - 2\nu - (1-\nu) \frac{u^2}{1+u^2} - (1-2\nu) \frac{y^2}{r^2(1+u^2)} - \frac{y^2 u^4}{(1+u^2)^2(u^4+z^2)} \right] \end{aligned} \quad (2-4b)$$

$$\frac{\tau_{xy}^N}{p_o} = \frac{-xyz u^3}{(1+u^2)^2(u^4+z^2)} + (1-2\nu)J \quad (2-4c)$$

$$\frac{\sigma_{zz}^N}{p_o} = \frac{-z^3}{u(u^4+z^2)} \quad (2-4d)$$

$$\frac{\tau_{zx}^N}{p_o} = \frac{-xz^2 u}{(1+u^2)(u^4+z^2)} \quad (2-4e)$$

$$\frac{\tau_{yz}^N}{p_o} = \frac{-yz^2u}{(1+u^2)(u^4+z^2)} \quad (2-4f)$$

$$\frac{\sigma_{xx}^T}{fp_o} = - \left[ \frac{\sigma_{yy}^T}{fp_o} + \frac{\sigma_{zz}^T}{fp_o} \right] - x(1+\nu) \left[ \arctan\left(\frac{1}{u}\right) - \frac{u}{(1+u^2)} \right] \quad (2-4g)$$

$$\begin{aligned} \frac{\sigma_{yy}^T}{fp_o} = & 2\nu x \left[ -\frac{3}{8} \arctan\left(\frac{1}{u}\right) + \frac{u}{4(1+u^2)^2} + \frac{3u}{8(1+u^2)} - \frac{y^2u^5}{(1+u^2)^3(u^4+z^2)} \right] \\ & + (1-2\nu)z \frac{\partial J}{\partial y} \end{aligned} \quad (2-4h)$$

$$\frac{\sigma_{zz}^T}{fp_o} = - \frac{xz^2u}{(1+u^2)(u^4+z^2)} \quad (2-4i)$$

$$\frac{\tau_{yz}^T}{fp_o} = - \frac{xyz^3}{(1+u^2)^2(u^4+z^2)} \quad (2-4j)$$

$$\frac{\tau_{zx}^T}{fp_o} = z \left[ \frac{3}{2} \arctan\left(\frac{1}{u}\right) - \frac{1}{u} - \frac{u}{2(1+u^2)} - \frac{x^2u^3}{(1+u^2)^2(u^4+z^2)} \right] \quad (2-4k)$$

$$\begin{aligned} \frac{\tau_{xy}^T}{fp_o} = & 2\nu y \left[ \frac{1}{8} \arctan\left(\frac{1}{u}\right) - \frac{u}{8(1+u^2)} + \frac{u}{4(1+u^2)^2} - \frac{x^2u^5}{(1+u^2)^3(u^4+z^2)} \right] \\ & - \frac{y}{2} \left[ \arctan\left(\frac{1}{u}\right) - \frac{u}{1+u^2} \right] + (1-2\nu)z \frac{\partial J}{\partial x} \end{aligned} \quad (2-4l)$$

where

$$J = \frac{xy}{3r^4} \left[ \left(\frac{z}{u}\right)^3 - 3\left(\frac{z}{u}\right) + 2 \right] \quad (2-5)$$

and

$$u^2 = \frac{1}{2} \left\{ r^2 + z^2 - 1 + \sqrt{(r^2 + z^2 - 1)^2 + 4z^2} \right\} \quad (2-6)$$

The formulation used here, for spheres in sliding contact, is nondimensionalized such that the only inputs required are a Poisson's ratio ( $\nu$ ), coefficient of friction ( $\mu$ ), and magnitude of  $p_o$ . The stress has been normalized with respect to (w.r.t.)  $p_o$  and the contact patch is normalized w.r.t. itself and always is at  $r=1$ . Fig. 2-3 is an example contour plot. At points close to the surface, coordinate planes and axes, and at  $r=1$ , the limits of these functions were evaluated for efficiency and to avoid numerical difficulties.

With a 3D stress field well described, it is possible to generate the shape of the c-cracks according to the max principal stress trajectory for brittle materials by Frank and Lawn (1967). When max principal stress "trajectory" was used by Frank and Lawn, they left the phrase largely undefined. Generally, "trajectory" refers to some curve that intersects a family of surfaces at the same angle. However, for any given angle (say 90 degrees) there are an infinite number of surfaces that can cut through the contours of max principal stress values. It can be seen that they implied to generate a line that cut through the contours at 90 degrees and originated at the surface, near the edge of the contact patch, and thus followed something close to the direction of maximum change in the field. Doing so computationally in a 3D field can quickly become difficult as gradients of stress become demanding depending on the level of refinement necessary (especially near the surface) (no matter if the stress state is being evaluated using equations or the finite element method). Also, as the point of crack origin is not always in agreement to what is seen in experiment (Kocer and Collins, 1998) some perturbations about the contact periphery are necessary to see the changes in crack shape for a given stress field.

A trajectory approach, like Frank and Lawn (1967) was extended to three dimensions, where the 3D contours of the third (minimum) principal stress are plotted according to  $\sigma_3(1 + \varepsilon, 0, 0) = \sigma_3(x, y, z)$  where  $\varepsilon$  is a chosen small value that forces the contour value of interest to be near the periphery of the contact. This method functions well because it is orthonormal at the intersections of contours of the max principal stress and has a similar result to searching out the direction of max change in the max principal stress. However, it should be noted that the choice of epsilon is significant since the stresses on the periphery of the contact is quite rapid and two close adjacent contours will diverge from each other as distance from the contact periphery increases. The cracks displayed in Fig. 2-4 are examples of this procedure. The method is effective in generating cone cracks for normal contact and partial cone cracks for oblique contact. The generated cone angle of  $63^\circ$  to the vertical agrees with experimental observations (Kocer and Collins, 1998).

Briefly, similar crack shapes were also generated using two other techniques. For example, a maximum tensile stress approach, where the 3D stress field is searched for points which are maxima in the z direction according to  $\frac{\partial \sigma_1(x, y, z)}{\partial z} = 0$  and these points are then connected to form smooth, continuous plane originating at the contact periphery. Also, the plane of maximum change where the surfaces are produced by local maxima is investigated. [When investigating local maxima, the investigator is forced to choose a coordinate variable in which the max principal stress undergo maximum change. Here it is noted that the surfaces produced by  $\frac{\partial \sigma_1}{\partial r} = 0$  (for cone

cracks) and  $\frac{\partial \sigma_1}{\partial x} = 0$  (for c-cracks) agree best with experimental observation.] These two methods were seen to be similar when the derivatives were taken with respect to the mentioned variables.

Since the contact patch radius has been normalized w.r.t. itself, the crack shapes generated are attributable to all cracks that are generated by contacting spheres with the prescribed Poisson's ratio (which produces little effect when analyzing the parametric variation) and coefficient of friction but its size must be scaled to the crack-generating contact patch. The generated crack surface is smoothed by a moving average on a discrete number of evaluation points [by the smooth() function in Matlab (Mathworks, 2005)] and then patched for a 3D plane [by the patch() function (Mathworks, 2005)]. Since the surfaces produced by the above procedure are based on stress distributions alone, they can differ from the physical cracks whose extension is limited by the physics of dynamic brittle fracture. A stress-analysis based criterion to determine the crack depth can be explored in future work. For this work, surfaces were curtailed to show common cracking proportions observed through experiments.

### **2.2.2 Incremental Crack Growth Analysis**

Also generated was the 3D partial cone crack using the finite element method and an incremental crack growth procedure. Starting with an initial small penny shaped crack, the crack was then incrementally grown using the crack growth software FRANC3D/NG developed by the Fracture Analysis Consultants (2005) after being analyzed by the commercial finite element software ABAQUS (Dessault Systèmes, 2007). While FRANC3D/NG is normally used for fatigue crack growth, its abilities to incrementally grow and remesh cracks to simulate c-crack creation are used.

In 3D FEA, a small vertical half-penny flaw ( $a=10\mu\text{m}$   $b=10\mu\text{m}$ ) was inserted into a silicon nitride block ( $E=310\text{ GPa}$ ,  $\nu=0.28$ ). The body was meshed with a combination of quadratic hexahedral, pyramidal, and tetrahedral elements (so that the crack had collapsed hexahedral quarter point elements to preserve the singularity and avoid warning elements), which totaled around 25,000 elements. This part was then loaded according to Fig. 2-5 with an applied Hertz pressure distribution, as analyzed with the stress analysis technique and is fixed far-field. Far-field boundary conditions were simulated on this small cracked block using a submodeling technique (Dessault Systèmes, 2007) where displacements are interpolated from a larger block undergoing the same load orientation and is fixed at its furthest side. To grow a crack after the displaced state is calculated, stress intensity factors are calculated by the displacement correlation equations:

$$K_I = \frac{E}{4(1-\nu^2)} \sqrt{\frac{2\pi}{r}} (u_1 - u_2) \quad (2-7a)$$

$$K_{II} = \frac{E}{4(1-\nu^2)} \sqrt{\frac{2\pi}{r}} (v_1 - v_2) \quad (2-7b)$$

$$K_{III} = \frac{E}{4(1-\nu^2)} \sqrt{\frac{2\pi}{r}} (w_1 - w_2) \quad (2-7c)$$

The computed stress intensity factors are inserted into the maximum stress crack turning angle criteria and then the crack is extended an average length as specified by the user according to a relative extension power law written as:

$$\Delta a_{nodei} = \Delta a_{mean} \left( \frac{\Delta K_{nodei}}{\Delta K_{mean}} \right)^n \quad (2-8)$$

where the exponent,  $n$ , is iteratively chosen to avoid high gradients in the stress intensity factors along the crack front and the average length,  $\Delta a_{mean}$ , was often chosen to be about 10  $\mu\text{m}$ . Incremental remeshing was stopped once the relative proportions of cracks observed in experiment were reached. Images of incremental growth are shown for  $\mu=0.1$  and  $\mu=0.5$  in Fig. 2-6 and for  $\mu=0.5$  in Fig. 2-7.

### 2.3 Results On Crack Shape Determination

Three-dimensional crack shapes resulting from the stress-state analysis exhibit the following characteristics: (a) the shape of the cone crack is expectedly axisymmetric and exhibits the experimentally observed angle of approximately  $63^\circ$  to the vertical (Frank and Lawn, 1967) and (b) when spheres collide obliquely the resulting max tensile stress is in the wake of the contact and is the site of c-crack origination. From the stress-state examination, it is observed that a c-crack is unlikely to circumvent more than  $180^\circ$  about the contact patch since the other side of the contact region is in compression. Research on silicon nitride confirms that their circumference is between a third and a fourth of a complete circle (Hadfield et al., 1993b). Also, c-cracks tend to depart from the contact patch radii as friction increases (see Fig. 2-1b). Furthermore, a plot of the c-cracks produced as a result of different friction coefficients (Fig. 2-8) shows that the range of c-crack angles observed (Zhao et al., 2006) are accounted for and that higher coefficients of friction increase the radius of the c-crack on the surface and steeper cracks. The results are summarized in table 2-1.

Cross-sectional images produced by the methods are compared to those examined in experiment. Firstly, an array of cracks from Zhao et al. (2006) is shown which is a collection of “naturally” occurring (those which result from the manufacturing

process) c-cracks in  $\text{Si}_3\text{N}_4$  with a range in steepness (Fig. 2-9). Also displayed are images of artificially produced cracks (created in laboratory settings on finished balls) in Fig. 2-10 (courtesy of The Timken Company).

Reflecting on the incremental growth results it is observed that the range of crack shapes produced by the two analyses are quite similar and agree with the range of shapes that are observed in experiment. The incremental growth analysis may produce small perturbations from the actual crack shape that can expectedly result from an incremental remeshing technique. The incremental growth analysis also tends to have more curvature as it extends into the material as opposed to the stress state analysis. Also, the incremental results seem to conform to the contact patch more than the stress results that may be the result of the incremental approach. A superposed image of the incrementally grown crack was developed by importing the global coordinates of the created crack into Matlab and performing Delaunay triangulation (Mathworks, 2005) to obtain a series of triangles that were plotted as a triangular surface plot. The result is reminiscent of the actual mesh (see Fig.2-11). Comparing the two shapes, they are in excellent agreement on the midsection where increments were comparably smaller but were somewhat divergent on the surface.

As a result, it can be seen the benefits of both approaches. The incremental crack growth analysis is well supported by a history of LEFM-based analysis but regions of significant crack turning may take significant amounts of computational effort as the size of the  $\Delta a_{mean}$  must be decreased. The incremental growth analysis also produces a meshed part that the user can apply under any other type of loading for other analyses. The stress-state analysis is relatively fast to implement and runs without user

interaction. In addition, their good agreement may leave both as viable options for future analysts depending on the analyst's time and needs.

## 2.4 Conclusions

This analysis of oblique contacting spheres lead to the following conclusions:

1. Three approaches are presented that operate on the 3D subsurface stress field and effectively predict potential crack shapes for both the axisymmetric cone crack and the oblique resultant c-crack for Hertzian fracture.
2. An iterative, 3D crack growth simulation can also be used to generate the potential crack shapes.
3. Both methods to agree well with each other and experimental images.
4. The methods can predict a wide range of crack shapes observed in oblique interactions by varying the friction coefficient at the contact.
5. With knowledge derived from this investigation, it is possible to approximate a maximum periphery stress to induce cracking, an equation to determine the velocity required to induce cracking, and an approximation of the original flaw size from which cracks may nucleate.
6. An equation was derived for calculation of the maximum tensile periphery stress that drives crack nucleation, including the effect of friction.

While it was not originally intended for these analyses to be deterministic of crack shapes from the initial conditions of colliding spheres, results have indicated the expected range of crack shapes in three separate ways: experimental reflection, a stress-state analysis and an iterative growth technique.

With this family of crack shapes, one conducting an analysis on these types of cracks should consider the range of steepness and proportion produced by this analysis. Since the range of crack shapes produced is observed in experiment, an examination of the uncracked stress field can yield accurate predictions of crack shapes for brittle materials and propose the method to be used in other instances where a stress field is known (even by computational methods) and the stress field is torsion free

(Frank and Lawn, 1967) as long as the researchers note the possible variation of traction in the (small) contact region. Also, these results are in excellent agreement with the shapes produced by an iterative remeshing technique that requires the user to have an adequate mesh and a small increment of crack advance. As an added benefit, the iterative analysis creates a mesh suitable for analysis of c-cracks under RCF.

## 2.5 Figures

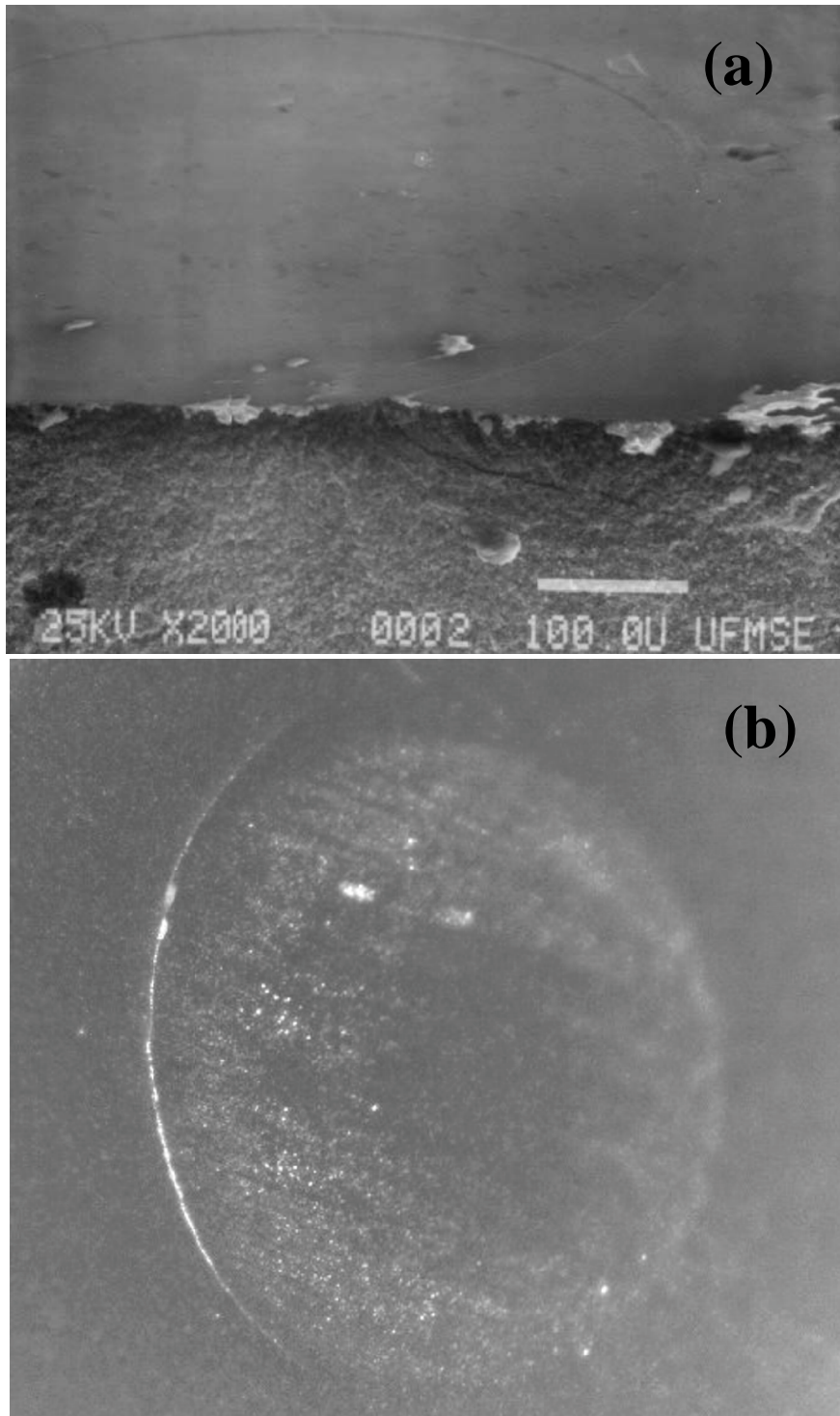


Figure 2-1. A) Example of a cone crack in silicon nitride (Mecholsky, 2008), B) Experimental image of oblique sphere interaction with contact patch and resultant c-crack shown. Image in proportion but scales are not shown (Image courtesy of The Timken Company).

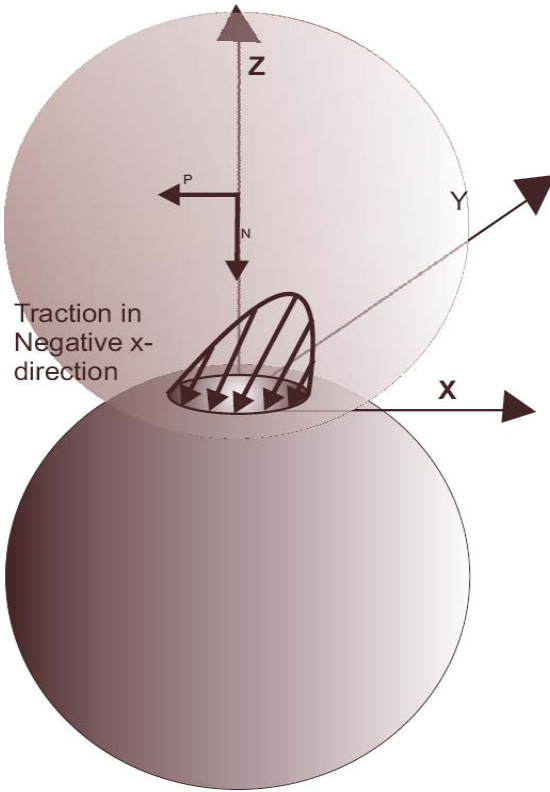


Figure 2-2. Diagram of coordinate system for the equations of stress for oblique colliding spheres.

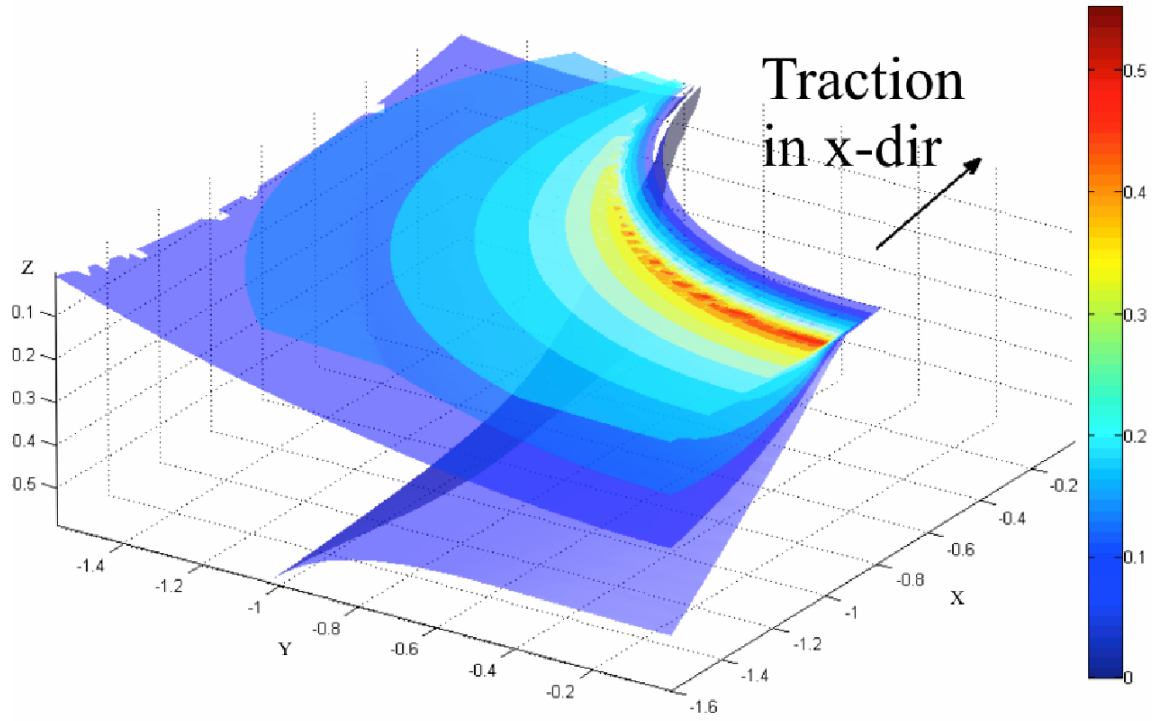


Figure 2-3. Surfaces representing constant values of the max principal stress field.

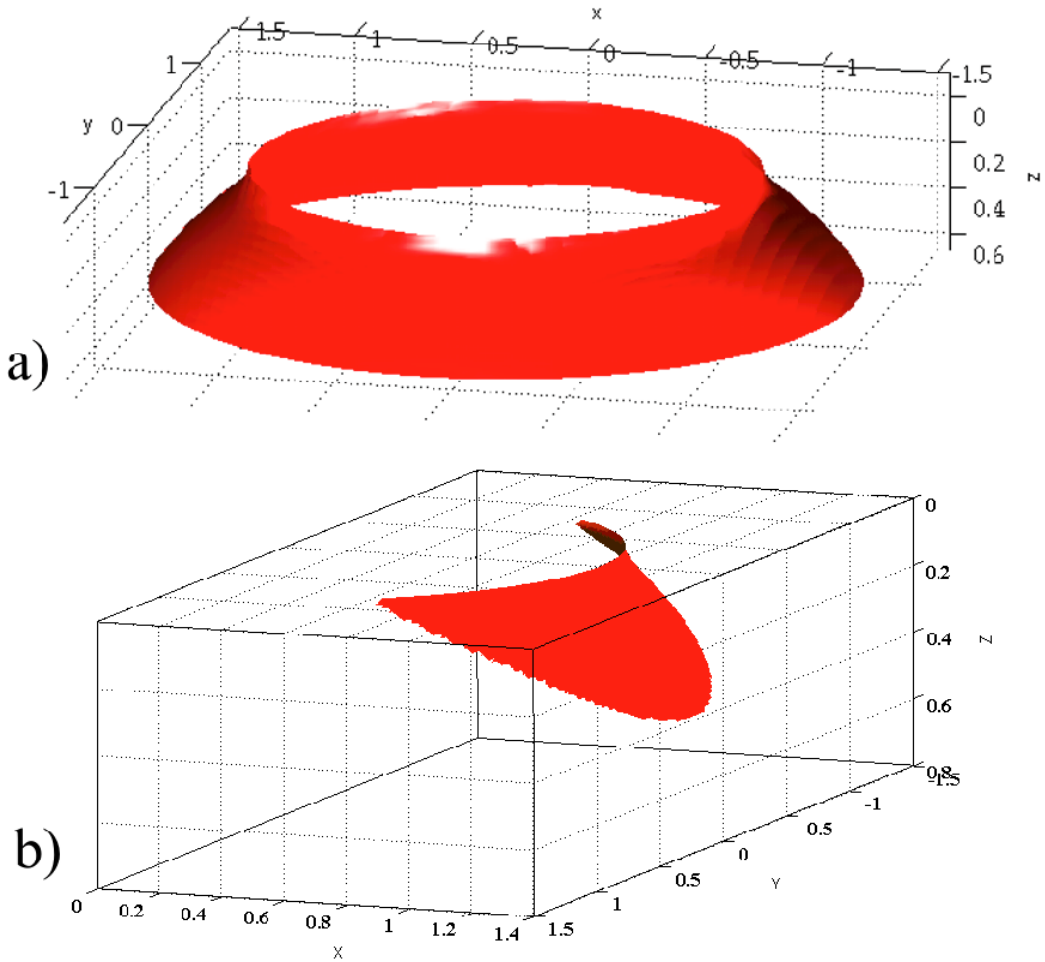


Figure 2-4. A) The cone crack as generated from the Hertzian stresses without traction with gradients of nondimensional max principal stress. B) A c-crack generated for  $\nu=0.3$  and  $\mu=0.1$ .

Table 2-1. Estimated c-crack geometries produced by different values of  $\mu$  from stress-state analysis.

$\mu$	Crack Radius	Angle to ball surface
0.1	1.07	48
0.2	1.12	54
0.3	1.17	63
0.4	1.22	72
0.5	1.28	77

Note: Crack radius is on the surface (nondimensionalized w.r.t. the contact patch) and the estimate of angle in degrees is measured down from the surface.

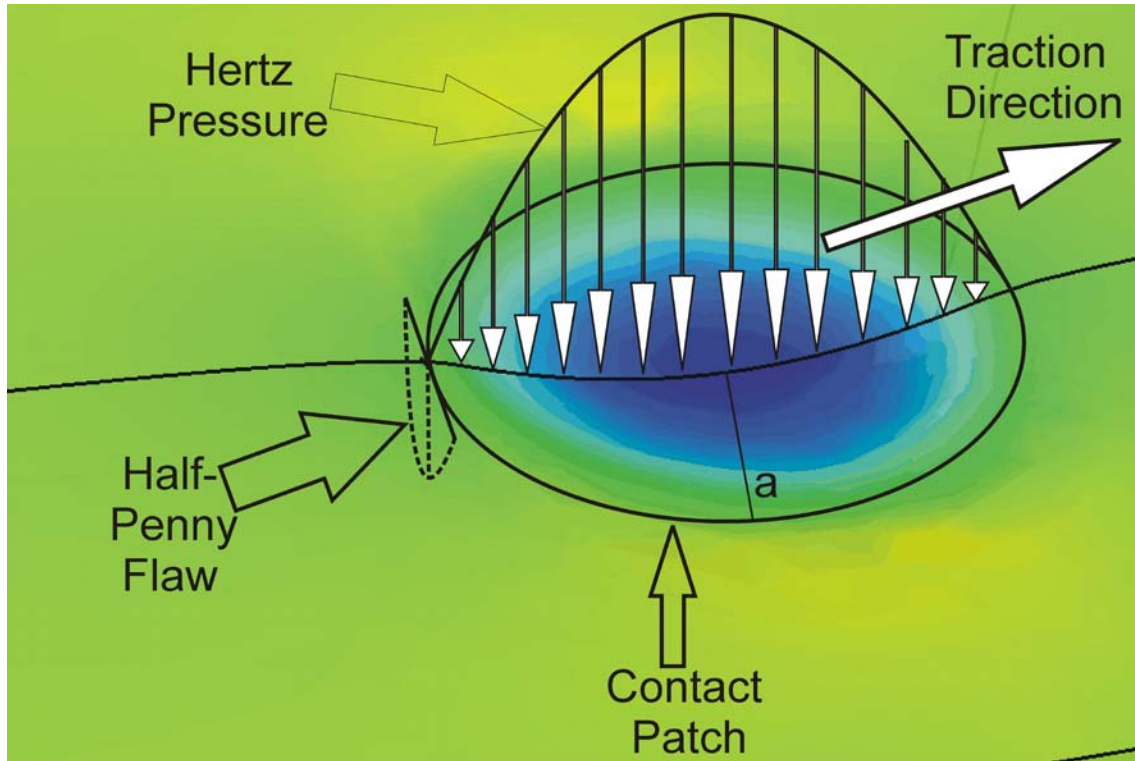


Figure 2-5. Initial configuration of crack and load at the beginning of the crack growth analysis in the FE model.

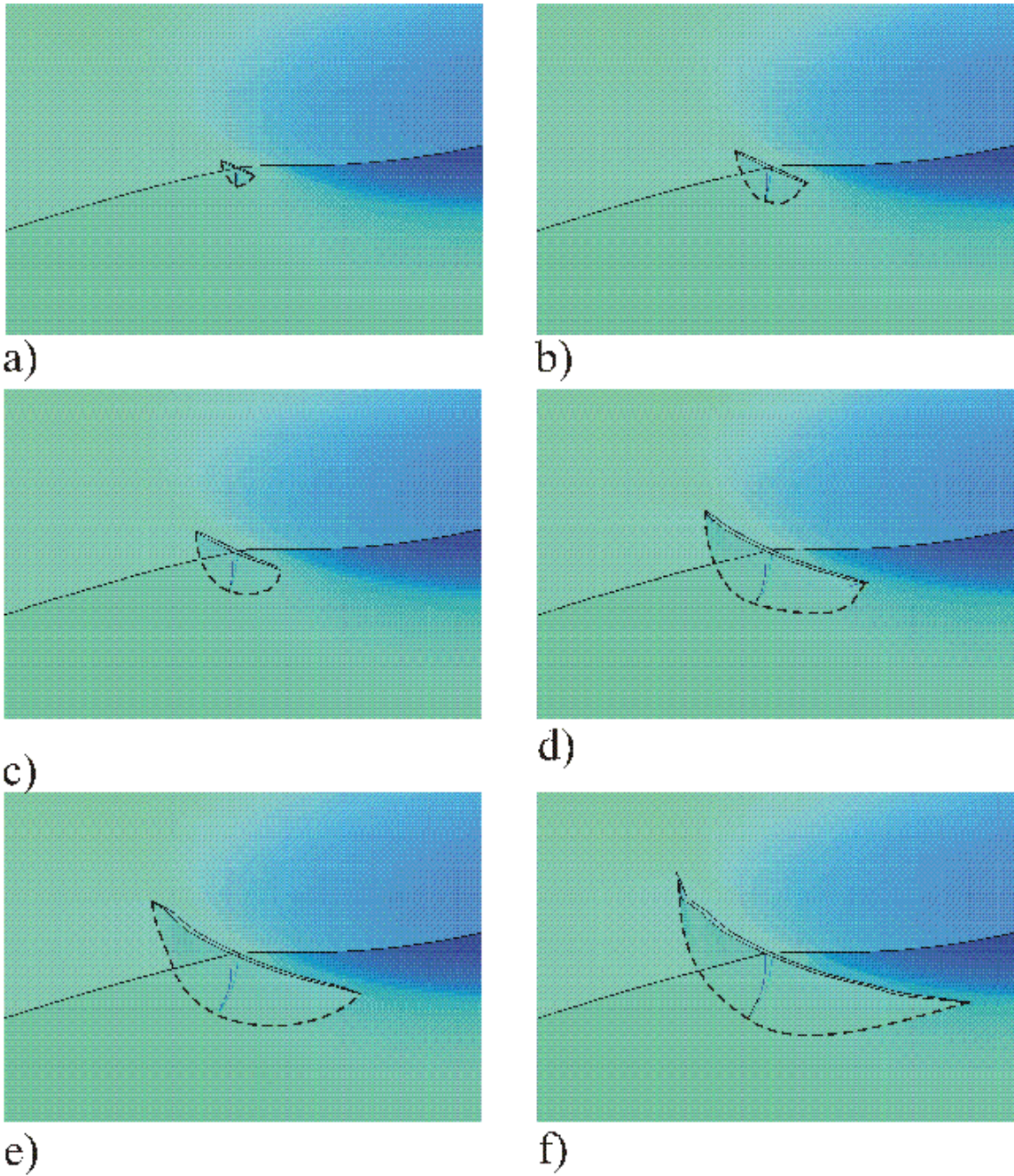


Figure 2-6. Incremental images of crack growth for  $\mu=0.1$ . a) half-width= $0.04a$  depth= $0.07a$  b) half-width= $0.07a$  depth= $0.14a$  c) half-width= $0.09a$  depth= $0.16a$  d) half-width= $0.11a$  depth= $0.32a$  e) half-width= $0.12a$  depth= $0.41a$  f) half-width= $0.15a$  depth= $0.58a$ .

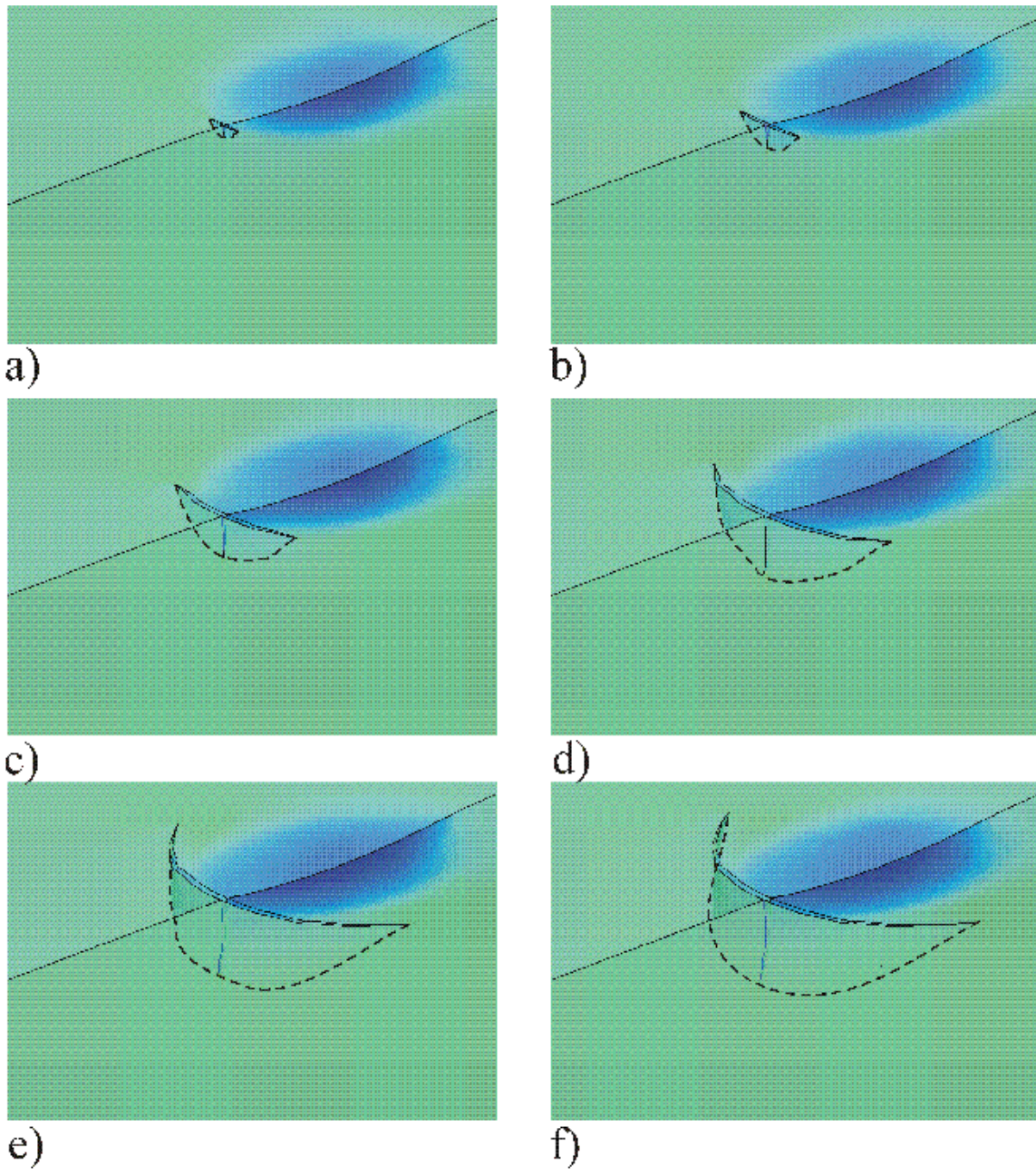


Figure 2-7. Incremental images of crack growth for  $\mu=0.5$ . a) half-width= $0.11a$  depth= $0.17a$  b) half-width= $0.17a$  depth= $0.35a$  c) half-width= $0.29a$  depth= $0.69a$  d) half-width= $0.39a$  depth= $1.07a$  e) half-width= $0.523a$  depth= $1.46a$  f) half-width= $0.59a$  depth= $1.59a$ .

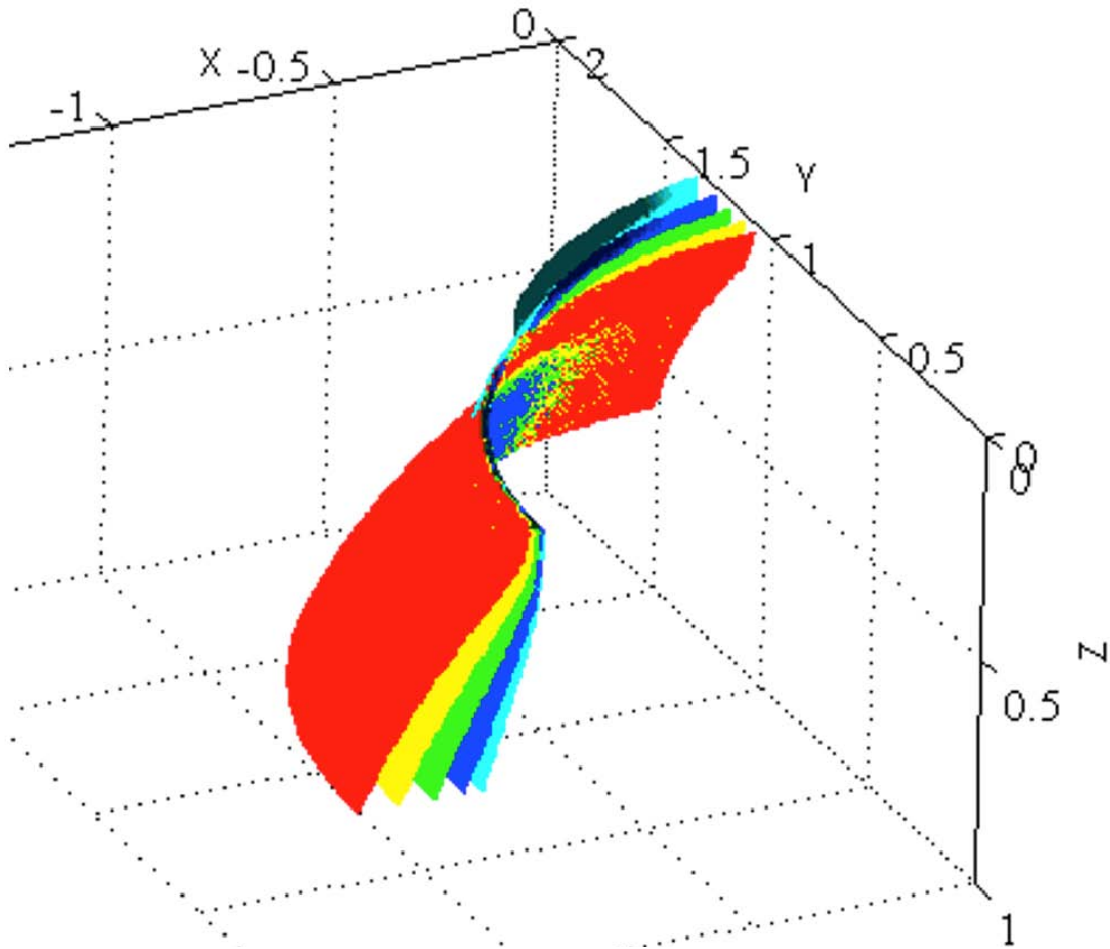


Figure 2-8. Cracks produced for  $\mu= 0.1, 0.2, 0.3, 0.4,$  and  $0.5$  and  $\nu=0.28$ . Note the increasing surface radius and steepness with the increase of the friction coefficient.

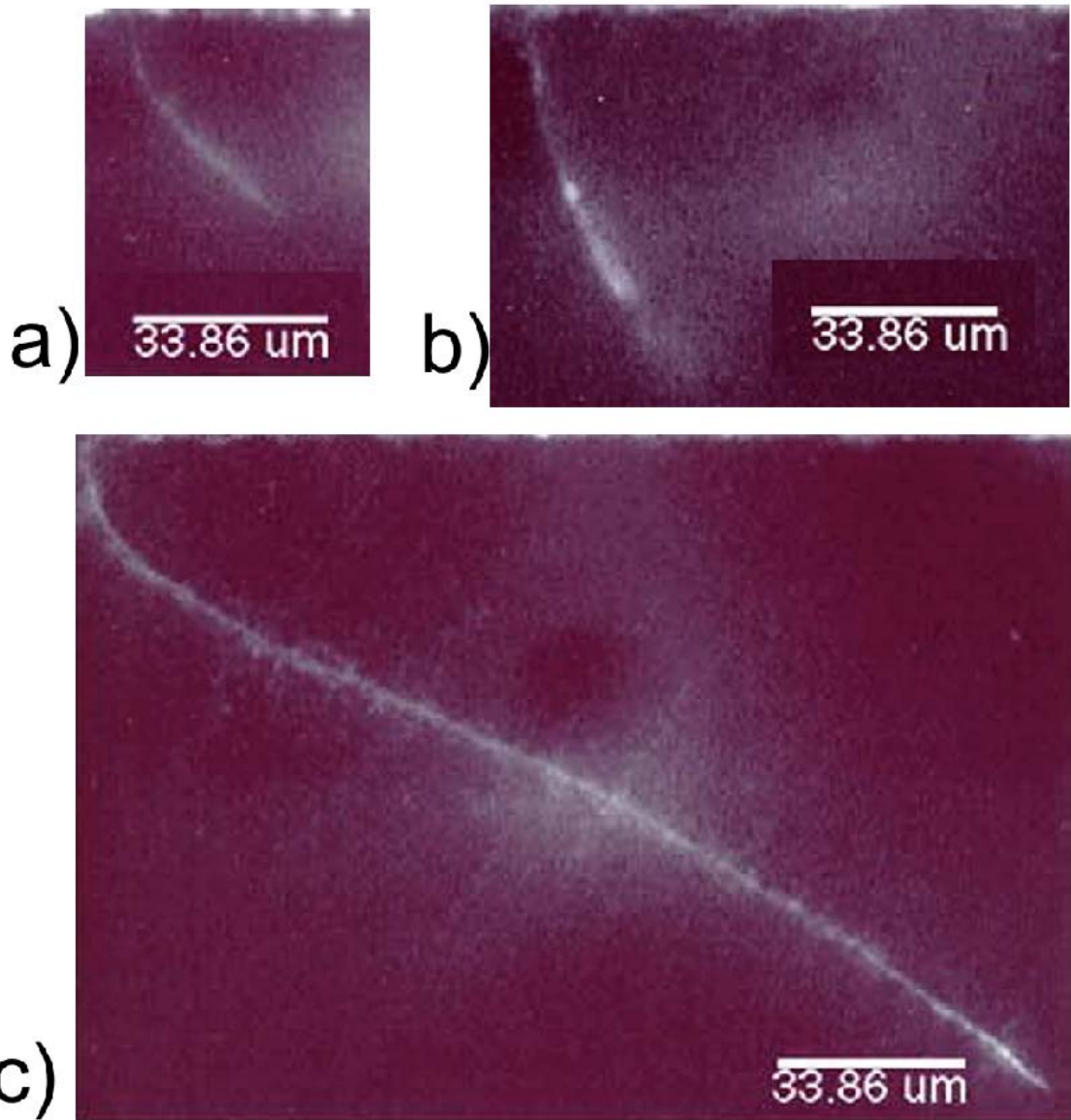


Figure 2-9. Cross-sections of multiple “natural” c-cracks on 12.7 mm diameter, grade 5 balls that (after manufacturing) had a typical 0.01  $\mu\text{m}$  roughness. See Zhao et al. (2006) for details.

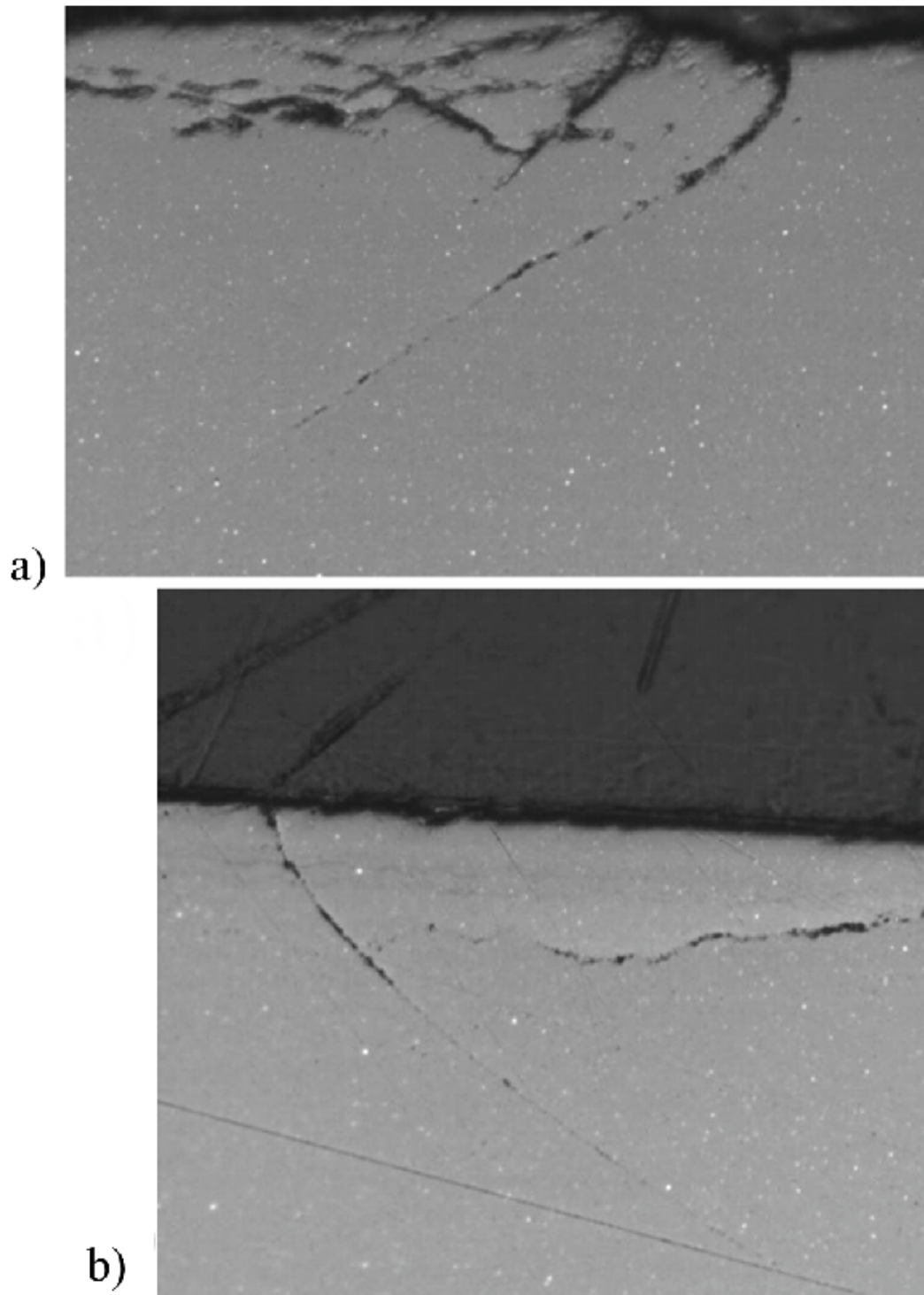


Figure 2-10. Cross-sections of artificially produced c-cracks. Images in proportion but scales are not shown. [Image courtesy of The Timken Company].

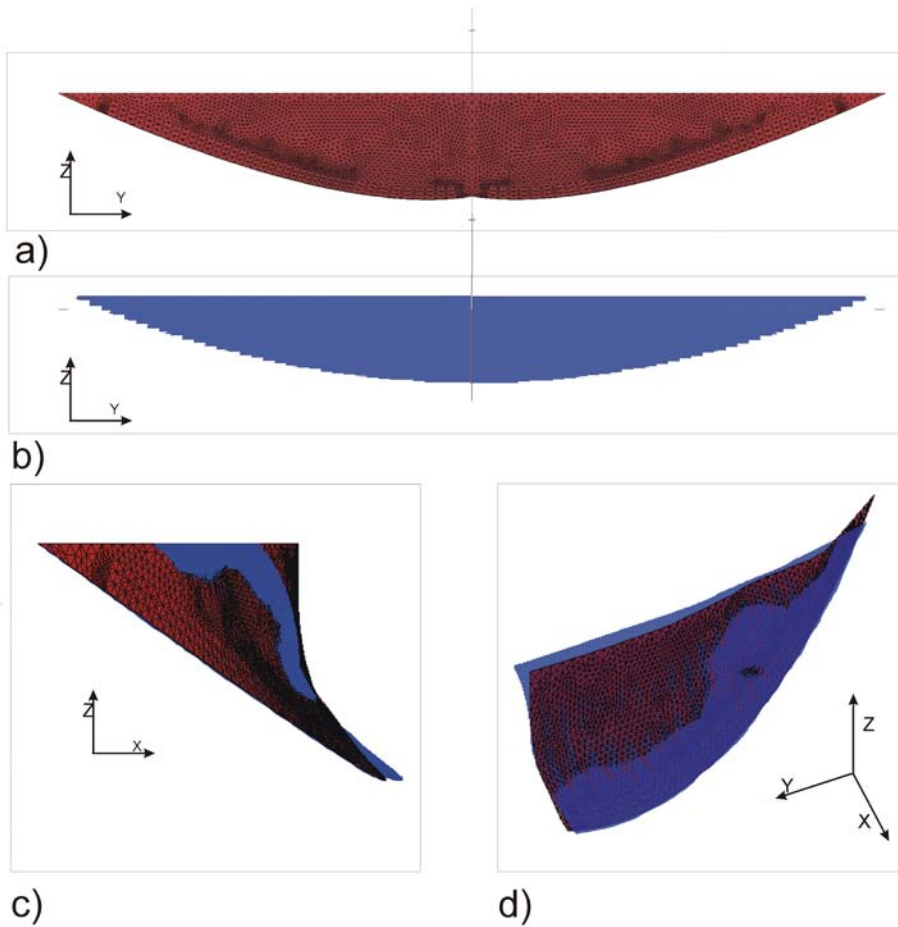


Figure 2-11. For  $\mu=0.1$ , from the front a) incremental growth crack, b) stress-state crack. Superposed images of half-cracks produced by the stress-state (in blue) and the incremental growth (in red) at c) the cracks midsection and d) from an azimuthal angle of  $45^\circ$  and a elevation angle of  $18^\circ$  as defined by matlab (Mathworks, 2005).

## CHAPTER 3 GENERAL MODELING ISSUES OF SURFACE FLAWS SUBJECT TO ROLLING CONTACT FATIGUE

### 3.1 Introduction

The partial cone crack has a very complicated shape as illustrated in chapter 2. It is not planar, like a semi-elliptical flaw, nor axisymmetric, like a cone crack. Modeling the shape accurately in order to calculate accurate SIFs for the geometry has been a focus of this research. A few of techniques to acquire the desired shape have been used where the first technique was dependent upon the complex use of splines to generate a 3D surface (see Fig 3-1).

In general, the simulation of a semi-elliptical crack is an advanced application of FEA code. In addition to the fact that the part has highly curved surfaces, it is also a closed geometry (two faces of the same body are immediately adjacent to each other) and this complicates meshing. The proper mesh density for a surface crack under RCF is really dependent on the purpose of the model. For the purpose of calculating accurate stresses, the user must not only have accurate enough meshes to account for the high stress gradients near the contact periphery but also to account for the  $1/\sqrt{r}$  singularity in the stress field because of the presence of the crack in the material. For the purpose of calculating SIFs, the mesh can be coarser but if the crack faces close than the contact calculated between them needs to be exceptionally accurate and this demands more refinement.

The model's boundary conditions are also quite complicated. There is contact between a ball and raceway (of different curvatures) whose interfacial traction is unknown. The contact patch is very small relative to the size of the entire cracked body and an entire cracked ball is not simulated, but a large portion of the ball whose edge

effects do not contribute to the overall analysis. In addition, the contact itself has high stress gradients near the contact periphery which should be properly accounted for with mesh density if stress results are required. At the same time, many look into the problem of cracks in rolling contact fatigue and attribute the growth mechanism to fluid penetrating the crack and the crack face shutting down, resulting in an interior pressure on the crack faces. This is neglected here due to the complex modeling issues of the fluid-structure interaction problem.

### **3.2 Computing Stress Intensity Factors**

For this analysis, computing stress intensity factors (SIFs) from the crack tip is an additional difficulty. By simply applying the cracked modeled specimen to tensile loading (or mode I loading) (see fig 3-4) will result in all three modes being present at the crack tip (see fig 3-5). This is due to the complex shape of the crack which can turn even the simplest loading into complex stress intensity factors. Whichever method of SIF calculation is chosen, it must be able to calculate for all three modes of crack tip displacement.

There are a few methods for SIF computation, but the main focus herein is on J-integral computation and displacement correlation. ABAQUS has a built in J-integral decomposition tool in order to extract SIFs where they are needed, however, this tool is not complete. Its formulation is based on energy methods and, even though ABAQUS is completely capable of solving a multiphysics problem, it omits multiple physical contributions (like heat, dynamic behavior, etc.) in SIF calculation. It even neglects a component of the traction term seen in

$$J_R = \int_{\Gamma} w dy - T_i \frac{\partial u_i}{\partial x} ds \quad (3-1)$$

which arises due to crack face contact (see fig 3-1). So even if the displacement of every node is computationally accurate, the final SIFs will be as though no contact was defined. Since the model is often in a state of compression somewhere, crack face contact needs to be properly accounted for in an external SIF calculation.

As a result, displacement correlation became easier to apply in this regard. No matter which physical interactions are influencing the crack opening, if the displacements are correct, so are the calculated SIFs. The theory for all three modes of crack opening can be written as:

$$K_I = \frac{E}{4(1-\nu^2)} \sqrt{\frac{2\pi}{r_d}} (u_1 - u_2) \quad (3-2)$$

$$K_{II} = \frac{E}{4(1-\nu^2)} \sqrt{\frac{2\pi}{r_d}} (v_1 - v_2) \quad (3-3)$$

$$K_{III} = \frac{E}{4(1-\nu^2)} \sqrt{\frac{2\pi}{r_d}} (w_1 - w_2) \quad (3-4)$$

Note that  $r_d$  is the radius from where the relative displacements are measured from the crack tip, and  $u$ ,  $v$ , and  $w$  correspond to the displacements in the  $x$ ,  $y$ , and  $z$  directions for the local coordinate system at the tip of the crack (see Fig 3-3). As of this writing, displacement correlation is not available in ABAQUS (v.6.7-1) and so an external code must be written. ABAQUS Python libraries have been used to construct a post-processing routine. Since the crack face and the crack tip are nonplanar, the coordinate system for displacement correlation must be calculated at each point SIFs

are extracted along the crack front. To illustrate the complexity of the post-processing routines, the following is done for the computation of SIFs via this method:

- Nodes near the crack tip (I have used the quarter-point nodes of the first element adjacent to the crack tip) are chosen and cataloged with their neighbors on the opposing faces.
- The radius for each of these quarter-point elements is measured to the crack tip.
- A coordinate system is created that has components tangent to the tip line, locally normal to the face, and in the direction of the crack plane. These are created by using Macros for establishing the relative positions of nearby nodes and cataloging their normalized directions for later scripting.
- The distances of the opposing nodes measured in the new coordinate system are substituted into the above equations.
- The resultant SIFs are output to a text file for later manipulation and are saved with the same file name as the job which the data has originated from.

For ease of use and flexibility, the displacement correlation routine was encoded via a Python code subroutine (using the ABAQUS Python library) that would run on job completion and output all three SIFs to an external text file for array manipulation.

### **3.3 Parametric Studies**

Even with the SIF calculation code written, there is still much work to be done in terms of the number of models to be run and how the resulting data will be organized for any parametric study. For example, a given model with a certain geometry may need to have 10 load orientations analyzed. This means that 10 jobs should be created for one .inp files which refer to different load files. After each analysis is completed, the post-processing code must save that resulting data so it can be easily found. Then this data must be read into software that can convert the units, manipulate the arrays, and create useful plots. This entire process should be automated and tell the user when it has

completed to remove user downtime. This has been done by using MATLAB in the structure below in Fig 3-6.

### 3.4 Physical Effects

The contact patch between a ball and raceway can vary in ellipticity based on the radii of curvature of the ball/raceway pair. There are two contact patches on opposite sides of each ball but that of the inner raceway is smaller and therefore has a higher max pressure in its distribution. See fig 3-7 for a visual description. If there exists a flaw on the ball surface and it is on the path where a contact patch will pass, then a crack will alternately see contact patches approach it and move away. See fig 3-8.

Once the models and the tools are set up, analysis may commence to see what physical effects drive up the SIFs. For example, there is the magnitude of the normal load, the shape of the load (i.e. the amount of ellipticity), the orientation of the load (on which side of the crack its on and how far away from the crack it is), the amount of traction that the load exhibits on the ball surface, the effect of friction between the two crack faces, if there is a pressure acting upon the crack faces, the crack depth, the crack width, and the amount of curvature on the crack face. For example, if the depth of crack is considered for analysis for geometry in 3-7 the below variation for  $K_I$  is obtained.

While most of these effects have been analyzed, the one that seems to exhibit the largest effect upon the SIFs is the amount of traction that exists between the ball and the raceway. The location of the load is even more important when traction exists at the contact interface. Even if the location of the load is limited to immediately next to the crack on the surface, there are still two possible directions of traction, resulting in four

possible load orientations. In reality, the most effective orientation for crack opening is illustrated below. See fig 3-10.

For a lubricated ball bearing contact the EHD viscous friction coefficient is in the range of 0.05 to 0.09. The effect of this surface traction on the SIFs is very significant as demonstrated in a plot below (see fig 3-11) which displays an increase of more than 250% as the coefficient of friction increases from 0 to 0.07.

### **3.5 Conclusions**

This chapter has discussed some of the main concerns with modeling a small non-planar surface flaw with a nonplanar crack tip. The benchmarks achieved include:

- Meshed models of nonplanar surface crack geometries were created (see Appendix B for a step-by-step illustration).
- Stress intensity factors are calculated in a geometry that can undergo compression with nonplanar crack face contact.
- Parametric studies were conducted in an organized fashion to analyze multiple effects.
- Trends were observed and are discussed in depth in chapter 5.

### 3.6 Figures

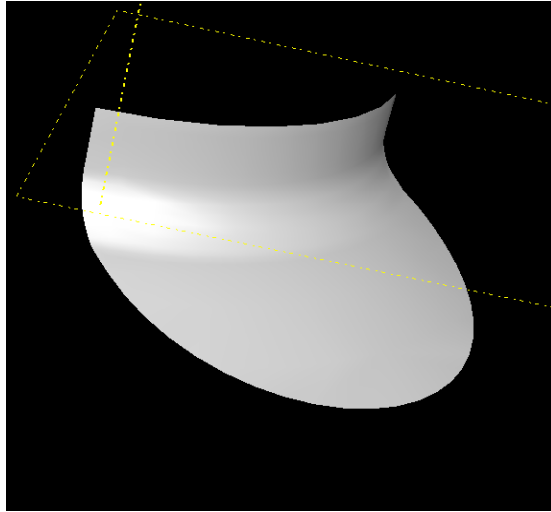


Figure 3-1. A partial cone crack geometry generated from some experimental cross-sections of the crack created with a spline technique.

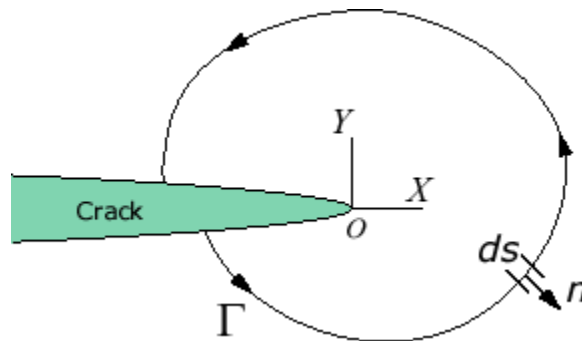


Figure 3-2. General J-integral equation reference coordinate system about the local crack tip.  $T_i$  is the traction term which is equivalent to the forces in the normal direction along the integral path which would be applied to the interior region if it was independent of its surrounding substrate in order to maintain the identical state of equilibrium.

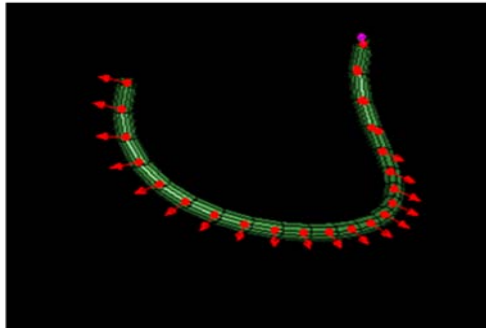
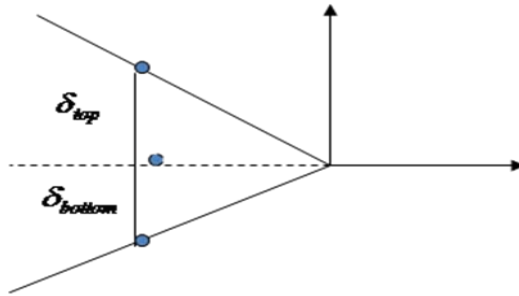


Figure 3-3. Crack tip coordinate systems for CTOD (crack tip opening displacement).

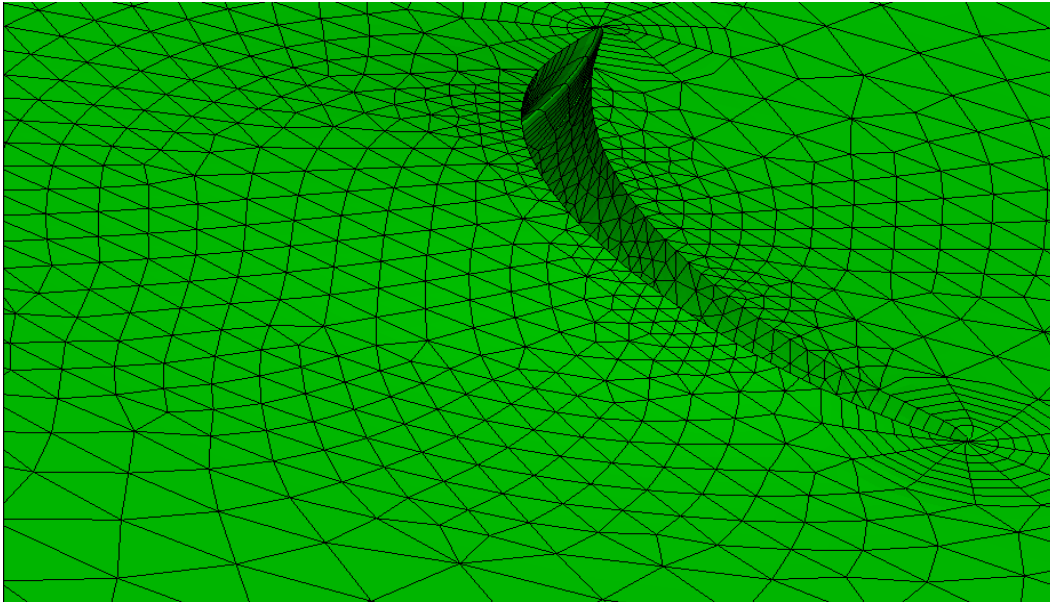
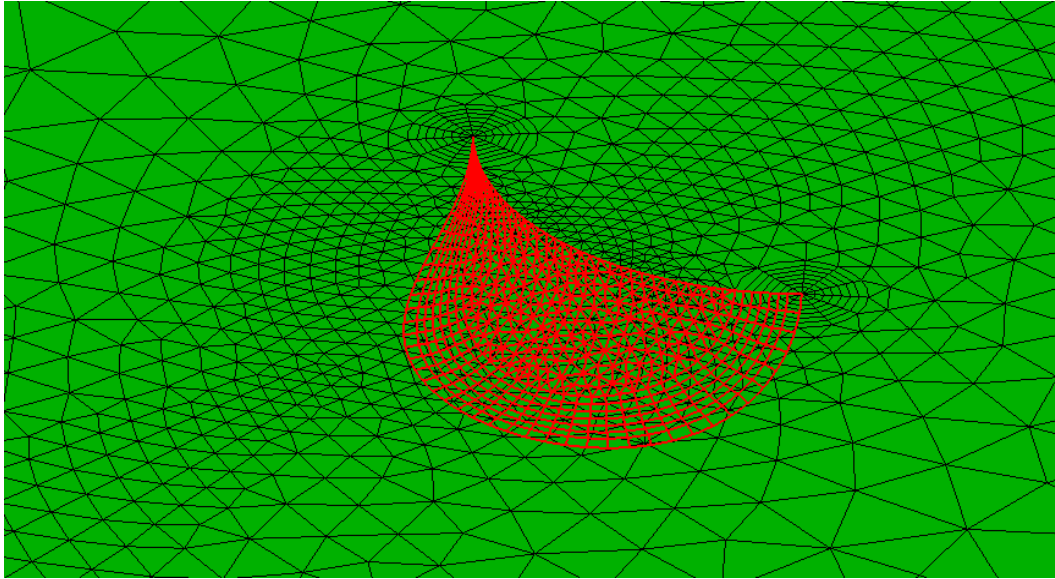


Figure 3-4. A c-crack specimen with subsurface crack face highlighted above. In tension below, indicating opening of the crack faces. Displacements exaggerated.

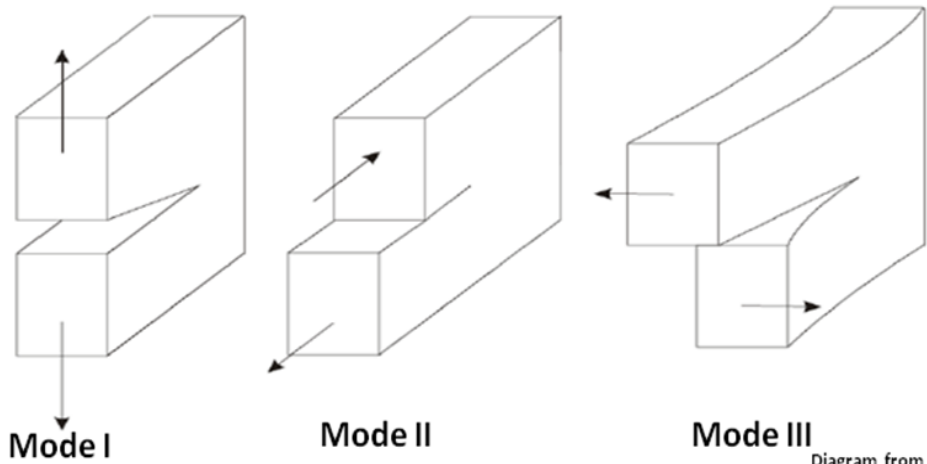
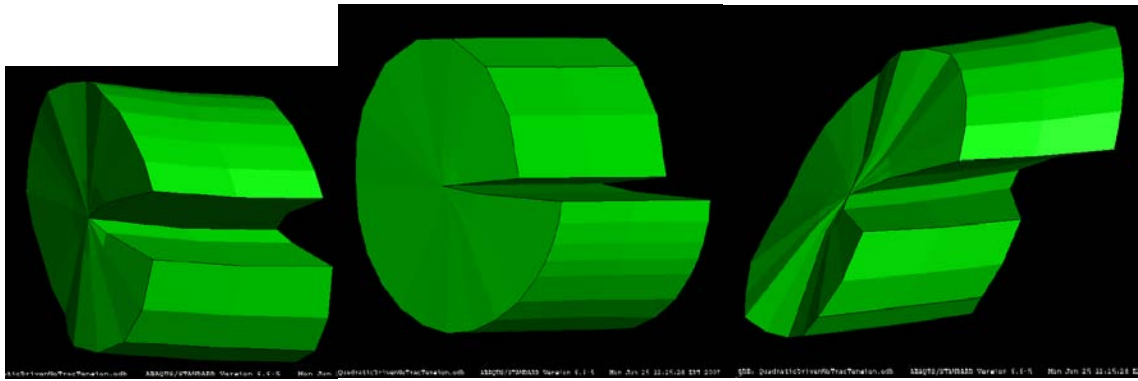


Diagram from Dr. Erik Knudsen

Figure 3-5. Elements from the crack tip in fig 3-3 reoriented to show that different parts of the crack tip undergo all three of the different types of deformation. (Displacements exaggerated.)

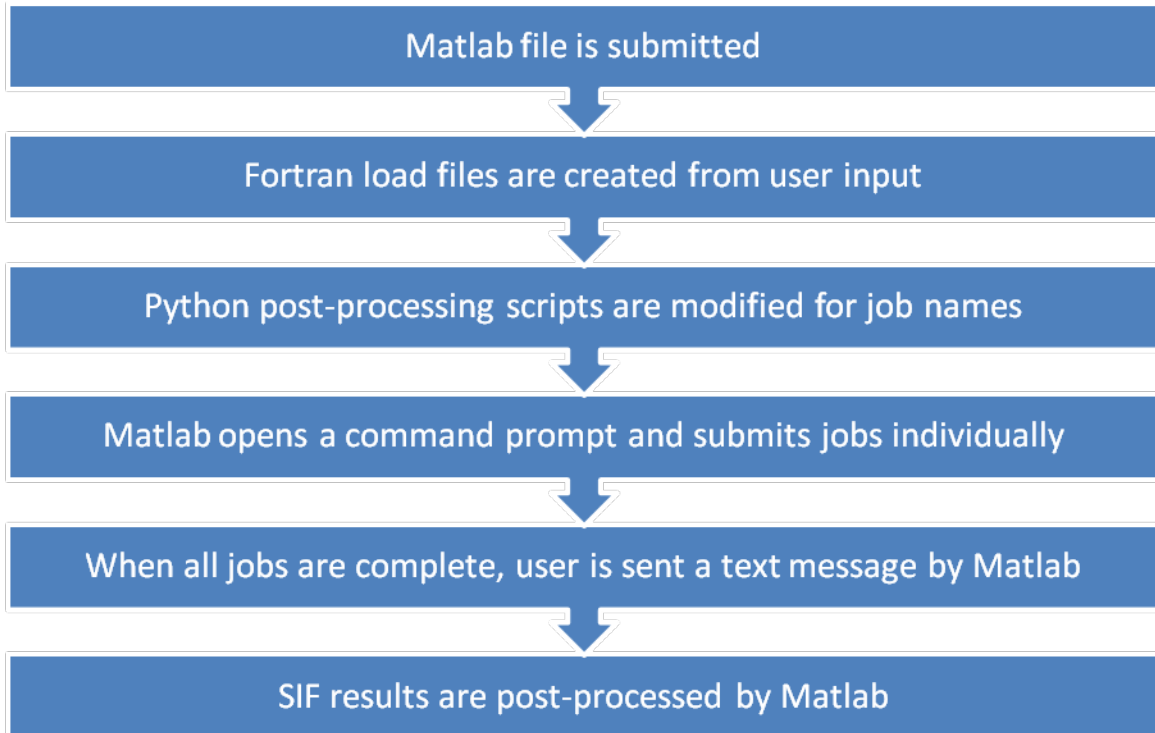


Figure 3-6. Visual illustration of the Matlab code which is used to create, submit, post-process, and organize the desired FEA results.

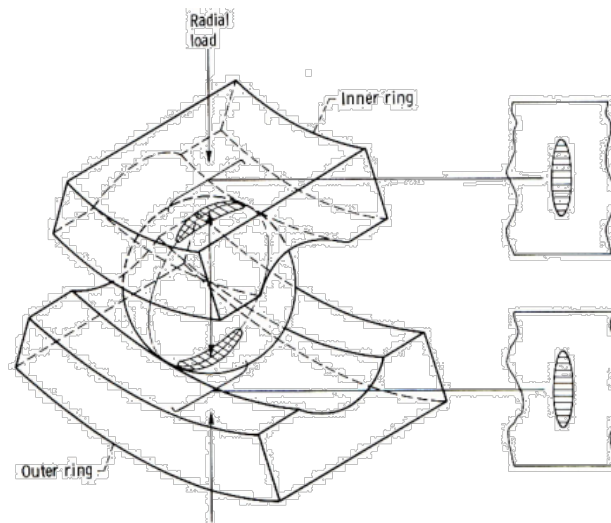


Figure 3-7. An illustration of a ball in a ball-bearing raceway system to indicate the location and orientation of the contact patches.

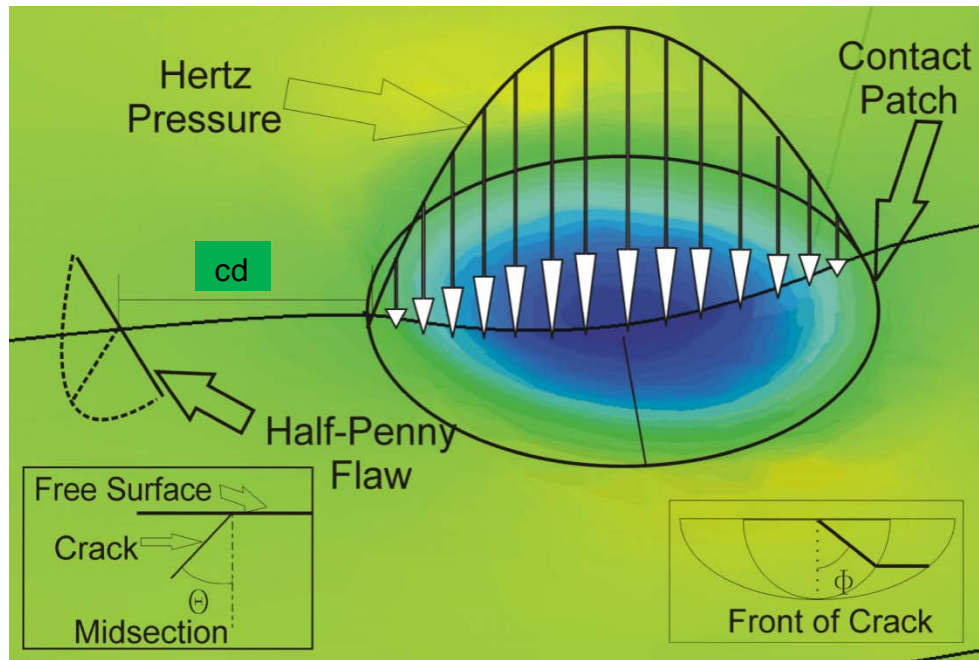


Figure 3-8. Relative orientation of an elliptical load near a surface crack indicating,  $c_d$ , a variable defining the change in distance between the crack and load in a single pass.

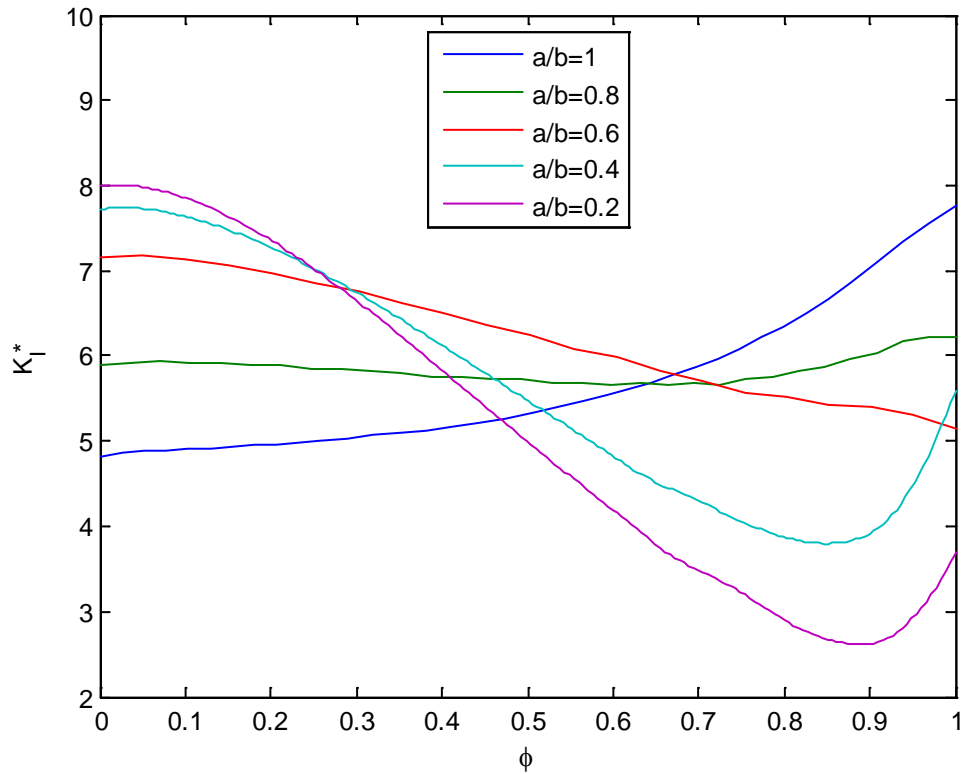


Figure 3-9.  $K_I$  for  $\theta=60^\circ$  near  $r=1b$  load for varying aspect ratio showing a semi-elliptical crack steeply angled to the surface will produce the SIFs in MPa for  $\rho_o=1$  MPa and for the geometry in fig 3-7 along the crack tip.

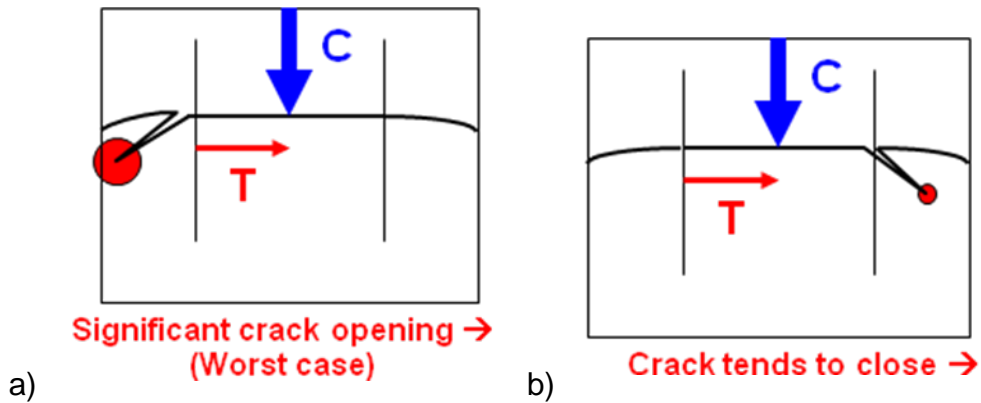


Figure 3-10. A) the location and orientation of load,  $C$ , and traction,  $T$ , to have the most amount of crack opening but if the traction direction is reversed as in B) the crack tends to close.

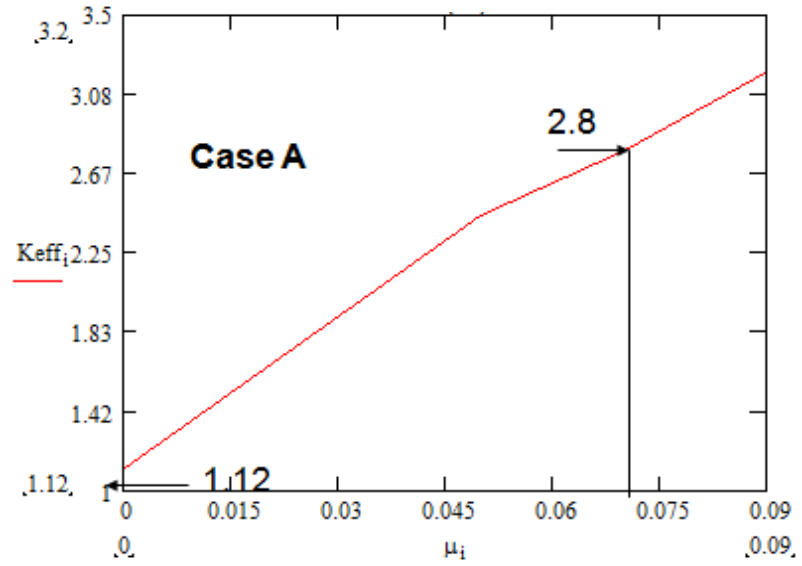


Figure 3-11.  $K_I$  as a function of the coefficient of friction on the surface for  $p_o=540$  ksi (3.7 GPa), Crack angle = 30,  $b=250$  mm,  $a=75$  mm,  $a/b=0.3$ .

## CHAPTER 4 EXPERIMENTAL ANALYSIS

This chapter focuses on the bodies of experimental work that has been analyzed by us, or has contributed to this work, in the pursuit of calculating a fatigue threshold,  $K_{th}$ . A mixed mode fatigue threshold has not been agreed upon in literature (see Chapter 1) and is necessary for computing what size flaws are allowed into service. The three tests discussed here are:

1. A novel test for fracture toughness (Piotrowski and O'Brien, 2006) for a fracture toughness parameter,  $K_c$ .
2. Brazilian disc (BD) testing for finding a mixed-mode fracture toughness,  $K_c$ .
3. A V-ring test for finding a mixed mode fatigue threshold parameter,  $K_{th}$ .

### 4.1 A Novel Fracture Toughness Test

An experimental analysis conducted by the Aerospace Corporation has contributed to figuring out how to treat these mixed mode SIFs for a single fracture parameter. In this new test, a Vickers indented ball is placed in the compression of opposing conformal platens (see Fig 4-1). This compression results in bulging at the equator and a tensile field along the surface where the cracks emanate from the Vickers indentation (Fig. 4-2).

With the magnitude of the tensile field determined from FEA and the flaw size known from measurements, SIFs can be calculated by combining the empirical equations of Newman and Raju (1981) with equations to account for the residual stress field induced by the indent, as below:

$$K_1^{app} = \sigma \sqrt{(\pi a / Q)} M_1 f_\phi \left[ 1 + 0.1(1 - \sin \phi)^2 \right] \quad (4-1)$$

$$M_1 = 1.13 - 0.09(a / c) \quad (4-2)$$

$$f_{\varphi} = \left[ (a/c)^2 \cos^2 \varphi + \sin^2 \varphi \right]^{1/4} \quad (4-3)$$

$$Q = 1 + 1.464(a/c)^{1.65} \quad (4-4)$$

And to account for the residual stress field:

$$K_{Ic}^{resid} = 0.016(E/H)^{1/2} (P/c^{3/2}) \quad (4-5)$$

(which ignores the correction from Smith and Scattergood (1992) for the crack shape dimensions). The SIFs are additively combined and the residual stress correction makes for a reasonable percentage of the final calculation, like one test would indicate:

$$K_{Ic} = 3.19 + 1.19 = 4.38 \text{ MPa}\sqrt{\text{m}} \quad (4-6)$$

Angled indentations are currently the subject of analysis to determine how the mixed modes of deformation contribute to the resulting fracture parameter. The plots resulting from this work are in fig 4-3 and 4-4 which indicate a lack of dependence on indentation load and crack size. The test is featured in Piotrowski and O'Brien (2002) and concludes that the mode I fracture toughness (for NBD 200 material) is  $4.85 \pm 0.36$  MPa $\sqrt{\text{m}}$ . For comparison the indentation that created the cracks on the specimens yield a fracture toughness of  $5.48 \pm 1.34$  MPa $\sqrt{\text{m}}$ .

## 4.2 V-Ring Test

### 4.2.1 Experimental Procedure to Determine Growth Regime

The single-ball, v-ring test consists of two opposing inner rings that squeeze a sandwiched ball as it rotates (see Fig. 4-5). The lower ring is rotated at a certain speed to drive rotation while the upper ring induces vertical load. The two contact paths on the sides of the ball are perfect locations for c-crack initiation and testing. Balls are cracked with a rigid pendulum device (see Fig. 4-6).

After placing the ball into the device the crack is subjected to RCF. After a sufficient number of cycles, the ball is presumed to survive and testing stops. If there is spallation before this number of cycles is achieved, an accelerometer is tripped and the test stops. The v-ring test has been mentioned in prior work for similar testing (Miner et al., 1996).

In order to determine what flaw size is so small that it will not grow under the expected life of the part, the following steps must be followed:

- Run flaws of known sizes and geometries under well-understood RCF conditions.
- Analyze specimens to determine which flaws grew to failure.
- Simulate each of these experiments in FEA to determine each sample's maximum SIFs.
- Combine the SIFs into one parameter,  $K_{eff}$ , that will bracket the possible values of  $K_{th}$ .

#### **4.2.2 Specimen Analysis**

Once testing is stopped images are taken by white-light microscope images and destructive grinding to determine depth and geometry. Once all tests are completed, the data is compiled in a plot of applied stress versus crack size on the surface. [This data was not available for publication.] (See fig. 7-1 for an example image.)

#### **4.2.3 Stress Intensity Factor Determination Of Individual Test Specimens**

The contact patch size was calculated for the prescribed load configuration using standard Hertzian contact theory. This contact patch was simulated as a pressure distribution in the ways mentioned in the simulation chapter of this document (chapter 3). The SIFs for each case of crack size and load magnitude were stored for later use. [This data was also unavailable for publication.]

#### 4.2.4 Calculating A $K_{eff}$

In simple fracture tests, the mode I stress intensity factor may be the only non-zero SIF. In this case it is straightforward to use the fracture toughness or the  $K_{th}$ , for either static or fatigue load experiments, to determine what loading conditions will lead to failure. However, in these rolling contact fatigue tests all three modes are present. How these three modes of fracture should be combined to determine a fatigue threshold has been the subject of study for many and has resulted in a wide variety of answers which have no common ground (Richard et al., 2009). For  $K_{th}$  we have continued to use the critical strain energy release rate (CSERR) discussed below.

#### 4.3 Brazilian Disc Test

Herein, the BD test is implemented to determine mixed-mode fracture toughness of silicon nitride. Silicon nitride has material properties that are favorable to hybrid bearing applications including a low coefficient of thermal expansion, corrosion resistance, and a third the density of common bearing metals (Jahanmir, 1994). The material also has a low fracture toughness of about  $6.0 \text{ MPa}\sqrt{\text{m}}$  (Piotrowski and O'Brien, 2006). In the course of the manufacturing process, silicon nitride balls are subjected to a lapping process, to achieve the final submicron accuracy in ball diameter and circularity, where the balls are susceptible to low-velocity ball collisions. These low velocity interactions induce small surface cracks on the surface of the ball that, under operating conditions in a ball bearing, are subjected to severe rolling contact fatigue (RCF) conditions (Levesque and Arakere, 2008). Under mixed-mode loading, crack growth can lead to spallation and, as a result, these surface cracks are the biggest contributors to ball (and therefore bearing) failure (Levesque and Arakere, 2008, Wang, 2000). If finite element analysis (FEA) can simulate these flaws under service

conditions, then the nature of the effective crack driving force resulting from stress intensity factors (SIFs)  $K_I$ ,  $K_{II}$  and  $K_{III}$  must be properly understood in order to determine whether or not a crack is in the regime of growth. Herein, the focus is on defining an effective mixed-mode fracture parameter for silicon nitride.

#### **4.3.1 Experimental Procedure**

Brazilian disc NBD 300 silicon nitride specimens are 25.4mm (1 in.) in diameter and 2 mm thick. They are cut from bar stock and polished to 0.05  $\mu\text{m}$  surface finish. The discs are pre-cracked using about 20 collinear Vickers indentations performed on a Zwick Vickers Hardness Testing Machine using 20 kg load such that the penny cracks, formed by individual indents, link up to form one long penny crack. Multiple indents are used because the load required to propagate a penny crack from a single indent is very high, causing the discs to fracture at the support platens rather than propagate the center crack. The dimensions of the cracks induced are recorded of table 1.

With the specimens prepared in this fashion, they are placed into a conformal fixture in the plane of loading with the cracks oriented vertically or slightly off the load line as illustrated in fig. 4-9. The specimens are then loaded at a rate of 100 lbs/min (faster loading can result in fracture occurring at the platens instead of growing the created center crack) until fracture and then the test is stopped.

The load at which the specimen cracked and dimensions of the crack are recorded for each specimen at a number of different angles to the load line (see Table 4-2). This information will be used to calculate SIFs for the specimens at fracture in FEA.

### 4.3.2 Analytical Expressions for Mixed-Mode Stress Intensity Factors

Prior research has used the equations for stress intensity factors (SIFs) for small (with respect to the specimen thickness) semicircular flaws (formed by Vickers indentation) loaded under mixed-mode conditions approximated by (Marshall, 1994):

$$K_I = Y_1 \sigma c^{\frac{1}{2}} \sin^2 \theta \quad (4-7)$$

$$K_{II} = Y_2 \sigma c^{\frac{1}{2}} \sin \theta \cos \theta \quad (4-8)$$

where  $\sigma$  is the applied stress,  $c = \sqrt{ab}$  is the equivalent semicircular crack length,  $a$  the length of the semi minor axis of the critical flaw and  $2b$  the length of the semi major axis of the elliptical crack.  $Y_1$  and  $Y_2$  are geometric constants which are equal to 1.65 and 1.55 respectively for indented specimens (Petrovic and Mendiratta, 1976). These equations were implemented to approximate the SIFs for semi-elliptical flaws from equations for angled through-cracks in a biaxial stress field with a geometric constant. Even though experimental observations indicate crack closure at angles around  $35^\circ$  (as there is observed specimen shattering at angles higher than this), these equations do not discern crack closure and will always give non-zero  $K_I$  values (excluding  $\theta=0^\circ$ ). Also, the equations (though attributed to a semi-elliptical crack) only gives SIF values for a single point along the crack front instead of giving SIFs along the entire crack front as could be expected and also neglect  $K_{III}$ . For  $b= 0.02\text{m}$  and  $a= 0.0025\text{m}$ ,  $K_I$  and  $K_{II}$  are plotted as a function of the angle that the specimen is loaded at in figure 4-10.

### 4.3.3 Stress Intensity Factor Calculation Via Finite Element Modeling

Numerical methods are resorted to for calculating stress intensity factors for this centrally cracked, three dimensional (3D) BD. The finite element method (FEM) is

utilized to model each of the cracked specimens under the load which induced cracking to calculate the critical SIFs. Firstly, the disk is modeled uncracked and subjected to a uniform pressure distribution over the small contact region on the top and bottom edges of the disk similar to as observed in experiment. The stresses at the center of the disk are compared to those calculated analytically before proceeding. The stresses at the center of the disc can be calculated according to:

$$\sigma_x(0,0) = \frac{2P}{\pi BD} \quad (4-9)$$

$$\sigma_y(0,0) = \frac{-6P}{\pi BD} \quad (4-10)$$

$$\tau_{xy}(0,0) = 0 \quad (4-11)$$

where  $y$  is in the direction of load,  $P$  is the total load,  $B$  is the specimen thickness, and  $D$  is the diameter of the disc (Mitchell, 1961) and the full stress state for an uncracked disc is given by:

$$\sigma_x = -\frac{2P}{\pi B} \left[ \frac{(R-y)x^2}{r_1^4} + \frac{(R+y)x^2}{r_2^4} - \frac{1}{2R} \right] \quad (4-12)$$

$$\sigma_y = -\frac{2P}{\pi B} \left[ \frac{(R-y)^3}{r_1^4} + \frac{(R+y)^3}{r_2^4} - \frac{1}{2R} \right] \quad (4-13)$$

$$\tau_{xy} = \frac{2P}{\pi B} \left[ \frac{(R-y)^2 x}{r_1^4} - \frac{(R+y)^2 x}{r_2^4} \right] \quad (4-14)$$

$$r_1^2 = (R-y)^2 + x^2 \quad (4-15)$$

$$r_2^2 = (R+y)^2 + x^2 \quad (4-16)$$

where variables are defined in figure 4-9. The 3D FE model stress results on the mid-plane of the disc showed excellent agreement with the analytical expressions (Eqs. 4-12 - 4-13).

The FE mesh for a 3D disc model with a center crack with varying angles to the load necessitates the use of submodeling as the disc is ten times wider than the crack but does not require the same mesh density. Also, for simplifying the remeshing process for cracks of different angles and aspect ratios, a smaller square submodel was used (See fig. 4-9). The boundaries of this model are displaced according to a submodeling technique, where the displacements are applied to the boundary of a small cracked block to simulate its being a part of a much larger half-space (Dessault Systèmes, 2008). Benchmark studies were conducted to ensure that the boundary of the submodel is sufficiently far away such that the crack presence does not affect its displacements.

The SIFs calculated for an analysis of mixed-mode  $K_c$  parameters was a two part process. Firstly, the meshed cracks are analyzed with FRANC3D/NG by M-integral decomposition where material is still treated as isotropic (Banks-Sills et al., 2005). The SIFs are computed as a function of position along the crack front, and not just at one location as in Eqs. (4-7 – 4-8). The SIFs calculated from the BD FEM simulations neglect the presence of indents and the resultant residual stress induced in the specimen. To correct for this, the effect of the residual stress is superposed on the mode I SIF using the well-known equation (Lawn, 1993, Anstis, 1981):

$$K_{Ic}^{resid} = 0.016 \left( \frac{E}{H} \right)^{1/2} \left( \frac{P}{c_d^{3/2}} \right) \quad (4-17)$$

where  $E$  is the Young's modulus,  $H$  is the hardness (and equal to 15.5 GPa according to indentation testing),  $P$  is the indentation load (196 kN), and  $c_v$  is the distance from the center of the last indent to the end of the large semi-elliptical crack (here 0.47 mm is used as measured in sample  $S_3$  for  $\theta=10^\circ$ ). So  $K_I$  is the result of superposition of mode I SIF contributions due to the stress field from the applied load computed via FEA and from the residual stress field:

$$K_I = K_I^{FEA} + K_I^{resid} \quad (4-18)$$

#### 4.3.4 Mixed-Mode Fracture Criteria

Once these SIFs are calculated, there are multiple equations that could be used to calculate an effective single mixed-mode fracture parameter. For this analysis, equations that have a basis in physical behavioral characteristics are relied upon rather than the multitude of empirical equations that have been proposed in other works (Qian and Fatemi, 1996). The non-coplanar strain energy release rate (NCSESR) criterion assumes that the crack growth starts at a critical value of the strain energy release rate and it grows in a direction along which it is maximal. It is defined by (Hussain et al., 1974):

$$K_{NCSESR} = K_I \left[ b_{11} - b_{12} \frac{K_{II}}{K_I} + b_{22} \left( \frac{K_{II}}{K_I} \right)^2 \right]^{1/2} \left[ \frac{1 - \frac{\gamma}{\pi}}{1 + \frac{\gamma}{\pi}} \right]^{\frac{\gamma}{2\pi}} \quad (4-19)$$

$$b_{11} = \frac{4(1 + 3 \cos^2 \gamma)}{(3 + \cos^2 \gamma)^2} \quad (4-20a)$$

$$b_{12} = \frac{32 \sin \gamma \cos \gamma}{(3 + \cos^2 \gamma)^2} \quad (4-20b)$$

$$b_{22} = \frac{4(9 - 5 \cos^2 \gamma)}{(3 + \cos^2 \gamma)^2} \quad (4-20c)$$

Griffith proposed a maximum normal stress (MNS) criterion where fracture nucleates when the maximum stressed point on the surface reaches a specific tensile stress and the direction of the crack growth is normal to it (Griffith, 1920). The fracture condition is given by (Jayatilaka, 1979, Chen et al., 1986):

At the crack depth,

$$K_{MNS} = \frac{1}{2} \left[ K_I (1 + 2\nu) + \sqrt{K_I^2 (1 - 2\nu)^2 + 4K_{III}^2} \right] \quad (4-21a)$$

On the surface,

$$K_{MNS} = \cos \frac{\gamma}{2} \left( K_I \cos^2 \frac{\gamma}{2} - \frac{3}{2} K_{II} \sin \gamma \right) \quad (4-21b)$$

where  $\gamma$  is the angle between the initial crack plane and the plane of propagation (shown in fig. 4-9).

Other methods of crack propagation, in mixed-mode conditions, have been proposed with energy considerations. Sih developed a theory based on the strain energy distribution near the crack tip and defined a parameter called the strain energy density factor,  $S$ , given by (Qian and Fatemi, 1996):

$$S = a_{11} K_I^2 + 2a_{12} K_I K_{II} + a_{22} K_{II}^2 + a_{33} K_{III}^2 \quad (4-22)$$

Sih (1974) proposed that crack propagates in a radial direction along which  $S$  is minimum and the crack growth starts at a critical value of  $S$ .

At the depth,

$$K_{MSE} = \left[ K_I^2 + \frac{1}{1-2\nu} K_{III}^2 \right]^{1/2} \quad (4-23a)$$

At the surface, where  $\eta = (3-\nu)/1+\nu$  and  $K_{II}=0$

$$K_{MNS} = \sqrt{\frac{1}{4(1-2\nu)} \left\{ 16\mu a_{11} K_I^2 + 2(16\mu) K_I K_{II} \sin \gamma a_{12} + \left[ \frac{4}{1+\nu} (1-\cos \gamma) + (1+\cos \gamma)(3\cos \gamma - 1) K_{II}^2 \right] \right\}} \quad (4-23b)$$

where, for Poisson's ratio of 0.25,

$$a_{11} = \frac{1}{16\mu} (1+\cos \gamma)(\eta - \cos \gamma) \quad (4-24a)$$

$$a_{12} = \frac{1}{16\mu} \sin \gamma (2\cos \gamma - (\eta - 1)) \quad (4-24b)$$

$$a_{22} = \frac{1}{16\eta} (\eta + 1)(1 - \cos \gamma) + (1 + \cos \gamma)(3\cos \gamma - 1) \quad (4-24c)$$

$$a_{33} = \frac{1}{4\mu} \quad (4-24d)$$

Sih's minimum strain energy density (MSED) hypothesis is the most accepted theory for failure in mixed-mode loading for brittle materials (Chen et al., 2002).

The fourth fracture criterion used for the calculation of  $K_{IC}$  is based on the assumption that the crack starts propagating at a critical value of the strain energy release rate in the same plane as that of the initial crack (Erdogan and Sih, 1963)

$$K_{GC} = K_I \left[ 1 + \left( \frac{K_{II}}{K_I} \right)^2 \right]^{1/2} \quad (4-25)$$

If the strain energy release rate is considered to be the most critical component to drive crack growth than is evaluated according to:

$$G = \frac{1}{E}(K_I^2 + K_{II}^2) + \frac{1}{2\mu}K_{III}^2 \quad (4-26)$$

(where  $\mu$  is the shear modulus) to calculate an critical strain energy release rate (CSERR) SIF parameter as if there was only one mode of crack tip displacement according to:

$$K_{GC} = \sqrt{EG_c} \quad (4-27a)$$

$$K_c = \sqrt{K_I^2 + K_{II}^2 + (1+\nu)K_{III}^2} \quad (4-27b)$$

The "coplanar method" becomes identical to using a CSERR,  $G$  or  $G_c$ . The equations used are the same rewritten as a single SIF parameter, [where only two parameters ( $K_I$  and  $K_{II}$ ) are present]. By ignoring the tearing mode of crack tip displacement  $K_{III} = 0$  and then:

$$G = \frac{1}{E}(K_I^2 + K_{II}^2) \quad (4-28)$$

and to substitute and rewrite:

$$K_{GC} = \sqrt{E\left(\frac{1}{E}(K_I^2 + K_{II}^2)\right)} = \sqrt{(K_I^2 + K_{II}^2)} = K_I \left(1 + \frac{K_{II}^2}{K_I^2}\right)^{1/2} \quad (4-29)$$

and this is the same as the CSERR criterion.

These equations have also been written by Qian as:

At the crack depth,

$$K_G = \sqrt{K_I^2 + \frac{1}{1-\nu}K_{III}^2} \quad (4-30a)$$

And at the specimen surface

$$K_G = \sqrt{\frac{1}{1-\nu^2} \left( \frac{1}{2} \cos \frac{\gamma}{2} \right)^2 \left\{ \left[ K_I (1 + \cos \gamma) - 3K_{II} \sin \gamma \right]^2 + \left[ K_{II} (3 \cos \gamma - 1) \right]^2 \right\}} \quad (4-30b)$$

For good measure, a couple of empirical equations are included for comparison.

From Tanaka (1996),

$$K_T = \left( K_I^4 + 8K_{II}^4 + 8 \frac{1}{1-\nu} K_{III}^4 \right)^{1/4} \quad (4-31)$$

Also, from Lucht (2009),

$$K_{Mi} = \sqrt{\left( K_I + B |K_{III}| \right)^2 + K_{II}^2} \quad (4-32)$$

where  $B=1$  reduces to more familiar equations.

#### 4.3.5 Analysis Procedure

The best mixed mode criteria will be determined by analyzing each of the theories by using SIFs that are calculated as a function of position on the crack front. Previous work has dealt with through cracks and only had two points where SIFs were necessary to be calculated and others have used empirical equations that only provide a single SIF for the entire crack front (Banks-Sills, 1998). Here FEA provides us the advantage of calculating SIFs along the entire crack front. The calculated SIFs are found in Figs 4-13 - 4-15.

Having these SIFs as a function of crack front position complicates matters. SIF combinations can be high at either the surface or the depth of the crack. On the surface, SIFs can be affected by the residual stress present from the multiple indents but there is no  $K_{III}$  component (which is the component that has the least amount of analysis in prior work). Only a battery of analyses can be conducted to see the variation of the mixed mode parameters between the experimental samples. We compare each

method where the crack meets the surface, the depth of the crack, and where the maximum value of the parameters is calculated on the crack front.

FEA requires the specimen dimensions as an input, load at fracture, and crack dimensions. The specimen dimension is well defined and has negligible error. The load at fracture and the crack shape are measured at the fracture of the specimen in experiment. While the load at fracture is measured by the load frame, its error is also quite negligible. The crack dimensions, however, are only determined by analyzing the fracture surface as in fig 4-20. By prescribing an average error of 50  $\mu\text{m}$  to the crack depth, then the resulting error in the SIFs would be:

$$K_{I,II,III} = \sigma_{x,y,xy} \sqrt{\pi(a \pm 50\mu\text{m})} \Rightarrow \text{Error in } K_{I,II,III} = \frac{1}{2} \left( \frac{50\mu\text{m}}{a} \right) \quad (4-33)$$

which is significant in the light of the specimen dimensions in table 4-2.

An additional amount of variation comes from the material itself. Just because specimens with the same size cracks of the same type of material are subjected to the same type of loads does not guarantee failure as a result of the variation that occurs within the material (and between materials of different grades, as well). In previous studies on fracture toughness of a different grade of silicon nitride (TSN 03 NH where only  $K_I$  was present in testing) had a variation of  $4.85 \pm 0.36 \text{ MPa}\sqrt{\text{m}}$  (Piotrowski and O'Brien, 2006).

#### 4.3.6 Results And Discussion

Stress intensity factors were calculated for each experimental study by simulating the measured crack dimensions under the load that induced failure. The SIFs were tabulated for reference. (See Table 4-1) The SIFs tabulated are those that occur where

the crack meets the surface of the specimen. These are plotted since this is where the angle of crack growth,  $\gamma$ , was measured on the experimental specimens. Also, at this location  $K_{II}=0$  which makes these  $K_c$  calculations easier and transferrable to future researchers. In addition, experimental knowledge indicates that the point where crack growth is likely to initiate is at this location

Due to the geometry of the experiment, as the angle of the crack increases,  $K_I$  decreases while  $K_{II}$  increases.  $K_{IC}$  is clearly measured for  $\theta=0^\circ$  and is very close to the 4.6 MPa $\sqrt{m}$  measured through indentation testing. Pure  $K_I$  loading seems to induce the smallest of the calculated  $K_c$  parameters but with  $K_{II}$  contribution the mixed-mode  $K_c$  ends up at an average  $5.89\pm 1.13$  MPa $\sqrt{m}$  (whose error is the calculated standard deviation among tests).

Figure 4-19 shows the fractured specimens as a function of the angle  $\theta$ . The fracture of the specimen at  $\theta=90^\circ$ , which consisted entirely of pure mode I loading, occurred along the initial plane of the flaw. However, at all other angles the crack deviated from its initial plane. At the same time, it can be noticed that the inclined crack deviates from its initial plane to propagate in a direction normal to the maximum principal stress. It was also seen that in some of the samples, the cracks did not encompass all the Vickers indents on the sample. The disk shattered to several pieces at  $\theta=55^\circ$  and at  $\theta=50^\circ$  (see figure 4-19(D)). Note that these angles correspond to  $35^\circ$  and  $40^\circ$ , respectively, from the loading axis. FEA demonstrated that there this observation was due to crack closure around  $31^\circ$  without accounting for the residual opening stress produced by the indent. Examples of cracks on the fracture surfaces are shown in Figure 4-3.

#### 4.4 Conclusions

1. A novel test to calculate  $K_c$  from Michael J. O'Brien (Piotrowski and O'Brien, 2006) was used to calculate fracture toughness from the cracks propagating from an indent as  $4.85 \pm 0.36 \text{ MPa}\sqrt{\text{m}}$  (compared to  $5.48 \pm 1.34 \text{ MPa}\sqrt{\text{m}}$  from the indentations) in TSN-03 NH.
2. V-ring testing was used to experimentally calculate a CFS.
3. V-ring tests were simulated to calculate  $K_{th}$  boundary.
4. Measured  $K_C$  and  $K_{IC}$  through BD test simulations.
5. Investigated applicability of mixed-mode parameters through FEA simulation of BD testing.
6. Characterized fracture toughness for silicon nitride as a function of mode-mixity based on multiple criteria.
7. The max strain energy release rate criterion seems to be most effective, as its standard deviation is lowest for all the visited methods and it predicts  $5.89 \pm 1.13 \text{ MPa}\sqrt{\text{m}}$  for fracture toughness for the silicon nitride tested.

## 4.5 Figures

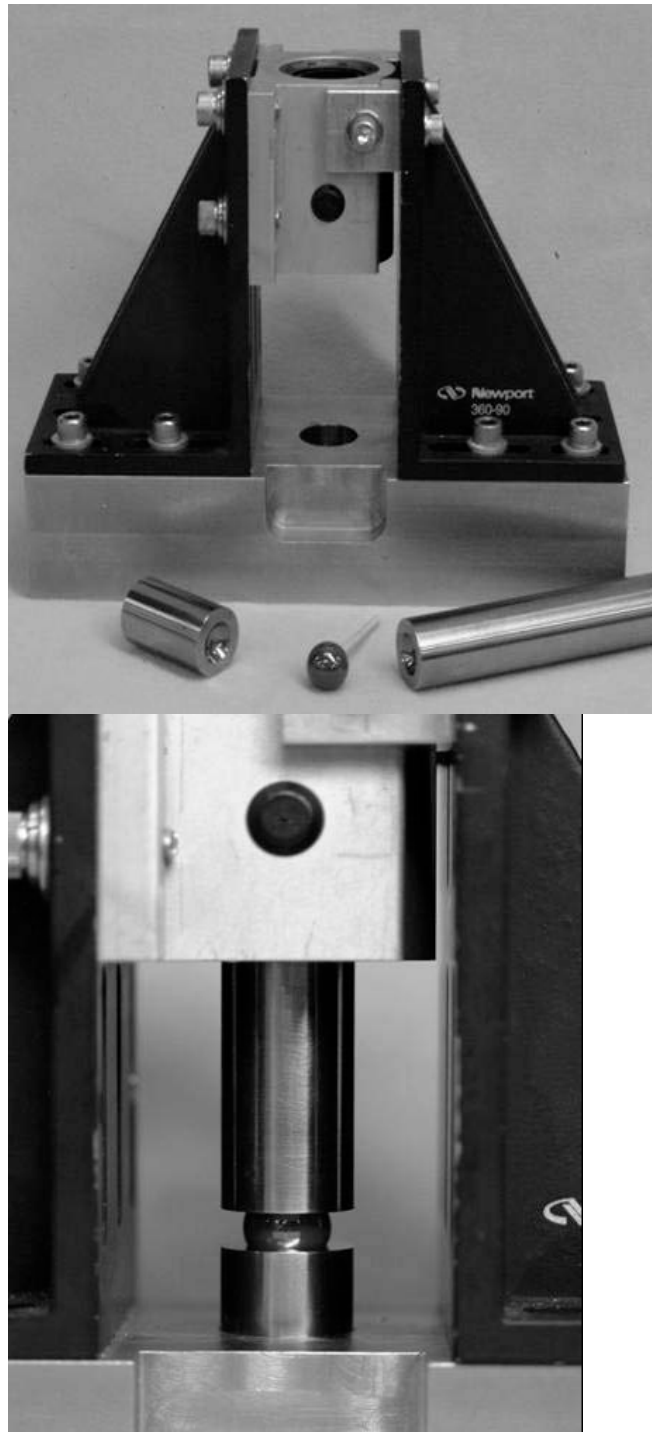


Figure 4-1. On the left, the designed fixture and a tested ball are displayed. On the right, the platens and ball are placed into the fixture in the orientation for testing.

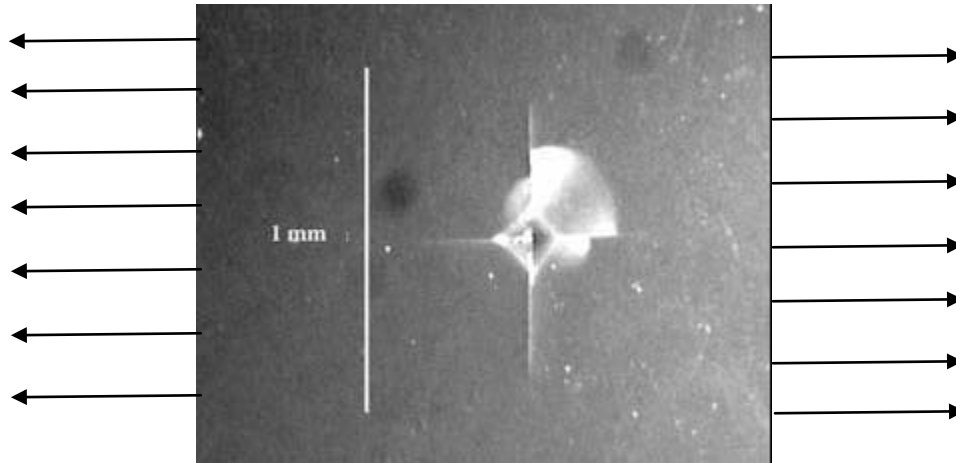


Figure 4-2. Close-up of indentation flaw, with measurement taken in the direction of growth due to applied load. Arrows indicate direction of tensile field.

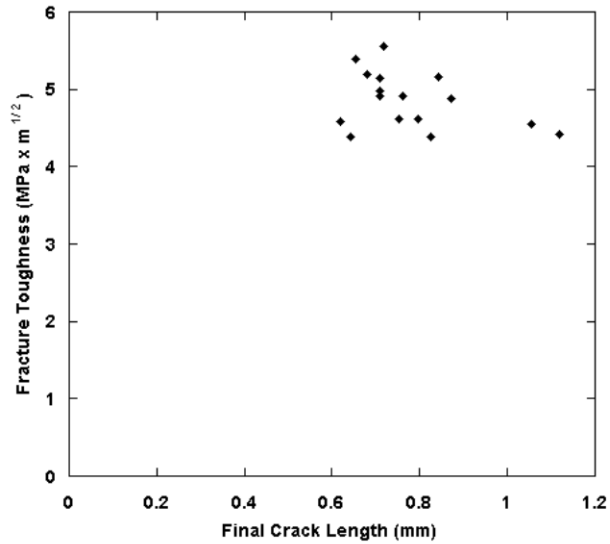


Figure 4-3. The fracture toughness of tested specimens versus the final crack length they became, indicating a lack of interdependence.

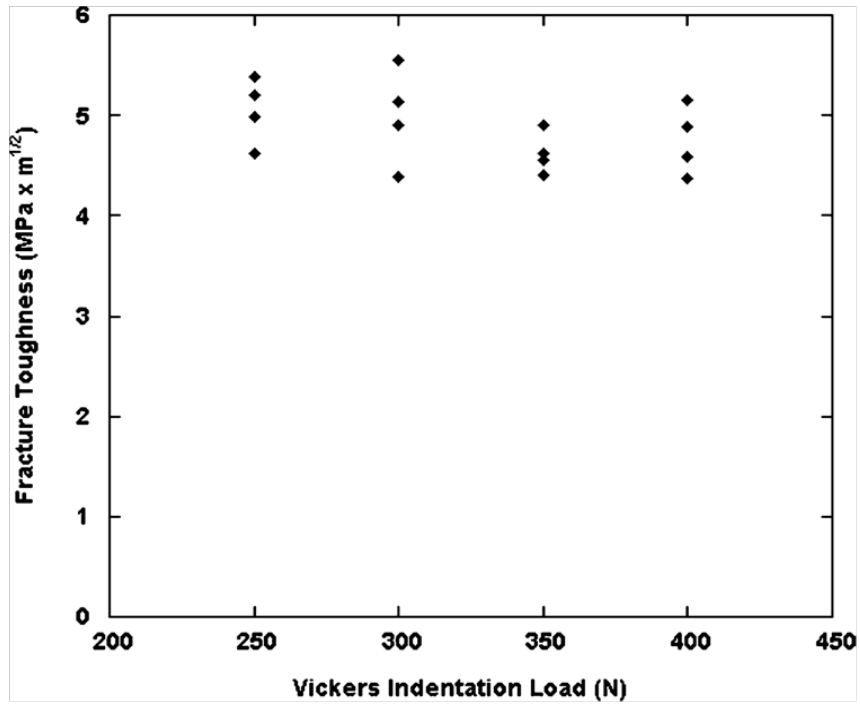


Figure 4-4. The fracture toughness of tested specimens versus the Vickers indentation load indicating a lack of interdependence.

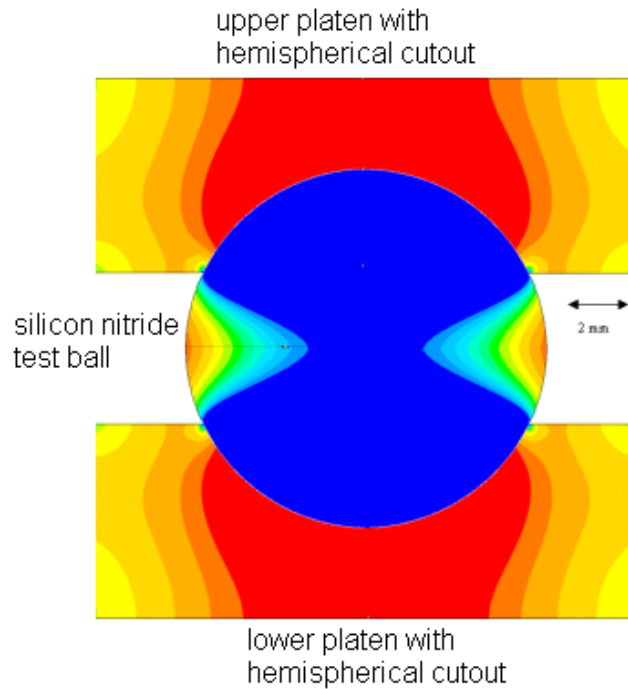


Figure 4-5. FEA of the ball in the platens undergoing compression, clearly indicating the tensile field along the equator of the ball.



Figure 4-6. Pendulum device for impacting balls and inducing cracks

# PW Single Ball Tester

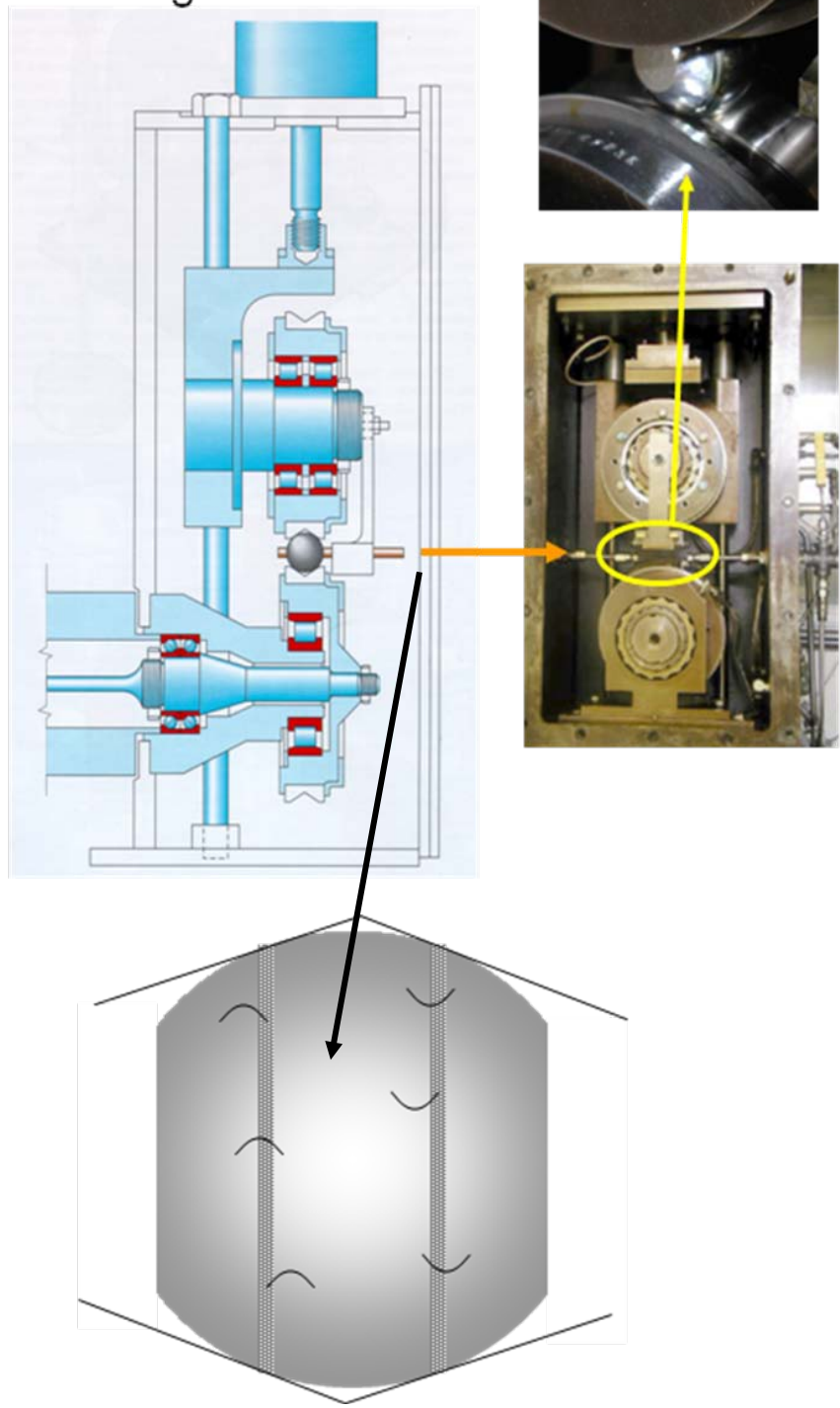


Figure 4-7. Images of V-ring single ball test rig. Lower image shows contact path and cracks oriented within them.

Table 4-1. V-ring test conditions for 28.575 mm (1 in.) balls. (Miner et al., 1996)

Test Property	Measurement
Hertzian Stress	3800 MPa (550 ksi)
Shaft Speed	7800 rpm
Stress Rate	$6 \times 10^6$ cycles/hour
Lubricant Flow Rate	3.4 kg/min (7.5 lb.min)
Lubricant Temperature	366°K (200°F)
Raceway Surface Finish	0.05-0.10 $\mu\text{m}$ (2-4 $\mu\text{in.}$ )

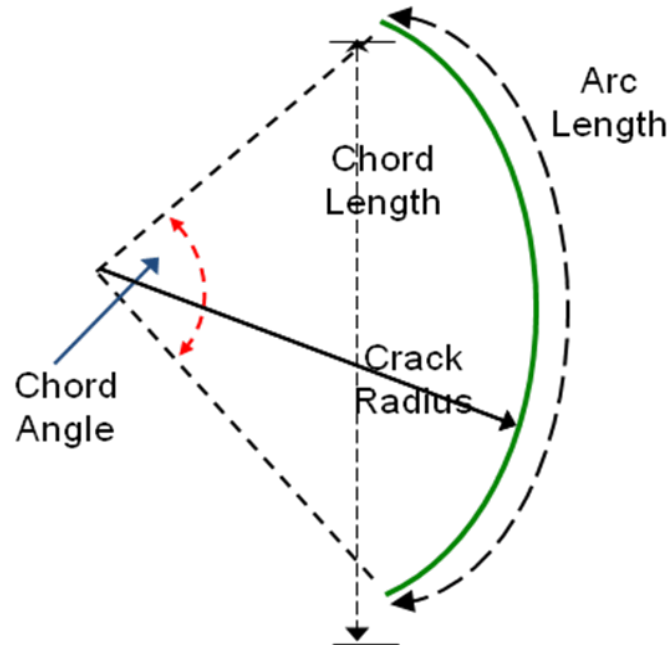


Figure 4-8. Diagram illustrating measurement parameters to classify a c-crack as observed on the surface of a cracked specimen.

Table 4-2. The sample number, turning angle, crack dimensions and fracture load of each specimen examined.

90- $\theta$ (deg)and Sample	$\gamma$ (deg)	2b (mm)	a (mm)	P (N)
0 S1	0	3.01	0.26	8940
0 S2	0	3.10	0.39	7659
10 S1	12	5.00	0.23	7200
10 S2	18	2.68	0.49	10640
10 S3	15	1.94	0.49	9341
20 S1	26	0.65	0.28	10100
20 S2	28	0.63	0.23	12342
20 S3	20	0.50	0.19	13950
30 S1	19	1.38	0.32	9870
30 S2	21	2.70	0.44	9010
30 S3	38	0.49	0.23	14540

Table 4-3. The mean  $K_c$  values in MPa $\sqrt{m}$  for each method  $\pm$  the standard variation ( $\sigma_{std}$ ).

Location	$K_{NCESR}$	$K_{MNS}$	$K_{MSE}$	$K_{GC}$	$K_{TAN}$	$K_L$
<b>Max</b>	6.19 $\pm$ 1.16	7.04 $\pm$ 1.59	6.72 $\pm$ 1.47	5.89 $\pm$ 1.13	7.55 $\pm$ 2.29	7.57 $\pm$ 1.28
<b>Surface (<math>K_{II}=0</math>)</b>	5.18 $\pm$ 1.49	2.25 $\pm$ 3.08	6.61 $\pm$ 1.57	4.96 $\pm$ 1.79	6.67 $\pm$ 2.09	7.04 $\pm$ 1.32
<b>Depth (<math>K_I=0</math>)</b>	3.25 $\pm$ 1.54	6.20 $\pm$ 1.35	6.67 $\pm$ 1.63	5.72 $\pm$ 1.13	7.14 $\pm$ 2.15	6.89 $\pm$ 1.49

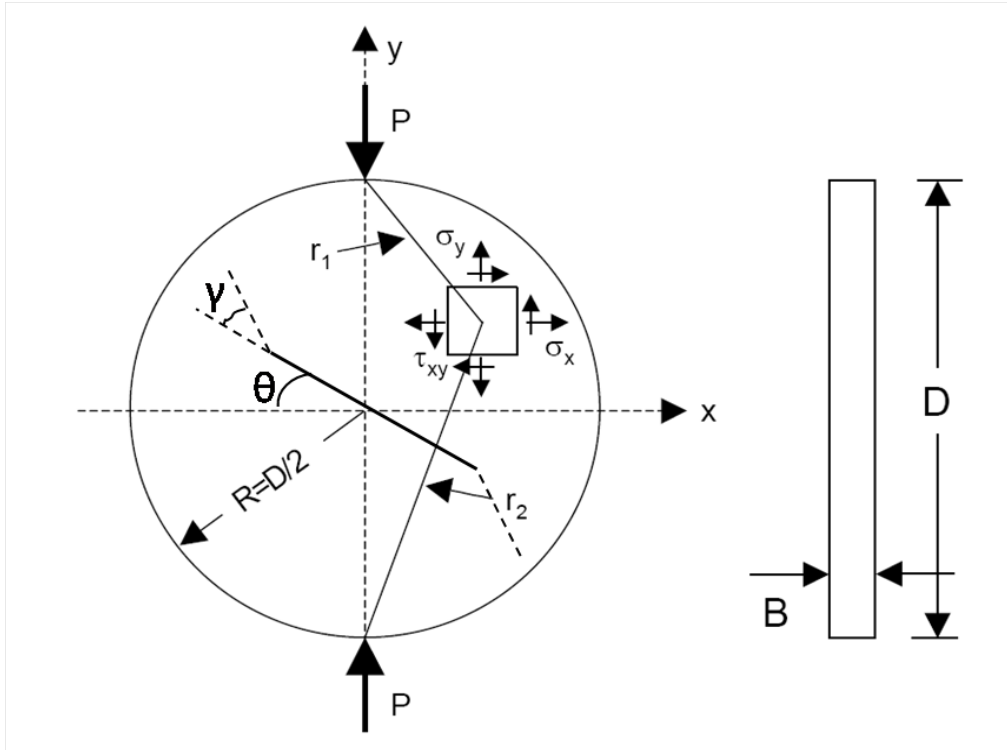


Figure 4-9. Schematic showing the flaw orientation on a Brazilian disk specimen as well as the coordinates and components used in the analytical stress equations.

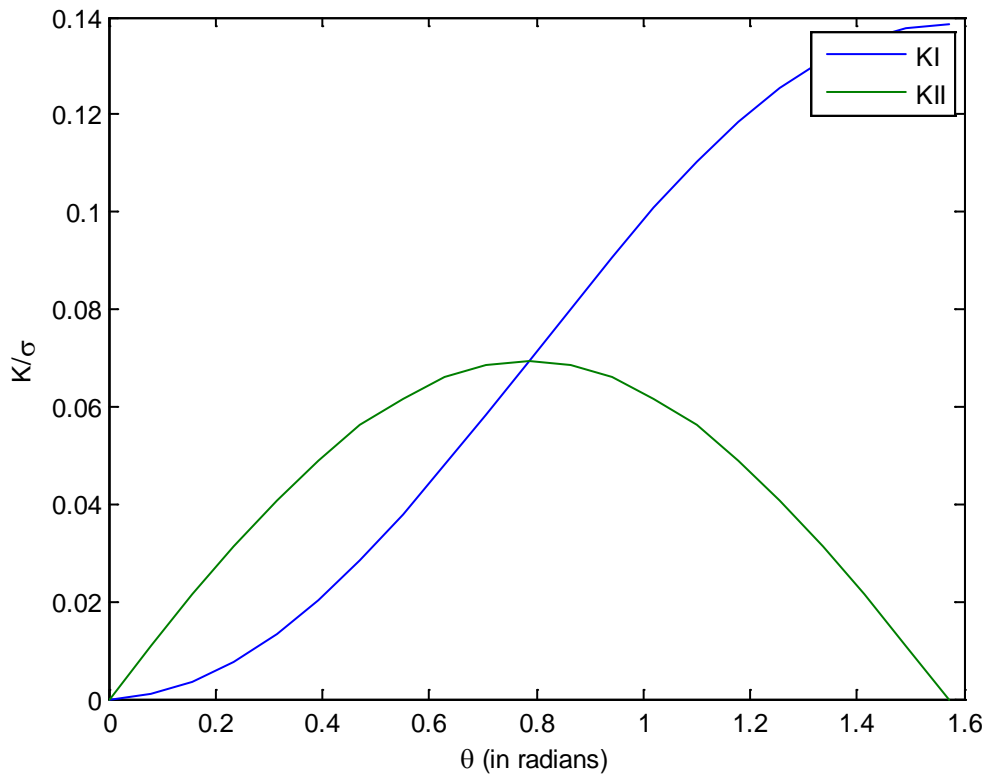


Figure 4-10. Nondimensionalized  $K_I$  and  $K_{II}$  (with respect to normal and shearing stresses respectively) from empirical equations for different angles of loading orientation for  $b=.02m$   $a=.0025m$ .

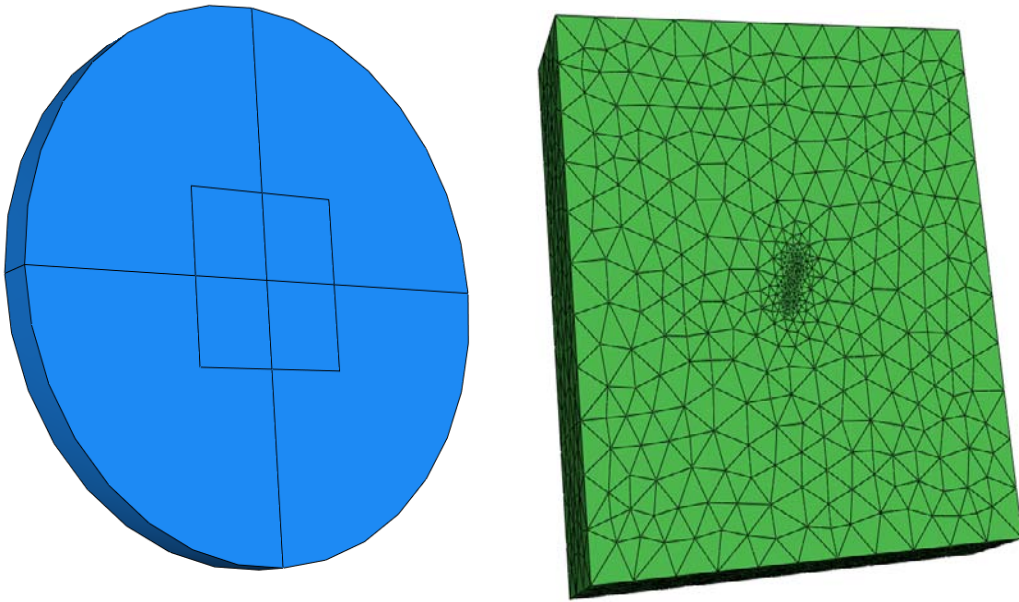


Figure 4-11. BD test model showing a) global uncracked model with square partition indicating submodel boundaries b) cracked meshed submodel for sample 2 for  $\theta = 20^\circ$  .

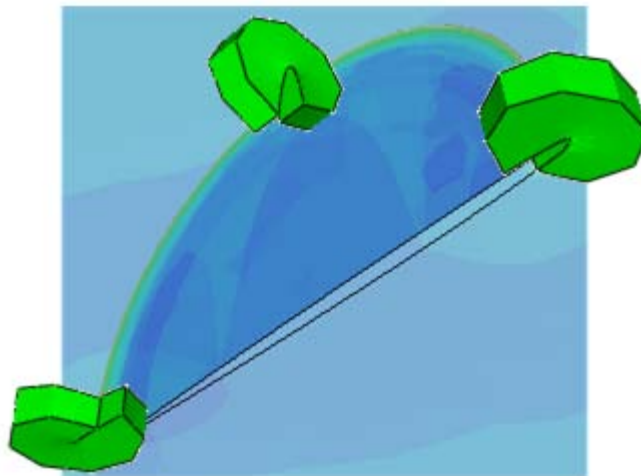


Figure 4-12. The displacement field of Sample 1 for  $\theta = 20^\circ$ , with a scale factor of 100 and translucency applied to view the crack superposed with elements of the circular contour regions to illustrate the presence of  $K_{II}$  at the face and  $K_{III}$  at the depth.

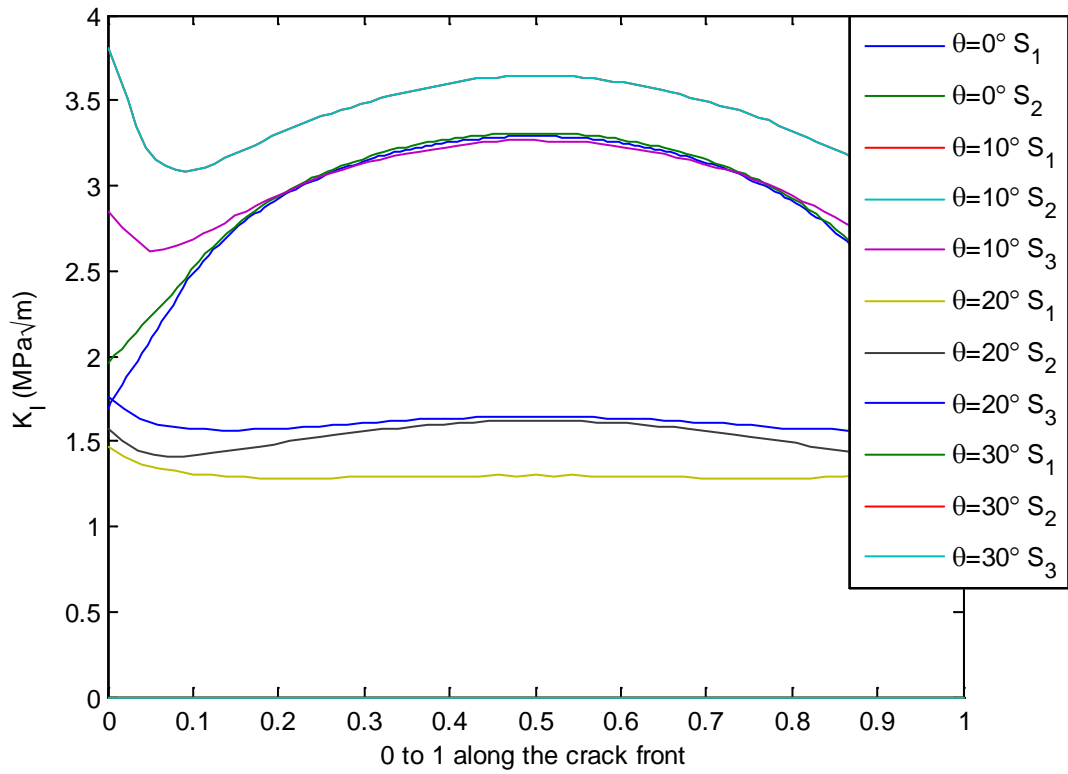


Figure 4-13.  $K_I$  for all analyzed specimens as a function of position along the crack front.

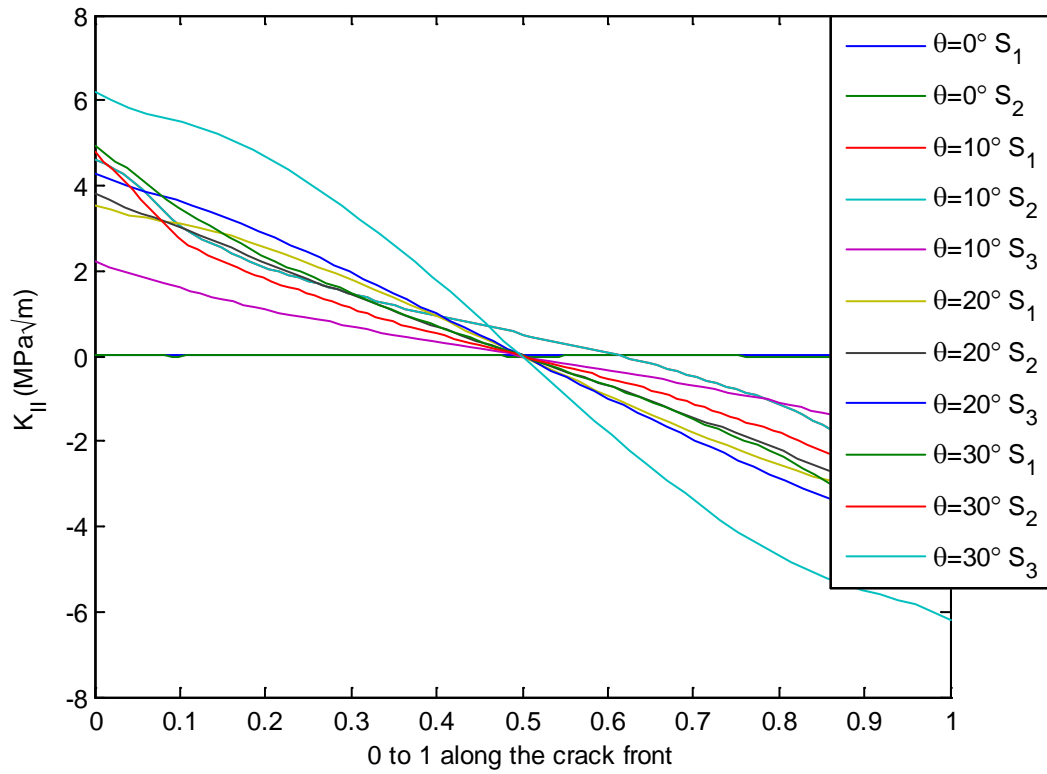


Figure 4-14.  $K_{II}$  for all analyzed specimens as a function of position along the crack front.

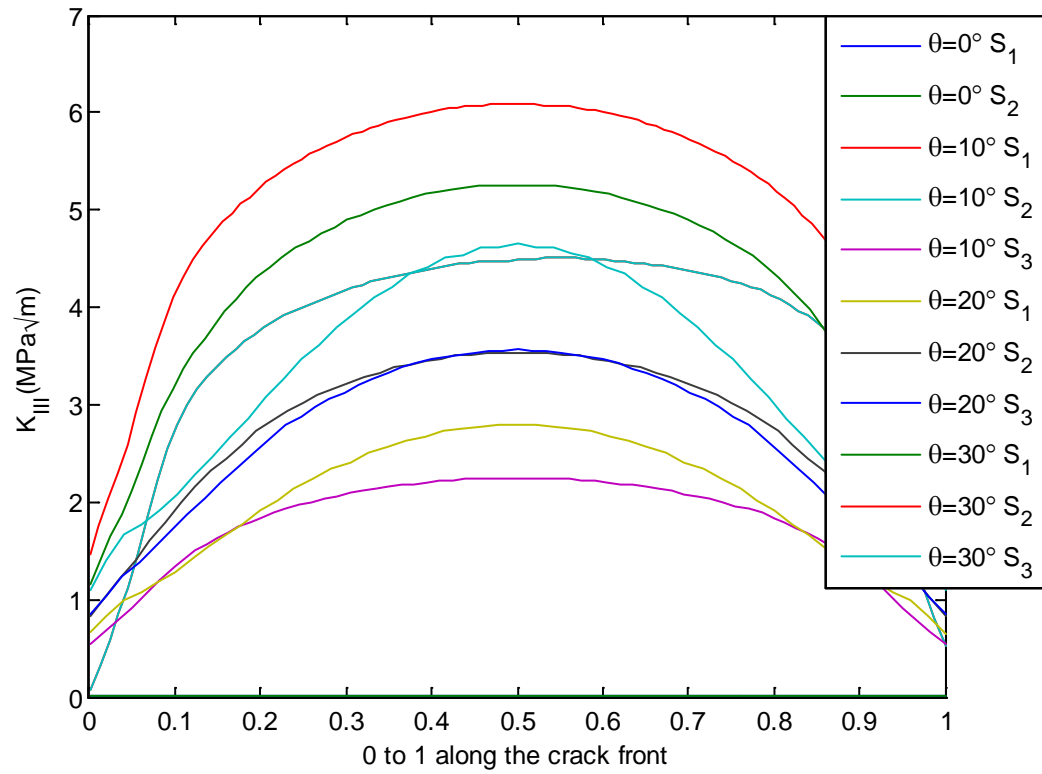


Figure 4-15.  $K_{III}$  for all analyzed specimens as a function of position along the crack front.

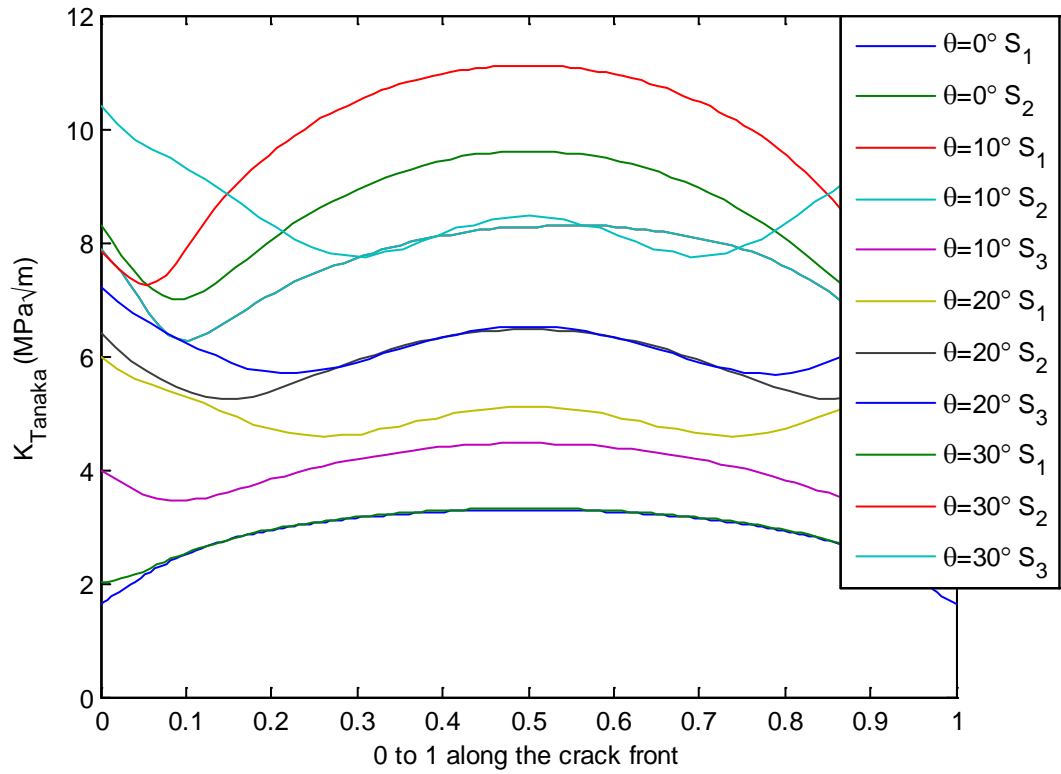


Figure 4-16.  $K_{eff}$  using Tanaka's relationship of three SIFs as a function of crack front position.

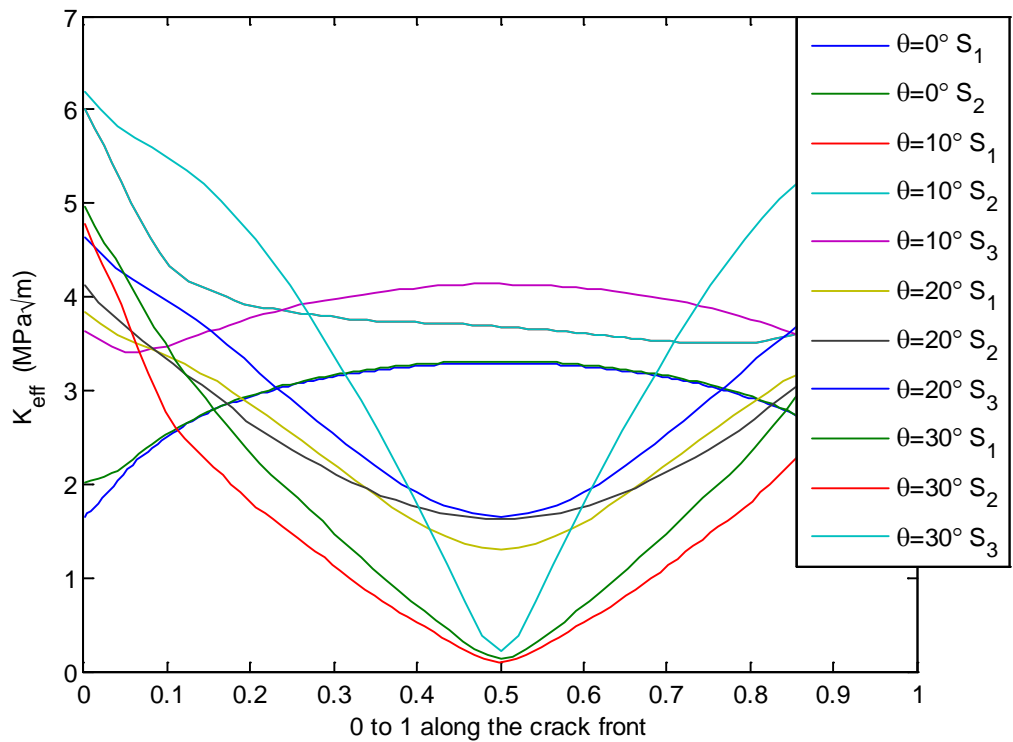
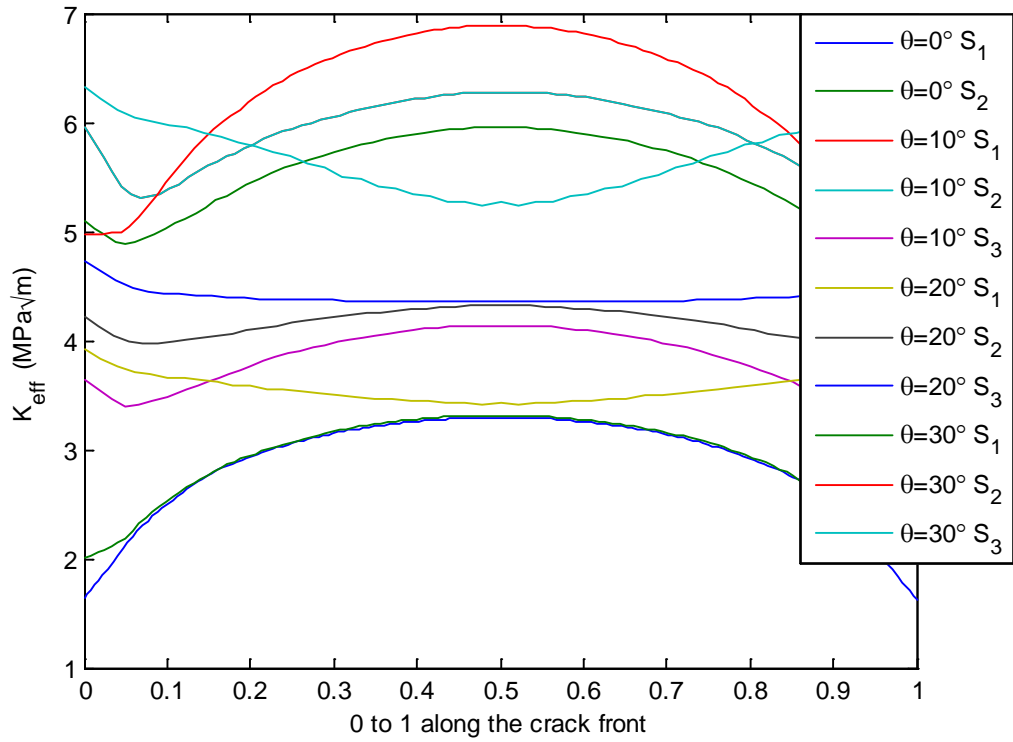


Figure 4-17.  $K_{eff}$  using the strain energy density release rate using all three SIFs as a function of crack front position where a) includes  $K_{III}$  and b) neglects it.

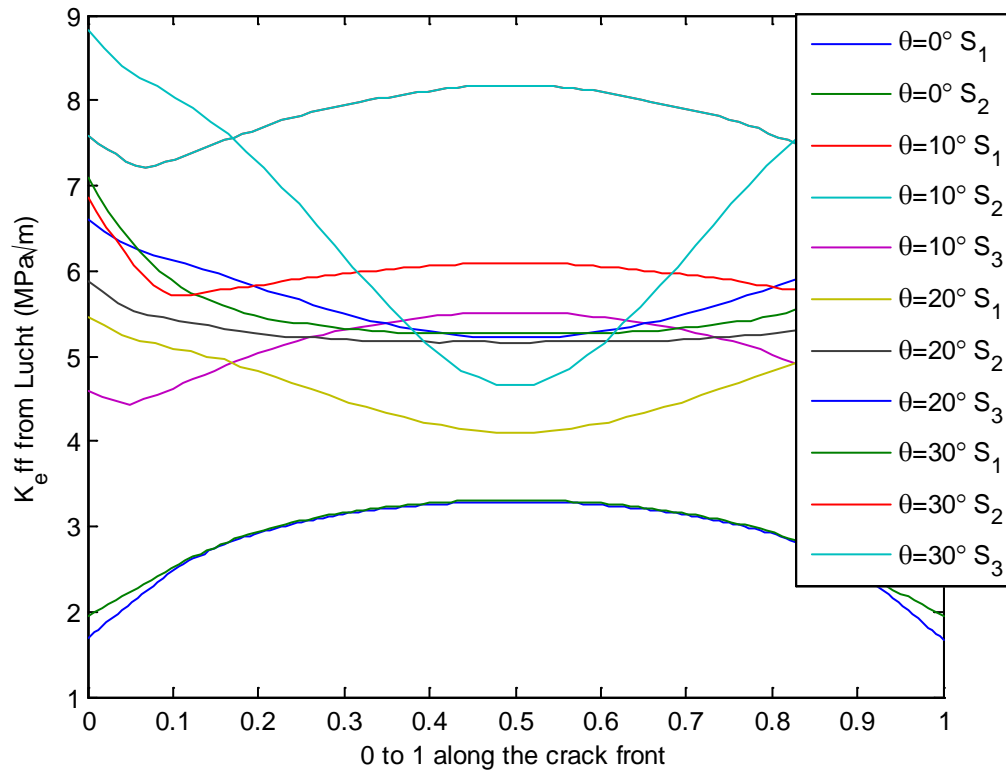


Figure 4-18. Plot of  $K_{Mi} = \sqrt{(K_I + B|K_{III}|)^2 + K_{II}^2}$  where  $B=1$ .

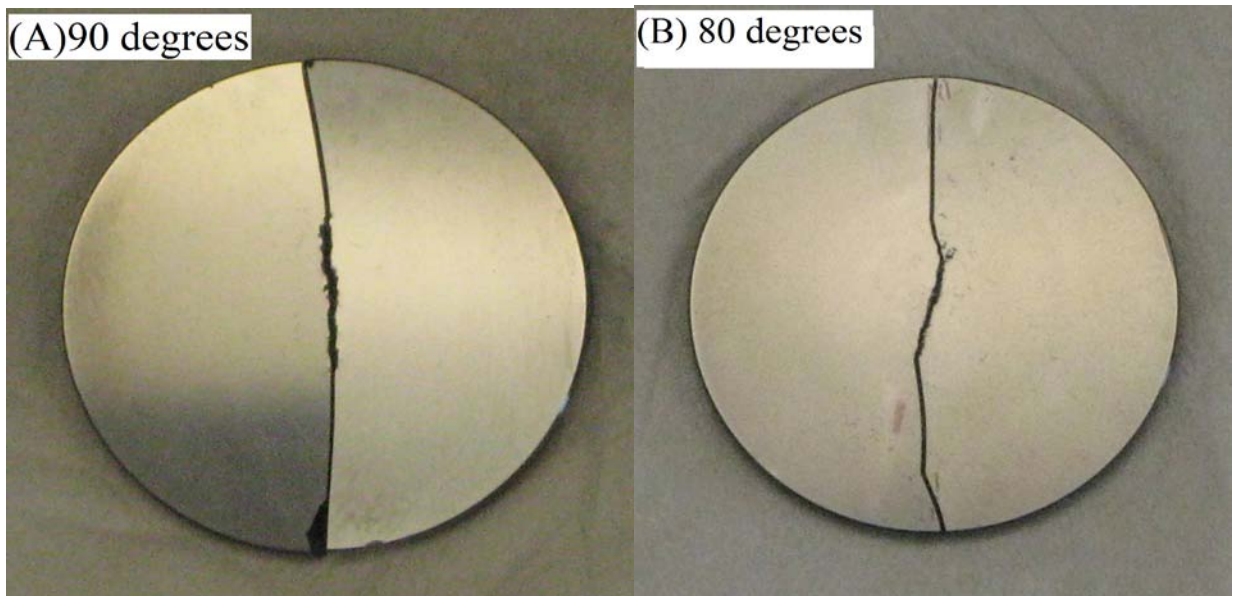


Figure 4-19. Fractured specimens at various values of  $\theta$ .

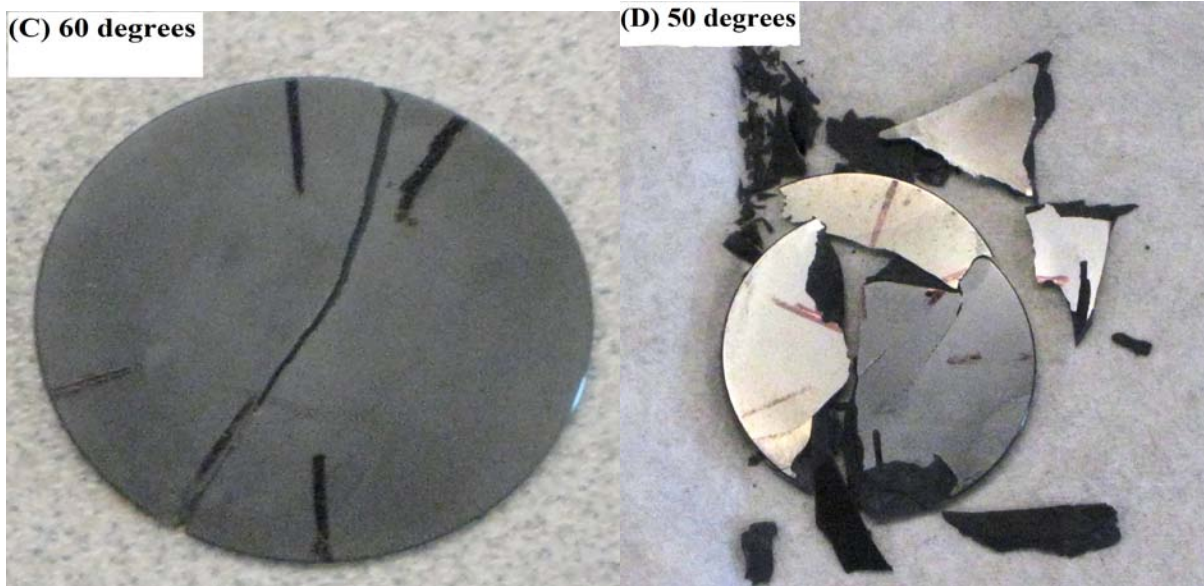


Figure 4-19. Continued

■

Figure 4-20. Fracture surface of BD specimen showing the crack front growing as it links up with newly formed cracks from indents along the surface.

CHAPTER 5  
CFS EVALUATION: COMPUTATIONAL INVESTIGATION

**5.1 Introduction**

Silicon nitride balls, used in hybrid ball bearings, are susceptible to failure from fatigue spalls emanating from pre-existing partial cone cracks that can grow under rolling contact fatigue (RCF). The range of 3D non-planar surface flaw geometries subject to RCF are simulated to calculate mixed mode stress intensity factors to determine the critical flaw size (CFS), or the largest allowable flaw that does not grow under service conditions. The cost of non-destructive evaluation (NDE) methods for silicon nitride balls scales exponentially with decreasing CFS and increasing ball diameter and can become a significant fraction of the overall manufacturing cost. Stress intensity factor variability is analyzed for variations of the location and orientation of the load relative to the crack, the geometry of load, and full-slip traction. The modeling techniques utilized in the creation of a 3D FEA model is discussed and the maximum tensile contact periphery stress is examined for effect on crack driving force under RCF. The CFS results are presented as a function of Hertzian contact stress, traction magnitude, and crack size.

The evaluation of a critical flaw size (CFS) is of immediate engineering relevance to the hybrid ball bearing industry towards defining refinement necessary for non-destructive evaluation methods for silicon nitride ball quality control. Also, a CFS can be applied for developing a fracture mechanics based life prediction methodology for hybrid bearings. The performance of hybrid silicon nitride ( $\text{Si}_3\text{N}_4$ ) ball/steel raceway bearings has been shown to be superior to their all-steel predecessors (Miner et al., Tanimoto et al.). However, silicon nitride balls are sensitive to surface defects and can fail from

fatigue spalls emanating from pre-existing c-cracks or partial cone cracks (see Fig. 5-1), due to crack growth driven by RCF (Hadfield et al. 1993a, Levesque and Arakere, 2008). Silicon nitride exhibits favorable material properties for application in hybrid high speed ball bearings such as high compressive strength, high hardness, a third of the density of steel, low coefficient of thermal expansion, and high corrosion and temperature resistance (Jahanmir, 1994). Unfortunately, they also have low fracture toughness ( $4-6 \text{ MPa}\sqrt{\text{m}}$ ) (Piotrowski and O'Brien, 2006).

Silicon nitride ball manufacturing involves a lapping process to achieve the sub-micron ball finishing dimension and surface characteristics that produces (unavoidable) low velocity ball collisions resulting in surface cracks nucleated by the radial tensile stress field which is maximal at the contact periphery (Levesque and Arakere, 2008, Wang and Hadfield, 2000). Partial cone or c-cracks are the result of the oblique impact of brittle spheres (Frank and Lawn, 1967) and these cracks are considered the most damaging surface defect that limits ball life in hybrid bearings under service conditions (Evans, 1993, Hadfield et al., 1993b). C-cracks are more commonly observed in sphere-to-sphere collisions and they not only have non-planar crack faces but also possess non-planar crack tips, as opposed to the axisymmetric cone cracks that result from the normal collisions of spheres. Figure 5-1 illustrates the 3D non-planar crack features of a c-crack. This increased complexity makes their shape more difficult to describe and, therefore, more complicated to analyze in any linear elastic fracture mechanics (LEFM) based analysis.

While the flaws (illustrated in Fig. 5-1) can be readily induced and are generally present, methods for their detection prior to service is still in development. Development

of a non-destructive evaluation (NDE) method is complicated because these cracks are often no more than 500  $\mu\text{m}$  (approximately the width of two human hairs) long on the surface and are difficult to find under a microscope. In addition, the material is nonconductive and only slightly translucent which complicates inspection procedures. From a fracture mechanics and structural integrity perspective, the largest allowable surface flaw that does not propagate under RCF loading is of design significance, and is termed the critical flaw size. The goal of this research is to present a systematic procedure to compute the CFS based on fracture mechanics principals, RCF loading, and ball material properties. This analysis is driven by the cost of NDE method for silicon nitride balls, which scales up very steeply with decreasing CFS and increasing ball diameter. Thus, the cost associated with NDE can become a significant fraction of the overall manufacturing cost of the silicon nitride ball.

Prior work has presented a qualitative and quantitative description of the range of possible partial cone crack shapes in three dimensions depending on the initial conditions of the interaction (coefficient of friction and contact patch size) during oblique spherical contact (Levesque and Arakere, 2008). With this range of possible nonplanar shapes characterized, they may be analyzed under RCF conditions that are seen in service, to determine which physical effects have the largest impact on crack tip displacement. Rolling elements are manufactured with silicon nitride because of the severe RCF conditions the material can withstand. These conditions are severe for any pre-existing surface flaws that exist. For example, in the case of a main shaft jet engine bearing inner ring rotating at 15,000 rpm, and as a worst-case scenario considering that the c-crack lies along the ball track (see Fig. 5-2), the crack can experience in excess of

90,000 fatigue cycles per minute (1,500 Hz), or 5.4 million cycles/hour. Furthermore, as the c-crack passes through the contact patch, the crack tip experiences a mixed-mode  $\Delta K$  loading at every point along the crack front. The effects of the location and orientation of the load relative to the crack, the geometry of load, the geometry of the crack and the respective effects on crack tip stress intensity factors (SIFs) and, therefore,  $\Delta K$  are presented. There is no published work concerning an elliptical Hertzian contact load inducing RCF for nonplanar c-cracks, which is what is most often seen in service applications. Herein, the discussed effects on the SIFs are analyzed in the ball bearing system and the process of extracting them.

## **5.2 Analytical Procedure**

### **5.2.1 Crack Geometries Induced By Oblique Interactions Of Silicon Nitride Balls**

The c-cracks produced during oblique interaction have multiple geometric features that need to be understood before modeling is undertaken. It can be shown that the crack size scales with the ball radius,  $R$ , and that the velocity needed to induce cone cracks is very low and can be shown to be proportional to  $R^3$  (see Appendix I). Also, it is noteworthy that the angular extend of the c-cracks have been observed to be roughly  $90^\circ$  to  $120^\circ$  (Levesque and Arakere, 2008, Wang, 2000). However, cracks that are the result of normal indentation of spheres have a weak correlation about the depth to which they extend into the material and exhibit considerable variation even for similar indentation conditions (Johnson, 1987). Avoiding generalities, the range of the geometry of cracks produced by ball-on-ball collisions was established in a paper, using a stress-state and numerical iterative growth and compared with experimental images (Levesque and Arakere, 2008). The angles to which the crack extends subsurface have already been bracketed within an established range in the same reference. The resultant shape

from these oblique interactions is complex and other prior works characterized the approximately modeled crack geometry with sets of parametric equations (Wang, 2000). However, the complexity of the shape leads to a difficulty in generalizing results and in finding which geometry of crack will be the most severely affected by RCF.

With this information in mind, the c-crack geometry can be modeled as a partial cone, or a partial frustum, whose dimensions are limited by inequalities which are equations of an offset cylinder. In other words, the shape is an axially revolved quarter ellipse with limitations to its extension in the  $r$ - and  $\theta$ -direction (considering cylindrical coordinates, see Fig. 5-3).

$$z = \frac{1}{a^*b^*} \sqrt{a^{*2} - (\sqrt{x^2 + y^2} - h)^2} + k \quad (5-1)$$

Where,

$$-\frac{1}{2}\theta_{range} \leq \tan^{-1}\left(\frac{y}{x}\right) \leq \frac{1}{2}\theta_{range} \quad (5-2)$$

$$h - a^* \leq \sqrt{x^2 + y^2} \leq \frac{1}{2} \sec\left(\tan^{-1}\left(\frac{y}{x}\right)\right) \left[ \frac{1}{h - a^*} - \sqrt{2} \sin\left(\frac{1}{2}\theta_{range}\right) + (h - a^*) \right] \quad (5-3)$$

where  $a^*$  and  $b^*$  are the axes of the ellipse on the  $x$ - and  $z$ - axis, respectively,  $h$  and  $k$  are the  $x$  and  $z$  coordinates of the center of the quarter ellipse, respectively and  $\theta$  is used to denote the fraction of a circle which the crack is seen to be on the surface of the specimen (see Fig. 5-3).

### 5.2.2 Finite Element Modeling Of A Three-Dimensional Surface Flaw

The shape of the crack is critical to understanding the difficulties of generating an adequate mesh for finite element analysis (FEA). In order to accurately model a crack for SIFs, quadratic elements are utilized to account for the large gradients of stress that occur throughout the model as a result of the Hertzian contact loading. To accurately model the crack tip stress, collapsed hexahedral elements are used at the tips with the midside nodes moved to the quarter-point (Andersson, 1996). Since hexahedral elements are utilized at the tip,  $C_1$  continuity of the shape functions is maintained, which is desirable especially if SIFs are intended to be extracted in the region just surrounding the crack tip. It is noteworthy to mention that others have developed methods to extract SIFs from tetrahedral based meshes, which simplifies meshing and remeshing in the instance of crack growth but there is still much variability in the method (Rajaram et al., 2000). However, it would be difficult to create a mesh that would be made of all hexahedral elements and avoid distorted warning elements considering that the geometry is curvilinear and closed. Through benchmark analyses types of meshes and their SIFs were tested against previously established solutions (like that of Newman and Raju, 1981). As a result, a tube of elements can be created which were hexahedral, about the crack tip region, but were tied to a bordering tetrahedral region that meshed the majority of the cracked body and maintain SIF accuracy.

SIF extraction from this mesh is feasible through a few methods (including stress matching, and virtual crack extension) but the most appropriate approach for the analyses is via crack tip opening displacement (CTOD) correlation since it accounts for the effects of all physical phenomena without a need to change its formulation (as in

contour integral, energy-based methods). The equations for displacement correlation can be written as:

$$K_I = \frac{E}{4(1-\nu^2)} \sqrt{\frac{2\pi}{r}} (u_1 - u_2) \quad (5-4a)$$

$$K_{II} = \frac{E}{4(1-\nu^2)} \sqrt{\frac{2\pi}{r}} (v_1 - v_2) \quad (5-4b)$$

$$K_{III} = \frac{E}{4(1-\nu^2)} \sqrt{\frac{2\pi}{r}} (w_1 - w_2) \quad (5-4c)$$

where  $E$  and  $\nu$  are the Young's modulus and Poisson's ratio,  $u$ ,  $v$  and  $w$  are the three displacements in the directions normal to the crack face, in the direction of the continuing crack plane normal to the tip, and tangent to the crack tip respectively, and  $r$  is the distance from the crack tip, where these displacements are measured. Figure 4a illustrates the CTOD coordinate system. Figure 4b shows the 3D displacement vectors at the tip of the nonplanar c-crack mesh.

The FEA model represents a computationally intense effort due to the dense mesh (for capturing the Hertz stress gradients) and implementation of quadratic elements (for moving the midside node of the tip elements to the quarter point, preserving the  $1/\sqrt{r}$  singularity at the crack tip), and accounting for contact accuracy. Mesh refinement for Hertz contact problems has been visited in other works (Gu, et al., 2005) usually for stress calculations. Here the displacements are of primary importance, especially those in the crack-tip vicinity. A mesh refinement study has been performed in the tensile region on the contact periphery and established guidelines for accurate determination of SIFs. The mesh density utilized is about 50 elements along the crack to the tip where the hexahedral region has 4-7 rings of elements in the contour region,

meaning that for this application each element near the tip is ~10 μm wide (which is the length of the longest grains in TSN-03 NH silicon nitride). Contact of the crack faces is defined by using a surface-based contact definition with no friction where a direct, iterative solver is used to achieve accurate displacement and stress field solutions.

The direct iterative solver must be used as the accuracy in displacement results required for adequate SIF calculations is high. The direct iterative solver is the most accurate solver available in ABAQUS (Dessault Systèmes, 2007). The mesh refinement previously established is based upon (a) refinement that the Hertz contact requires for adequate resolution and (b) refinement in the vicinity of the crack tip necessary for accurate displacements needed for SIF computation.

Loading is done via FORTRAN user subroutines DLOAD and UTRACLOAD for the normal and traction loads. The equations to describe the pressure distributions can be written as:

$$p(x, y) = p_o \sqrt{\frac{(x - x_d)^2}{a^2} - \frac{(y - y_d)^2}{b^2}} \quad (5-5)$$

and

$$f(x, y) = \mu p(x, y) \quad (5-6)$$

where  $x_d$  and  $y_d$  are the distances from the global coordinate system to the load center,  $a$  and  $b$  are the dimensions of the ellipse along these dimensions, and  $\mu$  is the friction coefficient for the moving load in a full-slip interaction (see Fig. 5-5).

### 5.3 Mixed-Mode Stress Intensity Factors Due to Rolling Contact Fatigue

For generalization, the trends observed in the SIFs for each of the possible physical parameters should be investigated and quantified. For example, if the max

Hertzian pressure is increased, the SIFs are mostly observed to directly scale with the value of  $P_o$ . The maximum continuous operating Hertzian contact pressure,  $P_o$ , typically encountered in turbine engine mainshaft hybrid ball bearings is in the range of 1.7-2.8 GPa (250-412 Kpsi), for achieving reasonable  $L_{10}$  fatigue life for the bearing raceway material. SIF results are presented at the upper end of that range, at 2.8 GPa, to obtain conservative estimates on CFS for ball material. For the orientation in Fig. 5-6 without traction, the linear effect of max pressure on SIFs is demonstrated in Fig. 5-7. This information may be applied by others in the field who require SIF calculations for similar phenomena but different magnitudes of pressure in their contact ellipse.

In the two dimensional case, the width of the contact, the angle of the crack, and the depth of the crack are enough parameters to define an RCF model (Bogdanski and Trajer, 2005). However, for 3D analysis, the model must be characterized by the load aspect ratio and specific crack dimension, making generalization of results difficult.

An analysis of SIFs as a function of approaching load is illustrated in Fig. 5-8. There are multiple static steps to analyze these c-cracks under a RCF cycle (or single passage of the load rolling over the crack). As the load approaches the  $K_I$  SIF increases until the load is very close to the crack tip, resulting in crack closure. At this point,  $K_I$  rapidly decreases to zero as the contact patch moves directly over the crack. As the contact patch advances further the crack tip opens due to the influence of the maximum tensile stress on the trailing edge of the load. While  $K_I$  reaches a second maximum in the trailing periphery edge, it is not as high as that of the approaching edge because the crack angle (illustrated in Fig. 5-6) is such that the depression from the load has a tendency to cause the crack to close as shown in Fig. 5-8. As the load moves away

from the crack all the SIFs eventually decay to zero. In figure 5-8, the relative orientation of crack tip and load allows for influence of the load at  $3a$  but  $K_I$  and  $K_{III}$  decay quickly thereafter. For design application, an effective stress intensity parameter is used that embodies all modes of crack deformation as:

$$K_{eq} = \sqrt{EG} = \left\{ E \left[ \frac{1}{E} (K_I^2 + K_{II}^2) + \frac{2(1-\nu)}{E} K_{III}^2 \right] \right\}^{0.5} \quad (5-7)$$

This representation of the three modes of crack-tip displacement was chosen due to its physical basis in fracture mechanics (since it utilizes the strain energy release rate,  $G$ ) (Anderson, 2005).

The most severe orientation of a purely normal load (i.e. no traction load) is such that the periphery stress is near the crack on the side where the crack is oriented (see Fig. 5-6). However, the distance to the center of the approaching load ( $x_d$ ) where max SIFs are calculated is affected by the crack angle.

### 5.3.1 Effect Of The Variation Of Load Ellipticity On Stress Intensity Factors

The ellipticity of the contact patch also influences the induced SIFs. For a generalized Hertzian elliptical contact seen in a ball-bearing the ellipticity ratio ( $b/a$ ) can vary depending on the raceway curvatures, speed, radial and thrust loads. A nearly circular contact patch is often seen in RCF test setups like the ball on rod test, the four- and five-ball tests, v-ring test and more. Also, if  $b/a$  is very small, the contact can be reminiscent of a line contact. Since the crack is moving with the rotating ball, the relative orientation of crack and load can vary greatly. The effect of ellipticity of load on the SIFs from the semi-minor axes is studied in Figures 5-9. Again, SIF results are presented for a peak Hertz stress  $P_o = 2.8$  GPa (412 kpsi). The circular case yields comparatively

higher SIFs. This is due to the nature of the stresses that circular loads can produce at their periphery (Johnson, 1987).

### **5.3.2 Comparison Of C-Cracks And Semi-Elliptical Cracks**

The range of possible crack shapes and sizes has been established by Levesque and Arakere (2008). The complex nonplanar 3D geometry of the c-crack requires parameters such as crack depth and angle, which are difficult to measure, and a function that represents the position of the surface and inequalities to indicate the end of the crack (see Eqs. 5-1-5-3). Also, some NDE inspection procedures can only detect the width of the crack on the surface. Much of this issue could be resolved by comparing c-cracks to a semi-elliptical flaw that is fully classified by three parameters (depth, width, and angle of inclination). The semi-elliptical crack also yields higher SIFs, for the same peak Hertz stress,  $P_o$ , leading to a conservative analysis and then the feasibility of simulation becomes much more accessible to other workers in the field. With this in mind, comparison of SIFs for the same orientation of elliptical contact load of both a c-crack and a semi-elliptical surface crack of similar width, depth and angle toward the surface, was completed. See the results in Fig. 5-10.

When the SIFs are compared, it can be noticed that considerable divergence in their values even though they occur in the same relative orientation to the load. However, the maxima and minima of each, though at different locations, are quite similar. As a result of the complex geometry and loading, all three modes of crack tip deformation are present. Modeling and experimental efforts need to collaborate to determine the best mixed-mode parameter for crack growth of brittle materials under these types of conditions for future design purposes.

### 5.3.3 The Effect Of Traction

Under elasto-hydrodynamic (EHD) lubrication conditions in a ball bearing, the effective friction coefficient at the contact is typically in the 0.05-0.09 range. Although the coefficient of friction appears to be low, it will be shown that it has a significant effect on the maximum SIFs reached. The direction of traction also becomes important. When traction is incorporated, it is seen that the worst case load moves immediately next to the crack and that the SIFs increase substantially (see Fig. 5-6). If the traction direction is reversed, the worst-case load jumps to the opposite side of the crack where the tensile stress field has the most effect. (It should be noted that this position will not have as high SIFs as that on the opposing side since the normal load only contributes to crack closure on that side of the crack.)

During RCF, the elliptical contact patch induces both normal and traction forces onto the ball surface. Since the bearings of interest are lubricated, the interfacial contact is in full-slip (a hydrodynamically lubricated contact) and the amount of traction on the surface is limited by the shearing properties of the lubricant that is in application. For the most part, it is found that  $\mu=0.05-0.09$  is an acceptable range for high speed bearing applications. The traction force is parametrically varied and the max stress intensity factor values along the front are plotted in Fig. 5-11 below.

It is quite apparent that the slope of the increasing SIFs is quite steep as the traction force is increased. For silicon nitride, the fracture toughness ( $K_{Ic}= 6.0 \text{ MPa}\sqrt{\text{m}}$ ) is reached when  $\mu=0.2$  (even though steel on silicon nitride has a friction coefficient of about  $\mu=0.15$ ) and indicates that the friction coefficient a required variable to evaluate a critical flaw size for ball bearing inspection. The reason for the strong influence of the friction coefficient is that the surface flaw is easily effected by surface behavior. In

addition, there are high normal loads that are directly contributing to a traction load according to  $f=\mu P(x,y)$  (where, for example, if there is a total load in the contact of  $P=2500$  lbf than, for  $\mu=0.07$ , the total traction load,  $f$ , is 175 lbf is contributing to crack opening).

### 5.3.4 Critical Flaw Size Evaluation Results

If the operating conditions of a bearing are known, and the material properties (especially the  $K_{th}$  for initiating crack growth) are established then a CFS (or flaw size so small that it experiences crack tip loading below the  $K_{th}$  threshold value under the operating conditions) can be found. These models can be generalized for exactly this application. For example, it has been established that the SIFs scale linearly with the max pressure,  $P_o$ , of the elliptical contact patch. It has also been established that a circular load will produce higher SIFs than the commonly found elliptical dimensions. In addition, it has been noticed that similar magnitudes of maximum SIFs across the crack front of c-crack and semi-elliptical flaws occur under identical loading conditions. It has also been established that traction has a significant effect on the SIFs for the RCF of surface flaws. With all these facts in mind, models can be ran that simulate a decreasing crack size near a circular load and plot the change in the SIFs as a function of the changing crack size. By nondimensionalizing the SIFs with respect to the max contact pressure ( $K_I^* = K_I / P_o \sqrt{a_c}$ ), the results can be generalized. The crack dimensions chosen were based on what is commonly observed in experiments. In this case, cracks have been modeled that have an aspect ratio of 0.3 and are angled 30° from the surface. Figure 12 displays the results. To utilize this graph, all that is needed is the effective threshold value  $K_{th}$  of the material, under mixed-mode loading, and the

CFS can then be looked up for design purposes after dimensionalizing the data for specific applications. For example, for  $P_o=2.8$  GPa,  $\mu=0.07$ , and  $a_c=0.5$ mm, if  $K_{th}=2.3$  MPa $\sqrt{m}$ , then the CFS is 500  $\mu$ m. The material property  $K_{th}$  can also be determined via RCF testing of c-cracked balls for specific contact loading conditions. For example, if a ball with a crack of  $a'=0.35$  mm, and has loading conditions of  $P_o=2.8$  GPa,  $\mu=0.07$ ,  $a_c=.5$ mm, than  $K_{th}=2.4$  MPa $\sqrt{m}$ .

## 5.4 Conclusions

The evaluation of a CFS has important engineering relevance towards defining limits for NDE methods for silicon nitride ball quality control, for reducing the cost of ball inspection, and for developing a fracture mechanics based life prediction methodology for hybrid bearings. To this end, it has been analyzed that complex surface cracks present in silicon nitride balls used in hybrid bearings subject to RCF, using 3D FEA and fracture mechanics principals. While the relative position of load affects the SIFs at any given instant, the max SIFs, used in a  $\Delta K$  calculation, are observed in trends and were utilized in the determination of the smallest allowable CFS. These observations include:

- Surface cracking can be induced in silicon nitride ball collisions with low velocities of  $\sim 16$  cm/sec
- Surface crack dimensions that result from collisions can be shown to scale linearly with ball radius,  $R$ , and the velocity to induce cracking with the cube of the ball radius,  $R^3$ .
- C-cracks are a complex shape that can be modeled through iterative growth, or solid modeling, where the shape has been characterized by equations.
- Maximum Hertzian stress,  $P_o$ , scales the SIFs for c-cracks in balls subject to RCF in a nearly linear fashion.
- Surface traction between the ball and the raceway and its direction has a significant detrimental effect on SIFs and crack driving force.

- The max SIFs are seen while the crack is on the edge of a circular load when compared to approaching elliptical loads.
- The semi-elliptical crack is simpler to model and does exhibit similar magnitudes of SIFs which are necessary for  $K_{th}$  calculations to determine a CFS.
- CFS can be determined from plot of SIFs versus crack dimension (Fig. 12) by looking up the appropriate mixed-mode effective threshold SIF value,  $K_{th}$ , which can be determined via RCF testing of c-cracked silicon nitride balls for specific contact loading conditions.

## 5.5 Figures

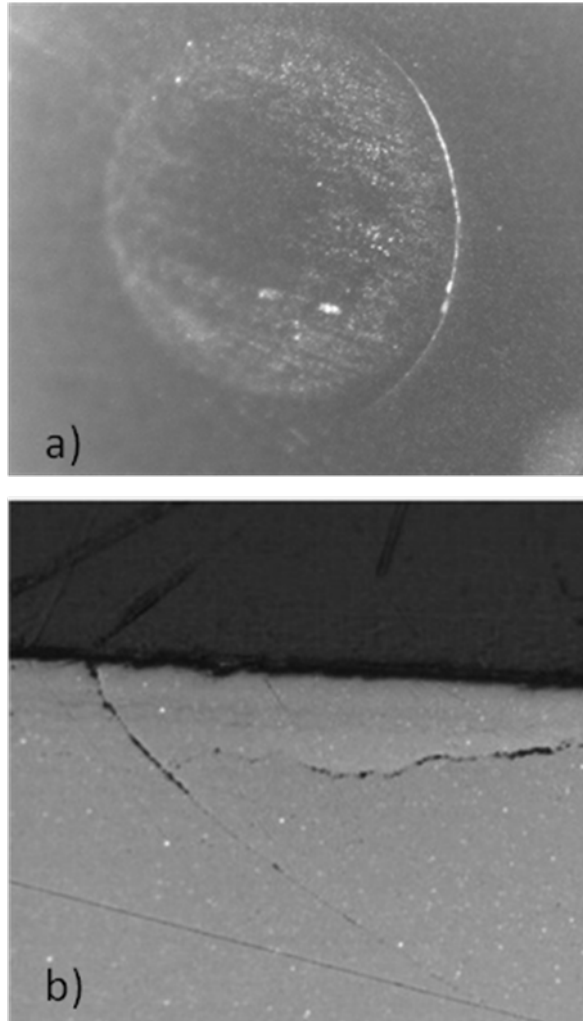


Figure 5-1. Images of artificially induced c-cracks a) ball surface view, and b) a subsurface cross-section extending into the material. [Courtesy of The Timken Company].

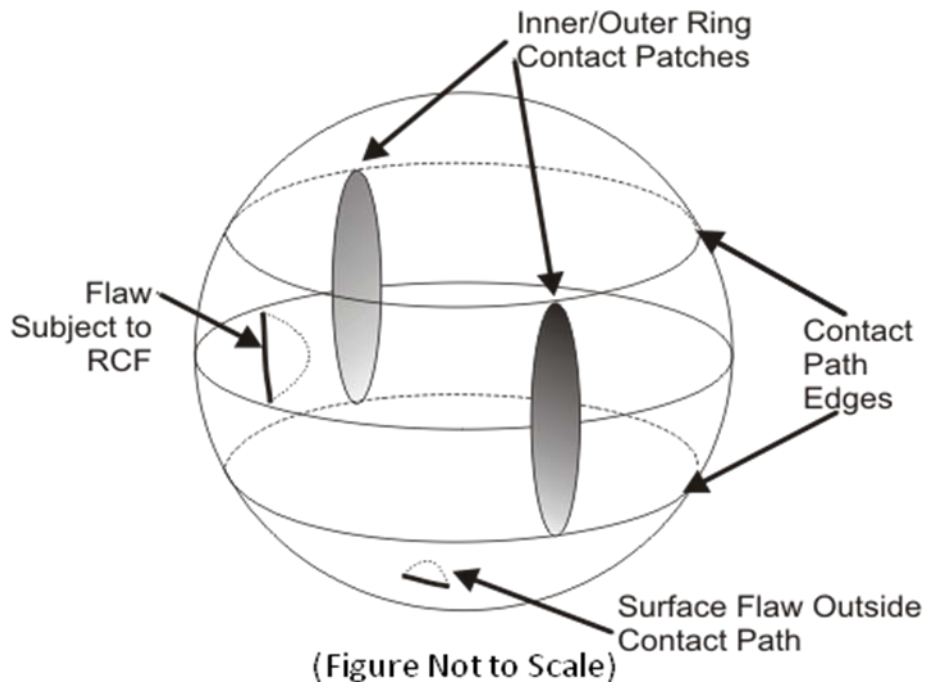


Figure 5-2. The elliptic contact patches on the ball surface and the band which they remain in. Cracks inside and very close to this region (assuming a fixed contact angle and attitude of ball rotation) will experience RCF.

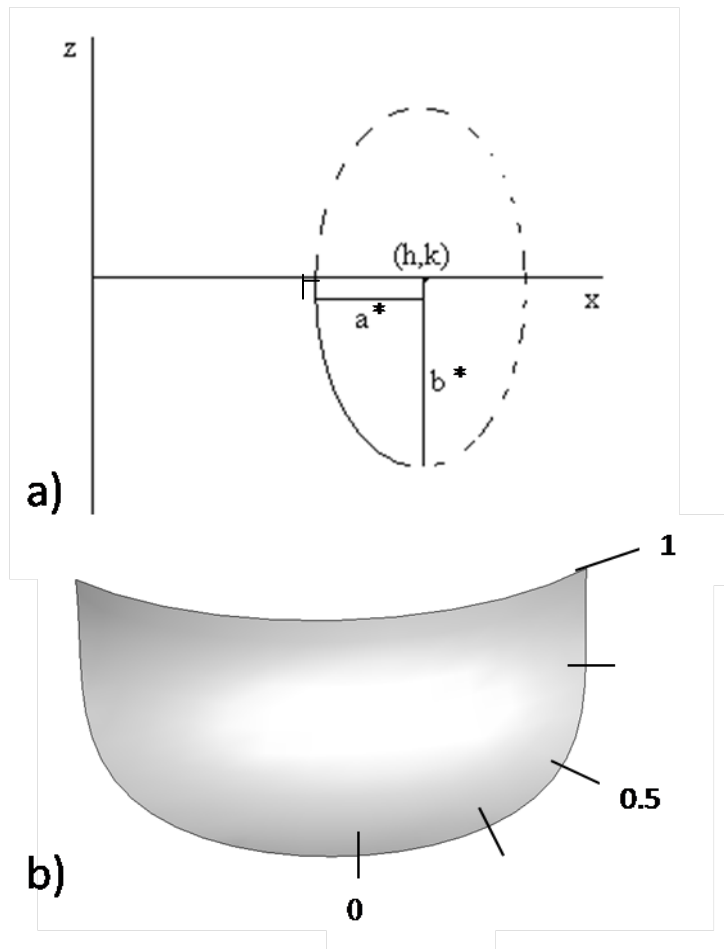


Figure 5-3. A) The coordinate system used in the equations to plot the C-crack and B) the rendered 3D crack with notation for the SIF plots to be discussed.

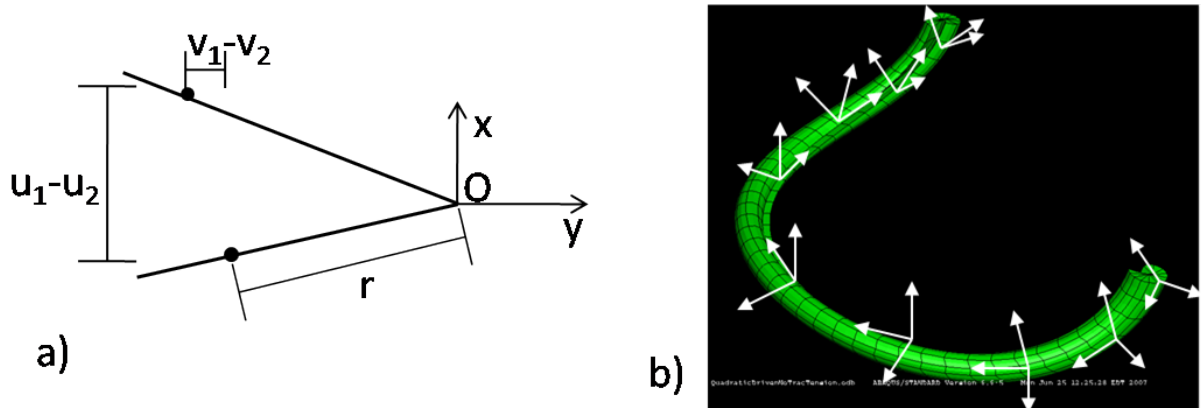


Figure 5-4. Illustration of A) displacement correlation variables around an opening two dimensional crack and B) the coordinate systems are different for each point near the crack tip at a few element borders.

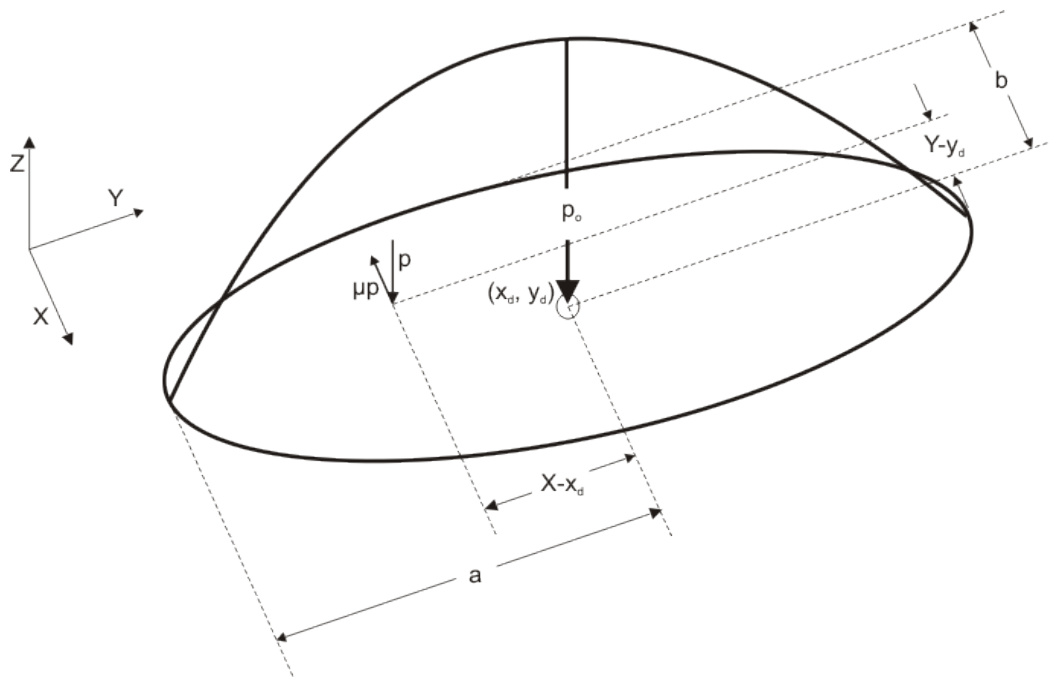


Figure 5-5. Elliptical Hertzian contact load coordinate system and variables for elliptical load simulation.

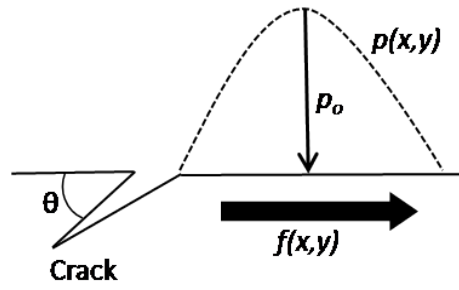


Figure 5-6. The cross-section of the general worst case orientation with traction for crack tip deformation. Here the traction direction acting on the silicon nitride surface is indicated and considerations of relative movement must be based on which surface is driving each contact which is different for inner and outer raceway interactions.

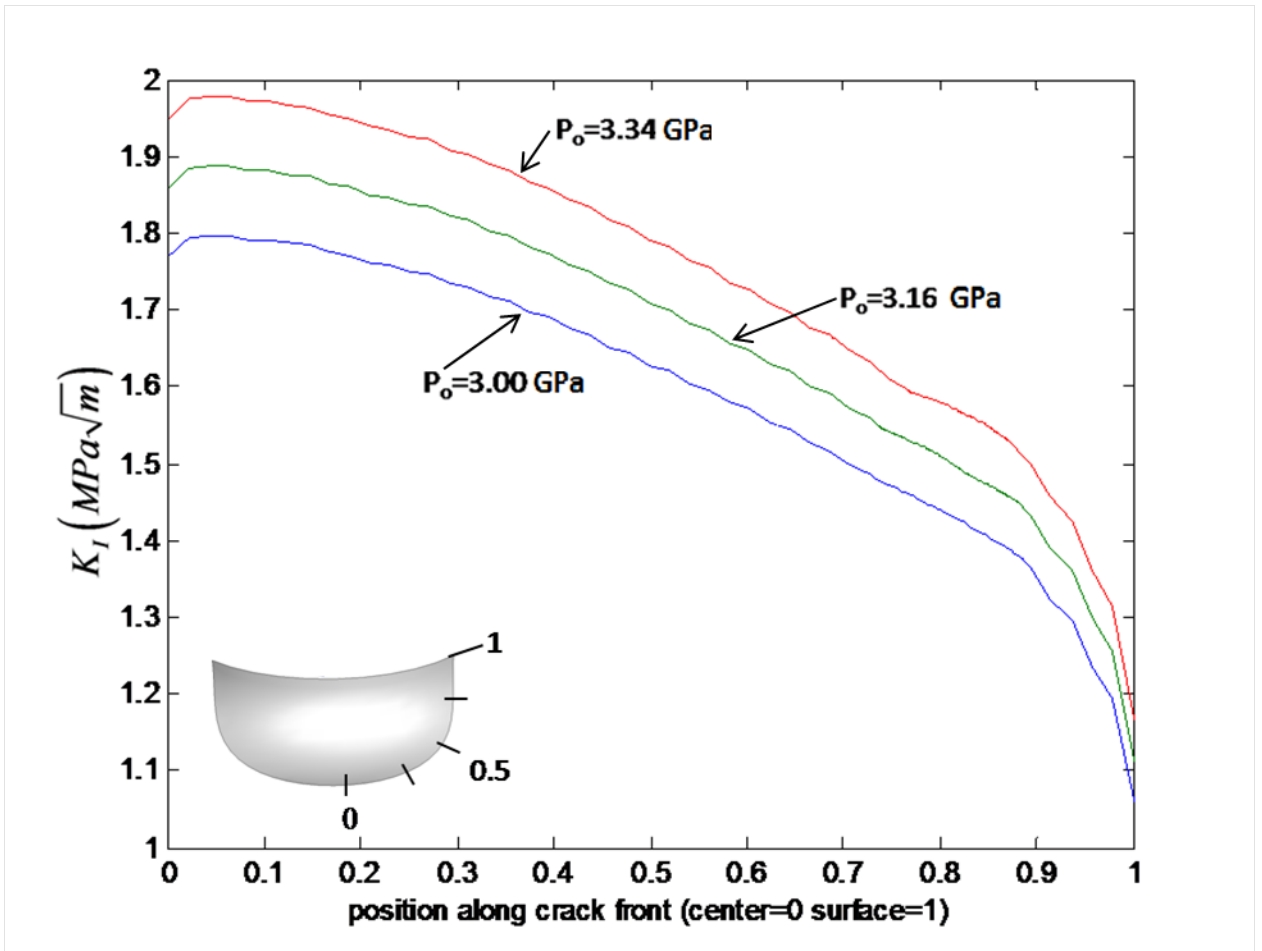


Figure 5-7.  $K_I$  stress intensity factor for a circular load ( $a_c=250 \mu\text{m}$ ) near a c-crack (width= $250 \mu\text{m}$ , vertical depth= $75 \mu\text{m}$ , and an angle of  $28^\circ$  to the surface) with a variation in the max pressure magnitude. The effect of a scalar increase in pressure is a near scalar increase in  $K_I$ .

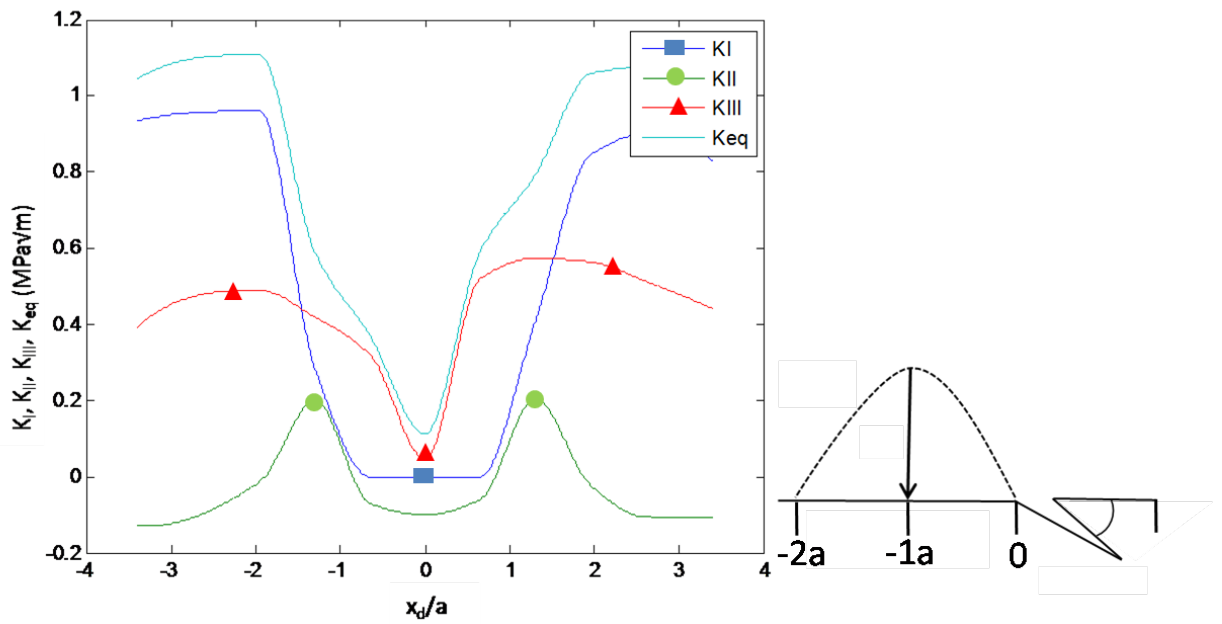


Figure 5-8. A plot of the three SIFs as a function of moving load of  $P_o=2.8$  GPa. When  $\text{abs}(x_d/a)=1$ , the load is just on the edge of the crack and the coordinate system is oriented where the crack breaks the surface. The maximum SIFs along the crack front are plotted and they occur around  $x_d/a=-1.7$  for this geometry crack and load.

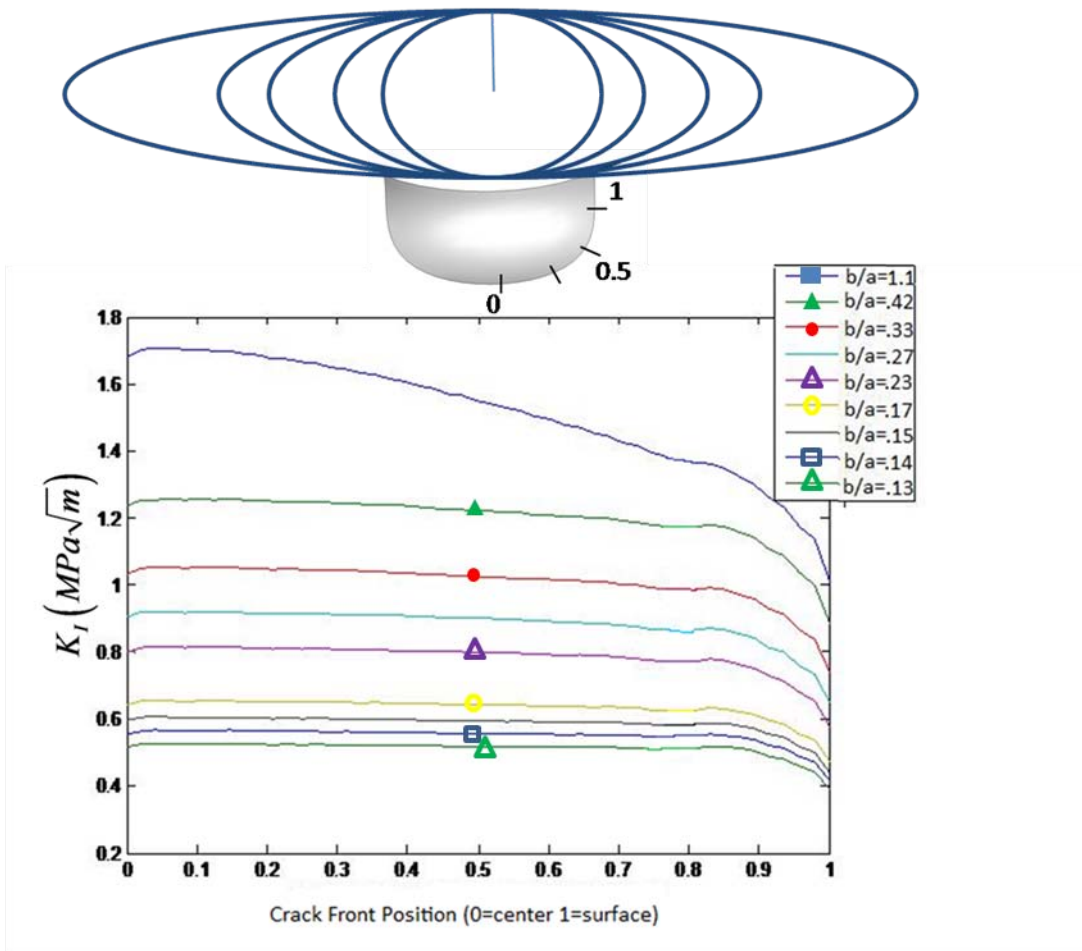


Figure 5-9. The effect of the ellipticity of the load, on the SIFs on the semi-minor axis of the ellipse, for  $P_0=2.8$  GPa (412 Kpsi).

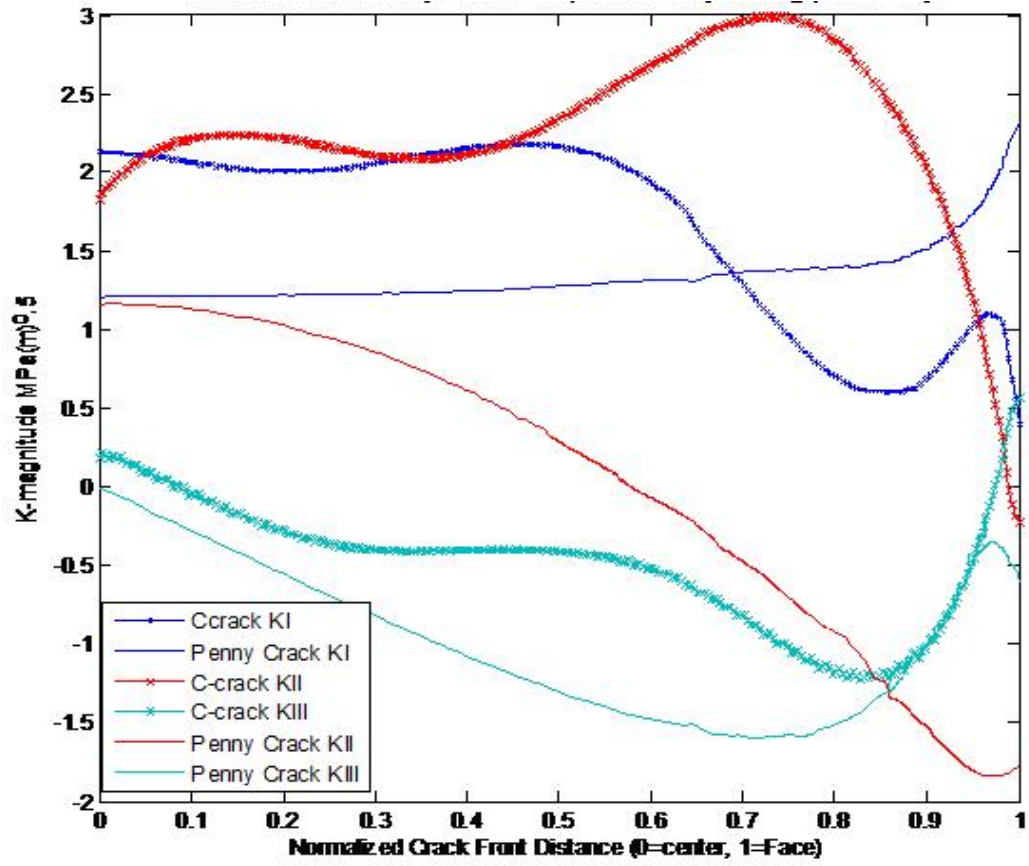


Figure 5-10. Superimposed SIFs for a c-crack and penny crack of similar dimensions under elliptical load ( $a=360 \mu\text{m}$ ,  $b=120 \mu\text{m}$ , and  $P_o= 3.7 \text{ GPa}$  (540kPsi)) where the surface crack is tangent to the semi-minor edge of the contact patch.

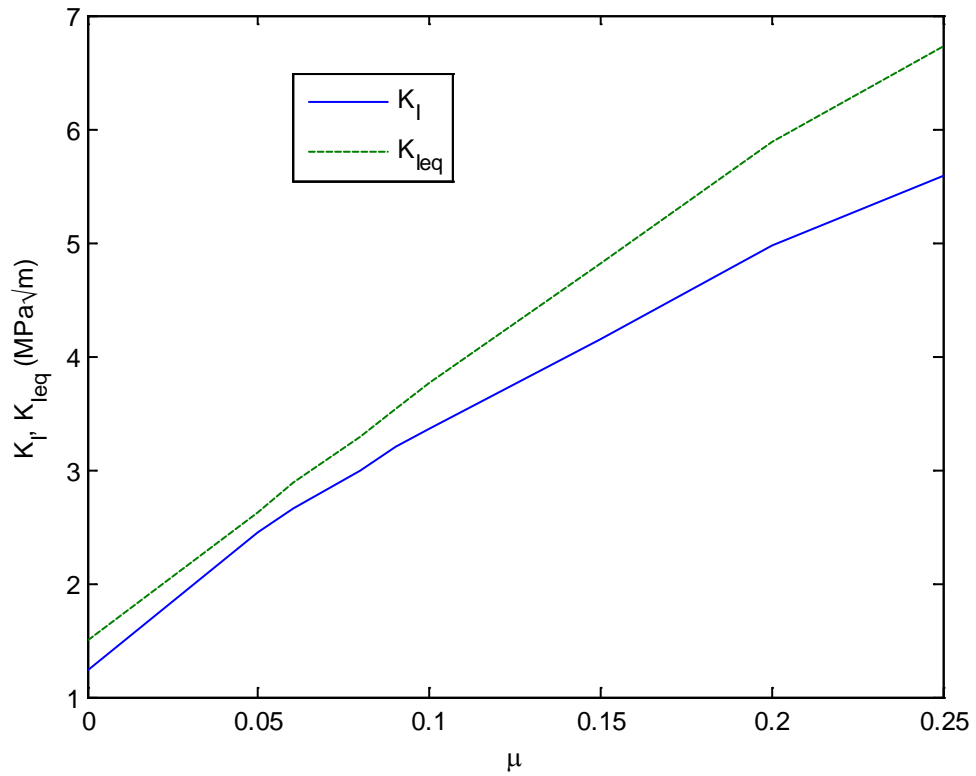


Figure 5-11. The max  $K_I$  found on the crack front of a semi-elliptical flaw that is  $30^\circ$  to the surface and has  $a'=250$   $b'=75$  as a function of varying friction coefficients on an elliptical contact patch in full slip for  $P_o=3.7$  GPa.

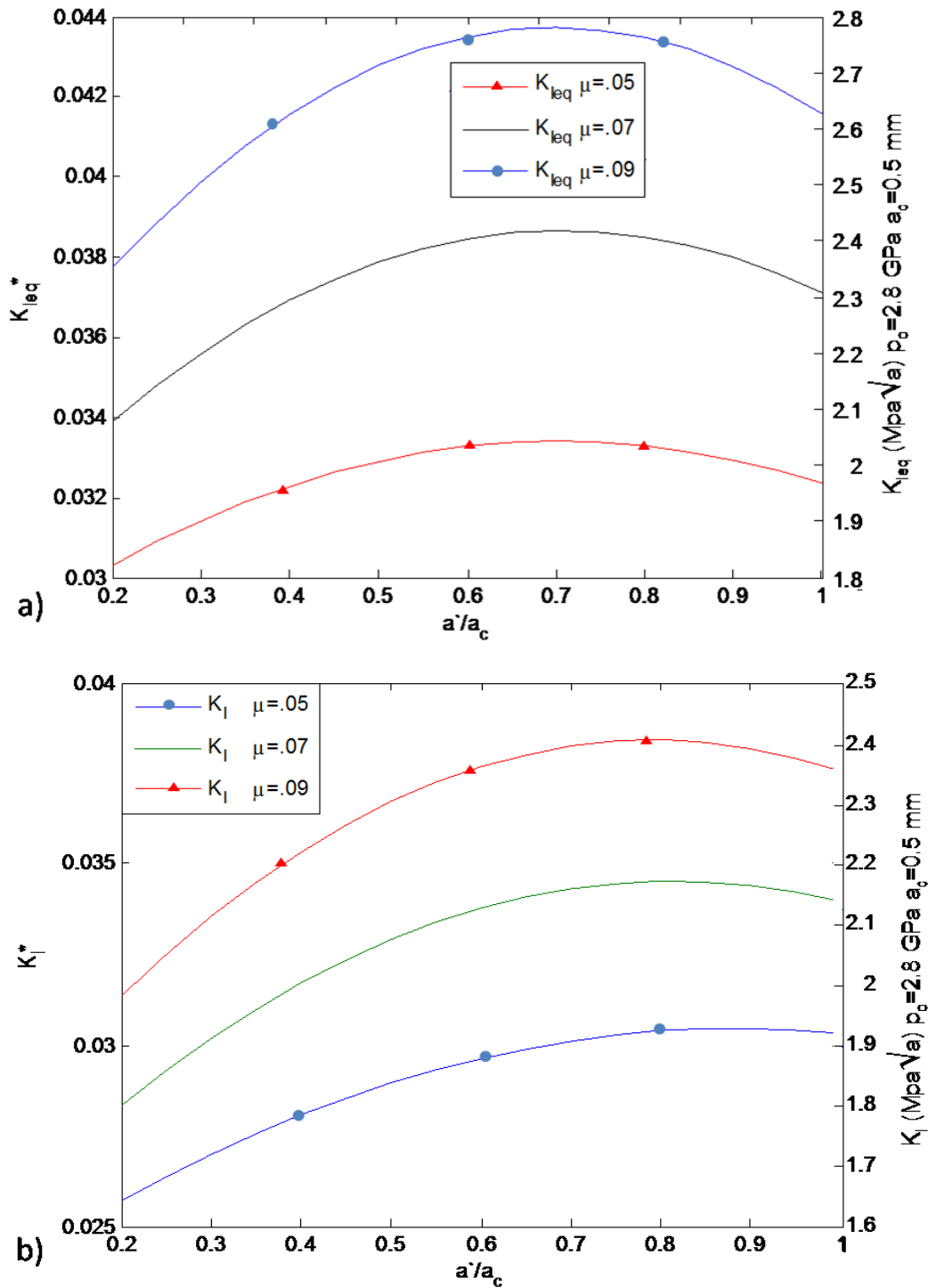


Figure 5-12. The nondimensionalized crack semi-width plotted against a) the max  $K_{I,eq}$  and b) the max  $K_I$  where nondimensional units are on the left and in  $\text{MPa}\sqrt{m}$  for  $p_0 = 2.8$  GPa and  $a_c = 0.5$  mm on the right. The SIFs are nondimensionalized by dividing the calculated values by  $p_0\sqrt{a_c}$ .

CHAPTER 6  
EMPIRICAL STRESS INTENSITY FACTOR EQUATIONS FOR SURFACE CRACKS  
UNDER RCF

**6.1 Introduction**

Reflecting on prior works, there are a few discrepancies. Real RCF produces a complex stress field that is not easily characterized by many of the above methods. In many cases  $K_I$  is sometimes supplied as a negative number, which, while physically impossible, has often gone unmentioned, i.e. effects of crack closure have been ignored. If  $K_I$  is supplied,  $K_{II}$  or  $K_{III}$  may not be supplied even though all modes of crack tip deformation are present and contributing to mixed-mode crack growth. Also, the problem requires a 3D analysis which rules out much of the prior work. Beyond this, previous results were often case-specific. The pre-existing surface flaws present in silicon nitride balls are typically partial cone cracks or c-cracks and their 3D crack geometry was described by Levesque and Arakere (2006). The c-cracks have non-planar crack faces but also possess non-planar crack tips, making their shape more difficult to describe and, therefore, more difficult to analyze in any linear elastic fracture mechanics (LEFM) based analysis. In this work, comprehensive results for the calculation of SIFs for semi-elliptical cracks under RCF are presented. In another chapter, a comparison of SIFs for partial cone or c-cracks and semi-elliptical cracks subject to circular and elliptical RCF will be presented that shows that use of semi-elliptical crack with circular contact leads to conservative estimates for critical flaw size, required for defining limits for non-destructive evaluation methods for silicon nitride ball quality control. The results generated are of immediate engineering relevance to the hybrid ball bearing industry towards evaluating critical flaw size and for developing a fracture mechanics based life prediction methodology for hybrid bearings. The empirical

curve fits will also be of relevance to other areas of component design where contact-initiated fatigue damage is important such as gears, roller bearings, and railway wheels.

## 6.2 Analysis

A detailed investigation of SIFs for a semi-elliptical flaw under rolling contact fatigue can only be properly done in 3D. This implies a 3D FEA analysis, as any analytical method would quickly become intractable under this complex stress state. We have modeled the penny crack for different aspect ratios, orientations of load, ellipticity of load, and angles to the surface. The resulting trends are plotted and are fitted to equations for ease of use.

The FEA model has been created using either FRANC3D/NG, as developed by the Fracture Analysis Consultants or ABAQUS. FRANC3D/NG makes it easier for the user to create meshes of cracked bodies with limited control of the mesh density. The mesh density is critical for both the accurate calculation of the crack tip opening displacements and for capturing the stress gradients of the Hertzian contact.

As alluded to, SIFs are calculated by using a displacement correlation technique as described by the equations:

$$K_I = \frac{E}{4(1-\nu^2)} \sqrt{\frac{2\pi}{r}} (u_1 - u_2) \quad (9-2)$$

$$K_{II} = \frac{E}{4(1-\nu^2)} \sqrt{\frac{2\pi}{r}} (v_1 - v_2) \quad (9-3)$$

$$K_{III} = \frac{E}{4(1-\nu^2)} \sqrt{\frac{2\pi}{r}} (w_1 - w_2) \quad (9-4)$$

However, SIFs could also be determined via J-integral decomposition through ABAQUS or the M-integral in FRANC3D/NG (Banks-Sills) but were not as data obtained

provided similar results and is intended to be used in other work reflecting on crack closure under RCF and neither method is currently formulated for accounting for the traction encountered on the crack faces during closure.

Quadratic elements are required by the Displacement correlation method for calculating SIFs since the insertion of a quarter point element greatly increases the accuracy of the model without a dramatic increase in mesh density. To reduce the size of the problem a technique referred to as submodeling is utilized, where displacements are applied to the boundary of a small cracked block to simulate its being a part of a much larger half-space. The contact load is applied to the surface with FORTRAN user subroutines DLOAD (and UTRACLOAD) for ABAQUS (see Fig 6-1). This load is applied up till the edge of the crack but not over the crack, as this would cause the applied pressure to be inaccurate (Fujimoto). Also, crack closure would result and the model would then require a contact algorithm on an already large quadratic, fracture model that would be accurate enough to yield crack tip displacements.

### **6.3 Crack Geometry**

Surface cracks can have a variety of shapes. Cone cracks have received much attention in the literature (Mackerle). Partial cone cracks are reviewed in separate paper (Levesque and Arakere) and have also been the subject of some analyses [Hadfield, 1993a, Hadfield, 1993b, Wang and Hadfield, 2000, Zhao, 2006]. Penny cracks seem to be the simplest of which to mesh and simulate in a 3D FEA analysis.

However, if attention were limited to the family of possible half-penny surface flaws, there remain only two features that can be altered, aspect ratio and angle towards the surface. Five aspect ratios have been analyzed ( $a/b=0.2, 0.4, 0.6, 0.8,$  and  $1$ ) under a few different angles ( $0^\circ, 45^\circ,$  and  $60^\circ$ ).

## 6.4 Orientation Of Load

As a surface flaw is subjected to rolling contact fatigue, a load is set in a direction across the free surface of the cracked body. In application, this pass of a load will happen repeatedly, subjecting the part to cyclic loading. While at each instant, the loads orientation generates a different set of SIFs as it moves along the surface, there is one orientation (for a given load size and magnitude) that produces the highest SIFs along the crack front. It is this orientation that is of most interest for a design analysis that would determine if the SIFs reach a critical value to induce fracture,  $K_c$ , initiate fatigue,  $K_{eff}$ , or will direct a growth analysis,  $\Delta K_{eff}$ .

In some orientations of load, the crack faces interpenetrated when contact was not defined, indicating crack closure occurred. The interpolation resulted in a negative  $K_I$  stress intensity factor but  $K_{II}$  and  $K_{III}$  remained identical. Comparing  $K_I$  along the front of a crack for an orientation with and without contact defined results in fig 6-2. Reflection indicates that simply setting the  $K_I=0$  when  $K_I<0$  is conservative, under conditions of crack closure. It must be noted that the coefficient of friction for contact elements between the crack faces was set to zero. For non-zero friction between the crack faces it is possible that closure might couple modes of deformation. Contact is computationally very difficult to implement in these problems because traction encountered on the crack faces during closure is not satisfactorily incorporated into the J-integral decomposition in ABAQUS and necessitates the use of displacement correlation for evaluating K-solutions. However, this procedure has been successfully implemented and will be discussed in a future work on modeling concerns for these types of problems.

While the tensile region is maximal on the periphery of the contact patch in an uncracked body (according to the stress solution), this does not necessarily mean that this same position is where the maximum SIFs will occur. So, to find the worst case load orientation the distance between the contact patch edge and the crack center at the surface was perturbed and SIFs calculated for these orientations. The SIFs of multiple contact patch positions relative to the crack were compared and the position that yielded the highest SIF was chosen for curve fitting. These distances for each model are given in Table 1. It was noticed that this distance tends to decrease as load size is increased and as crack aspect ratio decreases (and the crack tip is generally closer to the surface) for the more vertical cracks (as this allows their tip to be more generally located in the small tensile region about the contact).

### 6.5 Load

Rolling contact fatigue can have multiple different shapes of pressure distribution, but if the two contacting bodies can be characterized with two radii of curvature each, as in a Hertzian contact, then the contact patch will be elliptical. For bodies whose radii of curvature are identical the contact patch is circular and its pressure distribution is

$$P(x, y) = p_o \sqrt{1 - r^2} \quad (9-5)$$

It is important to note that the radial tensile stress region at the edge of contact is both small and quickly decays with increasing depth into the material. Also, it clearly shows that the stress state is quite far from anything that can be considered as far-field. The absence of a clearly identifiable far-field stress seen by the crack makes the curve fits more complicated than those employed by the widely referenced paper by Newman and Raju (1981)

Empirical equations for circular loading of penny cracks at a few angles are provided. The range of size of circular loads has been nondimensionalized with respect to the crack half-width and has been analyzed for the  $r=1b$ ,  $2b$ , and  $3b$  cases, which should cover the majority of cases which would be of engineering interest. The data obtained from FEA was fit to the equations:

$$K_I = p_o \left( a_1 + a_2x + a_3x^2 + a_4x^3 + a_5x^4 \right) g f_\phi \sqrt{\pi \frac{a}{Q}} \quad (9-6)$$

$$K_{II} = p_o \left( b_1 + b_2x + b_3x^2 + b_4x^3 + b_5x^4 \right) g f_\phi \sqrt{\pi \frac{a}{Q}} \quad (9-7)$$

$$K_{III} = p_o \left( c_1 + c_2x + c_3x^2 + c_4x^3 + c_5x^4 \right) g f_\phi \sqrt{\pi \frac{a}{Q}} \quad (9-8)$$

In this way, the results can be easily fit with very little error (~0.5%) and can be easily nondimensionalized. It is noted that when  $a/b \leq 1$ ,  $Q$  is approximated by the equation:

$$Q = 1 + 1.464 \left( \frac{a}{b} \right)^{1.65} \quad (9-9)$$

Also,

$$g = 1 + 0.1(1 - \sin \phi)^2 \quad (9-10)$$

$$f_\phi = \left[ \left( \frac{a}{c} \right)^2 \cos^2 \phi + \sin^2 \phi \right]^{\frac{1}{2}} \quad (9-11)$$

While the fit uses components of the Newman and Raju fit (1981), it is more involved because of the complex 3D subsurface stress field and the steep stress gradients at the edge of contact to crack tip. The coefficients for these cases are provided in Table 2-4.

## 6.6 Results

As a consequence of running these analyses for different aspect ratios and angles, a few notable trends can be seen as a result. Firstly, the location along the crack front where the SIFs are the highest can change based on crack depth and angle. Generally, the shallower cracks can have their SIFs toward the crack center while the deeper cracks tend to have their SIFs highest near the surface.

For a single load size the worst-case crack is non-obvious. See figs. 6-3-6-5. By reflecting on the results, it is observed that the  $\theta=45^\circ$   $a/b=1$  case has the highest SIFs for the  $r=2b$  and  $3b$  cases. In these situations, the highest SIFs occur near the free surface. For the  $r=1b$  case, it is observed that the  $\theta=60^\circ$ ,  $a/b=0.2$  case has the highest SIFs and this occurs at the deepest portion of the crack. Neither of these observations is intuitive. In fact, they display that it is not always the steepest or the longest of cracks which will have the highest SIFs under a given load, but rather an interesting combination thereof which varies with load size.

The variation of SIFs across the crack front also brings many issues in terms of crack growth. For example, if the highest SIFs are produced by a certain geometry crack and these SIF values are largest near the free surface, if this crack grows it will grow wider on the surface rather than into the depth. Then the geometry may become one which yields relatively lower SIFs than its former shape. This means the crack which produces the highest SIFs, for a given geometry and load, may not be the worst geometry crack under RCF because its shape evolution effects its SIFs and so the worst crack geometry is something that can be revisited in future work.

The above graphs contain every model created for each of the three types of load. The trends between models of the same angle but different depths is quite smooth

and is reflective of the transitions of the stress state as a crack is longer. The trends between cracks of different angles is less obvious as the change in angle places the cracks in a different part of the stressed state. Quite surprisingly, the trends in  $r=3b$  seems smooth between all 15 models graphed even though the load orientation may not be identical for all models and the tip location may be quite different. This trend is observed because the larger contact patch produces lower stress gradients.

### **6.7 Conclusions**

Three-dimensional FEA was performed on a parametric variation of semi-elliptical flaws under circular RCF patches to provide a set of comprehensive empirical equations for mixed-mode SIFs applicable in the hybrid ball bearing industry and other contact fatigue applications. Modeling concerns have been addressed and a modeling framework has been provided for analyzing these types of geometry and load. The parametric variation of load size, crack angle, and crack depth displayed a several interesting trends including the type of cracks that provide the highest SIFs for the given load geometry which is neither the deepest crack nor the steepest crack all the time. The comprehensive and accurate ( $\sim 0.5\%$ ) empirical equations for the  $K_I$ ,  $K_{II}$ , and  $K_{III}$  SIFs presented are of immediate engineering relevance to the hybrid silicon nitride ball bearing industry towards evaluating critical flaw size, and for developing a fracture mechanics based life prediction methodology. The empirical curve fits will also be of relevance to other areas of component design where contact-initiated fatigue damage is important such as gears, roller bearings, and railway wheels.

Table 6-1. The  $x_d$  distances (nondimensionalized w.r.t. the crack semi-width) where  $K_I$  was maximal.

$r =$	$1b$	$2b$	$3b$
$\theta = 0^\circ$ $a/b = 1.0$	1.3	1.0	0.875
$\theta = 0^\circ$ $a/b = 0.8$	1.3	0.875	0.875
$\theta = 0^\circ$ $a/b = 0.6$	1.1	0.875	0.875
$\theta = 0^\circ$ $a/b = 0.4$	0.95	0.625	0.75
$\theta = 0^\circ$ $a/b = 0.2$	0.95	0.625	0.625
$\theta = 45^\circ$ $a/b = 1.0$	1.0	0.625	0.5
$\theta = 45^\circ$ $a/b = 0.8$	1.25	0.5	0.5
$\theta = 45^\circ$ $a/b = 0.6$	1.25	0.5	0.5
$\theta = 45^\circ$ $a/b = 0.4$	1.25	0.5	0.375
$\theta = 45^\circ$ $a/b = 0.2$	1.25	0.5	0.375
$\theta = 60^\circ$ $a/b = 1.0$	0.0	0.0	0.0
$\theta = 60^\circ$ $a/b = 0.8$	0.0	0.0	0.0
$\theta = 60^\circ$ $a/b = 0.6$	0.0	0.0	0.0
$\theta = 60^\circ$ $a/b = 0.4$	0.0	0.0	0.0
$\theta = 60^\circ$ $a/b = 0.2$	0.0	0.0	0.0

Table 6-2. Coefficients for all parametric cases for  $K_I$ ,  $K_{II}$ , and  $K_{III}$  for  $\theta = 0^\circ$ .

angle	aspect ratio	load size (a)	coefficients				
			5	4	3	2	1
<b>0°</b>							
$K_I$	1	1	0.00057	-0.00152	0.00233	-0.00027	0.00209
		2	0.00160	-0.00449	0.00743	-0.00082	0.00529
		3	0.00326	-0.00928	0.01603	-0.00172	0.01017
	0.8	1	0.00631	-0.00882	0.00516	-0.00059	0.00240
		2	0.01813	-0.02534	0.01571	-0.00173	0.00654
		3	0.03734	-0.05212	0.03330	-0.00359	0.01313
	0.6	1	0.01528	-0.02003	0.00842	-0.00108	0.00250
		2	0.04472	-0.05859	0.02521	-0.00318	0.00712
		3	0.09423	-0.12337	0.05377	-0.00671	0.01478
	0.4	1	0.01711	-0.02316	0.00882	-0.00120	0.00232
		2	0.05121	-0.06928	0.02663	-0.00361	0.00688
		3	0.10771	-0.14566	0.05629	-0.00760	0.01439
	0.2	1	-0.00905	0.00734	-0.00285	0.00021	0.00181
		2	-0.02741	0.02232	-0.00860	0.00063	0.00546
		3	-0.05815	0.04745	-0.01823	0.00135	0.01153
$K_{II}$	1	1	-0.00005	0.00059	-0.00135	0.00011	0.00043
		2	-0.00011	0.00167	-0.00400	0.00030	0.00130
		3	-0.00027	0.00369	-0.00867	0.00063	0.00286
	0.8	1	0.00167	-0.00220	-0.00033	-0.00009	0.00027
		2	0.00517	-0.00691	-0.00083	-0.00031	0.00078
		3	0.01093	-0.01453	-0.00185	-0.00065	0.00167
	0.6	1	0.00260	-0.00398	0.00072	-0.00020	0.00015
		2	0.00788	-0.01206	0.00224	-0.00062	0.00042
		3	0.01667	-0.02550	0.00476	-0.00132	0.00086
	0.4	1	-0.00058	-0.00043	-0.00017	-0.00006	0.00007
		2	-0.00190	-0.00114	-0.00055	-0.00018	0.00018
		3	-0.00423	-0.00215	-0.00124	-0.00036	0.00037
	0.2	1	-0.00502	0.00535	-0.00209	0.00023	0.00001
		2	-0.01555	0.01661	-0.00647	0.00071	0.00003
		3	-0.03324	0.03555	-0.01384	0.00152	0.00006
$K_{III}$	1	1	-0.00072	0.00206	-0.00129	-0.00047	-0.00003
		2	-0.00215	0.00613	-0.00383	-0.00136	-0.00009
		3	-0.00457	0.01299	-0.00804	-0.00290	-0.00019
	0.8	1	-0.00349	0.00719	-0.00367	-0.00026	-0.00002
		2	-0.01045	0.02144	-0.01095	-0.00071	-0.00007
		3	-0.02215	0.04527	-0.02312	-0.00145	-0.00015

Table 6-2. Continued

angle	aspect ratio	load size ( <i>a</i> )	coefficients				
			5	4	3	2	1
0.6		1	-0.00218	0.00543	-0.00275	-0.00041	-0.00001
		2	-0.00651	0.01619	-0.00823	-0.00121	-0.00004
		3	-0.01380	0.03416	-0.01738	-0.00250	-0.00009
0.4		1	0.00440	-0.00286	0.00054	-0.00079	0.00000
		2	0.01361	-0.00898	0.00172	-0.00242	-0.00001
		3	0.02883	-0.01913	0.00369	-0.00510	-0.00001
0.2		1	0.01197	-0.01271	0.00448	-0.00119	0.00001
		2	0.03696	-0.03926	0.01385	-0.00369	0.00004
		3	0.07848	-0.08338	0.02941	-0.00783	0.00009

Table 6-3. Coefficients for all parametric cases for  $K_I$ ,  $K_{II}$ , and  $K_{III}$  for  $\theta = 45^\circ$ .

angle	aspect ratio	load size (a)	coefficients				
			5	4	3	2	1
<b>45°</b>							
$K_I$	1	1	0.03069	-0.06817	0.05008	-0.01249	0.00783
		2	0.05798	-0.12787	0.10044	-0.02374	0.01392
		3	0.06165	-0.13609	0.11087	-0.02560	0.02027
	0.8	1	0.25896	-0.37265	0.16790	-0.02668	0.00796
		2	0.47901	-0.68372	0.32295	-0.04879	0.01569
		3	0.50815	-0.72296	0.34653	-0.05168	0.02271
	0.6	1	0.01294	-0.01710	0.00755	-0.00106	0.00249
		2	0.32412	-0.36314	0.13671	-0.01950	0.01478
		3	0.12658	-0.08750	0.02082	-0.00246	0.02104
	0.4	1	0.08439	-0.06357	0.00203	-0.00421	0.00718
		2	0.14478	-0.15116	0.04963	-0.00780	0.01204
		3	0.09795	-0.10360	0.03560	-0.00500	0.02300
	0.2	1	0.02247	0.00565	-0.02538	-0.00281	0.00998
		2	-0.01594	0.02200	-0.01337	-0.00007	0.01610
		3	-0.03883	0.04039	-0.01662	0.00126	0.02068
$K_{II}$	1	1	-0.02901	0.05987	-0.07188	0.01255	0.04438
		2	-0.02804	0.06717	-0.09026	0.01562	0.05196
		3	-0.02127	0.06061	-0.08914	0.01507	0.04856
	0.8	1	-0.15705	0.17951	-0.14463	0.01446	0.04219
		2	-0.08488	0.07200	-0.10265	0.00823	0.04500
		3	0.00015	-0.02817	-0.05834	0.00234	0.03989
	0.6	1	0.00480	-0.00766	0.00272	-0.00063	0.00019
		2	0.97142	-1.49346	0.60414	-0.10156	0.03866
		3	1.02226	-1.53021	0.62327	-0.10318	0.03278
	0.4	1	-0.08691	0.12303	-0.13284	0.00258	0.02877
		2	-0.01543	-0.05833	-0.02924	-0.00684	0.02684
		3	0.05186	-0.12077	0.00423	-0.00754	0.01685
	0.2	1	-0.17706	0.30827	-0.18665	0.00855	0.01485
		2	0.06102	-0.06311	-0.02082	-0.00388	0.00863
		3	0.12743	-0.16371	0.03198	-0.00820	0.00413
$K_{III}$	1	1	-0.02890	0.10038	-0.09167	-0.00947	-0.00268
		2	-0.02893	0.11510	-0.10462	-0.01713	-0.00316
		3	-0.02652	0.10900	-0.09448	-0.01920	-0.00290
	0.8	1	-0.09734	0.25130	-0.16807	-0.00512	-0.00214
		2	-0.03831	0.21799	-0.16516	-0.01420	-0.00229
		3	-0.01420	0.18514	-0.14208	-0.01526	-0.00202

Table 6-3. Continued

angle	aspect ratio	load size ( <i>a</i> )	coefficients				
			5	4	3	2	1
	0.6	1	0.00117	0.00032	-0.00057	-0.00048	-0.00001
		2	0.10361	0.00956	-0.05369	-0.01667	-0.00096
		3	0.04763	0.10309	-0.09433	-0.00746	-0.00105
	0.4	1	0.25381	-0.26703	0.08972	-0.03561	-0.00028
		2	0.39896	-0.42784	0.15003	-0.04753	-0.00017
		3	0.56860	-0.61293	0.22239	-0.05780	0.00015
	0.2	1	0.17767	-0.13319	0.05089	-0.05330	-0.00111
		2	0.16738	-0.15268	0.04809	-0.03087	-0.00064
		3	0.17233	-0.16379	0.05305	-0.02531	-0.00044

Table 6-4. Coefficients for all parametric cases for  $K_I$ ,  $K_{II}$ , and  $K_{III}$  for  $\theta = 60^\circ$ .

angle	aspect ratio	load size (a)	coefficients				
			5	4	3	2	1
<b>60°</b>							
$K_I$	1	1	0.00022	0.00219	-0.00166	0.00151	0.01305
		2	-0.00154	0.00912	-0.00541	0.00388	0.02207
		3	-0.00407	0.01589	-0.00991	0.00569	0.02850
	0.8	1	0.00580	0.00104	-0.00646	0.00132	0.01405
		2	-0.00649	0.02848	-0.01860	0.00504	0.02342
		3	-0.02152	0.05393	-0.03099	0.00769	0.02959
	0.6	1	-0.00992	0.02657	-0.02304	0.00145	0.01485
		2	-0.04943	0.07986	-0.04148	0.00617	0.02394
		3	-0.07570	0.11359	-0.05482	0.00858	0.02964
	0.4	1	0.19388	-0.20215	0.05007	-0.01112	0.01417
		2	0.18599	-0.22079	0.07396	-0.01166	0.02164
		3	0.12169	-0.15525	0.05367	-0.00837	0.02604
	0.2	1	0.13338	-0.10915	0.00607	-0.00692	0.01262
		2	0.08585	-0.09914	0.02550	-0.00562	0.01888
		3	0.01541	-0.03383	0.00914	-0.00297	0.02266
$K_{II}$	1	1	-0.00062	-0.00185	-0.00699	-0.00085	0.01279
		2	0.00082	-0.00312	-0.00757	-0.00122	0.00995
		3	0.00176	-0.00287	-0.00670	-0.00122	0.00437
	0.8	1	0.00520	-0.02522	-0.00543	-0.00325	0.01226
		2	0.01770	-0.04188	0.00250	-0.00464	0.00800
		3	0.02757	-0.04846	0.00790	-0.00505	0.00245
	0.6	1	0.04532	-0.07520	0.00876	-0.00680	0.01044
		2	0.04845	-0.08291	0.01570	-0.00701	0.00509
		3	0.04929	-0.07602	0.01641	-0.00641	-0.00023
	0.4	1	-0.15883	0.19031	-0.11165	0.00839	0.00678
		2	0.11770	-0.17533	0.04090	-0.00955	0.00119
		3	0.31135	-0.40073	0.13295	-0.02029	-0.00317
	0.2	1	-0.36183	0.47099	-0.22470	0.02001	0.00731
		2	-0.05244	0.05544	-0.05487	0.00289	0.00191
		3	0.15749	-0.19656	0.04810	-0.00870	-0.00180
$K_{III}$	1	1	0.00218	-0.00133	0.00088	-0.01215	-0.00111
		2	0.00378	-0.00180	0.00232	-0.01097	-0.00098
		3	0.00263	0.00168	0.00087	-0.00567	-0.00056
	0.8	1	0.03250	-0.03575	0.01271	-0.01721	-0.00131
		2	0.04629	-0.04433	0.01722	-0.01513	-0.00107
		3	0.03760	-0.02715	0.01109	-0.00829	-0.00060

Table 6-4. Continued

angle	aspect ratio	load size ( <i>a</i> )	coefficients				
			5	4	3	2	1
0.6		1	0.06033	-0.05899	0.01928	-0.02105	-0.00187
		2	0.06898	-0.05935	0.02020	-0.01772	-0.00148
		3	0.05150	-0.03334	0.01189	-0.01070	-0.00087
0.4		1	0.37372	-0.38473	0.14244	-0.05317	0.00015
		2	0.60388	-0.64698	0.23694	-0.05732	0.00054
		3	0.59932	-0.63865	0.23462	-0.04821	0.00062
0.2		1	0.49753	-0.49000	0.18141	-0.06698	0.00012
		2	0.82548	-0.87869	0.31396	-0.07222	0.00066
		3	0.82666	-0.88589	0.31707	-0.06345	0.00078

### 6.8 Figures

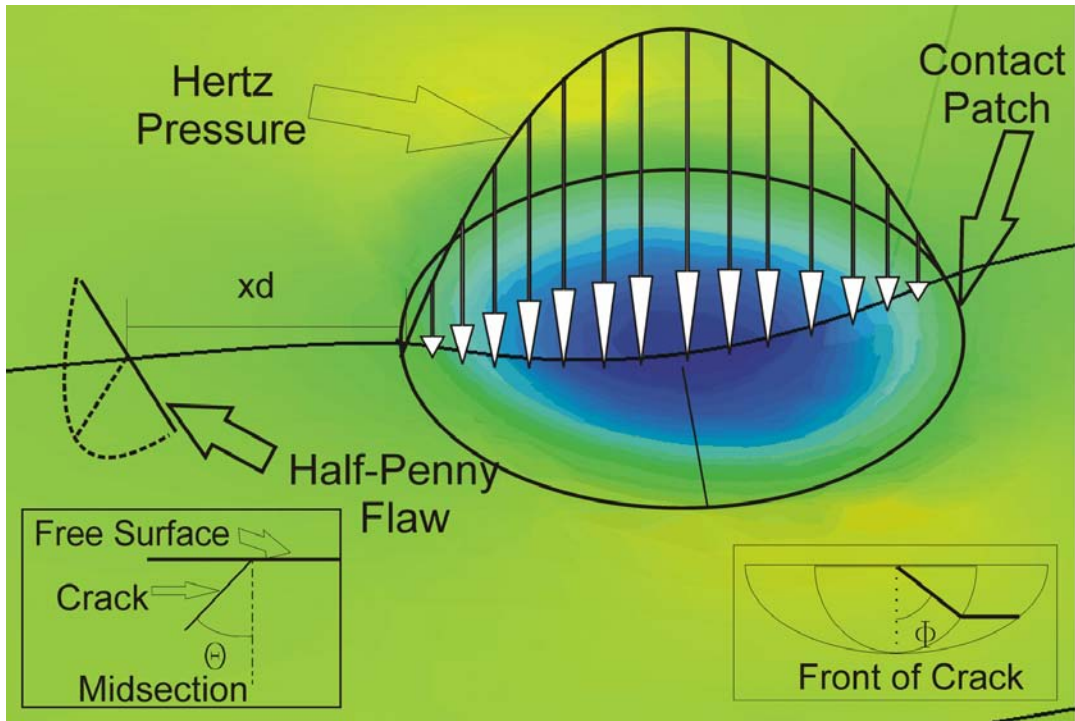


Figure 6-1. Model configuration displaying orientation of load and defining variables  $\theta$ ,  $\phi$ , and  $x_d$ .

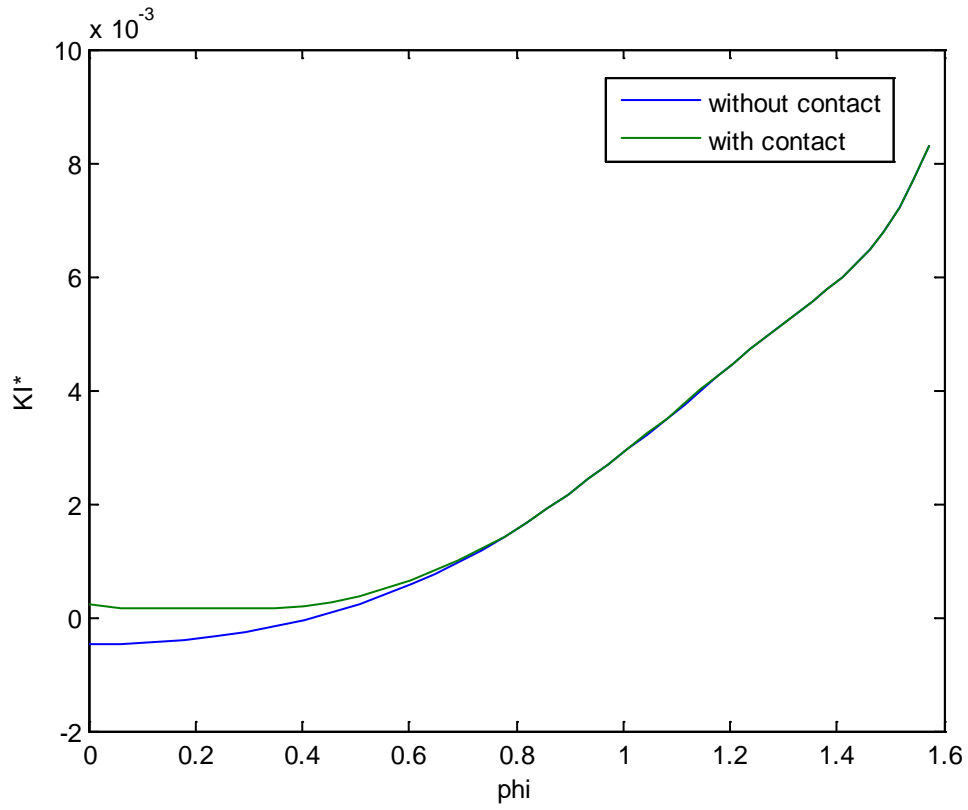


Figure 6-2.  $K_I$  for a single load geometry with and without contact defined.

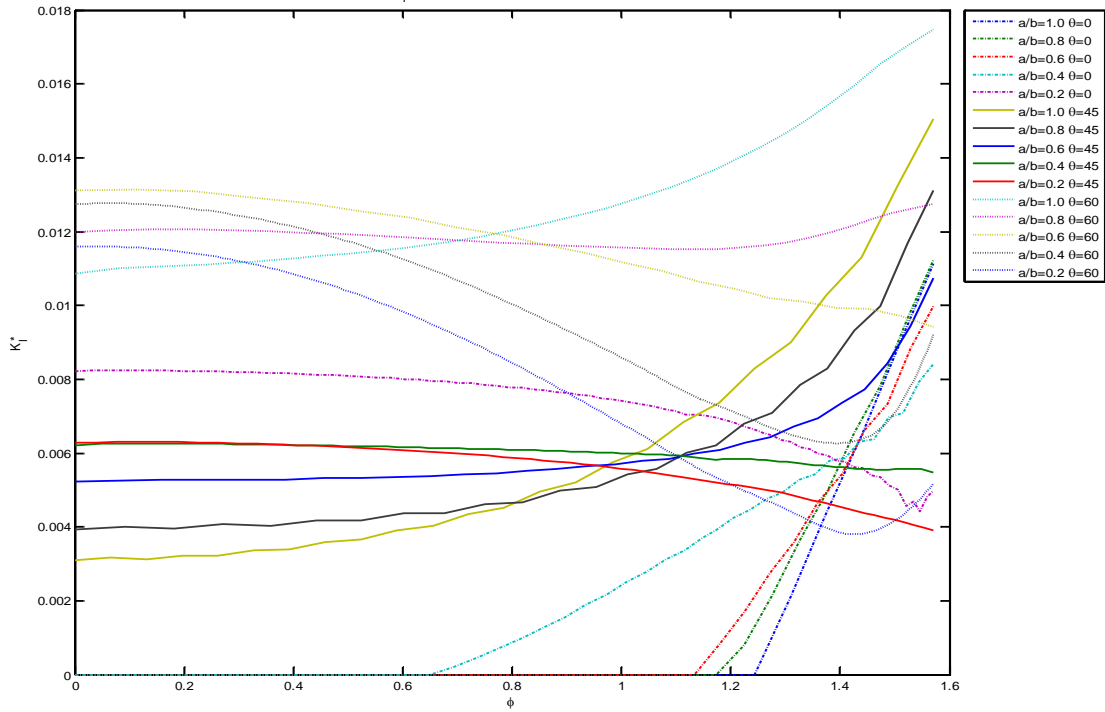


Figure 6-3.  $K_I$  for  $r=1b$  along the crack front for all variations of crack angle and depth.

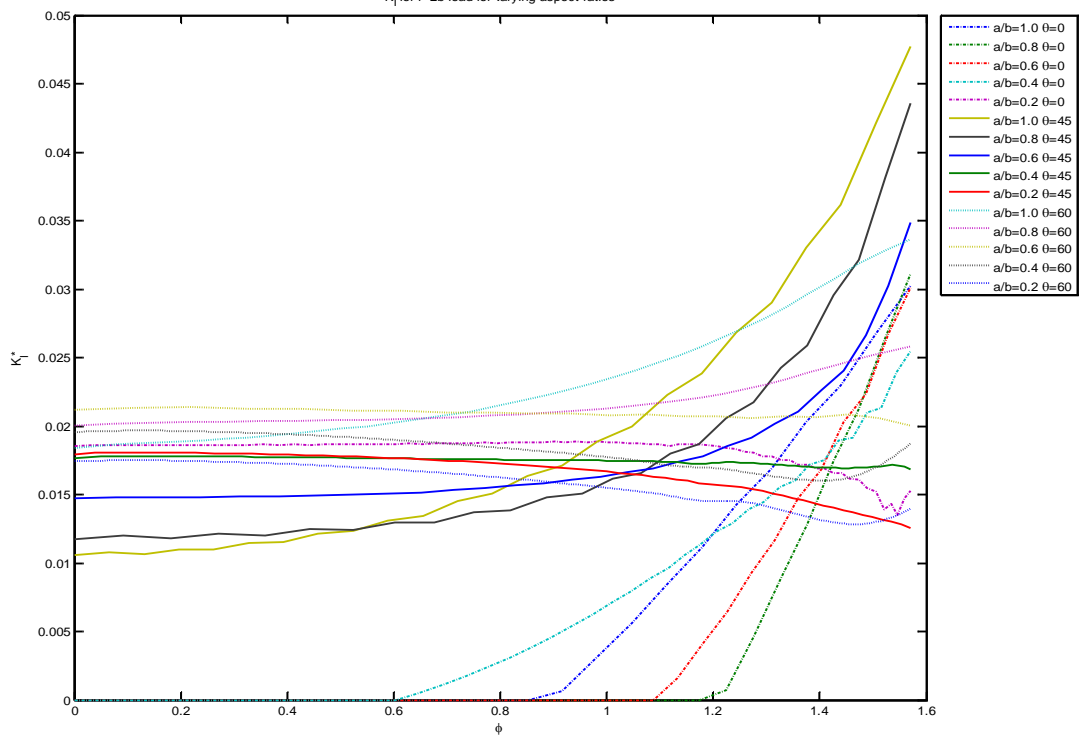


Figure 6-4.  $K_I$  for  $r=2b$  along the crack front for all variations of crack angle and depth.

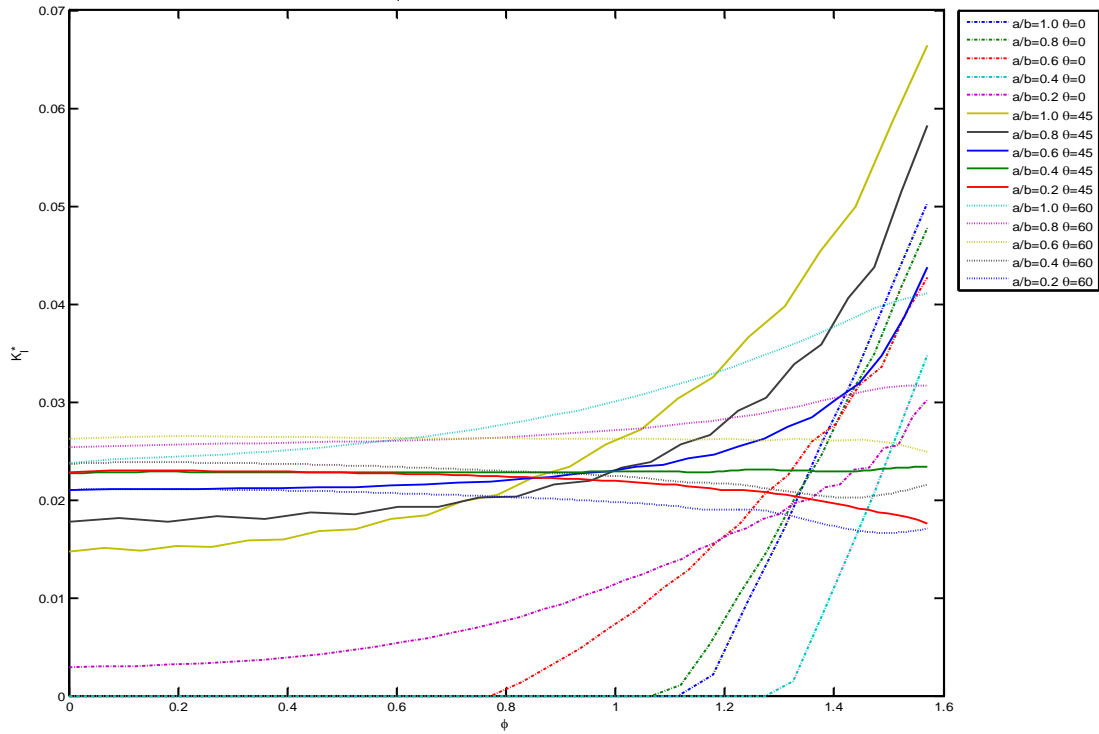


Figure 6-5.  $K_I$  for  $r=3b$  along the crack front for all variations of crack angle and depth.

CHAPTER 7  
UNCERTAINTY ANALYSIS FOR FATIGUE FAILURE PROBABILITY OF SILICON  
NITRIDE ROLLING ELEMENT

**7.1 Introduction**

Ball and roller bearings are widely used in a variety of industrial machinery to allow relative motion and support load in rotating shafts. In conventional ball bearings, with metal raceways and balls, subsurface originated spalling and surface originated pitting have been recognized as the dominant modes of failure due to rolling contact fatigue (RCF). Bearing subsurface material is subjected to RCF cycles that induces a complex triaxial stress state, nonproportional loading, high hydrostatic stress component, and changing planes of maximum shear stress during a loading cycle, and eventually leads to a subsurface crack. Spalling occurs when subsurface cracks propagate towards the surface to form a surface spall (Sadeghi et al., 2009). This mechanism is the dominant mode of failure in rolling element bearings that have smooth surfaces and operate under elastohydrodynamic lubrication (EHL) conditions. Surface originated pitting occurs in cases where surface irregularities in the form of dents or scratches are present. Here, cracks initiate at the surface stress concentrators and thereafter propagate at a shallow angle to the surface (Bower, 1988). This mechanism of failure is more common in gears where substantial sliding occurs between the contacting surfaces.

Aircraft engine manufacturers have been aggressively pursuing advanced materials to meet mainshaft bearing requirements of advanced engines for military, commercial and space propulsion. These requirements include bearings with extended life, superior corrosion resistance, surface durability and tribological performance. Hybrid bearings utilize silicon nitride balls and steel raceways to achieve considerably

longer fatigue lives, to have similar thermal behavior, to last up to five times longer in oil starvation conditions (Miner et al., 1996, Tanimoto et al., 2000) and perform well under corrosive conditions (Klemm, 2002). Silicon nitride balls have many physical properties which allow for bearing technology advancement including low density and high compressive strength but also have low fracture toughness of  $4-6 \text{ MPa} \sqrt{\text{m}}$  (Piotrowski and O'Brien, 2006). This low fracture toughness, in combination with unavoidable ball to ball collisions in the manufacturing (lapping) process often results in ring or *c*-cracks (partial cone cracks) (Cundill, 1996). These flaws can grow under RCF when placed in service and result in a spall on the ball surface, (Fig 7-1) (Levesque and Arakere, 2008).

The failures caused by surface cracks of silicon nitride ball bearings under rolling contact have been addressed by 'ring or *c*-cracks' and 'wedge effect' models. In the *c*-crack model the Hertzian contact stresses occurring around the circumference of the bearing contact area is thought to dominate the crack growth. The lubricant is assumed to have no effect on the crack growth. In the wedge effect model the fluid pressure is thought to penetrate into the crack by contact pressure. When the fluid is pressurized by the maximum contact pressure at the contact center it is thought to cause crack growth. The mechanisms of these two models have been investigated separately. A surface crack is likely to be affected by the stresses used in both models as a ball passes over the crack. The stress intensity factor (SIF) at the crack tip is also adversely affected by the presence of friction-induced traction forces at the contact. However, effects of the fluid pressure are not well understood or characterized yet and the dominant mode of failure is thought to be crack growth driven by SIFs arising from the contact patch passing over the *c*-crack. Partial cone or *c*-cracks are considered the most damaging

surface defect that limits ball life in hybrid bearings under service conditions (Evans, 1983, Hadfield et al., 1993b).

The fatigue damage process in ceramic rolling elements is very different from metal balls. RCF in metal bearings is manifested as a flaking off of metallic particles from the surface of raceways and/or rolling elements. As described earlier, this process commences as a crack *below* the surface and is propagated to the surface, eventually forming a pit or *spall* in the load-carrying surface. Bearing fatigue life estimation is still largely based on the seminal probabilistic life model by Lundberg and Palmgren (LP), proposed in 1945. Despite many improvements to the LP model current probabilistic bearing life prediction methods are based on the ISO standard set up in 1989 and continue to rely on extensions to the LP model, are empirical in nature, and include variables that are obtained from extensive experimental testing. The LP theory states that for bearing rings subjected to  $N$  cycles of repeated loading the probability of survival  $S$  is given by,

$$\ln \frac{1}{S} = A \frac{N^e \tau_0^c V}{z_0^h} \quad (7-1)$$

where,  $\tau_0$  is the maximum orthogonal shear stress in the contact,  $z_0$  is the corresponding depth at which this stress occurs and  $V$  is the stressed volume of material. The parameters  $A$ ,  $c$  and  $h$  are material characteristics that are determined experimentally. The parameter  $e$  is the Weibull slope for the experimental life data plotted on a Weibull probability paper.

Metals are weaker in shear than tension. In contrast to metallic materials,  $\text{Si}_3\text{N}_4$  material is weaker in tension than compression or shear. The LP methods cannot account for this difference in material behavior. Furthermore,  $c$ -cracks already exist on

the ball surface and hence subsurface crack initiation and subsequent growth to a spall is not pertinent to ball failure. A fracture mechanics methodology that evaluates the *critical flaw size* (or the largest allowable flaw size such that growth does not occur under the service conditions) in balls is required, since failure typically occurs, for hybrid bearings, when the effective SIF at the crack tip equals the mixed-mode fracture toughness of the silicon nitride ball material.

The largest allowable surface flaw that does not propagate under RCF loading is of design significance, and is termed the critical flaw size (CFS). A systematic procedure to compute the CFS based on fracture mechanics principles, RCF loading, and ball material properties has been recently presented by Levesque and Arakere (2009). Non-destructive evaluation (NDE) techniques are being developed and used on each ball in order to determine if it is acceptable to enter service (Wang, 2000). The resolution to which each ball is inspected, as determined by the CFS, has a strong effect on the cost of each ball and has been analyzed deterministically in prior work (Levesque and Arakere, 2009). The cost of NDE method for silicon nitride balls scales up very steeply with decreasing CFS and increasing ball diameter. Thus the cost associated with NDE can become a significant fraction of the overall manufacturing cost of the silicon nitride ball.

Brittle materials inherently exhibit considerable variation in material mechanical and fracture properties. For example, there is a significant variation in the depth of a crack from a controlled impact (Lawn, 1967, Wang and Hadfield, 2000). Also there is a noted variation in the fracture toughness specimen to specimen (for example  $4.85 \pm 0.36 \text{ MPa}\sqrt{\text{m}}$ , Piotrowski and O'Brien 2006).

## 7.2 Modeling Rolling Contact Fatigue Orientation Effects

Finite element analysis techniques have been developed to analyze 3D nonplanar surface flaws for stress intensity factor calculation (SIF) (Levesque and Arakere, 2008). Mesh density must be accurate enough to account for the strong gradients in stress from the contact patch and element types must allow SIF extraction. SIF calculation is done by the displacement correlation method, which can be written as:

$$K_I = \frac{E}{4(1-\nu^2)} \sqrt{\frac{2\pi}{r_d}} (u_1 - u_2) \quad (7-2a)$$

$$K_{II} = \frac{E}{4(1-\nu^2)} \sqrt{\frac{2\pi}{r_d}} (v_1 - v_2) \quad (7-2b)$$

$$K_{III} = \frac{E}{4(1-\nu^2)} \sqrt{\frac{2\pi}{r_d}} (w_1 - w_2) \quad (7-2c)$$

It is noted that  $r_d$  is the radius from where the relative displacements are measured from the crack tip, and  $u$ ,  $v$ , and  $w$  correspond to the displacements in the  $x$ ,  $y$ , and  $z$  directions for the local coordinate system at the tip of the crack.

With models for SIF calculation built for a crack whose width is 250  $\mu\text{m}$  and 75  $\mu\text{m}$  depth angled 30° to the surface. These specific dimensions were chosen since they have been experienced to be a set of dimensions that have been observed in experiment (Wang, 2000) and have exhibit high stress intensity factors when compared to other geometries (Levesque and Arakere, 2009). Loading is done via FORTRAN user subroutines DLOAD and UTRACLOAD for ABAQUS (Dessault Systèmes, 2007) for the normal and traction loads. The equations to describe the pressure distributions can be written as:

$$p(x, y) = p_o \sqrt{\frac{(x - x_d)^2}{a^2} + \frac{(y - y_d)^2}{b^2}} \quad (7-3)$$

and

$$f(x, y) = \mu p(x, y) \quad (7-4)$$

where  $x_d$  and  $y_d$  are the distances from the global coordinate system to the load center,  $a$  and  $b$  are the dimensions of the ellipse along these dimensions, and  $\mu$  is the friction coefficient for the moving load in a full-slip interaction (see Fig. 7-2). For the specific cases that were analyzed, an elliptical load aspect ratio of 1/8 and a  $\mu=0.07$  were used, which is believed to be representative of lubricated ball bearing contacts.

The stress intensity factors are calculated in all three modes. For implementation in determining what combination of these three modes of crack displacement have met a fatigue threshold, or  $K_{th}$ , the critical strain energy release rate (CSERR) (Levesque et al., 2009) is utilized as adapted from Anderson (2005) and can be written as.

$$K_{eq} = \sqrt{K_I^2 + K_{II}^2 + (1+\nu)K_{III}^2} \quad (7-5)$$

For simplification, the SIFs (calculated from displacement correlation) as calculated as a function of crack tip position are combined them into a single parameter (via CSERR) and have then chosen the highest value along the crack front as the representative value to determine if crack growth can occur for each orientation.

For an uncertainty analysis, the highest  $K_{eq}$  for a randomly oriented crack relative to the moving contact patch must be calculated. Here, a few assumptions are made. The contact patch passes on the ball surface in a band and does not change direction for the entire sequence (see Fig 7-3). The load magnitude and the traction magnitude and direction do not change relative to the elliptical contact. As the load passes around

the ball, there exists only one position where the max SIF is reached and this orientation is the nearest to the contact patch and on the opposite side of the traction direction. This maximum position can be classified with two variables: the lateral position of the crack relative to the center of the contact patch,  $x_D$ , and the angle that the crack makes on the surface relative to the contact patch tangent,  $\varphi$ . (Herein, the distance of the crack to the center of the contact load in the  $y_D$  direction is always 0 for maximum SIFs.) (see Fig. 7-3) Parametric studies for these two parameters have been analyzed and their effects separated as independent parameters in Figs 7-4 and 7-5.

### **7.3 Uncertainty Analysis**

In this section, uncertainty analysis of estimating the failure of silicon nitride ball bearings is presented using surrogate modeling and Monte Carlo simulation. The fatigue failure model in the previous section is based on the effective stress intensity factor, which depends on the size, direction and location of a crack; fracture toughness of the material; and applied loads. However, it is difficult to determine if a bearing may fail or not because there are many uncertainties in the practical operating environment. For example, an existing crack may not fail if its location is out of the contact path with bearing track or its size is too small. Thus, the failure of a bearing can only be evaluated in terms of probability. The goal of this section is to evaluate the probability of fatigue failure of silicon nitride ball bearings under representative operating conditions.

#### **7.3.1 Uncertainty Quantification**

The first step in uncertainty analysis is to quantify the uncertainty of the input parameters. Table 1 summarizes input parameters that are used in uncertainty analysis. Some parameters are considered to be deterministic, while the others are random. Even if all bearings do not have the same diameter due to manufacturing tolerances, it

is considered a deterministic value because its uncertainty is relatively small compared to others and its contribution to the uncertainty in fatigue failure is also small. In general, the uncertainty in the applied pressure is large. In fact, it is known that the applied load is the largest source of uncertainty. However, a deterministic value of the maximum applied pressure is used in uncertainty analysis due to the following two reasons: first, it is difficult to characterize probabilistic distribution of the applied load, and second, it will provide conservative estimate of the probability of failure.

Major uncertainties are related to the crack configuration. Based on inspection data (Cundill, 1996), a new silicon nitride ball bearing can have many micro cracks on the surface. Levesque and Arakere (2008) showed that these cracks can be modeled using half-penny-shaped cracks with a specific size, aspect ratio and orientation. Since the manufacturing process does not have any preference in the orientation of nucleated cracks and ball orientation in the assembly can vary often, it is assumed that they are uniformly distributed between  $0^\circ$  and  $180^\circ$  (see fig 7-2). For the same reason, the location of crack is also uniformly distributed on the ball surface. Based on sample measurements by (Wang, 2000), it is reported that the initial crack size can be between 200 and 350 microns. Since no probabilistic distribution information is available, it is assumed that the initial crack size is uniformly distributed between the minimum and maximum sizes.

Piotrowski and O'Brien (2006) have computed the fracture toughness value for the silicon nitride ball bearings when an applied force generates a tensile hoop stress. The fracture toughness value, computed from 16 experiments shows a uniform variation within 12% of the nominal value. Thus, the uncertainty of the fatigue threshold is

modeled using a uniform distribution with the nominal value of 2.8 MPa $\sqrt{m}$  and is in the suggested range of 2-4 MPa $\sqrt{m}$  (Wang, 2000).

### **7.3.2 Surrogate Modeling – Uncertainty Propagation**

In the uncertainty propagation stage, the input uncertainties are propagated through the governing physics of the system to yield uncertainty in output, which is the effective stress intensity factor. Traditionally, Monte Carlo simulation (MCS) is often employed for this purpose where many samples of input random variables are generated according to their distribution types and samples of output variable are produced by solving the governing equation with each set of input variables. This stage is computationally intensive because it involves 3D finite element modeling and volume integrals. For example, for given values of input parameters, the computation of effective stress intensity factor takes about 144,000 sec in desktop computer with 2 processors. In order to identify the effect of input uncertainty on the output uncertainty numerous repetitions of this calculation are required, which can quickly become impractical. Thus, the key issue in uncertainty analysis is how to effectively propagate the input uncertainty to the output uncertainty.

There are many methods available in uncertainty propagation that use approximation. First-order reliability method (FORM) (Allen and Camberos, 2009), second-order reliability method (SORM) (Allen and Camberos, 2009), importance sampling method (Cano et al., 1996), and MCS are a short list of available methods. Except for MCS, all other methods use approximation in either output variable itself or its distribution type, which inevitably involves error especially when the governing system equation is complex. Herein, surrogate modeling techniques (FAC Viana, 2009) are utilized to approximate the relation between input parameters and output. Instead of

black-box type surrogate model, physics-based surrogate modeling is employed to represent the relationship more effectively. Once the surrogate model is obtained, uncertainty in output variable can easily be calculated using MCS because the computational cost of function evaluation using the surrogate model is negligible.

It is observed that the effective stress intensity factor for cracks on ball bearings can be characterized with four parameters: applied contact pressure, lateral position of crack with respect to contact patch, orientation of crack with respect to contact path, and initial crack size. Thus, the uncertainty propagation can be written in a general form of:

$$K_{eq} = f(p_0, x_D, \phi, a) \quad (7-6)$$

where  $p_0$  is the applied pressure at the center of contact patch,  $x_D$  is the normalized lateral position between the center of contact patch and the center of crack,  $\theta$  is the angle between a line perpendicular to the contact path and the orientation of crack, and  $a$  is the length of surface crack. Although the explicit expression of function  $f$  is unknown (or, sometimes it is an implicit function), it can be evaluated for given input parameters using finite element analysis and volume integrals.

The idea of surrogate modeling is to approximate the function  $f$  using a simple analytical function (Queipo et al., 2005). The general procedure of surrogate modeling is to generate several samples, called design of experiment, and to fit a function using these samples. First, a number of samples are chosen based on different criteria, such as full factorial design or Latin hypercube sampling. The larger the sample size, the better the quality of approximation. However, each sample means expensive finite element analysis. In order to have a reasonable accuracy, the number of samples for

the case of four variables will be around 100. The number of required samples exponentially increases as the number of input variables increases. Once all samples are available, they are used to fit a function. In general, the functional form is fixed with unknown coefficients, which are to be found by minimizing the error between the function and samples.

In general, surrogate modeling does not require detailed knowledge on the physical problem; it can be considered as a black-box. Herein, however, the surrogate model is simplified by observing the physical behavior of the system, in which the effective stress intensity factor can be expressed as a function of the four parameters in the following form:

$$K_{eq} = \frac{P_0}{2700 \text{ MPa}} \times f_1(x_D) \times \frac{f_2(\phi)}{2.5} \times \sqrt{\frac{a}{250}} \quad (7-7)$$

First, the stress intensity factor,  $K_{eq}$ , is proportional to the contact pressure because the material response is linear elastic and stress increases linearly with the applied load. In addition,  $K_{eq}$  is proportional to the square root of crack size, which is basically identical to the traditional definition of stress intensity factor. Since these two relations are simple and explicit, there is no need to introduce approximation using surrogate modeling. On the other hand the effects of lateral position and orientation are not straightforward, and thus, require approximation as in Eq. (7-7). An important point in the above equation is that the effects of these two parameters are decoupled. This can be easily explained that if two cracks are located in different lateral positions, the failure mechanism will still be the same except that the magnitude of contact periphery stress will be different In the above equation. It is assumed that the aspect ratio of the

semi-elliptical crack, the cracks angle to the surface and that the elliptical contact patch aspect ratio remain constant.

After simplifying the relationship between input variables and output, the initial surrogate model with four variables can now be simplified to two surrogate models with a single variable, which is much more computationally efficient to build and more accurate. To simulate the variation in SIFs due to orientation, seven equally-spaced simulations are generated for the orientation angle and five for the lateral position within their ranges and are interpolated between for computational accuracy.

The next step is to choose a surrogate model. The difficulty is that there is no single surrogate that outperforms all others. Depending on functional behavior, one surrogate performs better than the others. In general, however, the functional behavior is unknown a priori. One of the best practices is to build multiple surrogates using the sampled data and choose the best one. It is generally accepted that cross-validation (Myers and Montgomery, 2002) is a good tool to choose the best surrogate. This procedure is relatively inexpensive under the assumption that obtaining a sample requires expensive finite element analysis, but surrogate modeling can be finished without requiring intensive computation. In this chapter, four different surrogates are considered: Kriging, Radial Based Neural Network (RBNN), Support Vector Regression (SVR), and fourth-order polynomial response surface (PRS). Different surrogates have different characteristics. For example, the Kriging always pass the sampled data points, while PRS does not pass the data point exactly. However, that does not mean that the former is more accurate than the latter. The accuracy of a surrogate should be measured at data points that are not used in fitting the surrogate.

Figures 7-4 and 7-5 show the approximation of  $f_1(x_D)$  and  $f_2(\theta)$ , respectively, using four different surrogate models. Since all four surrogates are close to each other, it is difficult to tell which surrogate is the best. Without having additional test points, cross-validation can be used to find the best surrogate. In cross-validation, one data point is dropped in fitting the surrogate and the error is measured at the dropped data point, which is called a prediction error. If this procedure is repeated for all data points, the root mean square of prediction errors (PRESSRMS) can be used as an indicator of accuracy. PRESSRMS is a well established parameter to compare the effectiveness of surrogates. The smaller the PRESSRMS value is, the more effective the surrogate is. Table 7-1 compares the PRESSRMS values for all four surrogate models. It shows that Kriging is a good model to fit the lateral position, while PRS is good for the orientation.

### **7.3.3 Uncertainty Analysis – Monte Carlo Simulation Using Surrogate**

Once surrogate models are selected, it is used to evaluate the uncertainty of stress intensity factor according to the uncertainty in input parameters. Since function evaluation in the surrogate model is very fast, MCS can be used for that purpose. The procedure is to generate many samples of input parameters according to their distribution types and to apply them to the surrogate model to generate samples of stress intensity factors. From the data in Table 7-1, it is relatively easy to generate samples of uniformly distributed crack sizes and orientations using a random number generator. However, generating samples of lateral positions is not straightforward because they are uniformly distributed on a sphere.

The method to uniformly distribute points on a sphere is based on Archimedes theorem, which is stated as “*the axial projection of any measurable region on a sphere on the right circular cylinder circumscribed about the sphere preserves area.*” The

physics behind this theorem is explained in the Shao and Badler (1996). According to the theorem, two independent uniformly distributed random variables,  $z \sim U[-1, 1]$  and  $\theta \sim U[0, 2\pi]$  are sampled based on their distribution types. Each combination of  $(z, \theta)$  corresponds to a sample of a point on the surface of the sphere, whose coordinates are given by

$$(x, y, z) = \left( \sqrt{1-z^2} \cos \theta, \sqrt{1-z^2} \sin \theta, z \right) \quad (7-8)$$

This method uniformly distributes points on the surface of a unit radius sphere. The normalized lateral position  $x_D$  in Eq. (7-8) is equivalent to  $x$  in Eq. (7-6) if the coordinate system is set such that the center line of contact patch is on the  $yz$ -plane. For given dimensions of ball bearing in Table 1, the crack will be located within the contact patch if

$$|x_D| \leq \frac{b'}{d} \quad (7-9)$$

During MCS, a crack is located randomly on the surface of the ball bearing, whose lateral position is calculated from Eq. 7-8. If the crack lies within the contact patch according to Eq. 7-9, the effective stress intensity factor is calculated using Eq. 7-7.

The objective is to calculate the probability of fatigue failure of the silicon nitride ball bearing under input uncertainties described in Table 7-1. Here, the failure mode is defined when the effective stress intensity factor is larger than the fatigue threshold. For that purpose, a limit state function is first defined as

$$g = K_{eq} - K_{th} \quad (7-10)$$

and the probability of failure is defined by

$$P_F = \text{Prob}(g > 0) \quad (7-11)$$

In MCS, the probability of failure is calculated by counting the number of samples that are failed. When the total number of random samples is  $N$ , the probability of failure can be calculated by

$$P_F = \frac{1}{N} \sum_{j=1}^N I_j(g) = \frac{N_F}{N} \quad (7-12)$$

where  $I_j$  is an index function whose value is one when the argument is positive and zero otherwise, and  $N_F$  is the number of failed samples. Due to the random nature of MCS, different sets of samples yield different values of probability of failure; exact  $P_F$  can only be calculated when the number of samples is infinity. The standard deviation of the probability of failure can be estimated using

$$\sigma_{PF} = \sqrt{\frac{P_F(1-P_F)}{N}} \quad (7-13)$$

Note that the standard deviation is inversely proportional to the number of samples.

Table 7-2 shows the results of uncertainty analysis using MCS and surrogate modeling. In order to see the effect of samples, two different sets of samples are used: one with  $10^5$  and the other with  $10^6$  samples. Samples of the uncertain input parameters are randomly generated according to their distributions and output samples of effective stress intensity factors are calculated using Eq. (7-7). Since the fracture toughness is also random, the samples of effective stress intensity factors are compared with that of fracture toughness to determine the number of failure cases. In the table,  $N_C$  is the number of samples in which cracks are located within the contact patch, and  $N_F$  is the number of samples that fail. It is clear that the uncertainty in the probability,  $\sigma_{PF}$ , decreases as the number of samples increases. It can be concluded that for given

uncertainties in input parameters, the chance that a ball bearing may fail is about 0.5%. In practice, the failure probability will be lower because the maximum applied load is used.

Figure 7-6 shows the plot of cumulative distribution function (CDF) of the limit state function  $g = K_{eq} - K_{th}$  for the case of  $10^5$  samples. In order to emphasize the failure probability,  $1 - \text{CDF}$  is plotted in log-scale. The ordinate value at  $g = 0$  is the value of failure probability. The discontinuity in the slope near  $g = -2.5$  is due to the fact that those cracks lying outside the contact patch do not fail and, hence, do not contribute the stress intensity factor calculation. As can be observed in the plot, the slope of the CDF curve near  $g = 0$  is high, which means that the failure probability can be improved significantly by slightly increasing shifting the limit state function. This can be achieved in various ways, such as using a material with higher  $K_{th}$  or reducing initial crack size that can reduce  $K_{eq}$ .

#### 7.3.4 Parameter Study

Even if the accuracy of the failure probability depends on uncertainty quantification of input parameters, it can still provide the possibility of improving the failure probability. An important question is how much the failure probability can be improved by modifying the input uncertainty. For example, the initial distribution of crack size was uniform between 200 and 350 microns. If the manufacturing technology is improved such that the largest initial crack size is reduced by 10%, then it would be beneficial to estimate how much the probability of failure can be improved. In practice, it is not feasible to change the lateral position and the orientation of cracks as they are random by nature. However, the initial crack size and the fracture toughness can be modified by using different manufacturing technology or different materials.

Table 7-3 compares the probability of failure when the initial distribution of crack size is reduced from  $U[200, 350]$  (original) to  $U[200, 335]$  (improved). Both cases use the same number of samples,  $10^6$ . Note that reducing uncertainty in initial crack size by 10% improves the probability of failure by 20%. A similar trend can be observed when the fracture toughness is increased from  $U[2.464, 3.136]$  to  $U[2.531, 3.360]$ . The effect of this improvement on the probability of failure is tabulated in Table 7-4, in which the probability of failure is improved by 20%. It is noted that improvements on either the distribution of crack size or the distribution of fracture toughness has similar effect on the probability of failure. Table 7-5 shows the combined improvements when both the initial crack size and the fracture toughness are improved. It turns out that the probability of failure can be improved by 44% due to this change.

Figure 7-6 plots the variation of the probability of failure with the percentage reduction of crack size. It is noted that a higher reduction in the crack size leads to lower probability of failure. For a 40% reduction in crack size, original material's probability of failure could improve by 71%, while for a tougher material, the improvement in probability of failure is about 77%.

In order to isolate the effects of location and orientation of crack, the probability of failure is computed for a deterministic crack size. Figure 7-7 plots the variation of the probability of survival as a function of the crack size. Low crack sizes have a very high probability of survival. As the crack size increases, the probability of survival decreases and the decrease is less for a tougher material.

Piotrowski and O'Brien (2006) has computed the fracture toughness for silicon nitride ball bearings when the applied force produces hoop stress. Assuming a very

tough material that its fracture toughness values conform to the range Piotrowski and O'Brien (2006) mentioned at  $\pm 12\%$  uniform variation about  $4.5 \text{ MPa} \sqrt{m}$ , an attempt is made to find the variation of probability of survival as a function of crack size.

Figure 7-8 plots that variation. Tougher material allows the presence of higher crack lengths. Figures 7-6, 7-7 and 7-8 could be used in good conjunction to optimize the combination of material and NDE techniques' cost with the safety of the ball bearings.

#### **7.4 Conclusions**

This represents the first uncertainty analysis of probability of survival of ceramic rolling elements involving a statistical investigation on ball survival rates dependent on fatigue threshold, crack size, and crack orientation in a rolling contact fatigue system.

The main conclusions of the work are as follows:

- Finite element models were used to calculate stress intensity factors for surface cracks under rolling contact fatigue.
- An empirical equation was developed for a mixed-mode fracture parameter to account for the variation in crack position, load magnitude, and crack size.
- Statistical techniques have been developed to determine the probability of ball failure under service conditions.
- As the crack size increases, the number of possible orientations for failure increases gradually.
- Decreases in the upper bound of allowable crack sizes has a similar effect as increasing the fatigue threshold of the material.
- For high fatigue thresholds, the possibility of ball failure is low but increases steadily for larger crack sizes.

## 7.5 Figures

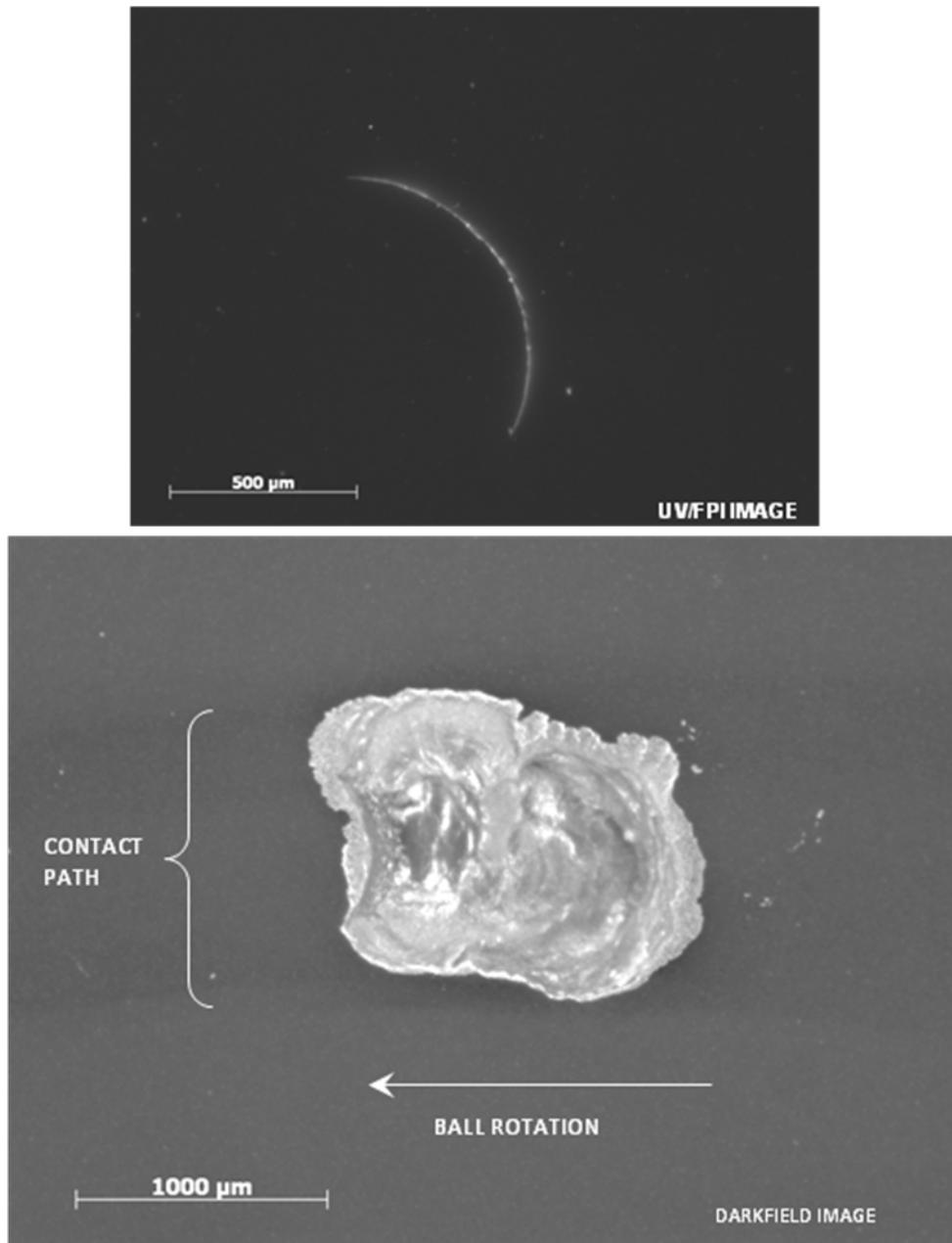


Figure 7-1. Before and after of a partial cone crack placed under rolling contact fatigue [Image courtesy of The Timken Company].

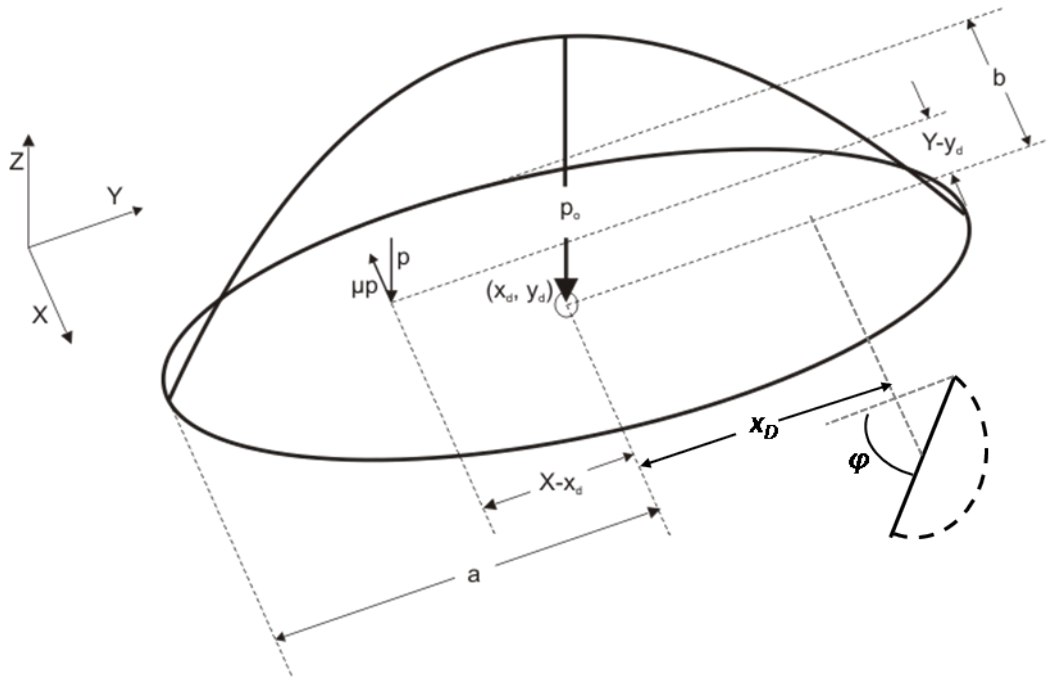


Figure 7-2. Elliptical Hertzian contact load coordinate system and variables for elliptical load orientation simulation.

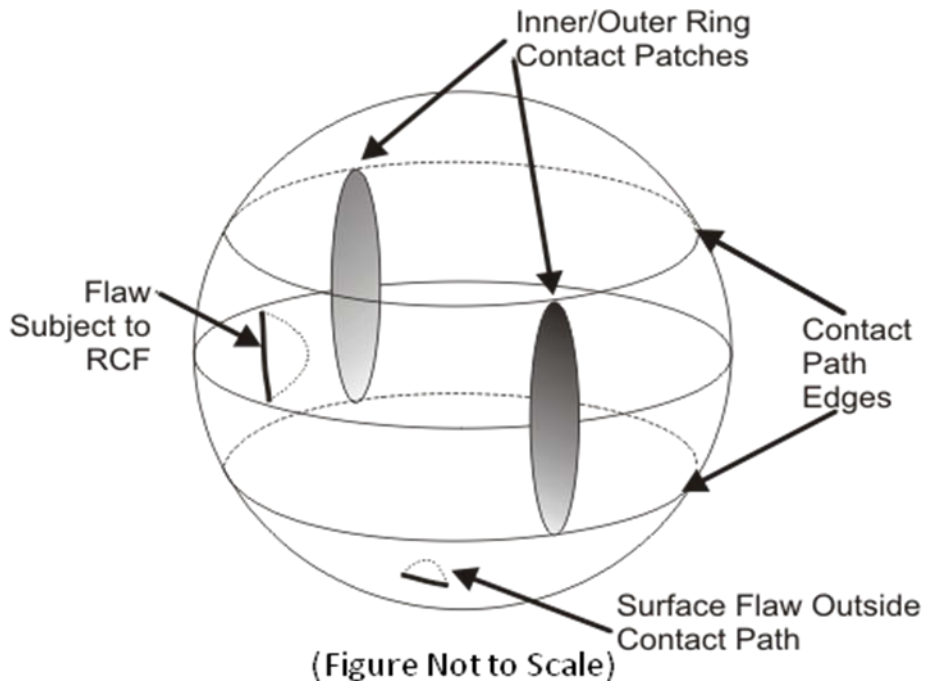


Figure 7-3. The elliptic contact patches on the ball surface and the band which they remain in. Cracks inside and very close to this region (assuming a fixed contact angle and attitude of ball rotation) will experience RCF.

Table 7-1. Input parameters and their distributions for uncertainty analysis

Parameter	Type	Value (or distribution)
Diameter of ball, $d$	Deterministic	25 mm
Width of contact patch, $b'$	Deterministic	8 mm
Pressure, $p_0$	Deterministic	2.7 GPa
Friction coefficient, $\mu$	Deterministic	0.07
Fracture toughness, $K_{th}$	Random	$U[2.464, 3.136]$ MPa $\sqrt{m}$
Crack length, $a$	Random	$U[200, 350]$ $\mu m$
Crack orientation, $\phi$	Random	$U[0^\circ, 180^\circ]$
Crack position, $x_D$	Random	Uniformly distributed on the sphere

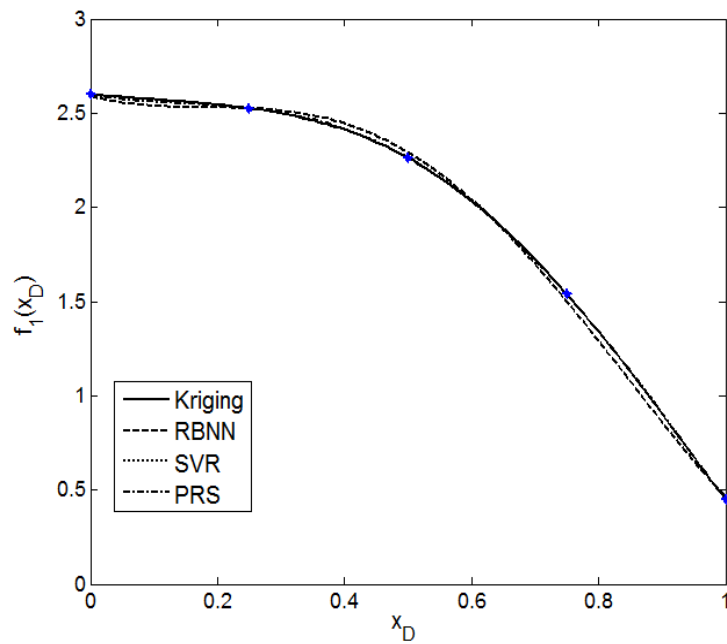


Figure 7-4. Surrogate models for the contribution of lateral position to the stress intensity factor

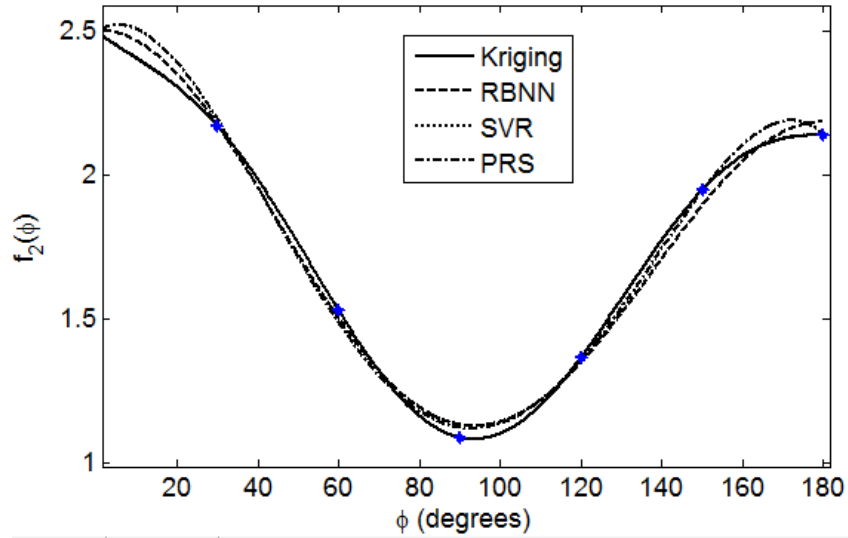


Figure 7-5. Surrogate models for the contribution of crack orientation to the stress intensity factor

Table 7-2. Cross validation errors (PRESSRMS) for different surrogate models

Model	PRESSRMS	
	Lateral position	Angular position
Kriging	0.1187	0.3921
RBNN	0.2597	0.1895
SVR	0.6224	0.4388
PRS	0.2308	0.1658

Table 7-3. Probability of failure values for different sample sizes

$N$	$N_C$	$N_F$	$P_F$	$\sigma_{PF}$
100,000	67,816	557	5.57E-03	2.35E-04
1,000,000	679,338	5,990	6.00E-03	7.71E-05

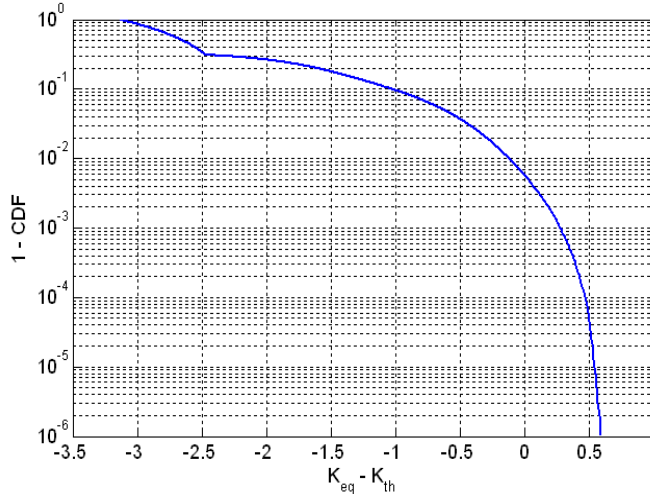


Figure 7-6. Cumulative distribution function of the limit state function  $g = K_{eq} - K_{th}$

Table 7-4. Effects of improvements pertaining to crack size on probability of failure

Case	$N_F$	$P_F$	$\sigma_{PF}$
Original	5,990	6.00E-03	7.71E-05
Improved	4,548	4.50E-03	6.73E-05

Table 7-5. Effects of improvements pertaining to fracture toughness on probability of failure

Case	$N_F$	$P_F$	$\sigma_{PF}$
Original	5,990	6.00E-03	7.71E-05
Improved	3,391	3.40E-03	5.81E-05

Table 7-6. Effects of combined improvements pertaining to crack size and fracture toughness on probability of failure

Case	$N_F$	$P_F$	$\sigma_{PF}$
Original	5,990	6.00E-03	7.71E-05
Improved	2,492	2.50E-03	4.98E-05

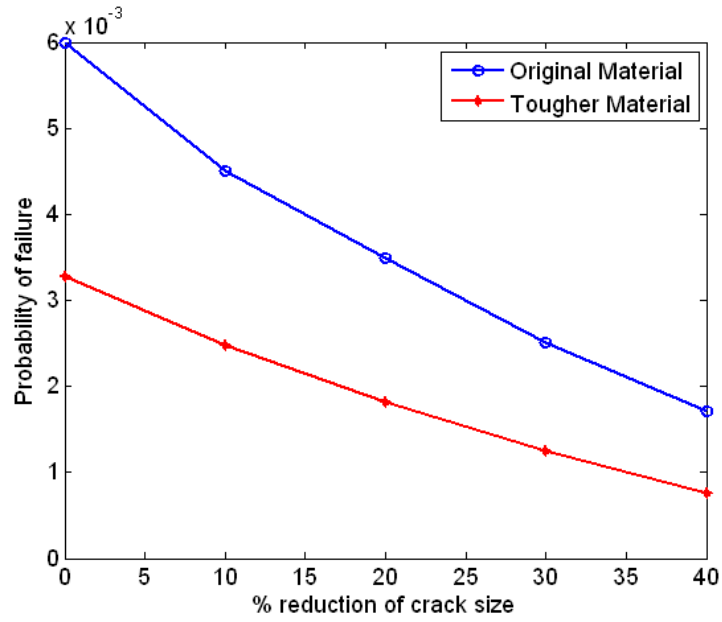


Figure 7-7 Variation of probability of failure with percentage reduction of crack size.

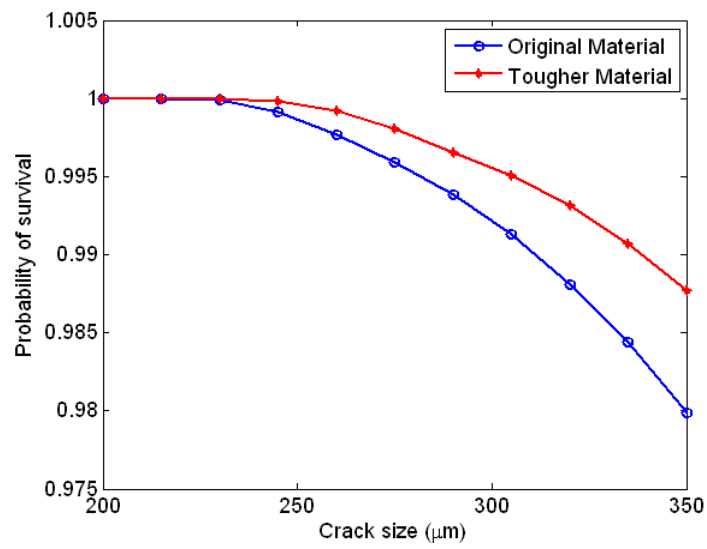


Figure 7-8. Variation of probability of survival with crack size.

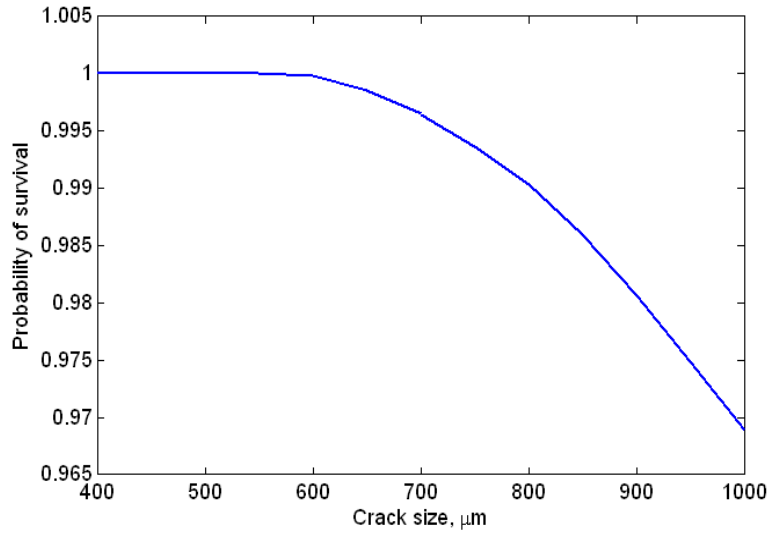


Figure 7-9. Variation of probability of survival with crack size for a  $K_{th}$  of  $4.5 \pm 0.54$  MPavm.

## CHAPTER 8 DISCUSSION AND CONCLUSIONS

### 8.1 Discussion

The fatigue damage process in ceramic rolling elements is very different from metal balls. Silicon nitride balls, used in hybrid ball bearings, are susceptible to failure from fatigue spalls emanating from pre-existing *c*-cracks that can grow under RCF. In contrast, RCF in metal bearings is manifested as a flaking off of metallic particles from the surface of raceways and/or rolling elements. This process commences as a *subsurface* initiated crack *below* the surface and propagates to the surface, eventually forming a pit or *spall* (Sadeghi et al., 2009). Bearing raceway fatigue life estimation models are still mostly based on the seminal probabilistic life model by Lundberg and Palmgren (LP) proposed in 1945, and includes Hertzian subsurface stress computations and empirical material variables obtained from extensive experimental testing.

Metals are weaker in shear than tension. In contrast to metallic materials,  $\text{Si}_3\text{N}_4$  material is weaker in tension than compression or shear. The LP methods cannot account for this difference in material behavior. Furthermore, failure in ceramic hybrid bearings is a consequence of pre-existing *c*-cracks on the ball surface growing to a spall. Fatigue life estimation for ceramic balls therefore requires a fracture mechanics approach that evaluates the *critical flaw* size in balls, since failure typically occurs when the effective SIF at the crack tip equals the mixed-mode fracture toughness of the silicon nitride ball material. This approach is largely deterministic and radically different from the empirical lifing approaches used for metal bearing raceways and elements.

This thesis presents a comprehensive numerical and experimental life prediction methodology for ceramic balls subject to RCF using fracture mechanics principles. This

approach breaks new ground in the lifing of ceramic elements subject to RCF. The results are of immediate interest to the hybrid ball bearing and aerospace industry because of applications to military, commercial and space propulsion systems. The procedures and results generated have both scientific and technological relevance.

Contributions that are of scientific and intrinsic interest to fracture and contact mechanics are described below:

1. 3D nonplanar geometry of surface cracks nucleating from the tensile stress field at the contact patch periphery, during collision of ceramic balls, was determined from a stress-state analysis and iterative crack growth via FEA. The stress-state analysis utilized a closed-form subsurface stress field of contacting spheres with friction to compute the 3D “trajectory” of the max principle stress plot to generate the crack front.
2. First derivation of tensile stress field at the circular contact periphery including friction.
3. Determination of effective fracture toughness, under mixed-mode loading conditions with  $K_I$ ,  $K_{II}$  and  $K_{III}$  active, for silicon nitride.
4. Computation of mixed-mode SIFs for 3D nonplanar surface cracks subject to RCF.
5. Establishing the importance of surface traction towards dramatically increasing crack driving force during RCF.
6. Derivation of the tensile stress field at the elliptical contact periphery and recognizing that it controls the maximum SIF during RCF. Furthermore, the maximum SIF experienced by a crack due to an elliptic rolling contact is that generated by a circular contact enclosed by the ellipse, with the same max Hertz stress.
7. Computation of the critical flaw size, as a function of contact stress, traction condition and material fracture properties.

Contributions that are of engineering and industrial interest for the design of ceramic rolling elements are described below:

1. Derivation of minimum collision velocity required to initiate a surface crack between identical brittle spheres. Inclusion of friction at the contact decreases the velocity required to initiate a surface crack.
2. Development of a technique that can be used to predict the shape of any surface flaw from a known contact interaction. The cone and partial cone crack shapes

simulated are reminiscent of the range of surface crack geometries observed in manufactured silicon nitride balls.

3. Rendering and meshing of nonaxisymmetric nonplanar 3D surface cracks in FEA and analysis of the part subject to Hertzian rolling contact. Parametric studies were made possible by user created code to automate the creation of input files, loading and boundary conditions, and the post processing of the displaced states. Appendix B serves as an educational tool for future modelers.
4. Simulating the growth of 3D cracks via iterative remeshing methods in FEA.
5. Development of accurate curve fits for computing SIFs for surface flaws subject to rolling contact.
6. Development of probabilistic analysis to determine the survivability of the ball subject to a range of RCF conditions.
7. Integration of results from numerical and experimental investigations into a design methodology for silicon nitride (ceramic) balls subject to RCF.

## 8.2 Conclusions

The range of presented analyses combined in this document results in a complete treatment of surface flaws in brittle materials subject to RCF. From the determination of flaw shape from nucleation, to the effects of rolling contact fatigue it sees in service, to examining if failure is imminent, the possible analyses on flaw shapes under rolling contact fatigue is treated. The main contributions of this work are developed analysis tools for crack shape determination, the analysis of fatigue test experiments for measuring a  $K_{th}$ , and transferring the effect of each parameter on SIFs to the engineers who will design hybrid bearings to tolerate their service applications

## 8.3 Future Work

There remain a few issues that would improve this field. Firstly, the establishment of a  $K_{th}$  and  $K_c$  for all materials under a range of mixed mode behavior is requisite. As previously discussed, many have tried and the result is a myriad of empirical equations that are often material and experiment specific. Secondly, an

examination of the failure process of the crack as it grows to spallation is necessary as it has been visited by Wang (2000) and Kida (2002) but have lead to some disagreement as to the roles of wear between the crack faces and the affect of the lubricant, as well as, how the crack turns branches and eventually spalls to failure. Furthermore, reliable, nondestructive detection of surface flaws in a non-conducting opaque material for flaw morphology (including crack depth) has yet to found and could find immediate application if automated to find and categorize flaws.

## APPENDIX A THE NORMAL INDENTATION OF BRITTLE SPHERES

In chapter 1, it became clear that the crack nucleates and grows from the point in the trailing contact periphery of the oblique interaction, as that is where stress is at a maximum. With this knowledge, the contact of spheres can be reflected upon to develop predictive equations concerning crack nucleation.

There have been a few studies that have normally loaded silicon nitride spheres until cracking was detected by acoustic emission (Ichikawa et al., 1995a, Ichikawa et al., 1995b, and Ohgushi et al., 1996). Interestingly, they have found a range of the maximum Hertz contact pressure to induce cracking to be in the range of 14-18 GPa. With this number, it can be approximated that the velocity to impart collisions for normal interactions. It is noted that the maximum principal stress from a normal spherical contact on the surface contact periphery is

$$\sigma_{\max} = \sigma_{rr} = \frac{1-2\nu}{3} p_o \quad (\text{A-1})$$

Which, for a Poisson's ratio of 0.28, the normal contact equation yields,

$$p_o \approx 6.8\sigma_{\max} \quad (\text{A-2})$$

By substituting 16 GPa as the max pressure (the median of those pressures that have been observed to cause cracking) a maximum periphery stress of 2.3 GPa is calculated. To find the normal velocity to induce this stress (without the influence of traction) take:

$$p_o^* = \frac{3}{2\pi} \left( \frac{4E^*}{3R^{\frac{3}{2}}} \right)^{\frac{4}{5}} \left( \frac{5mV_z^2}{4} \right)^{\frac{1}{5}} \quad (\text{A-3})$$

(Johnson, 1987) and substitute eqn. A-2 for  $p_o$  to get:

$$V_z = \frac{51\sqrt{5}}{50} \frac{\sigma_c^{\frac{5}{2}} R^{\frac{3}{2}} m^{\frac{1}{2}}}{E^{*2}} \quad (\text{A-4})$$

Substituting, for a normal collision of silicon nitride bodies with a density of 2,600 kg/m<sup>3</sup> and radius of 6.35 mm (half-inch diameter), a velocity of only 16 cm/s is obtained, which would need to be verified by experiment. It is not surprising then that surface cracks are generated during low velocity collisions generated during the ball lapping operation. The impact velocity required to cause subsurface yielding during collision between a hard steel ball and a medium hard steel ball with an yield strength of 1 GPa is 14 cm/sec (Johnson, 1987), and for balls made of brittle material exhibiting minimal yielding such as Si<sub>3</sub>N<sub>4</sub> the impact energy is absorbed in the fracture surface generation.

It is also noted that the maximum periphery stress may be derived for sliding friction as well for use in maximum contact periphery stress criteria. First, the limits of the stress equations are taken as z and y approach 0 and x approaches 1 and then use the resulting components in the stress matrix to find the equation that represents the maximum root of the eigenvalue problem. The result is

$$\sigma_1(1,0,0) = \sigma_{\max|f} = p_o \left[ \frac{1-2\nu}{3} + \mu \frac{\pi}{2} \left( 1 + \frac{\nu}{4} \right) \right] \quad (\text{A-5})$$

which is expectedly a function of the contact pressure, the Poisson's ratio, and the friction coefficient. Comparing Eq. (A-6) with Eq. (A-2) it is noted that the  $p_o$  required to induce cracking is reduced with a nonzero friction coefficient.

Another approximation can be made from these results concerning crack nucleation. Taking the periphery stress to initiate cracking, 2.3 GPa, and the fracture

toughness of 6 MPa√m, (Piotrowski and O'Brien, 2006) we can calculate, using

$K = \sigma\sqrt{\pi a}$ , an initial flaw size of 0.21 μm (roughly 2/5th of the grain size) from which these larger cracks could nucleate.

How the radius of the ball affects the radius of crack can also be derived in a similar manner. For example, contact patch radius is

$$a_c = \left( \frac{3PR}{4E^*} \right)^{\frac{1}{3}} \quad (\text{A-6})$$

Rewriting

$$P = \frac{4E^* a_c^3}{3R} \quad (\text{A-7})$$

And the max pressure is

$$p_o = \left( \frac{3P}{2\pi a_c^2} \right) \rightarrow_{\text{substituting}} p_o = \frac{2E^* a_c}{\pi R} \quad (\text{A-8})$$

For cone cracking to start at the periphery

$$\sigma_{\max} = \frac{1-2\nu}{3} p_o \rightarrow p_o = 6.8\sigma_{\max} \quad (\text{A-9})$$

Substituting this and rearranging

$$a_c = \frac{13.6\pi R\sigma_{\max}}{E^*} \quad (\text{A-10})$$

So if the contact patch size is roughly the same as the crack radius than it scales linearly with ball radius ( $R$ ) assuming that the two interacting balls have the same radius.

NOTE:  $P$ =total load and  $E^* \equiv \left( \frac{1-\nu_1^2}{E_1} + \frac{1-\nu_2^2}{E_2} \right)^{-1}$  and  $R \equiv \left( \frac{1}{R_1} + \frac{1}{R_2} \right)^{-1}$

Before determining the critical flaw size, the size of the cracks can be discussed practically. As discussed above, the fracture toughness of Si<sub>3</sub>N<sub>4</sub> is low (about 6 MPa/m) (Piotrowski and O'Brien), and the resultant velocity to induce cone cracking of normally colliding balls is low. The velocity to induce cracking,  $V_z$ , has been derived (Levesque and Arakere) for normal ball collisions as:

$$V_z = \frac{51\sqrt{5}}{50} \frac{\pi \sigma_c^{\frac{5}{2}} R^{\frac{3}{2}} m^{\frac{1}{2}}}{E^{*2}} \quad (\text{A-4})$$

and determines that 16 cm/sec is a sufficient velocity to crack normally interacting 6.38mm (0.5 in) diameter balls. Substituting for the ball mass,  $m = \rho V = \rho \left( \frac{4}{3} \pi R^3 \right)$ , in Eq.

(A-4) yields:

$$V_z = \frac{51}{25} \sqrt{\frac{5}{3}} \frac{\pi^{\frac{1}{2}} \rho^{\frac{1}{2}} \sigma_c^{\frac{5}{2}} R^3}{E^{*2}} \quad (\text{A-11})$$

Equation (A-11) shows that the velocity to induce cracking is proportional to  $R^3$ .

The effect that the radius of the ball has on the size of the crack can also be calculated since contact patch radius is given by:

$$a_c = \left( \frac{3PR}{4E^*} \right)^{\frac{1}{3}} \rightarrow P = \frac{4E^* a_c^3}{3R} \quad (\text{A-12})$$

The max Hertzian contact pressure for a ball on ball interaction is

$$p_o = \left( \frac{3P}{2\pi a_c^2} \right) \rightarrow_{\text{substituting}} p_o = \frac{2E^* a_c}{\pi R} \quad (\text{A-13})$$

From prior work (Levesque and Arakere, 2008), cracking will occur when a maximum stress value is reached and for Hertzian contacts the max stress value in the

half-space is located just outside the contact region. For cone cracking to start at the periphery, the value of the maximum principal stress that must be exceeded is determined by eqn. A-3:

$$\sigma_{\max} = \frac{1-2\nu}{3} p_o \rightarrow p_o = 6.8\sigma_{\max} \quad (\text{A-3})$$

Substituting (A-13) and rearranging

$$a_c = \frac{3.4\pi R\sigma_{\max}}{E^*} \quad (\text{A-15})$$

Therefore, the contact patch size, and therefore the crack radius, scales linearly with ball radius ( $R$ ), assuming that the two interacting balls have the same radius.

## APPENDIX B BUILDING A C-CRACK MODEL

### First a note about scale

The following model was created in um. This is so the smallest elements (once meshed) are above ABAQUS' criteria to avoid flagging an error. The material properties are scaled to conform to this unit system.

### A crack discussion

Multiple geometries can be modeled currently with the exception of self-intersecting flaws and flaws that approach a surface at an angle.

First Create Part – C-crack

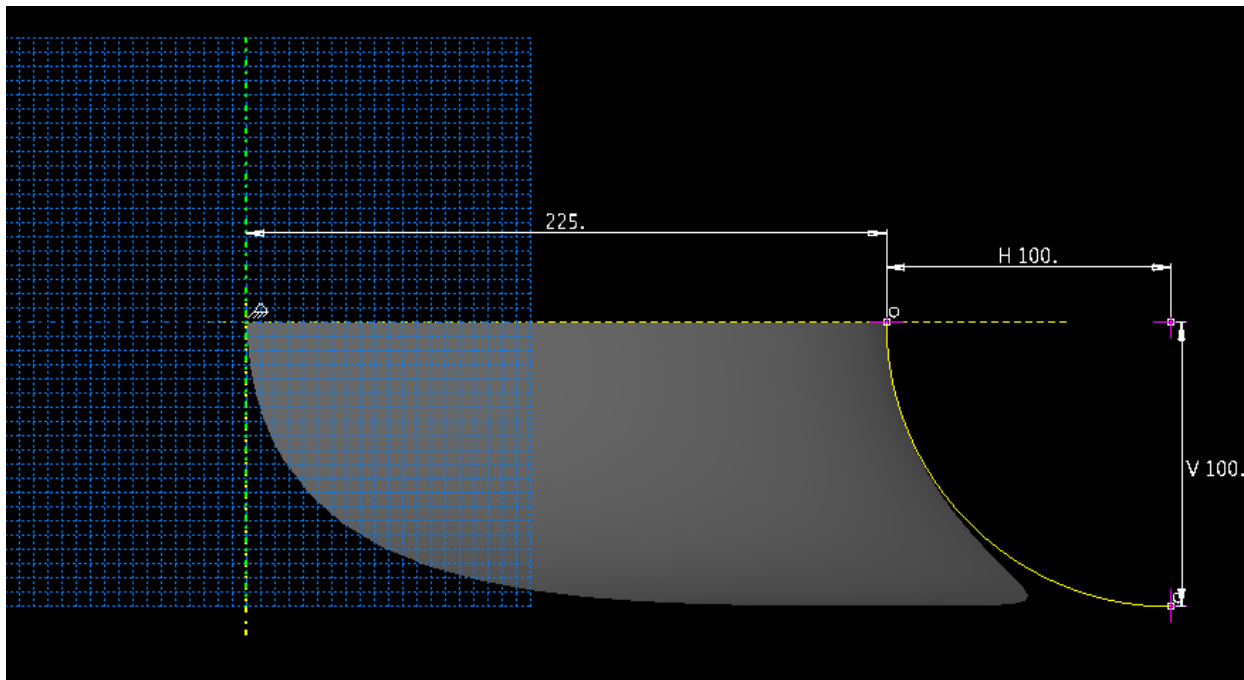


Figure B-1. Sketch module for creating a revolved part.

Revolved Shape – Create datum plane for next step

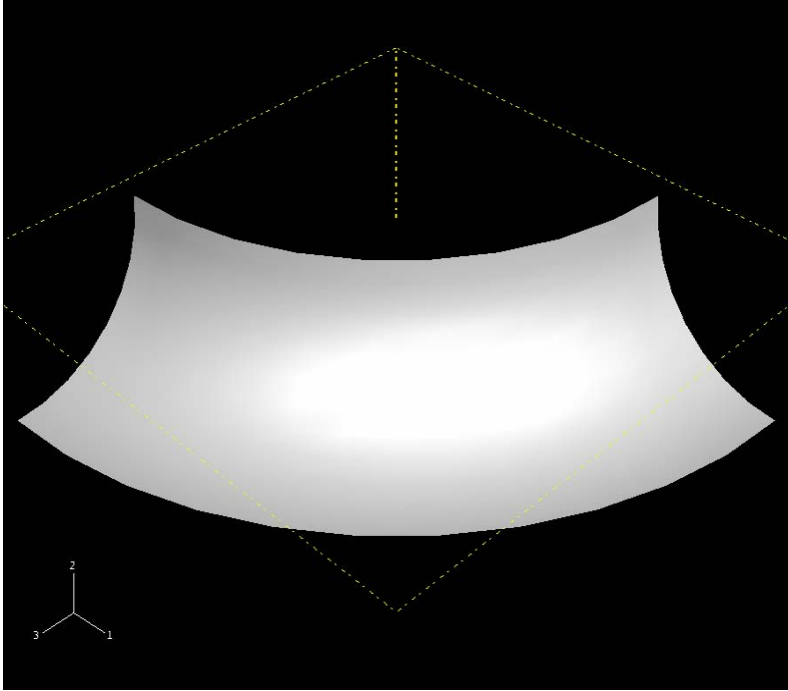


Figure B-2. Created revolved part.

Cut from top to limit extension

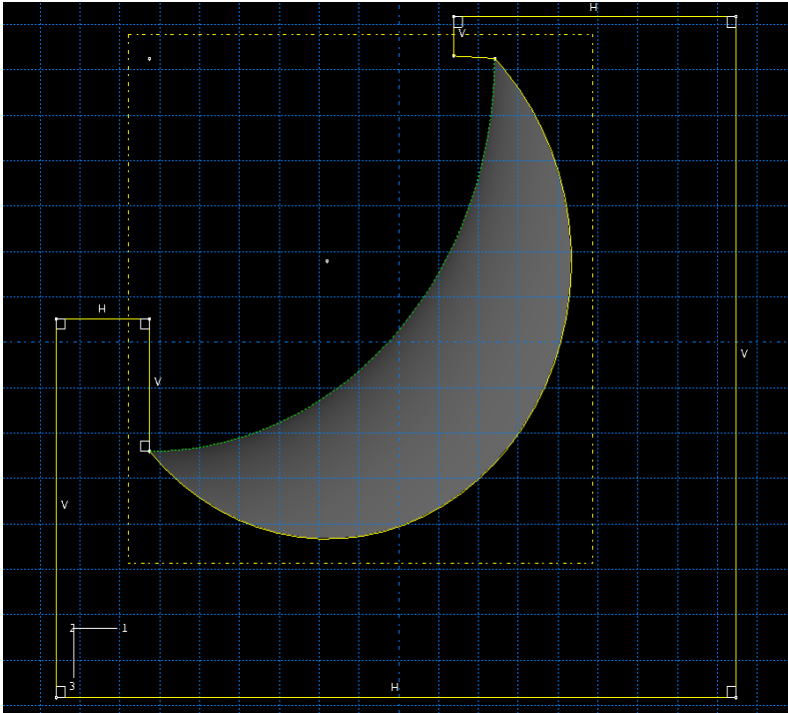


Figure B-3. Cutting the part from above

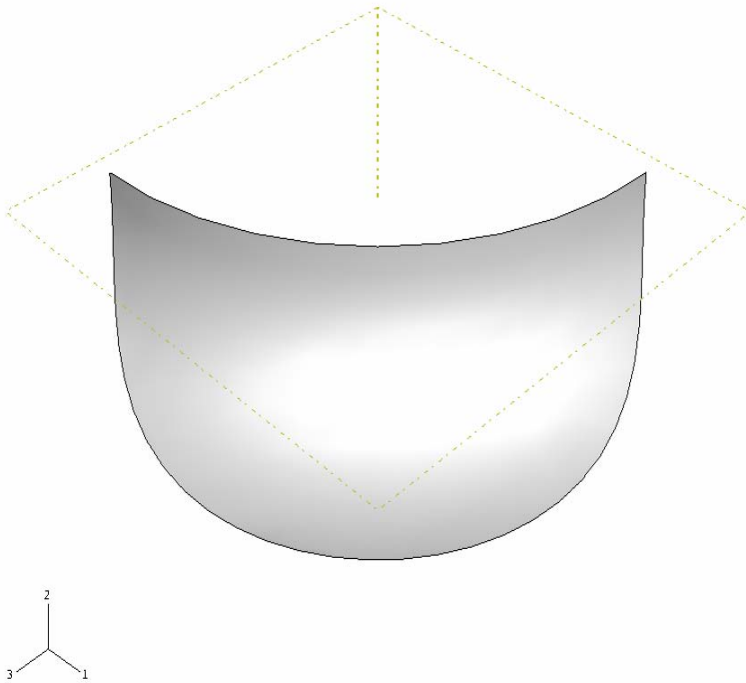


Figure B-4. The final crack shape.

### **Building Gen III crack**

Use experimentally obtained cross-section image and import via View>>>Image/Movie Options. Then trace with spline tool (in proper location for radius on face) and proceed as for Gen I.

### **Create a block to be cracked**

A block of dimensions about  $4a * 8a * 5a$  will be cut by crack. Retain edges. Note: cut the block with the crack.

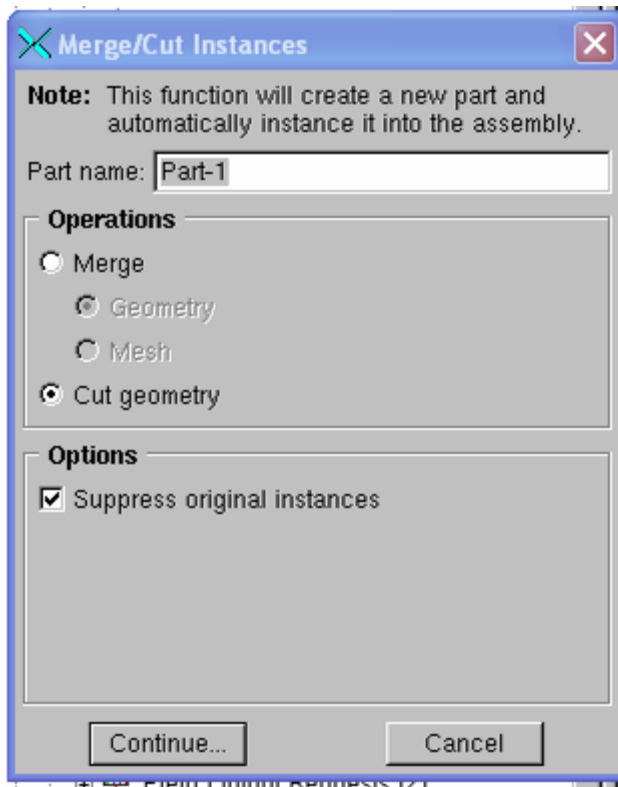


Figure. B-5. Merge/cut instances window.

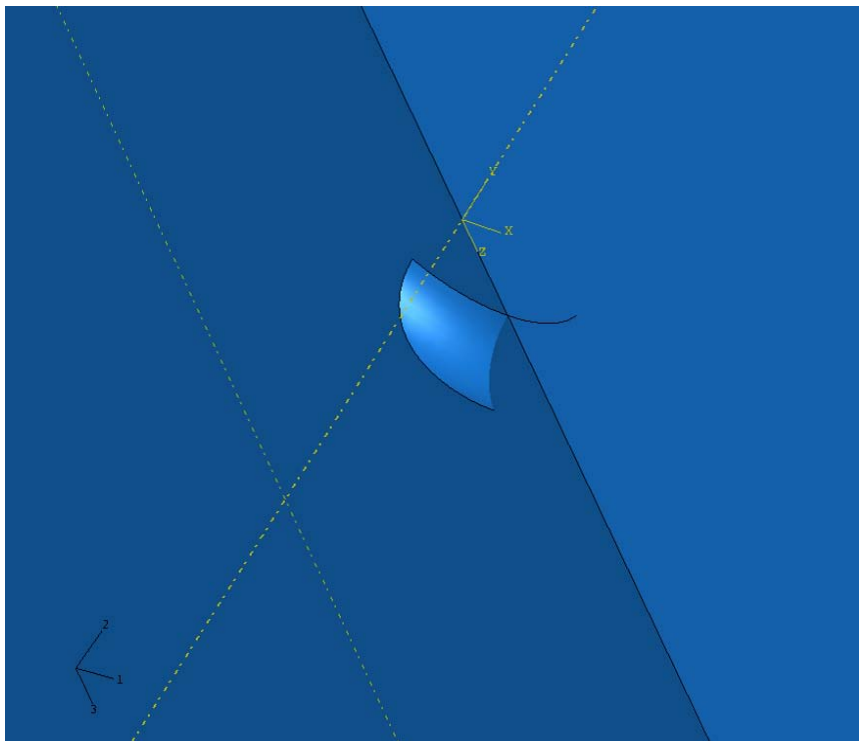


Figure B-6. Merging a crack with a block in the Assembly module.

### **Half symmetry constructed first**

It should be noted that the images presented are of a half-symmetry model. However, the creation of a full symmetry model is done ONLY by creating two half-symmetry models and merging them (as the partitioning is not robust enough to perform on a full symmetry model right-away).

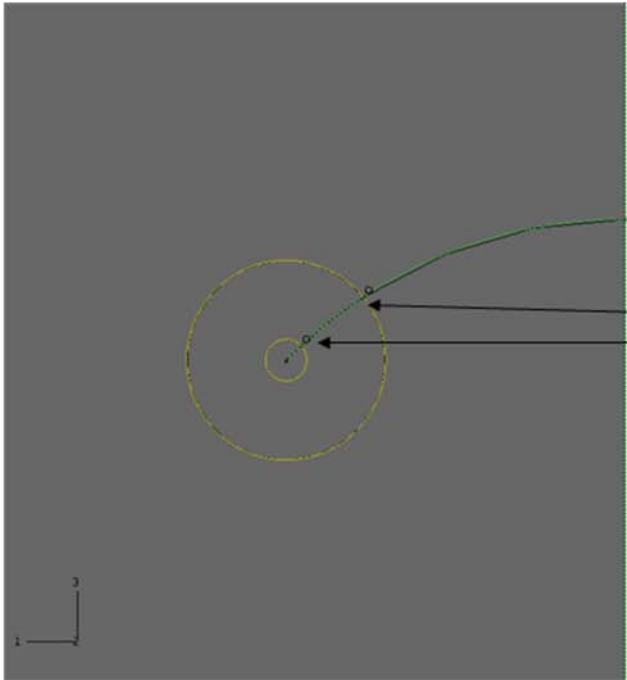
### **Partition time**

Now partition the model so that it may be feasibly meshed in the future. Swept Hex elements are needed in the contour region so these cells need to have six sides and no more than 90 degrees of a circle.

These partitions are done ON THE PART since this part will be used to create another part and these partitions are to be maintained.

### **Inner and outer circles**

The correct dimensions of these circles were found through trial and error. In general, the tube can be about  $.3a$  of the crack and the inner tube a fourth or less of that but do not try to be so small that meshing within this tube will not run.



Note that there are two circles created. They have a center at the crack tip and a point defining their radius ON THE CRACK.

Figure B-7. Partitioning the surface.

### Partition the cell

Sweep these circles along the crack tip to create tubular cells.

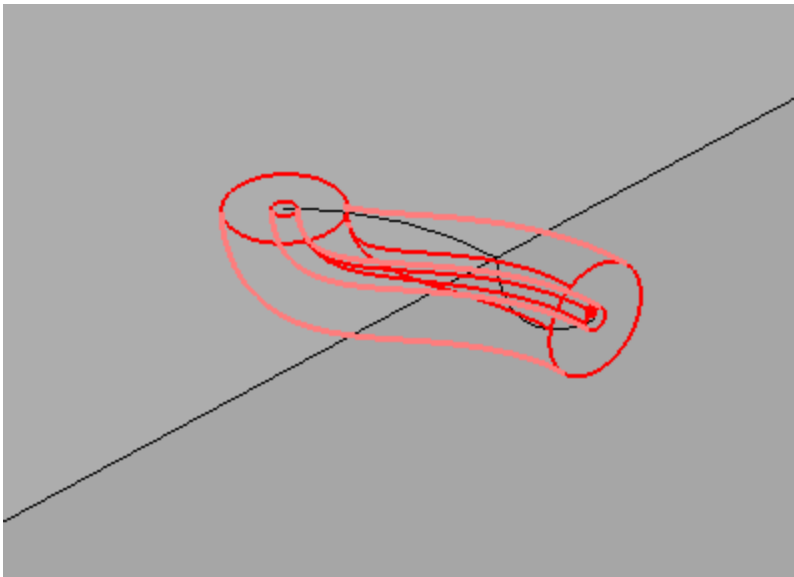


Figure B-8. Sweeping to partition the cell.

### One more cell partition to go

With the proper foresight, it is known that the modeler needs to have access to the crack faces. The following partitions are for this purpose.

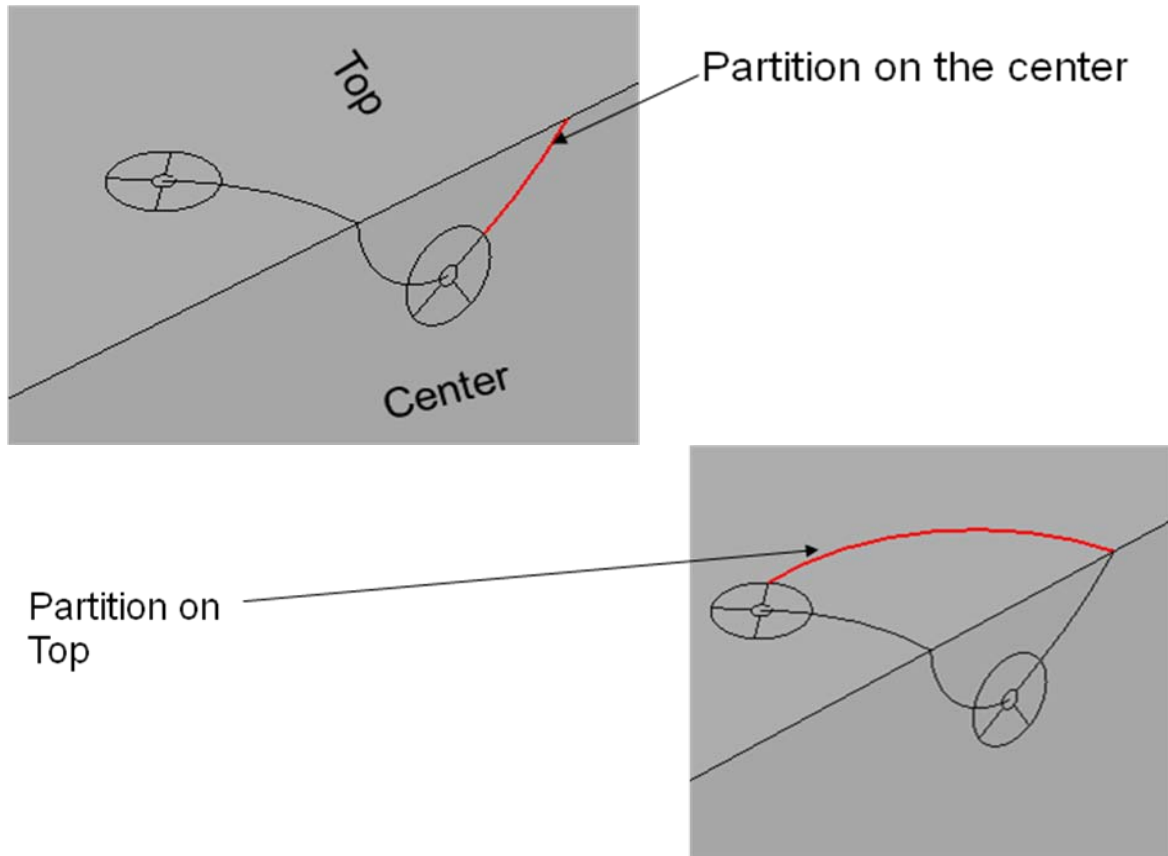


Figure B-9. Partitioning to get access to the crack face.

### **Set Declaration**

There is still quite a bit of work to do as current progress only has a geometry with no seam, crack, contact interaction, or way to get SIFs. For this manipulation, the following cells are to be sets. THESE SETS ARE CREATED ON THE PART SO THEY TRANSFER WHEN AN ORPHAN MESH IS CREATED.

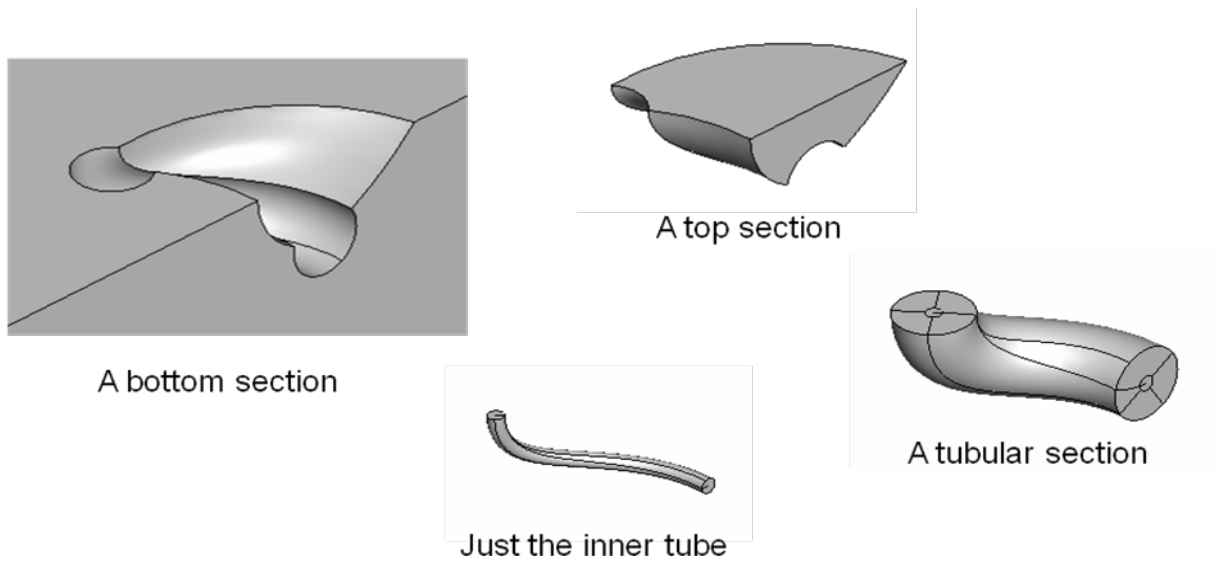


Figure B-10. Blown apart view of the different cells.

**In the interaction module, add a seam**

In order for the part to have crack faces and allow crack opening a seam must be inserted.

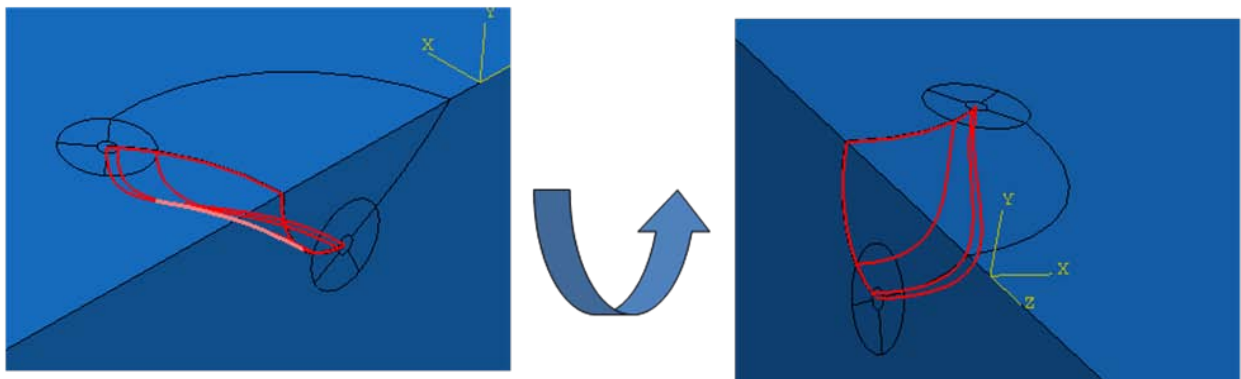


Figure B-11. Creating the crack seam.

**Define the crack**

Accurate crack tip displacements and SIFs are desired so a crack needs to be declared. This will give greater control in the mesh module.

Use the following settings: Q-vectors, .777, 0, -.63

Midside node parameter =0.25

Degenerate Element control at Crack Tip/Line: Collapsed element side, single node

This will give you the Q-vectors that will need to be changed (since the model is non-planar), collapsed, quarter-point elements.

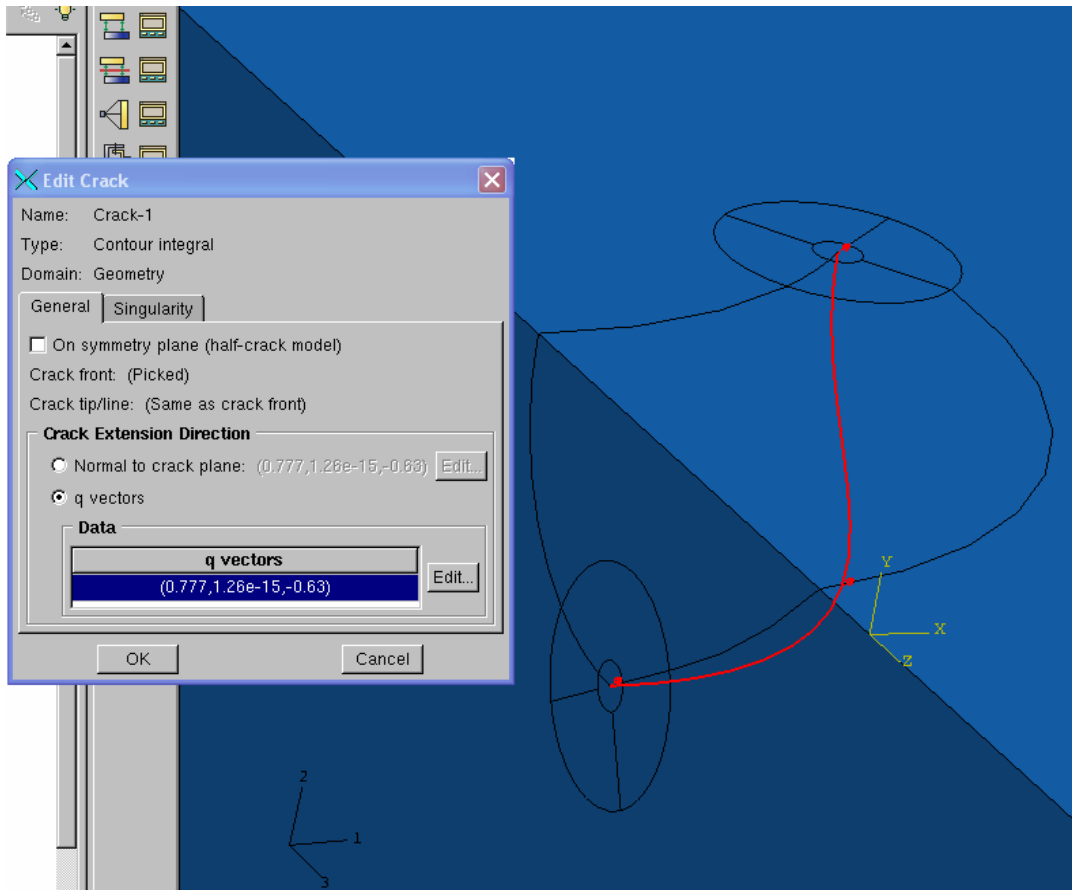


Figure B-12. Defining the crack.

## Loading and BCs

Create a User-defined load on the top surface.  
A symmetry condition if you have a half symmetry model.  
Submodel BC's on the remaining four/five faces. (More on this later).

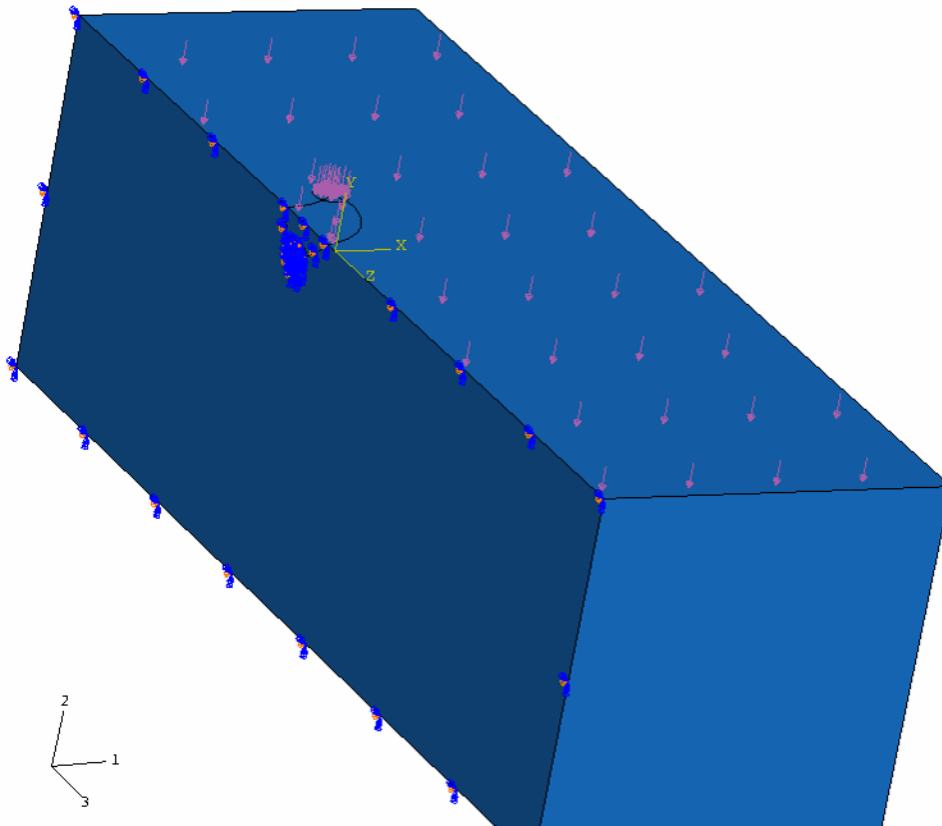


Figure B-13. Loads and boundary conditions defined on the assembly.

\*DLOAD

FORTRAN based code has been created which defines normal and traction pressures based on the global coordinate system.

$$N = P_o * \sqrt{1 - \left(\frac{x - x_{center}}{a}\right)^2 + \left(\frac{y - y_{center}}{b}\right)^2}$$

$$T = \mu N$$

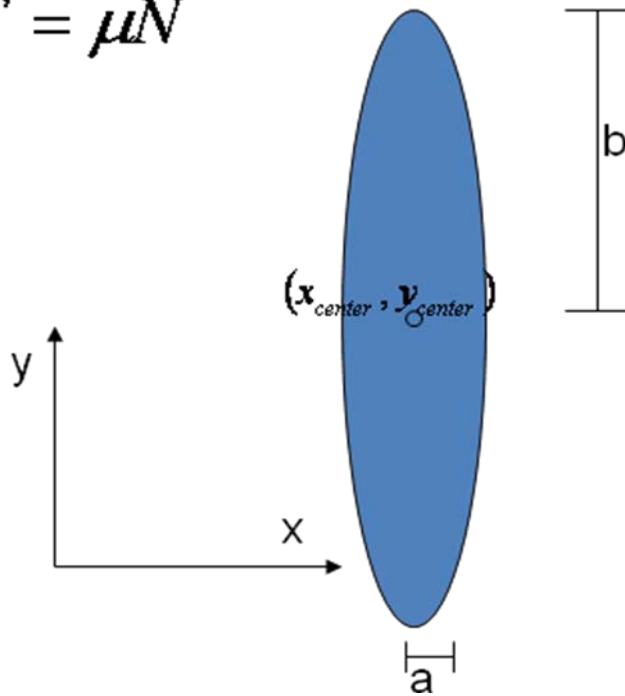


Figure B-14. Defining the user defined load.

### Meshing

#### A Short Course on How to Crash ABAQUS

Small Problem.... the brown areas, which can now be observed in the mesh module, are unmeshable. To solve this we will turn to virtual topology.

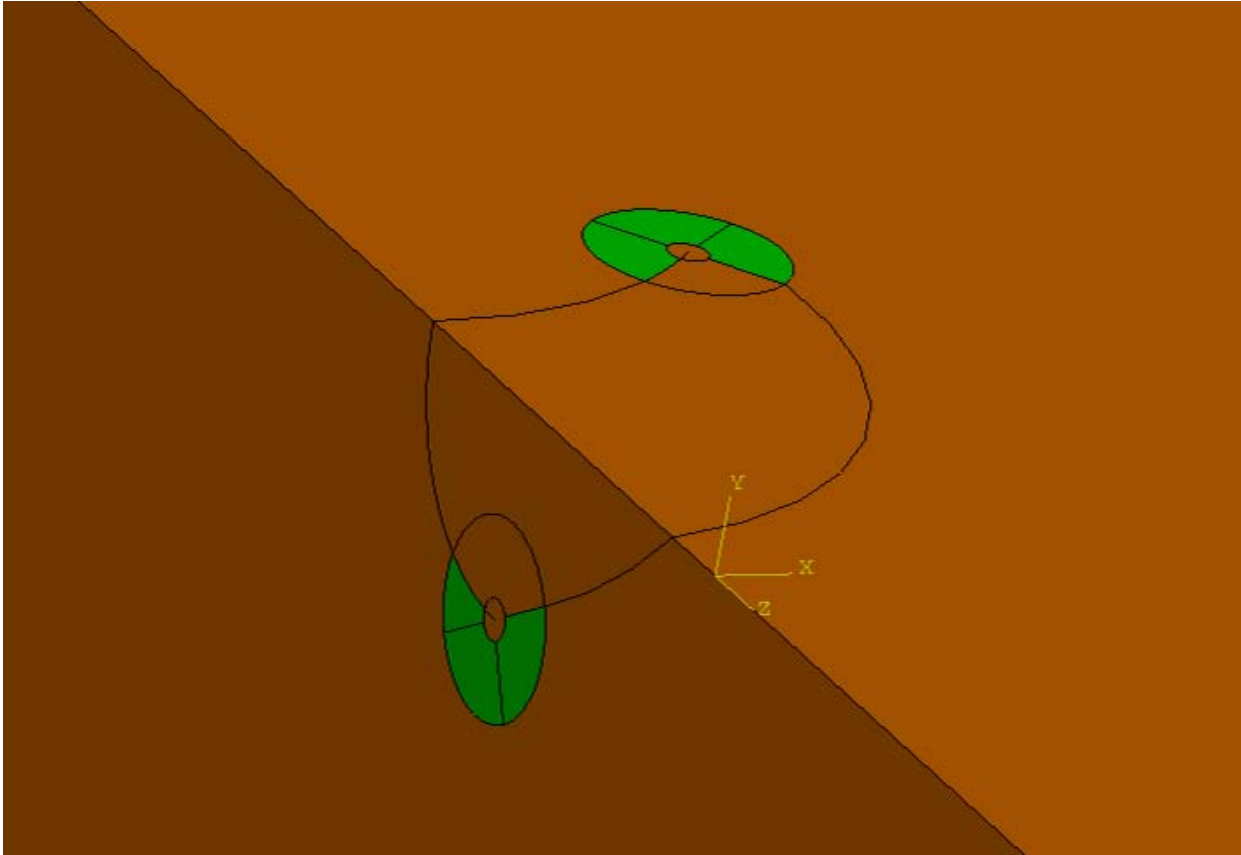


Figure B-15. The cracked part in the mesh module.

**Virtual topology**

Virtual topology is a tool that is used to merge small faces and edges so this partitioned geometry can be feasibly meshed. Basically, ABAQUS will spline a couple of surfaces together instead of having two separate surfaces. This is important since a hexahedral mesh requires (among other things) six sides in the cell.

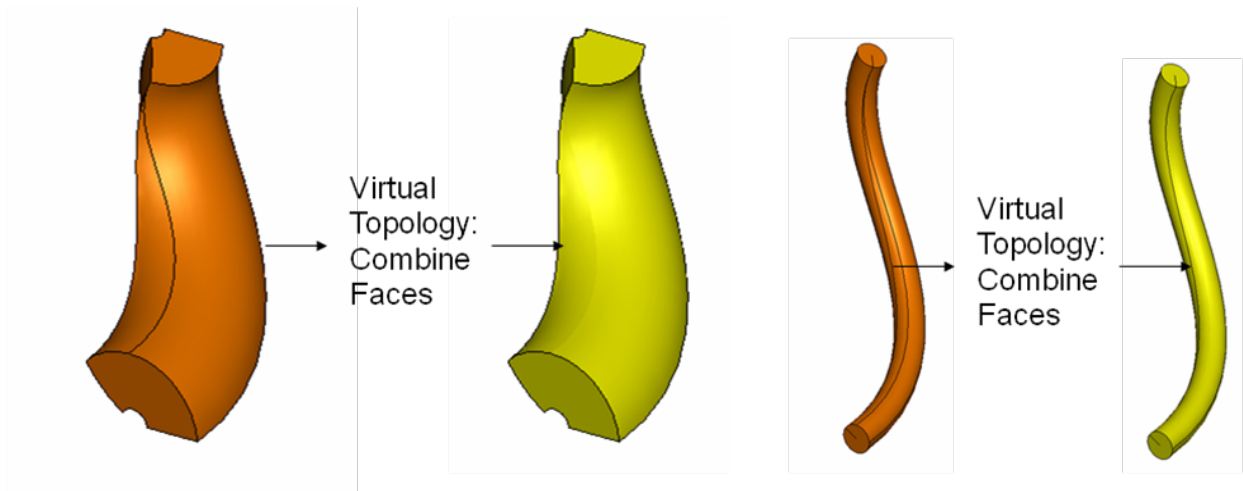


Figure B-16. Virtual topology on crack integration cells.

BETTER!!

### Reassign Element Types

Pink can be Tet meshed. This has been assigned via the “element type” selection for these (two) cells. Green can be hex structured and were easily allowed after the virtual topology was completed. Yellow will be swept wedges (though this assignment is converted by the crack definition to be collapsed quarter-point hex element).

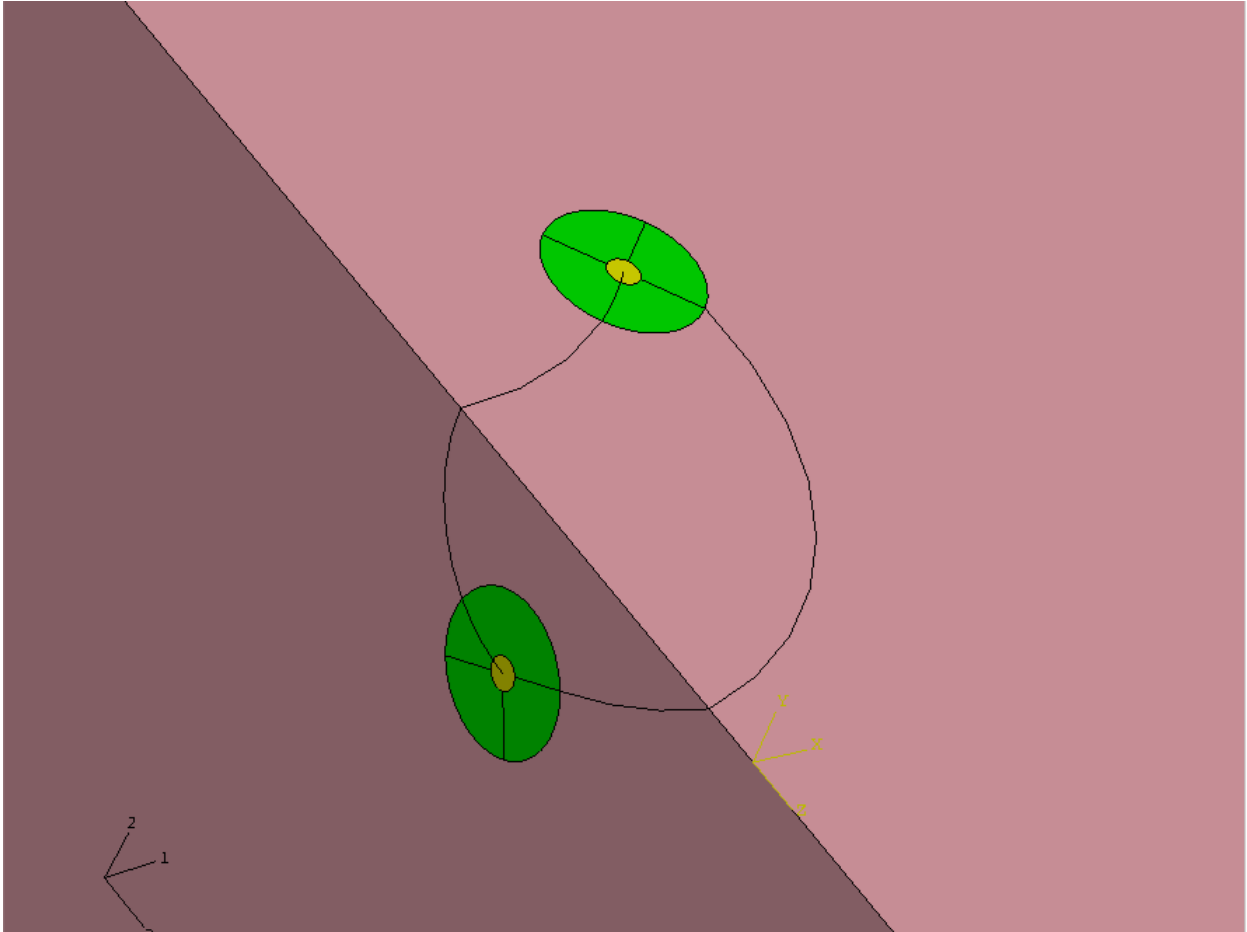


Figure B-17. Assembly after virtual topology is applied.

**Seeding the part**

Notice Biasing toward the crack, a fine mesh on the crack faces (for contact) and a given number of “element tubes” throughout the structure mesh. See B-18.

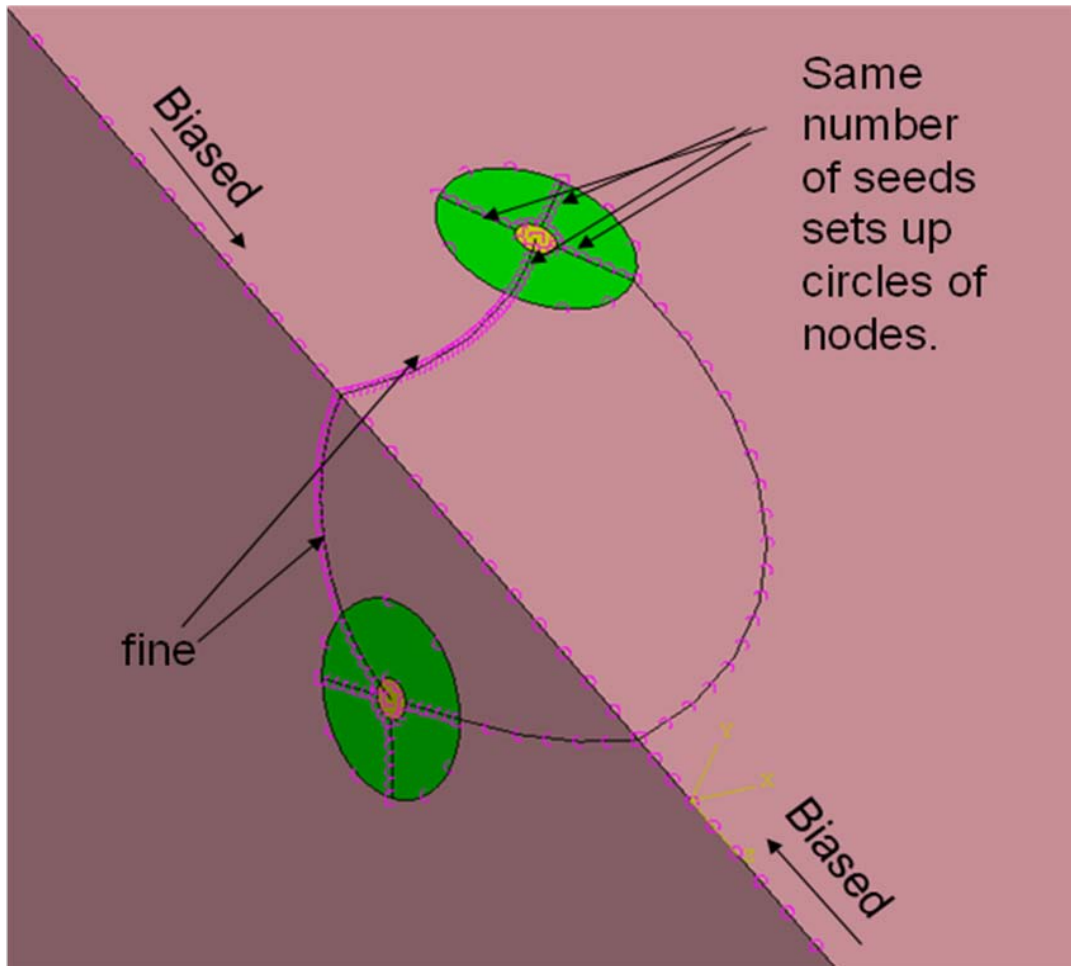


Figure B-18. Seeding the part for meshing.

### More on Seeding

Note that all lines parallel to the crack tip receive equal seeding to ensure rings of elements for contour integration. Seeding is an iterative process where the seeds must be tuned such that where two lines meet, ABAQUS may allow a reasonable number of elements. It may be better for you to fix the number of seeds in the contour integral region so that you have a specific number of contour integrals that can be taken and that the mesh on the inner most and outer most sections of the tube do not have improper aspect ratios for error in this region (remember: elements should be desirably square and anything with a .1 aspect ratio of element sides is not going to behave well).

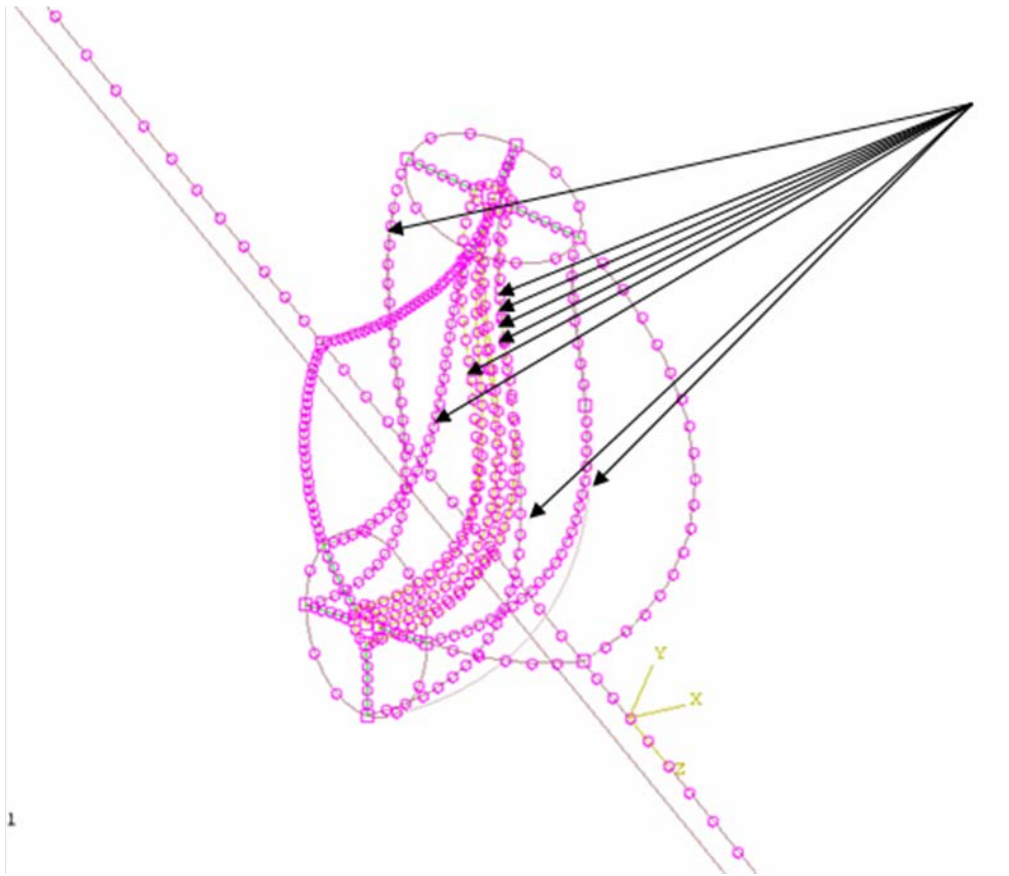


Figure B-19. All edges that exist near the crack front have the same number of seeds and nodes because this is the contour region and planes of nodes are needed.

### Mesh it

Take a break....this is almost halfway. As stated above, the seeding and meshing are currently (v. 6.7-1) an iterative process for this complex geometry and this particular geometry (because it is both complex and closed) will require much time. In terms of procedures to be completed this is around the halfway mark but in terms of effort exerted this may be where the user will spend the majority of their time.

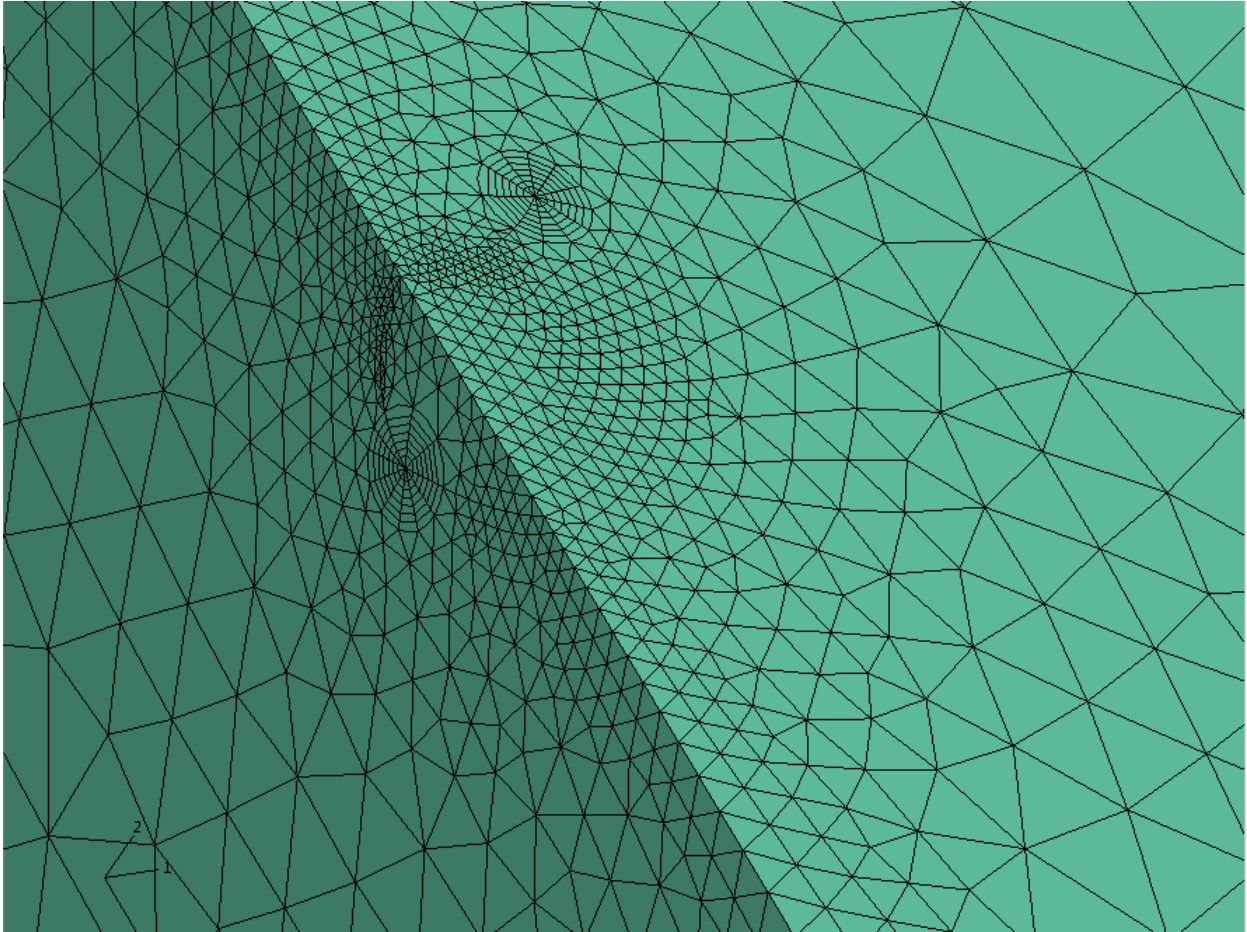


Figure B-19. Image of meshed crack.

### **Create an orphan mesh**

You need to move away from an eight sided, modifiable object to a multi-sided unmodifiable orphan mesh in order to: properly assign q-vectors, create sets for the top and bottom crack faces (individually), and properly assign contact.

Procedure:

Create a job>>Write inp then File>>Import Model>>select inp

Or in the mesh module>>create mesh part. The former method is used here.

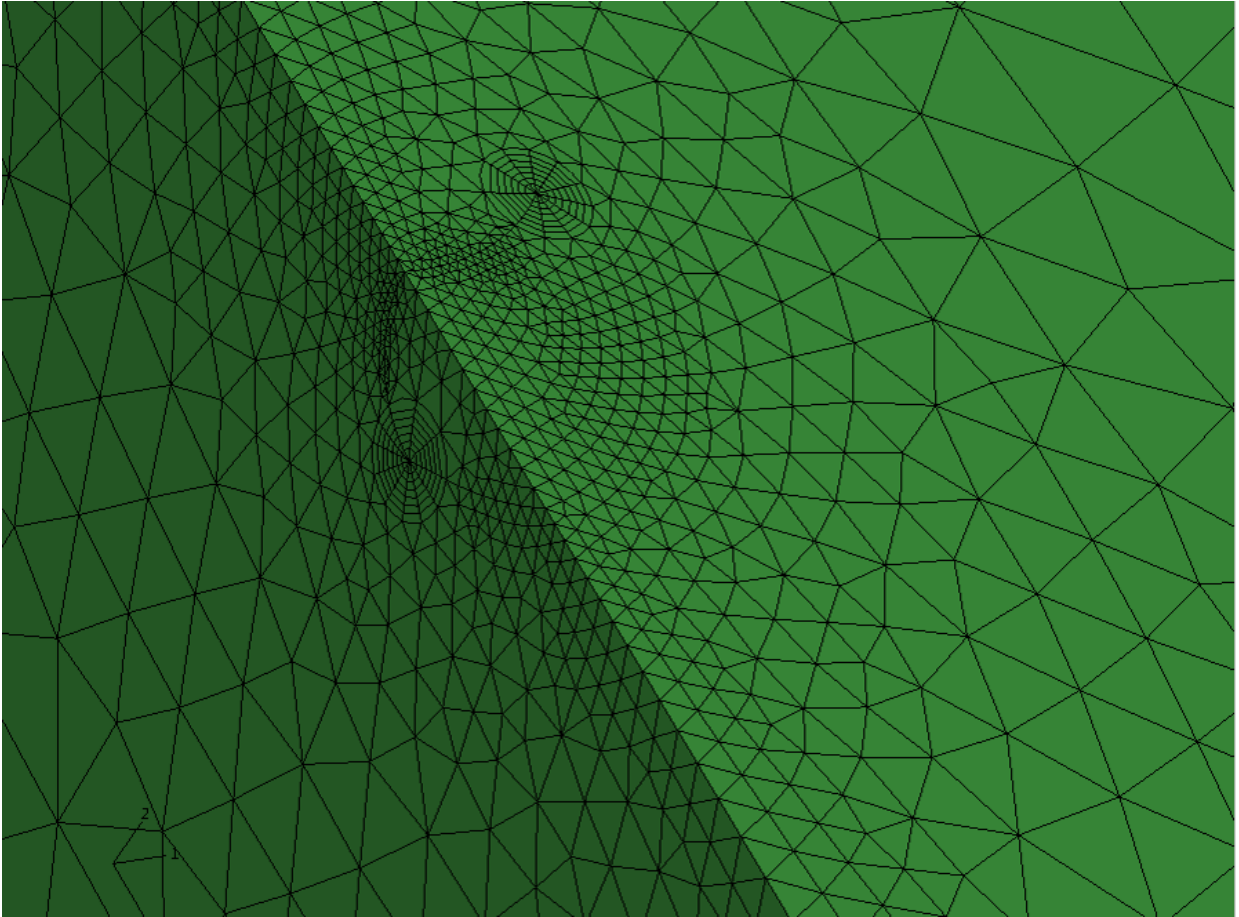


Figure B-20. Orphan mesh of crack.

### **Reassign the Q-vectors**

Each crack tip node must have an assigned q-vector for the contour integral. This can be done individually but is best repeated with the aid of a macro.

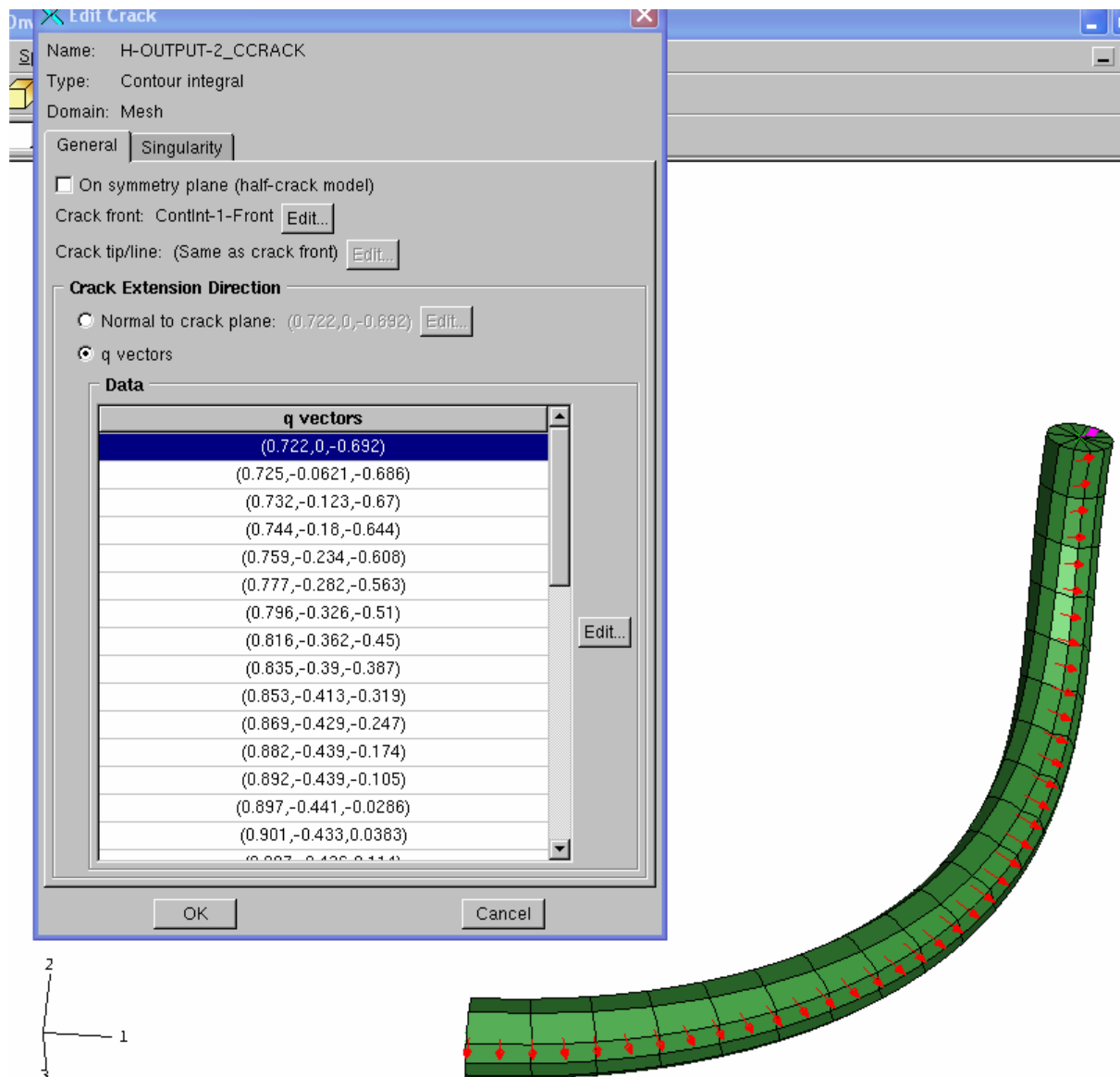


Figure B-21. Assigning the Q-vectors for each node on the crack tip.

### Assign Contact

Assigning contact in a closed geometry is difficult to begin with. In addition to this, it must be defined between crack faces, which share a line of nodes. On top of all this it must be accurate enough to be verified through a displacement matching algorithm ( $\sim 10^{-3} \mu\text{m}$ ).

### Contact Settings

Direct solver.

NLGEOM on.  
Initial step size dropped to .1  
Small Sliding.  
Direct normal contact, with frictionless sliding, and geometric properties assigned.  
Node-to-surface.

### Contact Schematic

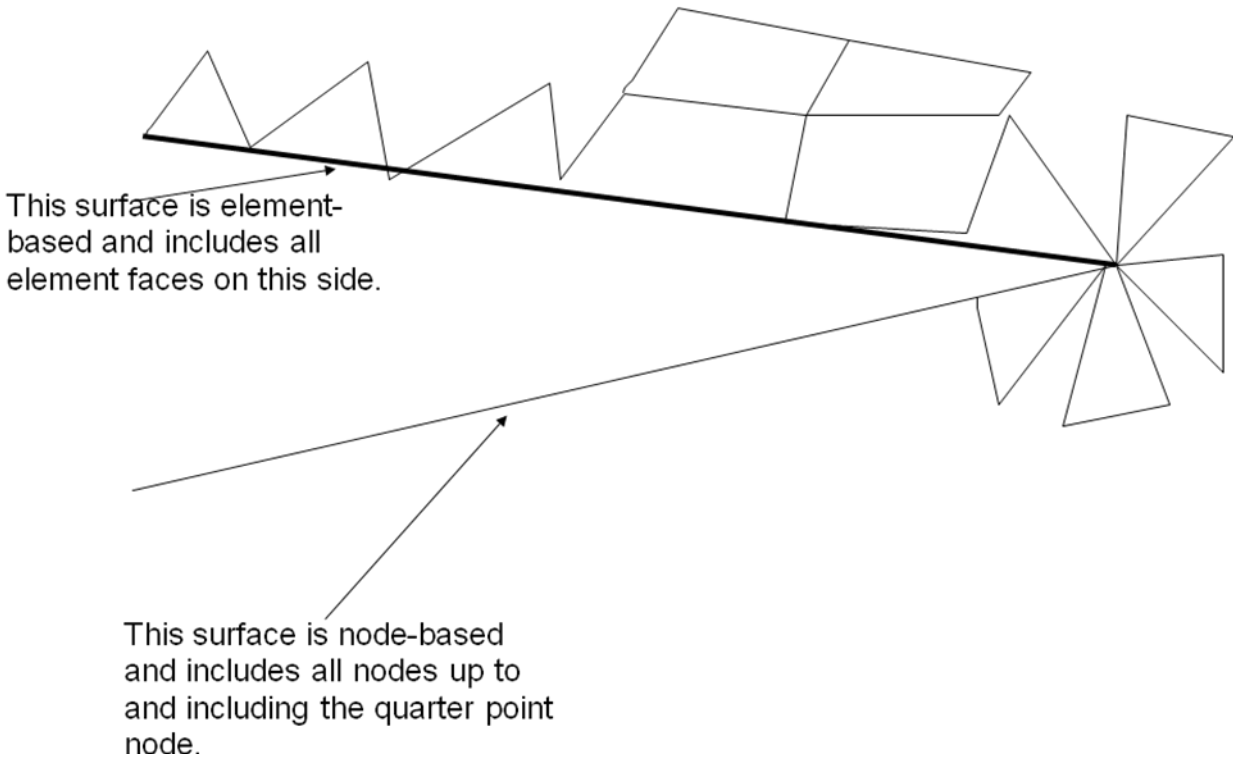


Figure B-22. Meshed crack face illustration of how crack contact is defined.

Please refer to the above figure which illustrates the only way you will successfully have the crack faces defined in contact and be accurate. (Note: self-contact will not work because of the issues related to calculating a vector normal to the surface at the crack tip and surface to surface contact will not work because the crack tip nodes will be shared among the two surfaces which results in errors upon submission.)

### Post Processing

Scripts were used to:

- Immediately plot results in Excel.

- Write all three ABAQUS SIFs to a text file with corresponding nodal distance along the crack front.
- Compute SIFs via Displacement Correlation.
- Clean up the folders.
- Please view individual scripts for details.

### Running the model

1. Write the DLOAD code for proper load orientation.
2. Submit the global model for analysis.
3. Submit the submodel for analysis. (The submodel will know to reference the global model only by the fact that it has a boundary condition stating that the surfaces in the material will have a global model and that the model's attributes, MB3 on the model>>Edit Attributes, reference the Job name where the global model is subjected to the load.) The global model should share the same coordinates in space (relative to the global coordinate system of each model) AND should have the same user subroutine referenced so that incompatibilities between the user defined load and the submodel displaced boundary condition don't try to tear apart certain elements.
4. Run the script to either generate K's (File>>Run Script) or extract the necessary data.
5. Save and close.
6. To post-process these SIFs, look for the text file in the working directory that has the same job name...these are formatted to be imported into MATLAB for other processing. (Note that the SIFs that are calculated are likely in units of  $\text{TPa}\sqrt{\text{m}}$  and need to be multiplied by 1000 to convert to  $\text{MPa}\sqrt{\text{m}}$ , which is conventional.)

**Note:** the entire procedure above could be automated for parametric study. For the desired purposes of this author, each parametric study was submitted by MATLAB through the command prompt, where pre-decided job names were decided for each run to later distinguish results. (Job names are important in automation as, not only will the global and submodels need to be able to identify each other, but the post-processing script must also access the proper submodel and generate a relevant name of the SIF output.)

## LIST OF REFERENCES

- Aliabadi, M. H. and Rooke, D. P. 1991. *Numerical Fracture Mechanics*. Southampton UK, Computational Mechanics Publications.
- Allen, M.S., Camberos, J.A., Comparison of Uncertainty Propagation / Response Surface Techniques for Two Aeroelastic Systems, *50th AIAA/ASME/ASCE/AHS/ASC Structures, Structural Dynamics and Materials Conference*, Palm Springs, CA, May 2009
- Andersson, M., 1996. Stress distribution and crack initiation for an elastic contact including friction, *International Journal of Solids Structures*, **33**, 3673-3696.
- Anstis, G.R., Chantikul, P., Lawn, B.R., Marshall, D.B., 1981. A critical evaluation of indentation techniques for measuring fracture toughness: I, direct crack mechanisms, *J. Am. Ceram. Soc.*, **64**, 533-538.
- Auerbach, F., 1891. Absolute Hardness, *Ann. Phys. Chem.*, **43**, 61-100.
- Awaji, H., Sato, S., 1978. Combined mode fracture toughness measurement by the disk test, *J of Engg Mat. And Tech.*, **100**, 175-182.
- Ayatollahi, M. R. and Aliha, M. R. M., 2005. Cracked Brazilian disc specimen subjected to mode II deformation. *Engineering Fracture Mechanics*. **72**, 493-503.
- Banks-Sills, L., Hershkovitz, I., Wawrzynek, P.A., Eliasi, R., Ingraffea, A.R., 2005. Methods for calculating stress intensity factors in anisotropic materials: Part I--z = 0 is a symmetric plane, *Eng. Fract. Mech.*, **72**, 15, 2328-2358.
- Bank-Sills, L., Travitzky, N., Ashkenazi, D., Eliasi, R., 1999. A methodology for measuring interface fracture properties of composite materials, *Int. J. of Fract.*, **99**, 3, 143-161.
- Bogdanski, S., Trajer, M., 2005, "A dimensionless multi-size finite element model of a rolling contact fatigue crack," *Wear*, **258**, 1265-1272.
- Burrier, H. I. 1996. Optimising the structure and properties of silicon nitride for rolling contact bearing performance. *Tribology Transactions*, **39**(2), 276-285.
- Cano, J.E., Hernández, L.D., Moral, S., (1996). Importance sampling algorithms for the propagation of probabilities in belief networks, *International Journal of Approximate Reasoning*, **15**, 1, 77-92.
- Carniero, F., Barcellos, A., 1953. Concrete Tensile Strength. Union of testing and research laboratories for Materials and Structures, **13**.
- Chen, S.Y., Farris, T.N., Chandrasekar, S. 1995. Contact mechanics of Hertzian cone cracking, *International Journal of Solids Structures*, **32**, 329-340.

- Chen, X.M., Jiao, G.Q., Cui, Z.Y., 1986. Application of Combined-Mode Fracture Criteria to Surface Crack Problems, *Engineering Fracture Mechanics*, **24**, 1,127-144.
- Desault Systèmes, 2007. *ABAQUS Theory Manual*, Dessault Systèmes, Providence, RI.
- Erdogan, F., Sih, G.C., 1963. Crack Extension in Plates Under Plane Loading and Transverse Shear, *J. Basic Eng. Trans. A.S.M.E., Ser. D.*, **85**, 519-527.
- Evans, A. G., 1983. *Progress in Nitrogen Ceramics*, edited by P. L. Riley, Martinus Nijhoff Publishers, The Netherlands. 595.
- FAC Viana, "SURROGATES Toolbox User's Guide," <http://fcchegury.googlepages.com>, Accessed October 20, 2009.
- Frank, F.C., Lawn, B.R., 1967. "On the theory of Hertzian Fracture," *Proc. Royal Soc. London Ser. A*, **299**, 291-306.
- Fracture Analysis Consultants, 2005. [www.fracanalysis.com](http://www.fracanalysis.com), Ithica, NY.
- Frank, F.C., Lawn, B.R., 1967. On the theory of Hertzian Fracture, *Proc. Royal Soc. London Ser. A*, **299**, 291-306.
- Freiman, S.W., Gonzalez, A.C., Mecholsky, J.J., 1979. Mixed-Mode Fracture in Soda-Lime Glass, *J. Am. Ceram. Soc.*, **62**, 3, 206-208.
- Fowell, R. J., 1995. Suggested method for determining mode I fracture toughness using Cracked Chevron Notched Brazilian Disc (CCNBD) specimens. *International Journal of Rock Mechanics and Mining Science & Geomechanics Abstracts*. **32**, 1, 57-64.
- Fujiwara, T., Yoshioka, T. Kitahara, T., Koizumi, S., Takebayashi, H. and Taka, T. 1989. Study on load rating property of silicon nitride for rolling bearing material. *Journal of JSLE International Edition*, **10**, 81-86.
- Galbato, A.T. , Cundill, R.T. , Harris, T.A., 1992. Fatigue life of silicon nitride balls, *Lubrication Engineering*, **48**, 11, 886.
- Gerstle, W. H. 1986. Finite and boundary element modeling of crack propagation in two- and three- dimensions using interactive computer graphics. *Dissertation Abstracts International Part B: Science and Engineering*. **47**, 2, 241.
- Griffith, A.A., 1920. The Phenomena of Rupture and Flow in Solids, *Philosophical Transactions, Series A*, **221**, 163-198.
- Gu, P., Nordlund, P., Asaro, R.J., Uang, C.M., 2005, "Crack face contact, frictional sliding and mesh design flexibility," *Comm. Numer. Meth. Engng.*, **21**, 209-217.

- Hamilton, G. M., Goodman, L. E., 1966. The stress field created by a circular sliding contact, *Journal of Applied Mechanics*, **33**, 371.
- Hamilton, G.M., 1983. Explicit equations for the stresses beneath a spherical sliding contact, *Proc. Inst. Mech. Eng.*, **217**, 2, 281.
- Hadfield, M. and Stolarski, T.A. 1995a. The effect of the test machine on the failure mode in lubricated rolling contact of silicon nitride. *Tribology International*, **28**(6), 377-382.
- Hadfield, M. and Stolarski, T.A. 1995b. Observations of lubricated rolling contact fatigue on silicon nitride rods. *Ceramics International*, **21**(2), 125-130.
- Hadfield, M., Stolarski, T.A., Cundhill, R.T., Horton, 1993a. Failure modes of ceramics in rolling contact, *S. Proc. Royal Soc. London Ser. A*, **443**, 607-621.
- Hadfield, M., Stolarski, T., Cundill, R.T., Horton, S., 1993b. Failure modes of ceramic elements with ring crack defects, *Tribology International*, **26**, 157-164.
- Hadfield, M., Stolarski, T.A., Cundill, R.T. and Horton, S. 1993c. Failure modes of pre-cracked ceramic elements under rolling-contact. *Wear*, **169**(1), 69-75.
- Hertz, H., 1896. *Hertz's Miscellaneous Papers*, McMillan, London.
- Hills, D.A., Nowell, D., Sackfield, A., 1992. *Mechanics of Elastic Contacts*, (Butterworth-Heinemann, Oxford), 203-208.
- Hussain, M. A., Pu, S.L., Underwood, J., 1974. Strain energy release rate for a crack under mixed mode I and II loading. *Fracture Analysis A.S.T.M. STP*, **560** 2-28.
- Ichikawa, M., Takamatsu, T., Shindou, N., Okabe, N. and Abe, Y., 1995. Ring crack initiation load of silicon nitride bearing balls, *JSME Int. J., Ser. A, Mechanical and Materials Engineering*, **38**, 2, 226-230.
- Ichikawa, M., Takamatsu, T., Matsuo, T., Okabe, N. and Abe, Y., 1995. Intra-ball and inter-ball variability of ring crack initiation load of silicon nitride bearing balls, *JSME Int. J., Ser. A, Mechanical and Materials Engineering*, **38**, 2, 231-235.
- Jahanmir, S., 1994. *Friction and wear of ceramics*, Marcel Dekker, Inc., New York, Basel, Hong Kong.
- Jayatilaka, A.S., *Fracture of Engineering Brittle Materials*, 90-107, Applied Science Publishers Ltd., 1979.
- Johnson, K.L., 1987. *Contact Mechanics*, Cambridge Press, Cambridge, 355-361.
- Khandelwal, P., Majumdar, B.S., Rosenfield, A.R., 1995. Mixed-mode high temperature toughness of silicon nitride, *J. Material Science*, **30**, 395-398.

- Klemm, H. 2002. Corrosion of silicon nitride materials in a gas turbine environment. *Journal of the European Ceramic Society*, **22**, 14-15, 2735-2740.
- Kocer, C., Collins, R. E., 1998. Angle of Hertzian cone cracks, *Journal of the American Ceramic Society*, **81**, 7, 1736-1742.
- Lawn, B.R., 1994. Indentation of ceramics with spheres: a century after Hertz, *Journal of the American Ceramic Society*, **81**, 1977-1794.
- Lawn, B., Fracture of Brittle Solids. Cambridge University Press, Cambridge, UK (1993).
- Lawn, B.R., 1967, Partial cone crack formation in a brittle material loaded with a sliding spherical indenter, *Proceedings of the Royal Society*, **299**, 307.
- Levesque, G., Arakere N.K., 2008. An investigation of partial cone cracks in silicon nitride balls. *International Journal of Solids and Structures*, **45**, 6301-6315.
- Love, A.E.H., 1927. *Treatise on the Mathematical Theory of Elasticity*, Dover Publications, New York.
- Lucek, J. W. 1990. Rolling wear of silicon nitride bearing materials. *ASME paper No. 90-GT-165*.
- Lucek, J. W. and Cowley, P. E. 1978. Investigation of the use of ceramic material in aircraft engine bearings. *Dept. of Navy, Code AIF-52032A*. Washington.
- Lundberg, G., Palmgren, A., 1952, Dynamic Capacity of Roller Bearings, *Acta Polytechnica, Mechanical Engineering Series*, Royal Swedish Academy of Engineering Sciences, Vol. 2, No. 4.
- Lundberg, G., and Palmgren, A., 1947, Dynamic Capacity of Rolling Bearings, *Acta Polytechnica, Mechanical Engineering Series*, Royal Swedish Academy of Engineering Sciences, Vol. 1, No. 3, pp 1-52.
- Mathworks, Inc., 2005. *MATLAB Function Reference Manual*, Version 7.0.4.365 (R14) Mathworks, Inc., Cambridge, MA.
- Mackerle, J., 2001. Finite element and boundary element analysis on indentation problems: a biography (1997-2000), *Finite Elements in Analysis and Design*, **37**, 811-819.
- Mackerle, J., 2002. Ceramics and ceramic matrix composites: finite element and boundary element analyses: a biography (1998-2000), *Finite Elements in Analysis and Design*, **38**, 567-577.
- Marshall, D. B., 1984. Mechanisms of Failure from Surface Flaws in Mixed-Mode Loading, *J.Am. Ceram. Soc.*, **67**, 2, 110-116.

- Marshall, D.B., Lawn, B.R., Mecholsky, J.J., 1980. Effect of Residual Contact stresses on Mirror/Flaw Size Relation, *J. Am. Ceram. Soc.*, **63**, 5-6, 358-360.
- Maw, N., Barber, J.R., Fawcett, J.N., 1976. The oblique impact of elastic spheres, *Wear* **38**, 101-114.
- Maw, N., Barber, J.R., Fawcett, J.N., 1981. The role of elastic tangential compliance in oblique impact, *Journal of Lubrication Technology*, ASME Transaction, **103**, 74-80.
- Mecholsky, J. 2008. Private Communication, Department of Materials Science and Engineering, University of Florida.
- Mi, Y., Aliabadi, M.H., 1995. An automatic procedure for mixed-mode crack-growth analysis, *Commun. Numer. Meth. Engng.*, **11**, (2), 167-177
- Mindlin, R.D., Deresiewicz, H., 1953. Elastic spheres in contact under varying oblique forces, *Journal of Applied Mechanics*, **75**, 327-344.
- Miner, J.R., Dell, J., Galbato, A., and Ragen, M. A., 1996. F-117-PW-100 hybrid bearing ceramic technology insertion, *ASME Journal of Engineering for Gas Turbines and Power*, **118**, 434-442.
- Mitchell, N.B., The Indirect Tension For Concrete, *Materials Research and Standards, ASTM*, October 1961, 780-788.
- Morrison, F. R. McCool, J. I. and Yonushonis, T. M. 1984. The load-life relationship for M50 steel bearings with silicon nitride ceramic balls. *J. of ASLE, Lubrication Engineering*, **40**, 153-159.
- Myers, R. H. and Montgomery, D. C. (2002), *Response Surface Methodology*, 2nd Ed., Wiley, New York, NY
- Newman, J.C. and Raju, I.S., 1981, An empirical stress-intensity factor equation for the surface crack," *Engineering Fracture Mechanics*, **15**, pp. 185.
- Ogden, William, 2008, Private Communication. Pratt & Whitney, Co.
- Ohgushi, K., Ichikawa, M., 1996. Fracture mechanics study of ring crack initiation in ceramics by sphere indentation, *JSME International Journal, Series A: Mechanics and Materials in Engineering*, **39**, 4, 489-495.
- Parker, R. and Zaretsky, E. V. 1975. Fatigue life of high-speed ball bearings with silicon nitride balls. *Trans. of the ASME, Journal of Lubrication Technology* (July), 350-357.
- Paris, P. and Erdogan, F. 1963. A critical analysis of crack propagation laws. *ASME Jour. Basic Eng.*, **85**, 528-534.

- Petrovic, J. J., Mendiratta, M. G., 1977. Correction of Mixed-Mode Fracture from Controlled Surface Flaws in Hot-Pressed Si<sub>3</sub>N<sub>4</sub>, *J. Am. Ceram. Soc.*, **60**, 9-10, 463.
- Petrovic, J.J., Mendiratta, M.G., 1976. Mixed-mode fracture from controlled surface flaws in hot pressed silicon nitride, *J Amer Ceram Soc*, **59**, 3-4, 163-167.
- Piotrowski, A. E., O'Brien, M. J., 2006. A novel test method to measure the fracture toughness of ceramic balls used in bearings, *Fatigue and Fracture in Engineering of Materials and Structures*, **29**, 558-572
- Qian, J. and Fatemi, A., 1996. Mixed mode fatigue crack growth: a literature survey. *Engineering Fracture Mechanics*. 55, 6, 1-10.
- Queipo, N.V., Haftka, R.T., Shyy, W., Goel, T., Vaidyanathan, R. Tucker, P.K. (2005). Surrogate-based Analysis and Optimization, *Progress in Aerospace Sciences*, **41**, 1-28.
- Rajaram, H., S. Socrate and D. M. Parks, 2000, Application of domain integral methods using tetrahedral elements to the determination of stress intensity factors, *Engineering Fracture Mechanics*, **66**, 5, 455-482.
- Rice, J.R. 1968, A Path Independent Integral and the Approximate Analysis of Strain Concentration by Notches and Cracks, *J. of Appl. Mech.*, **35**, 379-386.
- Richard, H.A., Fulland, M., and Sander, M. 2005. Theoretical crack path prediction, *Fatigue and Fracture in Engineering of Materials and Structures*, **28**, 3-12.
- Sackfield, A., Hills, D.A., 1983. A note on the Hertz contact problem: a correlation of standard formulae, *Journal of Strain Analysis for Engineering Design*, **18**, 2, 195-197.
- Sadeghi, F., Jalalahmadi, B., Slack, T.S., Raje, N., Arakere, N.K., (2009). A review of rolling contact fatigue, *Journal of Tribology*, 131, (Accepted for publication).
- Sih, G.C., 1974. Strain-Energy Density Factor Applied to Mixed-Mode Crack Problems, *Int. J. Fract.*, **10**, 3, 305-331.
- Shao, M., Badler, N. (1996), Spherical Sampling by Archimedes Theorem, *MS-CIS-96-02*, Department of Computer and Information Science, University of Pennsylvania, PA
- Smith, S.M., Scattergood, R.O., 1992. Crack-shape effects for indentation fracture toughness measurements, *J. Am. Ceram. Soc.*, **75**, 305-315.
- Tanaka, K., 1996. Fatigue Propagation from a Crack Inclined to the Cyclic Tensile Axis, *Eng. Fract. Mech.*, **55**, 6, 969.

- Tanimoto, K., Kajihara, K., and Yanai, K., 2000. Hybrid ceramic ball bearings for turbochargers, *SAE Paper* 2000-01-1339, 1-14.
- Tong, J., Wong, K.Y., Lupton, C., 2007. Determination of interfacial fracture toughness of bone-cement interface using sandwich Brazilian disks, *Engineering Fracture Mechanics*, **74** 12, 1904–1916.
- Wang L. Snidle RW. Gu L. 2000, Rolling contact silicon nitride bearing technology: A review of recent research. *Wear*, **246** 159-173.
- Wang, Y., 2000, "Failure modes of silicon nitride rolling elements with ring cracks," PhD Thesis, Bournemouth University, UK.
- Wang, Y., Hadfield, M., 2000. The influence of ring crack location on the rolling contact fatigue failure of lubricated silicon nitride: experimental studies, *Wear*, **243**, 157-166.
- Warrier, S.G., Jarmon, D.C., and Chin, H.A. 2000. Finite element analysis of the critical flaw size in hybrid silicon nitride bearing ball. *ASME Paper: 2000-GT-65*.
- Zhao, P., Hadfield, M., Wang, Y., Vieillard, C., 2006. Subsurface propagation of partial ring cracks under rolling contact Part 1. Experimental Studies, *Wear*, **261**, 382-389.
- Zhou, J., Wang, Y. and Xia, Y., 2006. Mode-I fracture toughness measurement of PMMA with the Brazilian disk test, *J. of Materials Science*, **41**, 17, 5778-5781.

## BIOGRAPHICAL SKETCH

George Arthur Levesque IV was born and raised in Dartmouth, Massachusetts. After completing Dartmouth High School in 2001, he attended Bridgewater State College in Bridgewater, Massachusetts and earned a Bachelor of Science degree in physics (with honors), mathematics, and criminal justice in 2005. Fall 2005, he attended the University of Florida direct PhD program in the Department of Mechanical and Aerospace Engineering as an Alumni Fellow under Dr. Nagaraj Arakere.